AMORPHOUS TERNARY DIFFUSION BARRIERS
FOR SILICON METALLIZATIONS

Thesis by
Jason S. Reid

In Partial Fulfillment of the Requirements
for the Degree of
Doctor of Philosophy

California Institute of Technology
Pasadena, California

1995
(Defended May 9, 1995)

© 1995
Jason S. Reid
All Rights Reserved

Ὅϖα

Acknowledgments

HALF WAY between Pooh's house and Piglet's house was a Thoughtful Spot where they met sometimes when they had decided to go and see each other, and sit down there for a little and wonder what they would do now that they had seen each other. One day when they had decided not to do anything, Pooh made up a verse about it, so that everybody should know what the place was for.

This warm and sunny Spot
Belongs to Pooh.
And here he wonders what
He's going to do.
Oh, bother, I forgot—
It's Piglet's too.

– A.A. Milne, The House at Pooh Corner.

Many of the experiments performed for this thesis would not have been possible without the kind assistance of others. Channing Ahn was immensely helpful in acquiring and analyzing the electron energy loss data at all hours of the night. The small-angle X-ray diffraction patterns were measured by Greg Beaucage of Sandia National Laboratories. Ron Ruiz of the Jet Propulsion Laboratory performed all of the scanning electron microscopy. Frank Cordone and Devendra Gupta of IBM performed the secondary ion mass spectrometry measurements. Carol Garland prepared the W-Si-N/Al cross-sections for transmission electron microscopy and thoughtfully supplied a steady diet of snails for my turtles. Matt Angyal of Cornell University measured the film stresses, performed the bias-thermal-stress tests, and teamed with David Lilienfeld of the National Nanofabrication Facility in fabricating and measuring the "topside" contact resistivity structures. Bill Dauksher of Motorola supplied the GaAs substrates for the stress measurements. Paul Smith and Ron Jones of the MDL at Sandia generously allocated many resources for constructing the shallow-junction diodes and "upside-down" contact resistivity structures, and loaned me a flatbed scanner. The staff of the MDL largely built the diode and upside-down contact resistivity strucutres, and contributed many helpful ideas to

the designs. Chris Apblett at Sandia assisted in fabricating the SiN membranes. Jon Custer at Sandia performed the 24 MeV Si^{4+} elastic recoil measurements of the WBN films.

Closer to the third floor of Steele, I deeply thank my advisor, Professor Marc-A. Nicolet, for providing an unparalleled research environment and infallible support. His thoughtfulness will always be warmly remembered. I am greatly indebted to Elzbieta Kolawa, my closest collaborator in the group, for introducing me to the field of diffusion barriers. Other collaborators who deserve thanks are Jen-Sue Chen, Richard Liu, Pekka Pokela, Gerard Keteffian, Donald Lie, Gang Bai, Tab Stephens, and Lou Halperin. Bruce Gorris, Bart Stevens, and Ed Yoho, who provided valuable technical assistance for the accelerator and sputtering systems, are also appreciated.

Channing Ahn, Matt Angyal, Jon Custer, Pam Gatts, and Elzbieta Kolawa generously proofread this thesis. Financial support for my research was provided by the Army Research Office and Sandia National Laboratories. I am particularly indebted to the Intel Foundation and to the Amoco Foundation for fellowships, and to Ron Jones and Paul Smith at Sandia for a summer internship. My mom, Leora, obtained several obscure published references and lightened my days with regular "News of the Weird" clippings. For several seasons of softball and basketball, I thank all of my teammates of the Infrared Sox and its various incarnations.

The late Professor Ken Greider of U.C. Davis deserves credit for instilling upon me a very human perspective on physics and shaping my attitudes as a researcher. His lessons on Clifford Algebra have left a lasting impression.

And to my wife, Niki: thank you for going to the library at midnight and slipping food under my door during the thesis writing. Your patience, love, and support will not be forgotten. I suppose I owe you an Appaloosa.

Abstract

Reactively sputtered from transition-metal silicide or boride targets in Ar/N_2 discharges, thin amorphous films of TM-Si-N (TM = Mo, Ta, Ti, or W) and W-B-N are investigated. Resistivity, density, stress, and structure are given as functions of composition, and in some cases, temperature. As-deposited films typically contain 100 to 900 MPa of compressive stress, which can be fully relaxed on <Si> substrates through annealing at 400 to 500°C. Transmission electron microscopy shows that most of the films are marginally amorphous with the scale of local order ranging from 0.5 to 1.5 nm. Small-angle scattering experiments reveal local chemically dissimilar regions within the films. When fully nitrided, Si appears to be preferentially bonded to nitrogen in the form of Si_3N_4 in the TM-Si-N films, according to extended energy loss fine structure (EXELFS) measurements.

According to tests on shallow-junction diodes, 100-nm thick TM-Si-N barriers are able to prevent aluminum overlayers from spiking the Si substrate at temperatures above aluminum's melting point, 660°C. The exceptional degree of stability is partly attributable to a 3 nm, self-sealing AlN layer which grows at the TM-Si-N/Al interface. By virtue of the self-sealing layer, secondary ion mass spectrometry (SIMS) measurements of $Ta_{36}Si_{14}N_{50}$ (100 nm)/Al (7 nm)/$Ta_{36}Si_{14}N_{50}$ (50 nm) trilayers after a 700°C/10 h vacuum anneal reveal no diffusivity of Al in $Ta_{36}Si_{14}N_{50}$ films.

The performance of the TM-Si-N and W-B-N barriers with copper overlayers is equally impressive. At the proper compositions, 100-nm barriers prevent copper from diffusing into the junction at 800°C or higher for a 30-min vacuum annealing. Diode failure typically corresponds to the crystallization temperature of the barrier, which can be reduced by the presence of copper. Once the barrier crystallizes, well-defined grain boundaries are introduced that provide fast diffusion paths for Cu. Paring the barriers' thickness down to 10 nm lowers the barriers' effectiveness to approximately 650°C. Bias stress testing of 10-nm TM-Si-N barriers with Cu overlayers on MOS capacitors reveals no penetration of Cu into SiO_2 during an 80 h

treatment at 300°C and 1 MV/cm applied field. Preliminary diffusion measurements of Cu in $Ta_{36}Si_{14}N_{50}$ films by SIMS yield an approximate diffusivity constant of D_{CU} = (0.014 cm^2/s) $\times$ exp(-2.7 eV/kT).

Through a microscopic four-point probe lithographically defined on a Cu/barrier/Cu trilayer stack, the specific contact resistances of barrier/Cu interfaces are determined for TM-Si-N, TiN, and W barriers. In all instances, the contact resistance is approximately 10^{-9} Ω cm^2 for as-deposited samples. The lack of difference among the barriers may be attributable to inadequate vacuum leading to interfacial impurities.

Table of Contents

Copyright Page ii
Acknowledgments iv
Abstract vi
Table of Contents viii

Chapter 1. Introduction 1

Chapter 2. Properties of Amorphous TM-Si-N (TM=Mo, Ta, Ti, or W) and W-B-N Thin Films 10
2.1 Deposition 10
2.2 Composition 14
2.3 Density 20
2.4 Electrical Properties 22
2.5 Loss of Volatile Species: Nitrogen and Argon 26
2.6 Mechanical Properties 30

Chapter 3. Structure 38
3.1 Introduction 38
3.2 X-ray Diffraction and Crystallization 40
3.2.1 Mo-Si-N 41
3.2.2 Ta-Si-N 42
3.2.3 Ti-Si-N 43
3.2.4 W-Si-N from a W_5Si_3 target 43
3.2.5 W-Si-N from a WSi_2 target 43
3.2.6 W-B-N 44
3.3 Transmission Electron Microscopy 45
3.4 Small-Angle X-ray and Electron Scattering 58
3.5 Extended Energy Loss Fine Structure (EXELFS) 65

Chapter 4. TM-Si-N Diffusion Barriers between Al and Si 79
4.1 Introduction 79
4.2 Evaluation of Amorphous, Nitrogen-Free TM-Si Barriers 84
4.3 Evaluation of Amorphous TM-Si-N Barriers 90
4.4 Concluding Remarks 92

Chapter 5. TM-Si-N and W-B-N Diffusion Barriers between Cu and Si, and Cu and SiO_2 104
5.1 Introduction 104
5.2 TM-Si-N/Cu and TM-B-N/Cu Thermodynamics 105
5.2.1 TM-N-Cu Systems 106
5.2.2 TM-B-Cu Systems 107
5.2.3 Si-N-Cu and B-N-Cu Systems 107
5.2.4 $TM_{v,vi}$-Si-Cu Systems 108
5.2.5 Thin-Film Experiments on $TM_{v,vi}$-Si-Cu Systems 109
5.2.6 Ti-Si-Cu and Ti-Si-N-Cu Systems 111
5.2.7 Summary of Thermodynamics 112
5.3 Stability of Nitrogenless TM-Si/Cu and W-B/Cu Metallizations 120
5.4 Stability of TM-Si-N/Cu and W-B-N Metallizations on <Si> 127
5.4.1 Mo-Si-N/Cu 127
5.4.2 Ta-Si-N/Cu 128
5.4.3 Ti-Si-N/Cu 130
5.4.4 W-Si-N/Cu 130
5.4.5 W-B-N/Cu 132
5.4.6 Comparison with Polycrystalline TiN Films 133
5.4.7 Remarks on TM-Si-N/Cu and W-B-N/Cu Metallizations 134
5.5 Thermal Diffusion of Cu in Ta-Si-N 143
5.6 Bias-Stress Testing of TM-Si-N/Cu on MOS Capacitors 153
5.7 Barrier/Cu Contact Resistance 158

Appendix I. Diode Process Flow 174
Appendix II. Process Flow for Fabricating Four-Point Probe Contact Resistivity Structures (topside approach) 181
Appendix III. Process Flow for Fabricating Four-Point Probe Contact Resistivity Structures (upside-down approach) 188

Chapter 1. Introduction

Diffusion barriers are thin films introduced between two materials to prevent their interaction. Industrially, important applications of diffusion barriers arise in microelectronic applications. Figure 1.1 shows a simplified cross-section of a multi-level metallization scheme to demonstrate the various uses of barrier materials in integrated circuits. In today's Very Large Scale Integration (VLSI) technology, the interconnect metal is sputtered Al (with a few percent of Cu) with W plugs deposited by chemical vapor deposition (CVD) sometimes serving as vias. Barriers are used to separate Al and silicide-contacting layers on Si, as well as to separate top-level Al interconnects and gold wire-bond pads. They also provide nucleation sites for CVD W [1-5] and act as a glue layer for reflowed Al [6-8] in vias. Additionally, barriers are often used to mechanically contain the interconnect to thwart electromigration as well as shunt the current flow when significant electromigration does occur. With the advent of copper metallizations, robust barriers will be needed to completely surround the Cu to preclude the thermal diffusion [9,10] and biased drift of Cu [11,12] through the SiO_2 interlevel dielectric.

In describing the requirements placed on diffusion barriers, it is instructive to briefly summarize a few of the salient processes necessary in fabricating a VLSI circuit. Following high-temperature anneals associated with thermal oxidation, dopant activation, and silicide formation at the incipient stages of integrated circuit fabrication, the barrier, interconnect, and via metals are introduced. Because of the high degree of conformality associated with CVD films, W made from a WF_6 precursor is often used to fill high-aspect ratio vias at a deposition temperature of 300 to 450°C [2,13]. Excess W outside the via may be removed through dry etching [14,15] or by chemical- mechanical polishing (CMP) [16,17]. If Al via material is desired, a deposition temperature of 400 to 500°C during sputtering is usually required to "reflow" the Al uniformly into high-aspect ratio vias in high-density circuits [6-8]. Similar temperatures are required for the reflow of Cu [18,19]. After patterning the first layer of interconnects ("Metal 1" in Figure 1.1), a dielectric layer is overlayed, which

is typically SiO_2 deposited by plasma-enhanced chemical vapor deposition with TEOS ($Si(OC_2H_5)_4$) precursors at a temperature of approximately 350°C or by curing spin-on glasses at 400°C [20,21]. Sometimes B or P are added to the SiO_2 to aid in planarizing the dielectric, reducing stress, and gettering sodium [20]. Otherwise, CMP may be used for planarization [22]. With subsequent vias etched through the dielectric, another layer of barrier, W, Al, and perhaps another barrier layer are added. In some instances, additional post-metallization sinterings as high as 500°C may be employed to reduce contact resistances [23]. The process is continued until all of the metal layers are fabricated, whereupon a top-level passivation layer is added.

From the preceding description, it is clear that a barrier must be able to contain Al or Cu at temperatures as high as 500°C for periods as long as 1 h. With present commercial circuits rapidly approaching 5 layers of interconnects, 0.25-μm wide vias, sub-5-nm gate oxides, and 50-nm shallow-junctions, very stringent requirements are placed on diffusion barriers. From electrical considerations, the barrier must furnish low contact resistance to the Al (or Cu), W, and silicides, and must be made sufficiently thin to minimize transverse resistances across the barrier and the via. Device manufacturers often desire a resistance of less than 1 Ω per via [24]. In the case of $0.25 \times 0.25\ \mu m^2$ vias, both the contact resistances and the product of the barrier's resistivity and thickness must therefore be below $10^{-9}\ \Omega\ cm^2$. With barrier resistivities often in the 100 to 1000 μΩ cm range, the barrier may need to be made thinner than 10 nm.

In formulating a barrier, the requirements are multifarious and mutually exclusive. For instance, a barrier's high degree of chemical intertness, which is needed to prevent the two flanking materials from interacting, is not always conducive to good adhesion and low contact resistance [25]. Even if chemical intertness in the bulk is achieved, the deposition of the barrier must produce a microstructure amenable to relatively few extended defects. At low temperatures, diffusion is often governed by grain boundaries or other extended defects rather than lattice diffusion

[26]. An excellent example of this situation arises with Ta barriers between Cu and Si. Tantalum and copper are thermodynamically immiscible in one another, yet a 100-nm Ta film does not prevent Cu from reaching the Si during a 450°C/30 min heat treatment [27]. The reason presumably stems from grain boundary diffusion of Cu through Ta.

In a tightly structured, multilayered integrated circuit, the barrier must also be mechanically congruous with its environment. To avoid cracking or delamination, the barrier should be under low stress and possess good adhesion. The coefficient of thermal expansion of the barrier should ideally match the surrounding materials. Additionally, in keeping with the definition of a diffusion barrier, the barrier should avoid any significant reaction with its environment. Any volume changes associated with the barrier's reaction can add additional stresses which can also lead to cracking or delamination.

Compendia of barrier works can be found in several reviews [28-34] as well as in Chapters 4 and 5 of this thesis. In general, barriers tend to be categorized according to a three-class scheme developed by Nicolet [28,33]. In one class, designated as "sacrificial barriers," adjacent materials controllably consume the barrier. The barrier functions for only a limited duration until the barrier is entirely exhausted. Elemental barriers such as Ti [35,36], V, and Cr [37,38] between Si substrates and Al overlayers demonstrate this behavior. By nature of the interfacial cleaning, sacrificial layers often yield low contact resistances, but their effectiveness in blocking interdiffusion is often marginal, especially when made very thin. "Stuffed barriers" work on the premise of decorating the grain boundaries of polycrystalline materials with light elements such as oxygen, nitrogen, or carbon. The exact impurity levels can often be controlled by changing the base pressure of the deposition system or the deposition ambient. With the grain boundaries "stuffed," fast diffusion between the grains can be significantly hindered. Mo and Ti-W films for Al are prototypical examples [39,40]. Unfortunately, stuffing a barrier can sometimes lead to adverse mechanical properties such as higher stress [40] or embrittlement [41,42]. Finally,

"passive barriers" do not react with their adjacent materials and afford very low diffusivities in a given temperature range. For Al metallizations, truly passive barriers are hard to achieve because of the nearly ubiquitous reactivity of Al [43]. Developing barriers for Al usually involves increasing the kinetic impediments to brake the reaction and increase the reaction temperature. Early transition metal nitrides, borides, and carbides tend to fall into the "passive barrier" category. In today's circuits, TiN is the prevailing barrier for Al. Given the lack of chemical reactivity of Cu with some early transition metals, nitrogen, boron, and carbon, the nitride, boride, and carbide barriers often provide passive protection from Cu diffusion.

This thesis gives a comprehensive overview of a nascent and unparalled class of amorphous or near-amorphous ternary diffusion barriers consisting of an early transition metal (Mo, Ta, Ti, or W), a metalloid (Si or B), and nitrogen. The films are produced through reactive rf-sputtering of a metal silicide or metal boride target in an Ar/N_2 discharge. In depositing any thin film, certain fundamental properties are always of interest. Chapter 2 gives a survey of the deposition conditions, relative compositions, electrical attributes, and mechanical properties as functions of temperature. The primary analysis methods include MeV ^{4}He backscattering, stylus profilometry, four-point probe resistivity measurements, and laser-read wafer curvature measurements. Chapter 3 discusses the structure and crystallization of the ternary barriers by means of X-ray diffraction, transmission electron microscopy, small-angle X-ray and electron scattering, and extended energy loss fine structure (EXELFS) experiments. In Chapter 4, the ternary barriers are evaluated as diffusion barriers between <Si> substrates and Al overlayers. In assessing the raw stability of the metallization, shallow-junction diodes (process flow given in Appendix I) are used as substrate material, which provide an extremely sensitive, yet practical means of evaluation. Ancillary techniques of X-ray diffraction, ^{4}He backscattering, scanning electron microscopy, transmission electron microscopy, and secondary ion mass spectrometry are also utilized to understand the stability and failure modes of the barriers. Similarly, Chapter 5 describes the stability of the barriers between <Si> substrates and Cu overlayers. The bias-temperature-stress testing of

barrier/Cu metallizations on MOS capacitors will also be reported. In addition, the barrier/Cu contact resistance measured using a novel, microscopic four-point probe technique applied to blanket Cu/barrier/Cu trilayer stacks is discussed in Chapter 5.

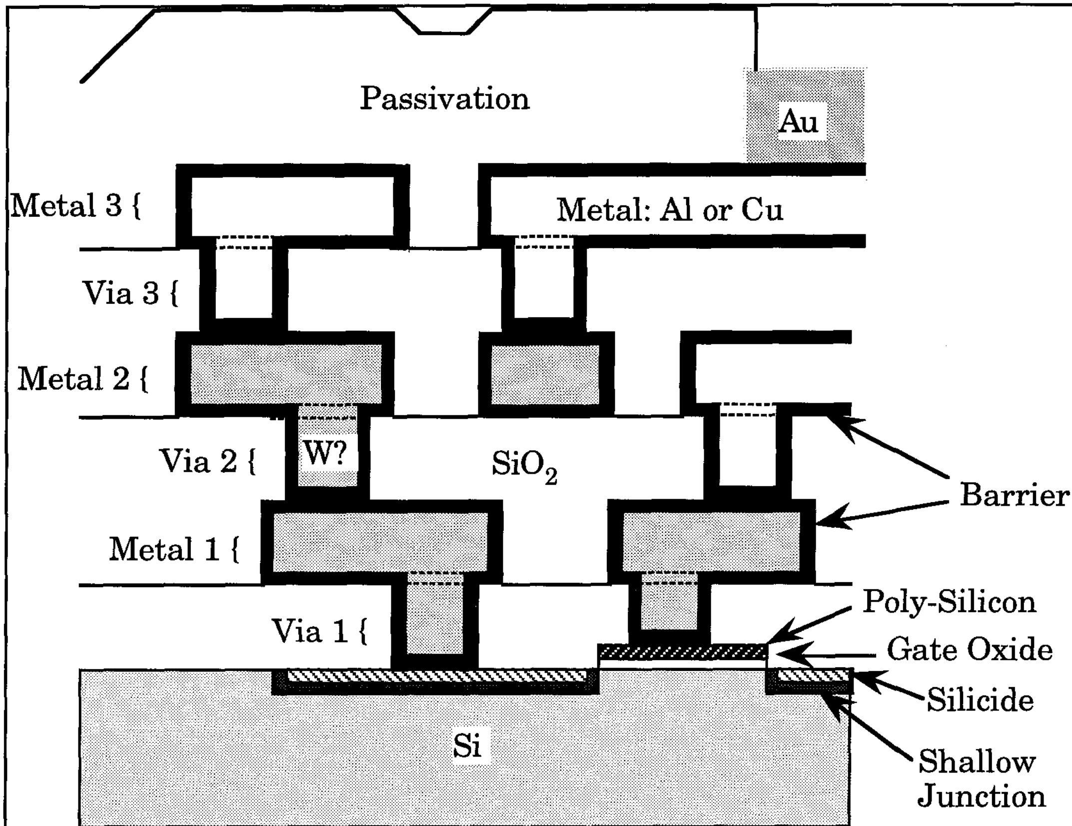

Figure 1.1. Simplified cross-section of a multi-level metallization scheme. In Al metallizations, total encapsulation of the metal is unnecessary. Because of the difficulty in implementing side-wall barriers on interconnects, a very thin blanket film of SiN covering the inconnects may be implemented in Cu metallizations.

References, Chapter 1.

[1] J.R.Creighton, *Thin Solid Films* 241, 310 (1994).

[2] J.R. Creighton and J.E. Parmeter, *Critical Reviews in Solid State and Materials Sciences*, 18, 175 (1993).

[3] Y.J. Lee, C.O. Park, D.W. Kim, and J.S. Chun, *J. Electronic Mat.* 23, 1075 (1994).

[4] E.S. Kim, C.M. Lee, J.G. Lee, and H.B. Im, *Materials Sci. and Eng. B* 17, 137 (1993).

[5] S.L. Lantz, A.E. Bell, W.K. Ford, and D. Danielson, *J. Vac. Sci. A* 12, 1032 (1994).

[6] M. Okihara, N. Hirashita, K. Hashimoto, and H. Onoda, *Appl. Phys. Lett.* 66, 1328 (1995).

[7] Z. Xu, H. Kieu, I.J. Raaijmakers, and A. Tepman, *Thin Solid Films* 253, 367 (1994).

[8] C. Yu, G.S. Sandhu, and T.T. Doan, *J. Appl. Phys.* 72, 1599 (1992).

[9] H. Miyazaki, H. Kojima, A. Hiraiwa, Y. Homma, and K. Murakami, *J. Electrochem. Soc.* 139, 3264 (1992).

[10] D. Gupta, K. Vieregge, and K.V. Srikrishnan, *Appl. Phys. Lett.* 61, 2178 (1992).

[11] J.D. McBrayer, R.M Swanson, and T.W. Sigmon, *J. Electrochem. Soc.* 133, 1242 (1986).

[12] Y. Shacham-Diamond, A. Dedhia, D. Hoffstetter, and W.G. Oldham, *J. Electrochem. Soc.* 140, 2427 (1993).

[13] A. Sherman, *Chemical Vapor Deposition for Microelectronics: Principles, Technology, and Applications*, Noyes Publications, Park Ridge, NJ (1987) chap. 4.

[14] P.E. Riley and T.E. Clark, *J. Electrochem. Soc.* 138, 3008 (1991).

[15] K. Koller, H.P. Erb, and H. Körner, *Appl. Surf. Sci.* 53, 54 (1991).

[16] F.B. Kaufman, D.B. Thompson, R.E. Broadie, M.A. Jaso, W.L. Guthrie, D.J. Pearson, and M.B. Small, *J. Electrochem. Soc.* 138, 3460 (1991).

[17] H. Landis, P. Burke, W. Cote, W. Hill, C. Hoffman, C. Kaanta, C. Koburger, W.

Lange, M. Leach, and S. Luce, *Thin Solid Films* 220, 1 (1992).

[18] D.C. Edelstein, C-K. Hu, C. Uzoh, and C. Cabral, presented at the Materials Reliability in Microelectronics V Symposium, Materials Research Society Spring Meeting, San Francisco, 1995 (in press).

[19] R.A. Brain, Ph.D. Dissertation, California Institute of Technology, in preparation.

[20] S. Wolf and R.N. Tauber, *Silcon Processing for the VLSI Era, Vol. 1*, Lattice Press, Sunset Beach, CA (1986) chap. 6.

[21] S. Wolf , *Silcon Processing for the VLSI Era, Vol. 2*, Lattice Press, Sunset Beach, CA (1990) chap. 4.

[22] I. Ali, S.R. Roy, and G. Shinn, *Solid State Technology* 37, 63 (1994).

[23] Y. Inoue, S. Tanimoto, K. Tsujimura, T. Yamashita, Y. Ibara, Y. Yamashita, and K. Yoneda, *J. Electrochem. Soc.* 141, 1056 (1994).

[24] Private Communication, D.B. Fraser, Intel Corporation.

[25] M. Ohring, *The Materials Science of Thin Films*, Academic Press, San Diego, CA (1992) pp. 440-443.

[26] D. Gupta, D.R. Campbell, and P.S. Ho, in *Thin Films–Interdiffusion and Reactions*, edited by J.M. Poate, K.N. Tu, and J.W. Mayer, Wiley-Interscience, New York (1978). p. 161.

[27] E. Kolawa, J.S. Chen, J.S. Reid, P.J. Pokela, and M-A. Nicolet, *J. Appl. Phys.*, 70, 1369 (1991).

[28] H.P. Kattelus and M-A. Nicolet, in *Diffusion Phenomena in Thin Films and Microelectronic Materials*, edited by D. Gupta and P.S. Ho, Noyes Publications, Park Ridge, New Jersey (1988) pp. 432-491.

[29] S.Q. Wang, *MRS Bulletin* 19, 30 (1994).

[30] S.Q. Wang, S. Suthar, C. Hoeflich, and B.J. Burrow, *J. Appl. Phys.* 73, 2301 (1993).

[31] R. de Reus, in *Intermetallic Compounds–Principles and Practice*, edited by J.H. Westbrook and R.L. Fleischer, John Wiley and Sons, Chicester, England (1993).

[32] J. Li, Y. Shacham-Diamand, and J.W. Mayer, *Materials Science Reports* 9,

1 (1992).

[33] M-A. Nicolet, *Thin Solid Films* 52, 415 (1978).

[34] D. Pramanik and V. Jain, *Solid State Technology* 36, 73 (1993).

[35] R.W. Bower, *Appl. Phys. Lett.* 23, 99 (1973).

[36] C.Y. Ting and B.L. Croder, *J. Electrochem. Soc.* 129, 2590 (1982).

[37] M. Bartur and M-A. Nicolet, *J. Electrochem. Soc.* 131, 1118 (1984).

[38] M. Bartur, Ph.D. Dissertation, California Institute of Technology (1984).

[39] S. Raud, J.S. Chen, and M-A. Nicolet, *Appl. Phys. A* 52, 15 (1991).

[40] I.J. Raaijmakers, T. Setalvad, A.S. Bhansali, B.J. Burrow, L. Gutai, and K-B. Kim, *J. Electronic Mat.* 19, 1221 (1990).

[41] Private communication with T.W. Workman, Intel Corporation, in discussing problems of wirebonding to metallizations containing stuffed TiW.

[42] ref. 25, pp. 564-566.

[43] T.B. Massalski, *Binary Alloy Phase Diagrams. 2nd ed.*, ASM International, Materials Park, OH (1990).

Chapter 2. Properties of Amorphous TM-Si-N (TM=Mo, Ta, Ti, or W) and W-B-N Thin Films

2.1. Deposition

Except where noted, all of the films studied in this thesis were deposited by rf (13.56 MHz) sputtering in Ar or Ar/N_2 discharges. The sputtering source was a 7.5-cm, water-cooled cathode with a fixed circular magnetron. A 2-cm-diameter permanent magnet producing an 8 kilogauss field resided on the central pole piece of the iron magnetron assembly. The magnetron served to bend secondary electrons emitted from the target along the plane of the target to increase local ionization, but at the expense of annular target erosion [1]. Although dc sputtering is commercially popular for depositing conductive films, rf systems do have some advantages other than the ability to deposit insulators. Because of the higher ionization efficiency, rf discharges permit lower operating pressures than their dc counterparts. Consequently, the pump tends to be throttled less in rf depositions, thus giving lower background pressures of water vapor and other gases.

The pumping system for the sputtering chamber consists of a cryopump lying below a camera-like shutter throttle valve. Above the throttle valve resides a cryogenic (-40°C) baffle used to pump water vapor preferentially when the cryopump is throttled. An oil-based mechanical pump performs the roughing evacuation prior to switching in the cryopump. The base pressure with the throttle valve completely open is approximately 1×10^{-7} Torr. However, with the cryopump throttled for sputtering, the background pressure rises to almost 1×10^{-6} Torr. In practical terms, about one monolayer of background gases impinges on the substrate per second during sputtering. Figure 2.1 shows the partial gas pressures obtained with a residual gas analyzer for the throttle valve completely open and closed for sputtering. Nitrogen, presumably sourced through the numerous "o-ring" seals in the system, is the predominant gas, followed by H_2O, CO_2, O_2, and Ar. Hydrocarbon levels are less than 10^{-8} Torr.

Several different sputtering targets were used to synthesize the barriers: Mo_5Si_3, Ta_5Si_3, Ti_5Si_3, W_5Si_3, and W_2B. To study the effect of changing the metal-to-silicon ratio, a WSi_2 target was also used. All targets were manufactured from hot-pressed powders by the Cerac Corp. of Milwaukee, Wisconsin. The targets were quoted as "typically 99.5% pure." Table 2.1 lists the manufacturer's spectroscopic analysis for some of the targets. Based on the manufacturer's x-ray diffraction, the targets are reacted into the thermodynamically-expected silicides and borides.

Just prior to loading into the sputtering system, the Si substrates were etched in 1:15 HF:H_2O. All of the barrier films were deposited with 300 W RMS forward power at 10 mTorr pressure with a fixed flow of 60 sccm. Samples sat statically on a stage located about 10 cm beneath the target. The ejected species therefore underwent several or more collisions before landing on the substrate. For almost all of the barrier depositions, the stage floated electrically. In the case of the Mo-Si and Mo-Si-N films, a -115 V dc substrate bias was applied to minimize oxygen content through resputtering of light chemisorbed species. The dc self-bias of the capacitively-coupled target was nominally around -500 V and tended to increase with increasing nitrogen content in the discharge. Typical deposition rates were approximately 15 nm/min according to stylus profilometry measurements. The deposition temperature induced from plasma heating appears to be in the 100 to 140°C range, based on the behavior of photoresist on substrates.

As detailed in Chapter 3, almost all of the as-deposited films are amorphous, as determined by X-ray and/or electron diffraction. An exception occurs in nitrogen-rich Ti-Si-N films, which have a partial nanophase character. Depending on composition, the nitrogen-free silicides crystallize between 550 and 900°C. With sufficient nitrogen, the crystallization temperature rises in all the systems to 800°C or higher.

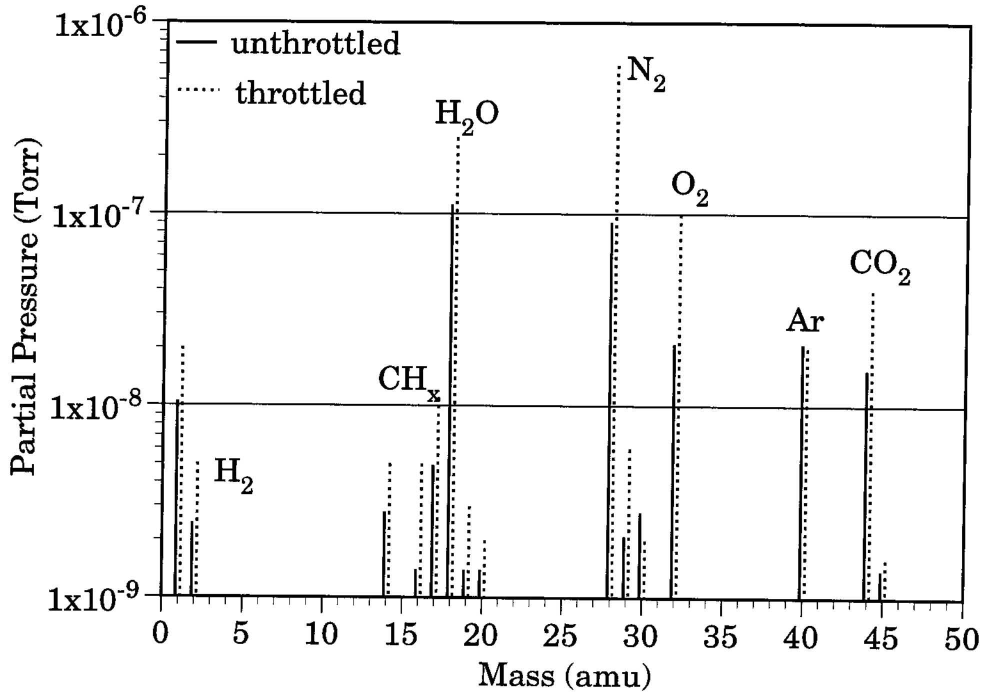

Figure 2.1. Residual gas analyzer scans of the sputtering system with the throttle valve completely open and partially closed for sputtering.

Table 2.1. Parts-per-million impurity levels in some of the sputter targets, as stated by the manufacturer.

Target	Al	B	Ca	Co	Cr	Cu	Fe	Mg	Mn	Ni	Si	Ti
Mo_5Si_3		50		80		20	600	800				
Ta_5Si_3	900		300			<100	<100	<100		900		
Ti_5Si_3	100		<10		10	100	1200	10		200		
W_5Si_3	200		<100		<100	<100	200	<100				
W_2B	200		<10			10	200	1000	100		100	300

2.2. Composition

Compositions were determined primarily through 2.0 or 2.5 MeV ^4He backscattering of the films deposited on carbon substrates, which afforded direct observation of elements heavier than the substrate constituent, carbon. The absolute accuracy level of the technique is approximately 5%. In the case of the W-B-N system, a 110 nm $\times$ 1 cm^2 silicon nitride membrane on a silicon frame was used as substrate to measure boron (Figure 2.2a). Additionally, the boron and hydrogen contents in W-B-N were measured by 24 MeV $^{28}Si^{4+}$ forward scattering at Sandia National Labs (Figure 2.2b).

The composition vs $N_2/(Ar+N_2)$ flow ratio is given in Figures 2.3a-f for films sputtered from the six targets. Oxygen and argon contents are typically around 2 at.% each for most of the barrier films. The Mo-Si-N films, however, harbor as much as 5 at.% oxygen when containing 30 to 50 at.% nitrogen. Without a substrate bias above -100 V dc, oxygen levels reach as high as 15 at.%. Native oxides on the W-B-N films are larger than on the silicon-based films. Hydrogen content is around 1 to 2 at.% for the W-B-N system.

Mass-dependent, preferential sputtering effects are clearly evident in the compositional trends of Figure 2.3. For the binary W- and Ta- silicide and boride films, the metal-to-silicon or metal-to-boron ratio is about 140% greater than their respective target's composition. In the lighter molybdenum system, $Mo_{74}Si_{26}$ films have a 70% greater ratio than the target composition of Mo_5Si_3. Still lighter, Ti-Si films match the target composition of Ti_5Si_3. With no *in-situ* diagnostics inside the sputtering system, the reason for the mass dependence is conjectural, especially when considering the complexities of rf sputtering. One possibility involves transient change in the stoichiometry of the target's surface. However, as the target erosion progress finally meets its steady-state bulk composition, the departure rate of the two species equals the target's composition (assuming no diffusion within the target). Given the reproducibility of the depositions, the transient effects outside

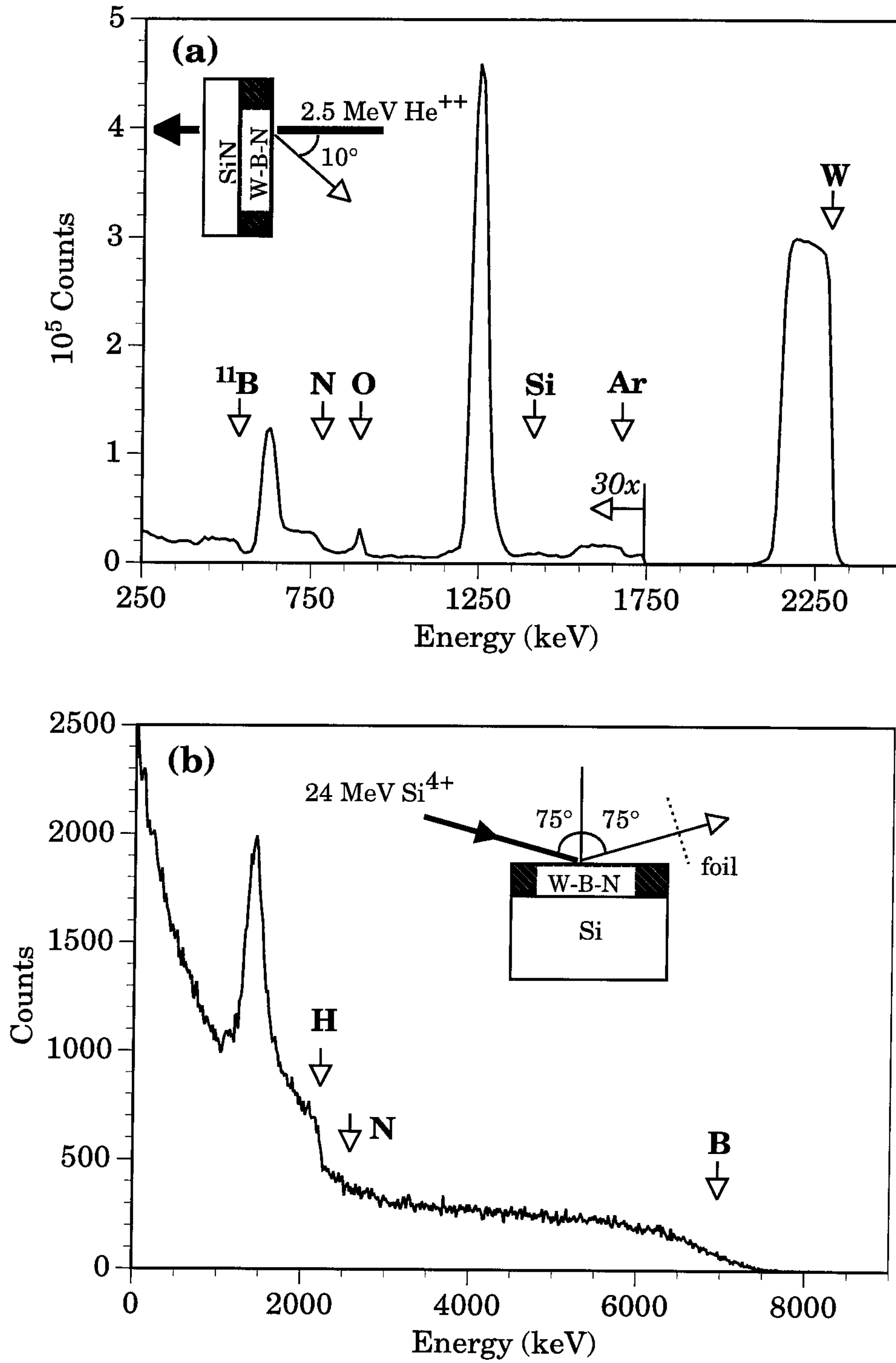

Figure 2.2. (a) 2.4 MeV ^4He backscattering of 130 nm $W_{64}B_{20}N_{16}$ films on a 110 nm silicon nitride membrane, and (b) 24 MeV $^{28}Si^{4+}$ elastic recoil scattering of the film on a <Si> substrate. Some of the W-B-N films exhibited an enhancement of hydrogen at the Si/W-B-N interface.

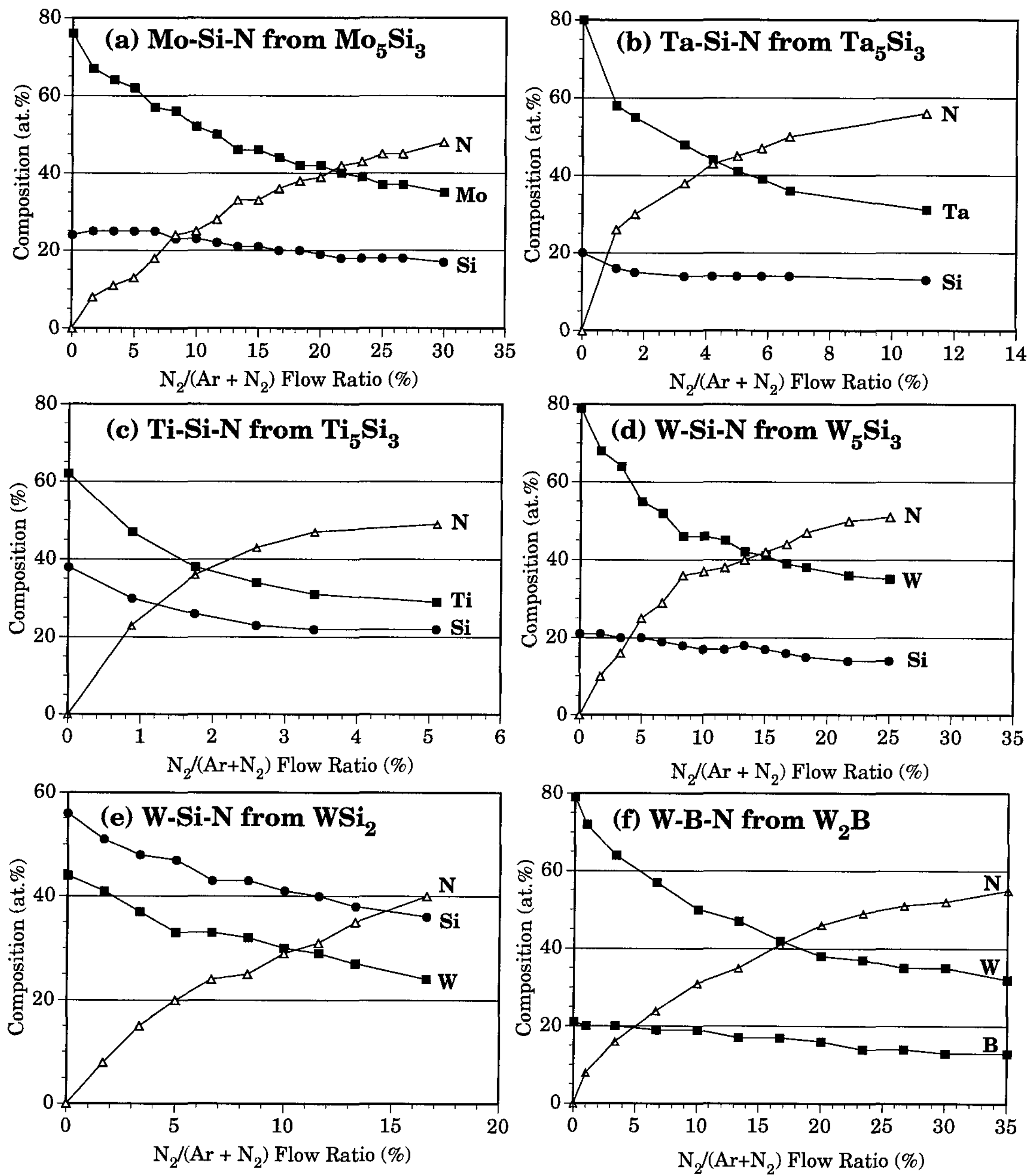

Figure 2.3. Compositional trends as a function of the partial N_2 flow ratio for films sputtered from Mo_5Si_3, Ta_5Si_3, W_5Si_3, WSi_2, Ti_5Si_3, and W_2B targets. The uncertainty is about ± 2 at.%.

steady-state conditions probably do not apply here. Another possibility for the mass-dependent stoichiometries is gas-phase scattering. Once ejected, atomic and molecular species will undergo collisions within the 10 mTorr discharge. Heavier species are more likely to be forward scattered than lighter components. Consequently, through gas-phase scattering, a larger flux of heavy species may be hitting the substrate directly below the target. Other variables affecting the binary films' composition include differences in sticking coefficients, incident energies, and resputtering phenomenon at the substrate.

Interestingly, for the cathode voltages used in sputtering the barriers, the lighter metalloid atoms may be more preferentially ejected in the direction of the target's normal direction than the heavier metal atoms, based on work by Olson et al. [2]. Complementarily, several investigators have studied 3-mTorr, dc-sputtering of Mo-, Ti-, and W-disilicides [3,4]. The low pressure was chosen to produce long mean free paths to circumvent gas-phase scattering. Directly underneath the target, the compositions of films sputtered from the Ti and W targets virtually matched the target compositions, but the Mo film showed an enhancement of Si. At larger angles from the target, all of the films showed an increase in the heavier metal content. The investigators noted that although preferential ejection predicts that the silicon content in the films should increase with larger metal masses, sticking coefficients also play an important role.

Figure 2.3 shows that nitrogen reactively incorporates itself into the films primarily at the expense of a decreased metal:silicon ratio, with the exception of the Ti-Si-N system. The metal:silicon and W:B ratios are still greater than the target composition in these nitrided systems, but the quotient does decrease with increasing nitrogen content. In the Ti-Si-N system, the Ti:Si ratio of 5:3 is virtually maintained independent of the nitrogen concentration. Affinity for nitrogen is greatest in the Ti and Ta systems. From the TM_5Si_3 and W_2B targets, the Ta-Si-N and Ti-Si-N systems contain 50 at.% nitrogen at flow ratios less than 5%, whereas the Mo-Si-N, W-Si-N, and W-B-N films require a flow ratio in excess of 25%. Comparatively, Ta-

and Ti-nitride films deposited from elemental targets typically contain more nitrogen than Mo- or W-nitrides under comparable sputtering conditions [5-10]. Although structurally similar, the Mo and W nitrides are far less thermodynamically stable than Ta and Ti nitrides, which may explain the differences in nitrogen incorporation for a given flow [11]. Changing the metal-to-silicon ratio in the tungsten silicide target dramatically changes the nitrogen content for the same flow conditions. Nitrogen is much more readily incorporated into films from the WSi_2 target than from the W_5Si_3 target. The reason may be a consequence of silicon's higher affinity for nitrogen over tungsten. Comparatively, our system produces stoichiometric Si_3N_4 at a $N_2/(Ar+N_2)$ flow ratio of only 5% from a polycrystalline Si target in a 300 W, 10 mTorr discharge. Thus, in the Mo-Si-N and W-Si-N films sputtered at low partial flows of N_2, nitrogen may be preferentially attached to silicon.

Serving as a template for surveying some of the physical properties of the ternary barriers, the compositional trends are also plotted on ternary diagrams for the four transition metal-Si-N [12] and W-B-N [12,13] systems in Figure 2.4. With their high degree of stability, Si_3N_4 and BN anchor most of the tie lines. The tie lines drawn with solid lines denote the equilibria at 1000°C. Tungsten and molybdenum nitrides, which tend to decompose above 700°C without the presence of nitrogen, are also included because of their relevance at room temperature. Tie lines between the tungsten nitrides and Si_3N_4 are therefore tentatively drawn to satisfy the phase rule as well as to account thermodynamically for the heavily nitrogen-laden compositions. For the Mo-Si-N system, Mo is experimentally known to sluggishly decompose Si_3N_4 at 1000°C. In addition, Gibbs free energy data do not predict the reaction to occur at lower temperatures because of the large negative entropy of formation of silicon nitride [14]. Accordingly, the Mo silicide-Si_3N_4 and Mo nitride-Si_3N_4 tie lines are included for systems at temperatures less than 700°C, as designated by dashed lines on the diagram.

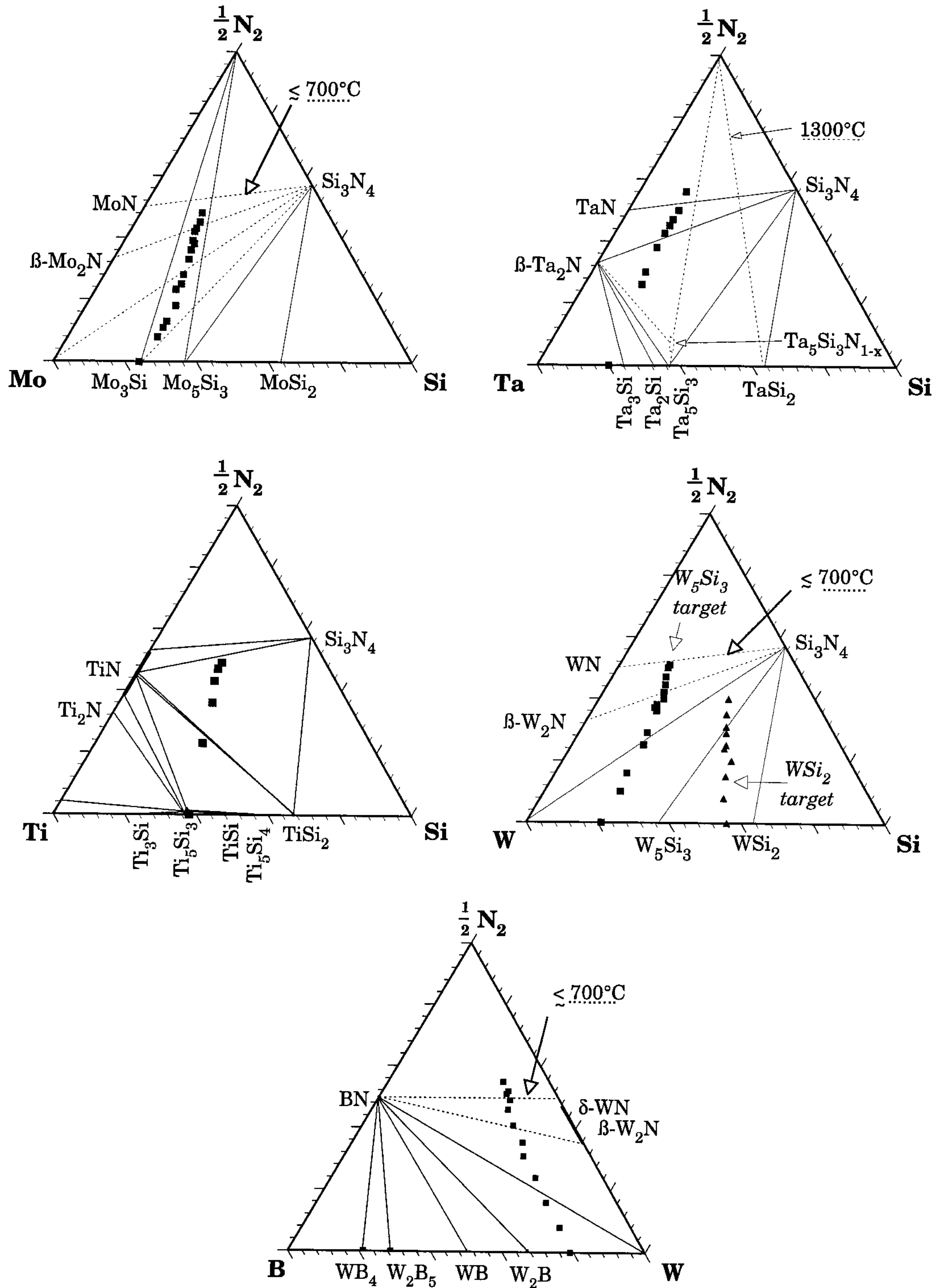

Figure 2.4. Experimental compositions from Figure 2.3 plotted on ternary phase diagrams of the Mo-Si-N, Ta-Si-N, Ti-Si-N, W-Si-N, and W-B-N systems. Solid lines denote the equilibrium tie lines at 1000°C. As noted, dashed lines designate the equilibria for other temperatures.

2.3. Density

Density was calculated by first obtaining atomic areal density data from ^{4}He backscattering spectrometry through the relation, $\Delta E_{metal} = [\varepsilon_o]_{metal}(Nt)$, where ΔE is the full-width-at-half-maximum of the metal signal, $[\varepsilon_o]_{metal}$ is the stopping cross-section associated with the metal in the so-called "surface energy approximation," and (Nt) is the areal density of the film [15]. With thickness known through stylus profilometry measurements (typically around 140 nm), the density may be obtained from dividing the areal density by the thickness.

Figure 2.5 shows the atomic density of the barrier films vs. nitrogen content for films sputtered from the six targets. The amorphous silicides all have densities approximately 6×10^{22} atoms/cm^3. In comparsion, the binary amorphous silicides tend to be less dense than their equilibrium bulk counterparts [16], as displayed on the right side of Figure 2.5. With the addition of 30 to 50 at.% nitrogen, the ternary silicide films achieve densities in excess of 8×10^{22} atoms/cm^3. The equilibrium metal nitrides and silicon nitride tend to be more dense than the silicides, which is consistent with the rise in density with increasing nitrogen content. W-B-N films sputtered from the W_2B target show a similar increase in density with increasing nitrogen content. They also have the highest densities for a given nitrogen concentration because of the large densities of bulk W_2B and BN.

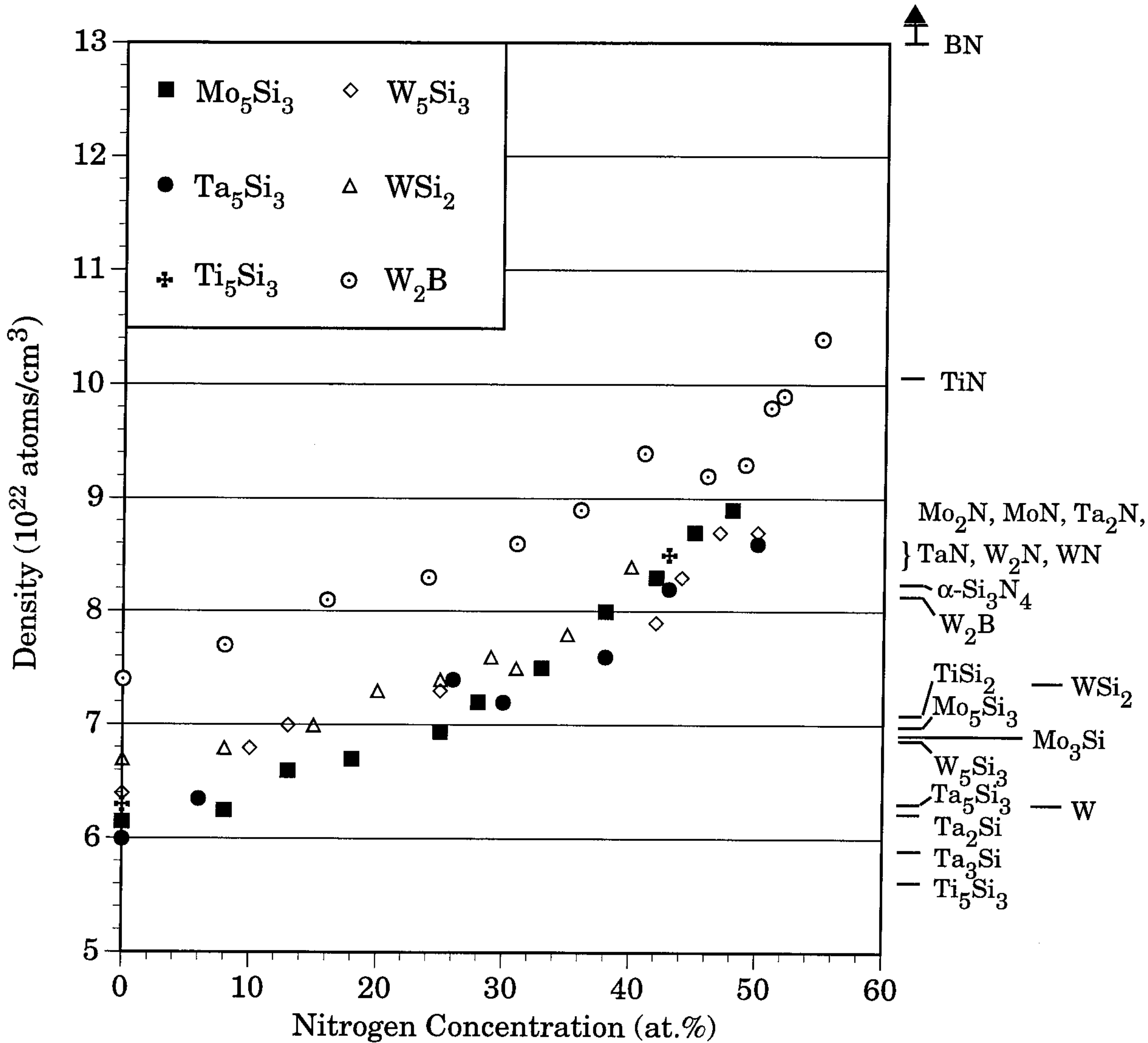

Figure 2.5. Atomic density vs. nitrogen concentration of the as-deposited films sputtered from the Mo_5Si_3, Ta_5Si_3, Ti_5Si_3, W_5Si_3, WSi_2, and W_2B targets. The uncertainty is about 8%. The bulk crystal densities for some silicides, borides, and nitrides are given on the right side of the figure.

2.4. Electrical Properties

The resistivity of the ternary systems produced from the six targets is given as a function of the films' nitrogen concentration in Figure 2.6. As-deposited, amorphous binary silicides and borides range in resistivity from a low of 190 μΩ cm for $Mo_{74}Si_{26}$ to a high of 300 μΩ cm for $W_{44}Si_{56}$. Not surprisingly, introducing nitrogen increases the resistivity of all of the systems. Although transition-metal nitrides often conduct as well as their silicide counterparts [11], boron- and silicon-nitrides are insulators. Any boron-nitrogen or silicon-nitrogen bonding in the films may not be conducive to electrical conduction. In addition, the metal-silicon and metal-boron ratios tend to decrease with nitrogen content, thus further suppressing the conduction, except for films from the WSi_2 target (Figure 2.3). Close examination of Figure 2.6 reveals distinct changes in the slope of resistivity vs. nitrogen concentration, which indicate different regimes in the local chemical ordering for the amorphous films. The effect is most obvious for the W-B-N films sputtered from the W_2B target. Coincidently, the changes in slope tend to occur with the crossing of tie lines in the ternary diagrams (Figure 2.4). The shifts indicate that the local structure of the amorphous films has similarities to the thermodynamically-expected bulk phases found on the ternary phase diagrams.

Through four-point probe measurements on a cold stage under 100 mTorr vacuum, the temperature coefficient of resistivity (TCR) of as-deposited $Ta_{36}Si_{14}N_{50}$ films is negative, as shown in Figure 2.7. The composition, $Ta_{36}Si_{14}N_{50}$ makes an excellent diffusion barrier, as discussed in Chapters 4-5. Moreover, Ta-Si-N is chemically related to Ta_2N, which is a commonly used material for thin film resistor applications. The absolute value of $Ta_{36}Si_{14}N_{50}$'s TCR almost linearly decreases with increasing temperature from -800 ppm/°C at -100°C, to 250 ppm/°C at +100°C. The change in the slope's sign at +100°C, which roughly agrees with the deposition temperature, may be a consequence of structural modifications. In contrast, the change at -100°C could be attributed to changes in the electronic conduction mechanisms. Although not quite as low as TaN (-100 ppm/°C) [17-19], the relatively low TCR

values of $Ta_{36}Si_{14}N_{50}$ films hold promise for thin-film resistor applications. With optimization of composition, deposition, and anneals, the absolute value of the TCR could conceivably be reduced.

Figure 2.8 shows a plot of the change in room-temperature sheet resistivity after a 1 h vacuum anneal with respect to as-deposited samples. The compositions tested here from the (Mo, Ta, and $W)_5Si_3$ and WSi_2 targets, typically with 40 to 50 at.% nitrogen, will also be shown to make very effective diffusion barriers in Chapters 4 and 5. All of the systems tend to exhibit a drop in sheet resistivity as the annealing temperature increases. $Mo_{35}Si_{17}N_{48}$ films are the most susceptible to the effects of the anneal, with a 10% drop in resistivity induced from an anneal at 500°C. $Ta_{36}Si_{14}N_{50}$, which appears to be the most inert of the four films, does not register any change in resistivity until the annealing temperature reaches 700°C. $W_{24}Si_{36}N_{40}$ films, sputtered from the WSi_2 target, deviate from the downward trend in resistivity from annealing at 1000°C. The $W_{24}Si_{36}N_{40}$ films also show a color change from metallic to red from a silver-like color after the 1000°C treatment. ^4He backscattering does not reveal much, if any, oxidation. Possibly, large-scale phase segregation between conducting (W-based) and dielectric (Si_3N_4-based) components of the film has occurred, thus effectively choking off and isolating the conducting portions of the film.

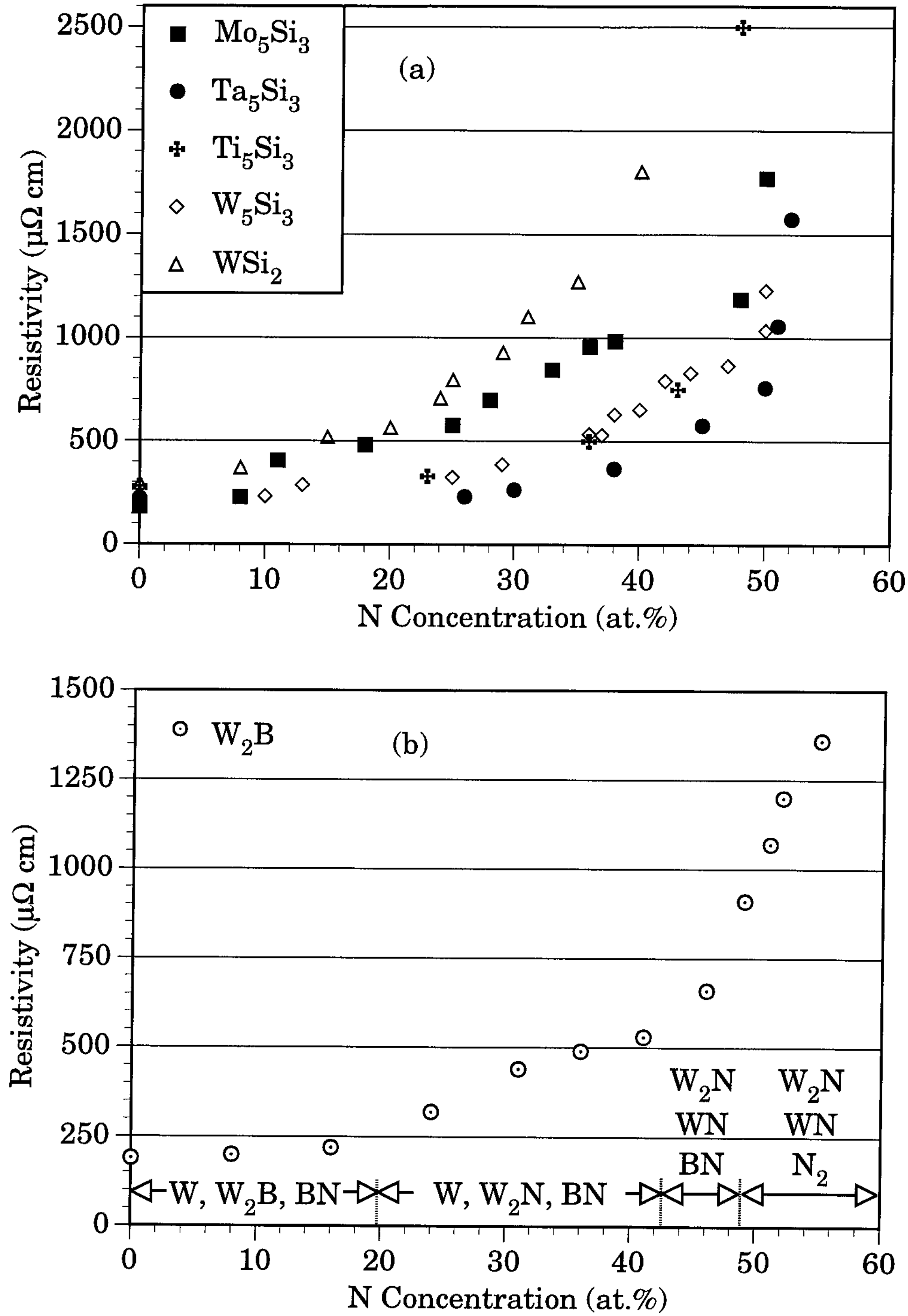

Figure 2.6. Resistivity vs. nitrogen concentration of as-deposited films on oxidized silicon: (a) films from the Mo_5Si_3, Ta_5Si_3, Ti_5Si_3, W_5Si_3, and WSi_2 targets, and (b) films from the W_2B target.

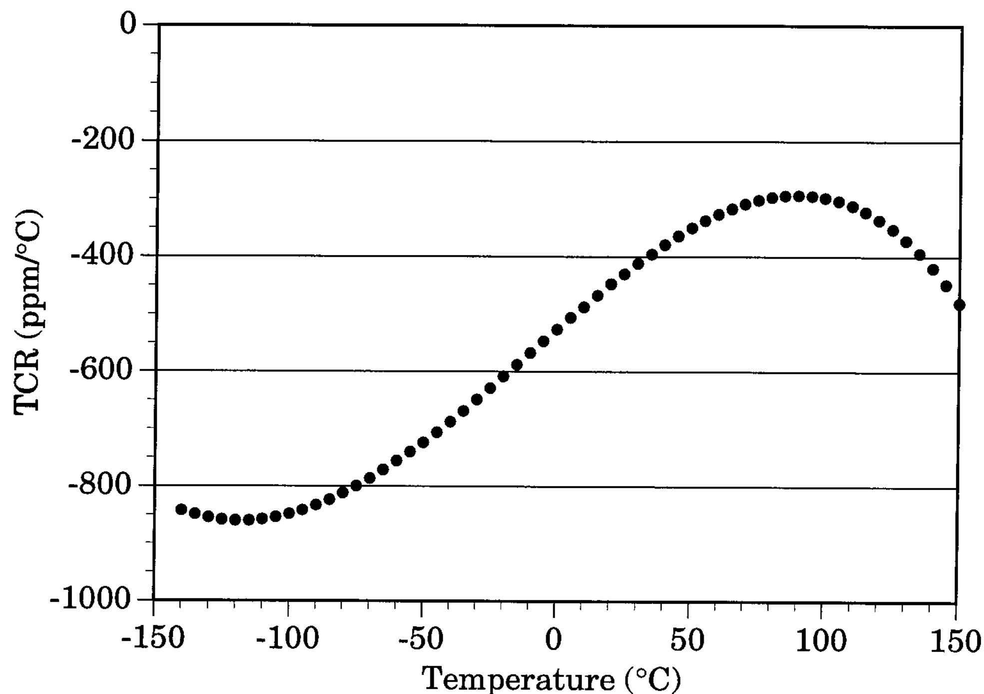

Figure 2.7. Temperature coefficient of resistivity (TCR) of a 130 nm $Ta_{36}Si_{14}N_{50}$ film on an oxidized silicon substrate. The temperature was first quickly reduced to -140°C and allowed to rise at roughly 2°C/min up to 130°C.

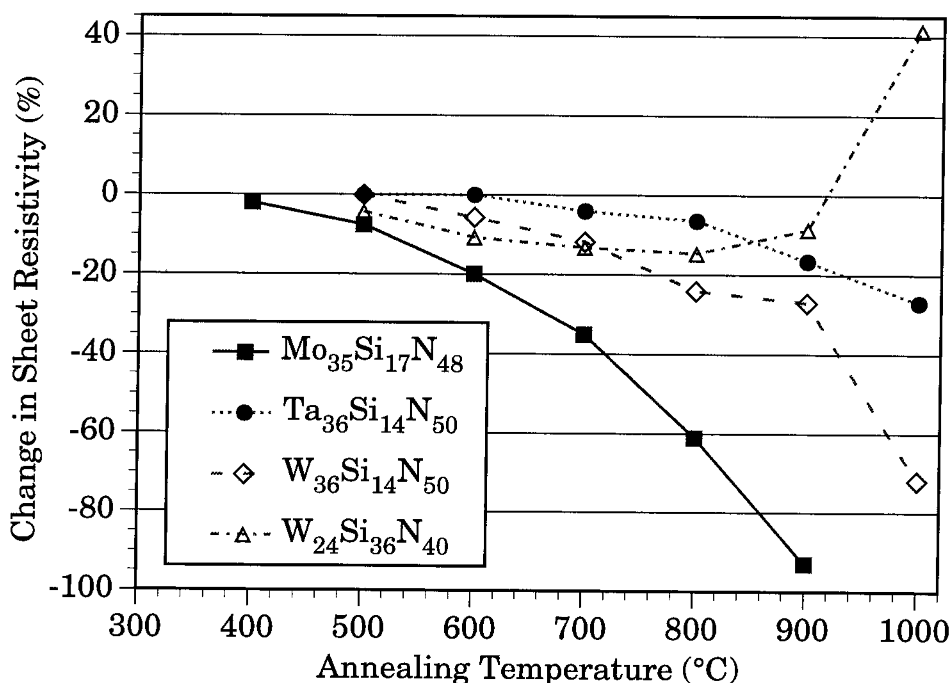

Figure 2.8. Sheet resitivity change in $Mo_{35}Si_{17}N_{48}$, $Ta_{36}Si_{14}N_{50}$, $W_{36}Si_{14}N_{50}$, $W_{24}Si_{36}N_{40}$ films on oxidized silicon after a 1 h heat treatment in vacuum.

2.5. Loss of Volatile Species: Nitrogen and Argon

Nitrogen loss incurred from annealing in vacuum was evaluated primarily from ^{4}He backscattering of films by comparing the ratio of the signal height of the transition metal to the oxidized-silicon substrate signal. As nitrogen escapes from the films, the relative backscattering yield from the transition metal will increase with respect to the substrate signal height. In some instances, the measurements were superceded by other techniques, namely ^{4}He backscattering of the films deposited on 120-nm thick SiN membranes, as well as energy-dispersive spectrometry (EDS) measurements in a scanning electron microscope. Both methods afford direct measurement of the nitrogen. Like the post-anneal resistivity measurements presented in the last section, only nitrogen-laden compositions were tested: $Mo_{35}Si_{17}N_{48}$, $Ta_{36}Si_{14}N_{50}$, $Ti_{34}Si_{23}N_{43}$, $W_{36}Si_{14}N_{50}$, $W_{24}Si_{36}N_{40}$, and $W_{42}B_{17}N_{41}$.

Based on the phase diagrams presented in Figure 2.4, only the Mo-Si-N films and the nitrogen-rich W-Si-N and W-B-N films are expected to liberate significant quantities of nitrogen during anneals at elevated temperatures. Figure 2.9 shows the relative amount of nitrogen lost for each tested composition as a function of annealing temperature. Figure 2.10 plots the nitrogen loss on the ternary phase diagrams. Presumably because of the relatively weak molybdenum-nitrogen bonding, the $Mo_{35}Si_{17}N_{48}$ films, sputtered from a Mo_5Si_3 target, most readily release nitrogen. The films begin to lose nitrogen at 700°C, placing the composition at $Mo_{38}Si_{18}N_{44}$, with still more nitrogen released with higher anneal temperatures. After all of the anneals, the remaining nitrogen concentration appears to be almost uniform throughout the film. As thermodynamically predicted, virtually all of the nitrogen is lost from Mo-Si-N during heat treatment at 1000°C.

$W_{36}Si_{14}N_{50}$ and $W_{42}B_{17}N_{41}$ films sputtered from W_5Si_3 and W_2B targets also liberate nitrogen, but not quite as readily as the Mo-Si-N system. Incipient loss occurs at 800°C rather than 700°C, with about 15% volatilization of the nitrogen for both systems. A 1 h treatment at 1000°C produced the compositions $W_{51}Si_{20}N_{29}$

and $W_{57}B_{23}N_{20}$, which lie close to the W-Si_3N_4 and W-BN tie lines. Consistently, the amount of nitrogen remaining in the films after annealing at 1000°C is plausibly accommodated by silicon and boron in the form of Si_3N_4 or BN. Thermodynamically, no further nitrogen loss at 1000°C is expected.

The three remaining studied films, $Ta_{36}Si_{14}N_{50}$, $Ti_{34}Si_{23}N_{43}$, and $W_{24}Si_{36}N_{40}$, do not release any measurable amounts of nitrogen during a 1 h anneal at 1000°C. The stability of the $Ta_{36}Si_{14}N_{50}$ and $Ti_{34}Si_{23}N_{43}$ films can be attributed to the high stability of tantalum- and titanium-nitrides, which unlike molybdenum and tungsten nitrides, do not readily decompose at elevated temperatures. In contrast, the cohesion of $W_{24}Si_{36}N_{40}$ films is probably based on their composition being on the nitrogen-depleted side of the W-Si_3N_4 tie line in Figure 2.4. Undoubtedly, some of the nitrogen is bonded to W in as-deposited samples, but the annealing process may transfer some of that nitrogen to silicon, thus tightly bonding the nitrogen into place. Increasing the annealing temperature to 1100°C does, however, cause a $Ta_{36}Si_{14}N_{50}$ film on <Al_2O_3> to relinquish about 70% of its nitrogen. The volatilization is consistent with the dashed tie lines of Figure 2.4 designating the equilibria of Ta-Si-N at the higher temperature of 1300°C.

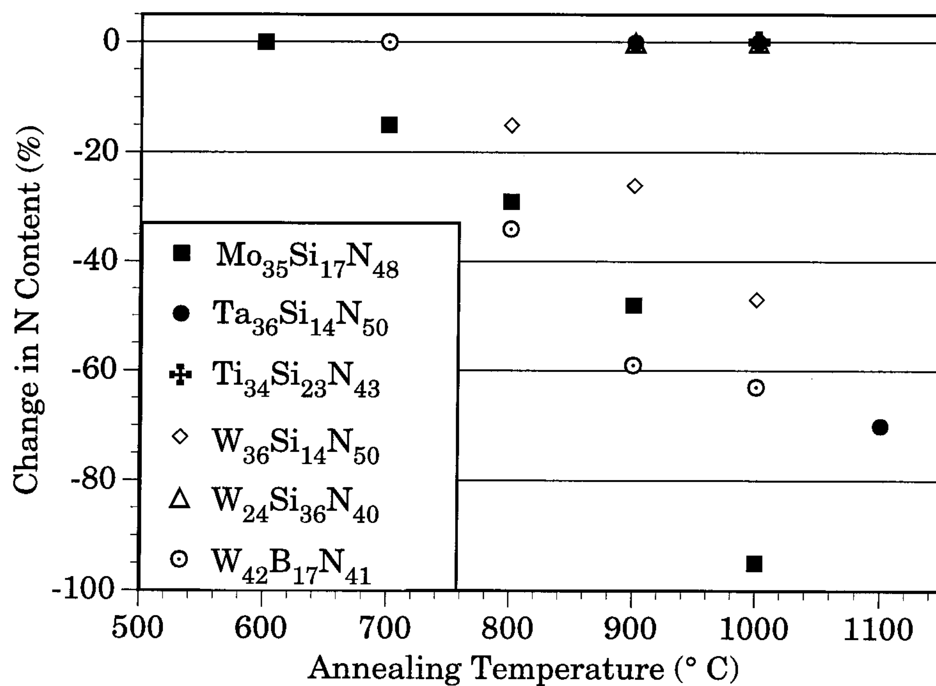

Figure 2.9. Percentage of nitrogen lost in ~130-nm thick $Mo_{35}Si_{17}N_{48}$, $Ta_{36}Si_{14}N_{50}$, $Ti_{34}Si_{23}N_{43}$, $W_{36}Si_{14}N_{50}$, $W_{24}Si_{36}N_{40}$, and $W_{42}B_{17}N_{41}$ films after a 1 h vacuum anneal. The uncertainty of the nitrogen loss is approximately ±3 at.%.

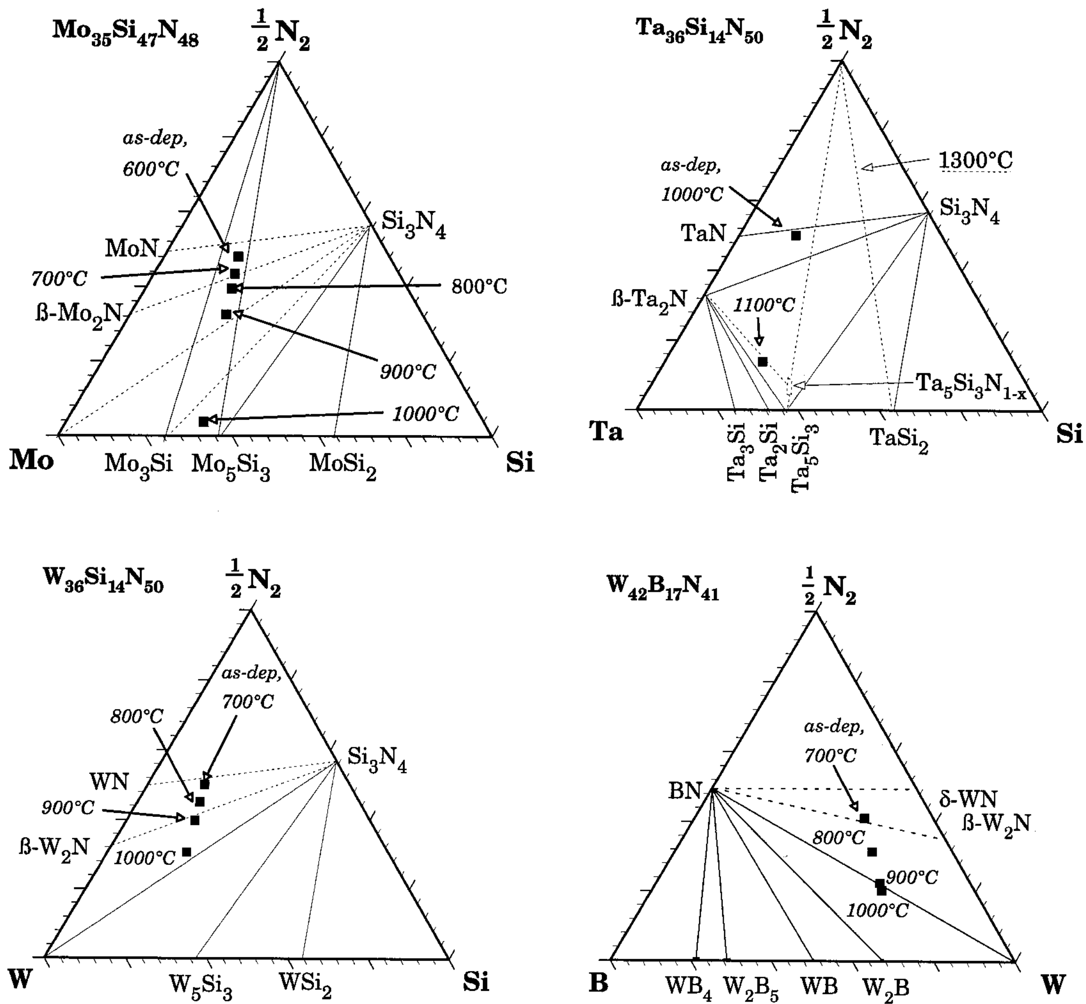

Figure 2.10. Ternary phase diagram plots of nitrogen loss for $Mo_{35}Si_{17}N_{48}$, $Ta_{36}Si_{14}N_{50}$, $W_{36}Si_{14}N_{50}$, and $W_{42}B_{17}N_{41}$ films after a 1 h vacuum anneal at the temperatures indicated. Uncertainty of the nitrogen loss is approximately ±3 at.%.

2.6. Mechanical Properties

By measuring the wafer curvature before and after deposition, the film stress may be determined from the Stoney relation [20]:

$$\sigma = \frac{E}{6(1-\nu)}\frac{D^2}{t\Delta R}$$

where $E/(1-\nu)$ is the biaxial modulus of the substrate, D is the substrate thickness, t is the film thickness, and ΔR is the net difference in radius of curvature. Strictly speaking, the film stress must be isotropic in the plane of the substrate for the Stoney relation to apply. For this study, only the (Mo, Ta, and W)-Si-N systems were considered. The substrate material was 5-cm-diameter (111)-Si and (100)-GaAs measuring 350 and 475 μm thick, respectively. The film thickness was held constant at 400 nm.

Through probable peening effects during sputtering [21], all of the as-deposited films contain compressive stresses, as listed in Table 2.2. Where examined, the choice of (111)-Si or (100)-GaAs substrates appears to make little difference in the as-deposited stress. With a deposition temperature of only 120°C, thermally induced stresses from cool-down are minimized, thus little difference from the choice of substrate is expected. The amorphous, nitrogen-free silicides had the lowest stresses, ranging from -130 MPa for $Mo_{74}Si_{26}$ films on (111)-Si to -440 for $Ta_{80}Si_{20}$ on (100)-GaAs. Nitriding during deposition tends to increase the compressive stress to around -600 MPa for films from the (Mo, Ta, andW)$_5Si_3$ target, and to almost -900 MPa for $W_{24}Si_{38}N_{38}$ from the WSi_2 target. Interestingly, the Mo-Si and Mo-Si-N systems have the lowest stresses for their respective binary and ternary groups with the application of a -115 V dc substrate bias. All of the as-deposited stress levels can conceivably be made more tensile by increasing the deposition pressure [21]. Nonetheless, the values presented here are in many instances less than the often GPa-range values for other commonly used sputtered diffusion barriers such as TiN [5,22-25], TiW [26], and WN [6,27].

At-temperature stress measurements of $Ta_{36}Si_{14}N_{50}$ and $W_{36}Si_{14}N_{50}$ films on (111)-Si and (100)-GaAs substrates during temperature ramps at 3°C/min to 500°C with subsequent cooling are shown in Figure 2.11. Starting at room temperature, both films on both substrates exhibit probable elastic changes in stress likely associated with thermal mismatch up to 120°C. Stress on (111)-Si becomes more compressive, whereas stress on (100)-GaAs tends to become more tensile. The behavior is consistent with the as-deposited films' thermal expansion coefficients lying in between that of (111)-Si (2.9 ppm/°C) and (100)-GaAs (5.7 ppm/°C). Once the temperature exceeds 120°C, which correlates to the deposition temperature, plastic behavior occurs. The films then show a monotonic decrease in the absolute stress up to 500°C. The trend is largely linear, with a slight change of slope at 375°C for $Ta_{36}Si_{14}N_{50}$, and 280°C for $W_{36}Si_{14}N_{50}$ films. While at 500°C for 30 min, the films further relax in stress by about 30 MPa. Upon cooling, the stress enters an elastic regime with linear changes in the tensile direction for films on (111)-Si, and to a lesser extent, the compressive direction for films on (100)-GaAs. Both slopes during cooling are approximately parallel to the slopes obtained from the elastic heating from 25 to 125°C. The final room-temperature stress is around 100 MPa for films on (111)-Si and -300 MPa on (100)-GaAs. Close inspection of the stress recorded during cooling of W-Si-N shows a small kink at around 300°C, which is reproducible during a second heating and cooling cycle up to 500°C. Reheating and cooling the Ta-Si-N films also reproduces the cooling trend obtained from the first thermal cooling cycle, thus verifying the elastic behavior from their first cool-down.

Not surprisingly, heating and recooling as-deposited $Ta_{36}Si_{14}N_{50}$ and $W_{36}Si_{14}N_{50}$ films on (111)-Si substrates heated up to 400 and 450°C produces similar results as those obtained from the 500°C ramps, except that the post-anneal, room-temperature stress is more compressive. A 450°C treatment produces a nearly stressless film at 25°C. The slight kinks in the elastic stress vs. temperature curves for $W_{36}Si_{14}N_{50}$, however, do not appear.

The irreversible stress changes during the initial temperature ramps are a

consequence of densification and deformation. Given that the stress release is in the direction of higher tensile stress, densification may be the predominant factor. Based on the results of the previous section, the temperatures are too low for the evolution of volatile species to be involved with any present densification processes. As will be explained in the next chapter, the ternary films retain their amorphous structure in excess of 800°C, so large-scale structural rearrangements are not a factor.

From the stress vs. temperature slopes obtained from the elastic cool-down presented in Figure 2.10, the films' biaxial moduli and the thermal expansion coefficients may be obtained through the Hooke's law relation, $d\sigma/dT = (E/1\text{-}\nu)_f(\alpha_s - \alpha_f)$, where σ is the stress, T is the temperature, $(E/1\text{-}\nu)_f$ is the film's biaxial modulus, with α_s and α_f respectively defining the thermal expansion coefficient of the substrate and film. Applying the relation for each of the substrates (two equations, two unknowns), $Ta_{36}Si_{14}N_{50}$ has a biaxial modulus of $(E/1\text{-}\nu)_{Ta\text{-}Si\text{-}N} \approx 280$ GPa, and a thermal expansion coefficient of $\alpha_{Ta\text{-}Si\text{-}N} \approx 6$ ppm/°C as shown in Figure 2.12. Assuming a Poisson ratio $\nu = 1/3$, which is typical of most materials, the Young's modulus is 190 GPa. $W_{36}Si_{14}N_{50}$ films have a somewhat lower biaxial modulus and coefficient of thermal expansion (Table 2.2). The values obtained here for $W_{36}Si_{14}N_{50}$ are in rough agreement with the Lahav et al. measurement of 6 ppm/°C at 25°C for amorphous $W_{56}Si_{38}N_6$ films [28].

Table 2.2. Stress values for as-deposited, 400-nm thick films, and mechanical properties of $Ta_{36}Si_{14}N_{50}$ and $W_{36}Si_{14}N_{50}$. Uncertainty of the stress is ±50 MPa.

Film	Stress on (111)-Si (MPa)	Stress on (100)-GaAs (MPa)
Mo_5Si_3 Target:		
$Mo_{74}Si_{26}$	-130	—
$Mo_{35}Si_{17}N_{48}$	-560	—
Ta_5Si_3 Target:		
$Ta_{80}Si_{20}$	-430	-440
$Ta_{36}Si_{14}N_{50}$	-620	-660
W_5Si_3 Target:		
$W_{80}Si_{20}$	-330	—
$W_{36}Si_{14}N_{50}$	-560	-504
WSi_2 Target:		
$W_{44}Si_{56}$	-280	—
$W_{24}Si_{36}N_{40}$	-870	—

mechanical properties:

$(E/1-\nu)_{Ta\text{-}Si\text{-}N} \approx 280$ GPa
$\alpha_{Ta\text{-}Si\text{-}N} \approx 6$ ppm/°C

$(E/1-\nu)_{W\text{-}Si\text{-}N} \approx 190$ GPa
$\alpha_{W\text{-}Si\text{-}N} \approx 5$ ppm/°C

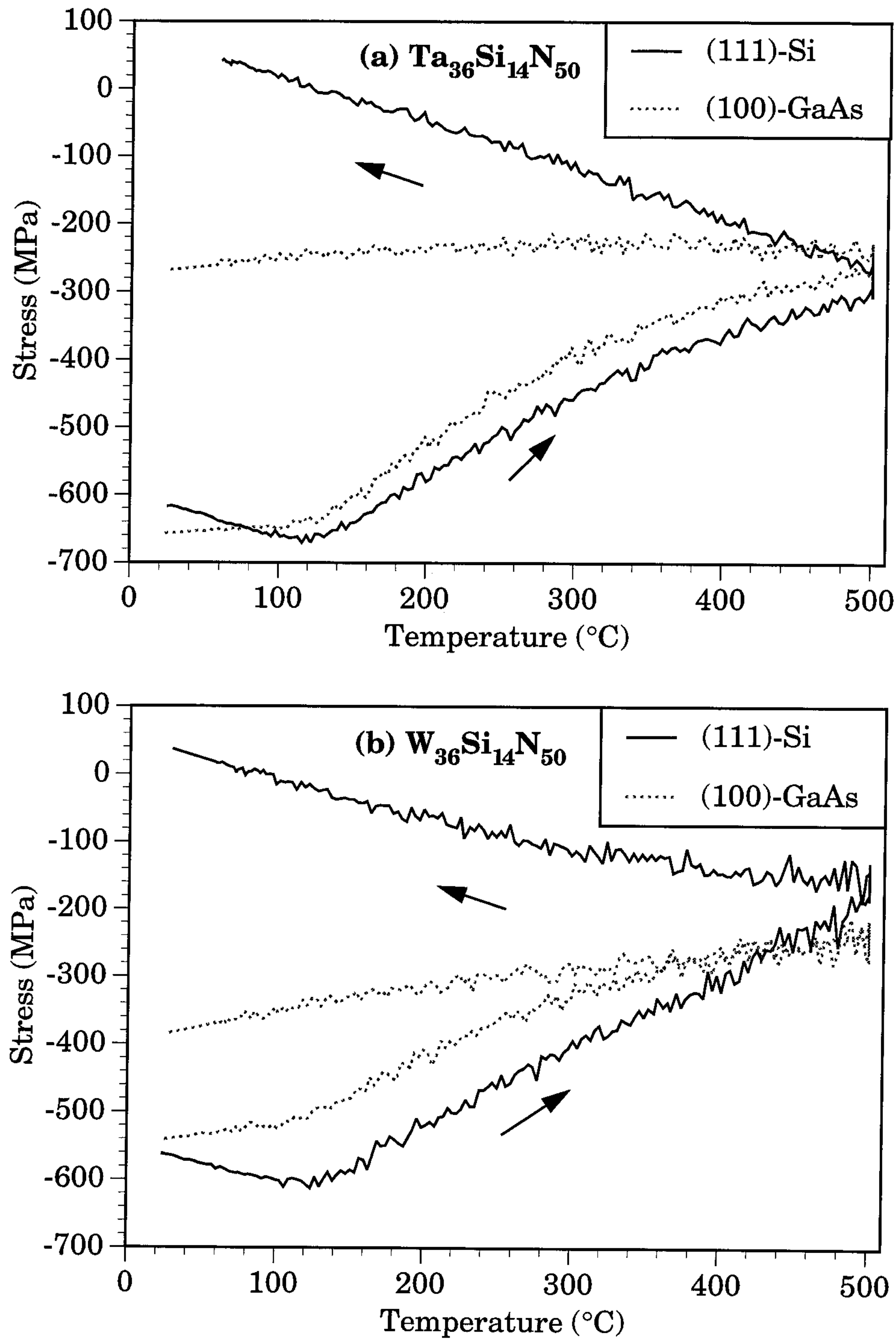

Figure 2.11. Stress vs. temperature for 400 nm $Ta_{36}Si_{14}N_{50}$ and $W_{36}Si_{14}N_{50}$ films on Si and GaAs substrates.

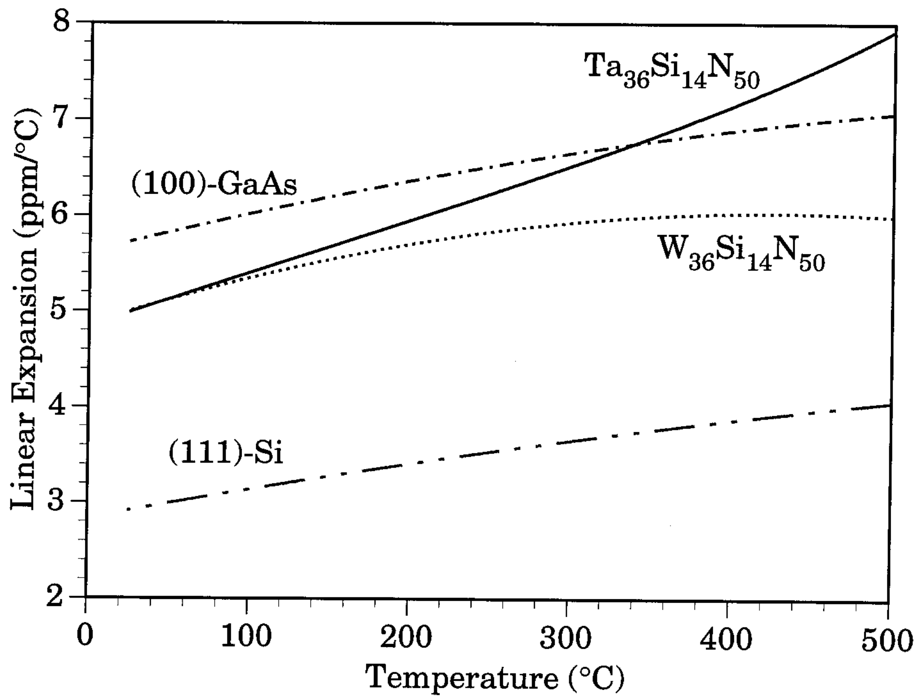

Figure 2.12. Extracted coefficient of thermal expansion for $Ta_{36}Si_{14}N_{50}$ and $W_{36}Si_{14}N_{50}$ films. For comparative purposes, values for (100)-Si and (111)-GaAs are included.

References, Chapter 2.

[1] B. Chapman, *Glow Discharge Processes*, John Wiley and Sons, New York (1980) p. 267.

[2] R.R. Olson, M.E. King, and G.K. Wehner, *J. Appl. Phys.* 50, 3677 (1979).

[3] Y. Murakami and T. Shingyoji, *J. Vac. Sci. Technol. A* 8, 851 (1990).

[4] T. Yamazaki, N. Ikeda, H. Tawara, and M. Sato, *Thin Solid Films* 235, 71 (1993).

[5] H.P. Kattelus, J.L. Tandon, C. Sala, and M-A. Nicolet, *J. Vac. Sci. Technol. A* 4, 1850 (1986).

[6] E. Kolawa, F.C.T. So, X-A. Zhao, and M-A. Nicolet, in *Tungsten and Other Refractory Metals for VLSI Applications II*, edited by E.K. Broadbent, Materias Research Society, Pittsburgh, PA (1987) pp. 311-317.

[7] K. Affolter, H.P. Katelus, and M-A. Nicolet, in *Materials Research Society Proceedings*, vol. 47, Materials Research Society, Pittsburgh, PA (1985) pp. 167-172.

[8] X. Sun, E. Kolawa, J-S. Chen, J.S. Reid, and M-A. Nicolet, *Thin Solid Films* 236, 347 (1993).

[9] M. Thuillard, T.W. Workman, E. Kolawa, and M-A. Nicolet, *J. Less-Common Metals* 145, 505 (1988).

[10] J.S. Reid, work on TiN and MoN films, unpublished.

[11] G.V. Samsonov and I.M. Vinitskii, *Handbook of Refractory Compounds*, IFI/Plenum, New York (1980).

[12] P. Rogl and J.C. Schuster, *Phase Diagrams of Ternary Boron Nitride and Silicon Nitride Systems*, ASM International, Materials Park, OH (1992).

[13] H.J. Goldschmidt, *Interstitial Alloys*, Plenum Press, New York (1967) p. 554.

[14] I. Barin, *Thermochemical Data of Pure Substances*, VCH Verlagsgesellschaft mbH, D-6940 Weinheim, Germany (1989).

[15] W-K. Chu, J.W. Mayer, and M-A. Nicolet, *Backscattering Spectrometry*, Academic Press, Orlando, FL (1978) pp. 61-64.

[16] TAPP Software for Macintosh, version 2.1, ES Microware, Hamilton, OH

1994.

[17] L.I. Maissel and M.H. Francombe, *An Introduction to Thin Films*, Gordon and Breach, New York (1973).

[18] L. Bos, *IEEE Trans. Components Packaging and Manufac. Technol.* 17, 359 (1994).

[19] C.L. Au, W. Anderson, D.A. Schmitz, J.C. Flassayer, and F.M. Collins, *J. Materials Res.* 5, 1224 (1990).

[20] G.G. Stoney, *Proc. Roy. Soc. London* A82,172 (1909).

[21] H. Windischmann, *Critical Reviews in Solid State and Materials Sciences* 17, 547 (1992).

[22] M. Elena, M. Bonelli, C.E. Bottani, G. Ghislotti, A. Miotello, P. Mutti, and P.M. Ossi, *Thin Solid Films* 236, 209 (1993).

[23] D. Maheo and J.M. Poitevin, *Thin Solid Films* 215, 8 (1992).

[24] P. Jin and S. Maruno, *Jap. J. Appl. Phys.* 31(5A), 1446 (1992).

[25] A.J. Perry, *J. Vacuum Sci. Technol A* 8, 3186 (1990).

[26] I.J. Raaijmakers, T. Setalvad, A.S. Bhansali, B.J. Burrow, L. Gutai, and K-B. Kim, *J. Electronic Mat.* 19, 1221 (1990).

[27] F.C.T. So, E. Kolawa, X-A. Zhao, and M-A. Nicolet, *Thin Solid Films* 153, 507 (1987).

[28] A. Lahav, K.A. Grim, and I.A. Blech, *J. Appl. Phys.* 67, 734 (1990).

Chapter 3. Structure

3.1. Introduction

Because of the quench rate and/or ion bombardment, vapor deposition techniques often produce amorphous compositions which are inaccessible through splat cooling [1,2]. For binary materials related to the systems studied in this thesis, many are known to form amorphous phases. All of the Group V and VI transition-metal silicides as well as titanium silicides can assume an amorphous structure when deposited by physical vapor methods [V:3,4, Nb:5-7, Ta:8,9, Cr:4,10,11, Mo:7,12,13, W:14-16, Ti:4,17-21]. The compositions required for the amorphous structures typically range from 0 to as high as 80 at.% transition metal. A very complete study by Kortright and Bienenstock on cosputtered, amorphous Mo-Ge system [2] may serve as an analog to structural trends expected in the amorphous silicides. In this study, low contents of Mo in amorphous Mo-Ge films augment the random tetrahedral network of amorphous germanium by producing discrete clusters bonded like intermetallic Ge-rich Mo-Ge compounds. From 23 to 50 at.% Mo, the amorphous structure contains correlations in bond lengths consistent with the intermetallic compounds, Mo_2Ge and $Mo_{13}Ge_{23}$. Dense-random-packing of hard spheres (DRPHS) models [22-24] does not adequately describe the structure. Above 50 at.% Mo, the average environment around Ge atoms changes little over films with 23 to 50 at.% Mo. However, the Mo-Mo distances decrease from a reduction in the chemical ordering. With a well-defined first peak and a bimodal second peak, the radial distribution functions obtained from X-ray diffraction patterns suggest DRPHS arrangements for alloys with above 50 at.% Mo.

Much less work has been performed on amorphous thin-film borides from the Group V and VI transition metals. Through chemical vapor deposition, Smith et al. produced amorphous tungsten boride films ranging from 20 to 40 at.% B [25]. Less than 20 at.% B produced a polycrystalline ß-W film. Corrosion-resistant amorphous Cr-B [26,27] and Mo-B [28] deposited by sputtering have also been investigated.

Ternary films consisting of Group V or VI transition metals and boron, combined with Ru [28-31], Re [32,33], or Fe [34-37], have garnered more attention. Structurally, radial distribution functions extracted from X-ray diffraction data for metal-rich $(W_{0.5}Ru_{0.5})_{80}B_{20}$ films are well-approximated by DRPHS models. Based on work on Fe-borides, amorphous Group V and VI transition-metal borides may be obtainable for 0 to 90 at.% metal [38].

Owing in part to their relatively simple equilibrium structures (e.g. NaCl, WC, Fe_2N prototypes), transition-metal nitrides are much more difficult to make amorphous than their silicide and boride counterparts [crystal structures: 39-41, Voronoi cells: 42]. Evaporating Group V and VI transition metals in vacuum above $\sim 10^{-7}$ Torr onto liquid-helium-cooled substrates can yield highly-disordered phases [43,44]. Substrate temperatures as high as 160 K can also give amorphous phases when evaporating Mo and Nb in a nitrogen ambient [45]. Electron diffraction analysis of the reactively-evaporated films with about 23 at.% of nitrogen have indicated atomic arrangements consistent with DRPHS models. By reactive sputtering at room temperature, amorphous or highly disordered Ta- [46-48], Cr- [49,50], Mo- [46,47,51,52], and W- [46,47,53-55] nitrides have been produced for compositions typically ranging from approximately 15 to 30 at.% N. The films often contain discrete crystalline material embedded in the amorphous matrix. Based on transmission electron microscopy observations, the concentration of the crystalline regions appears to be much greater in the Group V nitrides than in the Group VI nitrides, despite somewhat similar bulk-phase structures. The difference may be attributed to the larger thermodynamic stability of the Group V nitrides [41,56], which plausibly gives a higher driving force toward crystallization. Consistently, binary nitrides of the Group IV transition metals, which are more stable than the Group V nitrides, do not readily form amorphous phases at all.

Another binary subcomponent of the barrier ternary system, silicon nitride, is a well-known glass former with a very high crystallization temperature (>1000°C) [57,58]. The bonding is largely covalent, which gives rise to a random tetrahedral

network of four nitrogen atoms bonded to each silicon atom [59-61]. In contrast, BN does not form an amorphous phase quite so readily. The local microstructure of BN highly depends on the deposition conditions [62,63]. Amorphous-like BN films typically consist of hexagonal or cubic nanophase regions [64,65]. In depositing cubic-BN films, an amorphous phase can form in the first 5 nm of deposition, with subsequent growth of hexagonal and then cubic phases as the thickness increases [66].

The previous information surveys the glass-forming ability of the binary subcomponents in the ternary TM-Si-N and TM-B-N ternary systems studied in this thesis. Most of the binary systems easily form amorphous phases, with the exception of some of the nitrides. Considering the differences in equilibrium structure, lack of ternary phases (Figure 2.4), and lack of mutual solubilities [67], the structure of the amorphous ternary films may approximate that of their binary subcomponents. Trends in resistivity as discussed in Chapter 2 of this thesis reinforce this hypothesis. In this section, the structure of the ternary films is further investigated. Scattering experiments sampling successively higher regions of reciprocal space are analyzed through small-angle diffraction, wide-angle diffraction, and extended energy-loss fine structure (EXELFS) measurements for as-deposited and in some cases, annealed films. High-resolution transmission electron micrographs are also presented here to show the extent of the local order in the films. Because of their importance in the barrier studies of Chapters 4 and 5, most of the emphasis will be placed on the nitrogen-rich films.

3.2. X-ray Diffraction and Crystallization

By Read camera X-ray diffraction with Cu-K_α radiation, all of the as-deposited films sputtered from the Mo_5Si_3, Ta_5Si_3, W_5Si_3, WSi_2, and W_2B targets exhibited one or more broad diffraction halos characteristic of an amorphous material. In contrast, 100-nm-thick films sputtered from the Ti_5Si_3 target were nearly invisible by X-ray diffraction because of the samples' lack of scattering power and probable disordered structure. In the Mo, Ta, and W systems, the magnitude of the halos'

scattering vectors decreases with increasing nitrogen content, which suggests that the average distance between metal atoms may be increasing. Figure 3.1 shows X-ray diffraction spectra for four heavily-nitrided, as-deposited films, $Mo_{35}Si_{17}N_{48}$, $Ta_{36}Si_{14}N_{50}$, $W_{36}Si_{14}N_{50}$, and $W_{24}Si_{36}Si_{40}$, taken with an Inel position-sensitive detector. Like their respective transition-metal nitrides, Ta-Si-N appears to have the largest metal spacings, followed by Mo-Si-N and W-Si-N. From plausibly less dilution of the metal, the film with the least amount of nitrogen, $W_{24}Si_{36}N_{40}$, has the largest scattering angle.

The crystallization behavior of films sputtered from the non-titanium targets, as measured with the Read camera diffractometer, is given in Figure 3.2a-e. In all cases, the duration of the vacuum anneal was 1 h. For the silicide systems, the crystallization temperature tends to increase with increasing nitrogen content in the films. Crystallization temperatures of amorphous silicides range from 550°C for $W_{44}Si_{56}$ and $Mo_{74}Si_{26}$, to 900°C for $Ta_{80}Si_{20}$. Adding large amounts of nitrogen to the silicide systems pushes the crystallization temperatures into the 800 to 1000°C range. In most instances, the incipient crystallization is incomplete, with some residual amorphous structure sometimes remaining at higher temperatures. The structural changes detected by X-ray diffraction tend to be less sensitive than the post-anneal resistivity measurements shown in Figure 2.8. For the boride system, $W_{79}B_{21}$ films crystallize at 750°C. However, adding nitrogen to the boride system does not increase the crystallization temperature. Below, summary of each system is given.

3.2.1. Mo-Si-N

With more than several atomic percent of nitrogen, Mo-Si-N films from the Mo_5Si_3 target all begin to crystallize at 800°C into Mo_3Si. The crystallization is associated with destabilizing effects from loss of nitrogen, which can occur at temperatures as low as 700°C (Figure 2.9). Resistivity data from Figure 2.8 indicate structural changes as low as 500°C, albeit the films remain amorphous by X-ray

diffraction. Interestingly, the first phase formed (Mo_3Si) does not agree with the hypothetical room-temperature representation of the Mo-Si-N system in Figure 2.4, but is more consistent with the 1000°C representation. Assuming the molybdenum to be preferentially bonded to nitrogen in the nitrogen-saturated films, Mo- or Mo-nitrides may be expected as products. Speculatively, elemental Mo does form on a local scale, but quickly disassociates Si-N to form the silicide, Mo_3Si. Shorter anneal times may support this supposition. Annealing at 900°C also reveals only Mo_3Si. The thermodynamically expected coproduct, Mo_5Si_3, does not arise until 1000°C, at whichpoint virtually all of the nitrogen volatilizes from the speculative disassociation of residual Si-N by Mo. Additionally, the 1000°C treatment of all of the films produces weak reflections at d = 0.258, 0.226, 0.166, and 0.126 nm, which roughly fit an fcc lattice. A variant of ß-Mo is a tenable explanation [46,47].

3.2.2. Ta-Si-N

Presumably due in part to the stronger Ta-N bond that prevents nitrogen from escaping, Ta-Si-N films have the highest crystallization temperatures compared to the other systems. The Ta-Si-N films all crystallized at 950°C, which is somewhat lower than reported in a previous work [68], but nonetheless still represents a very high crystallization temperature. The difference may be connected with varying amounts of trace impurities (typically $< 0.2\%$ total) in the two Ta_5Si_3 targets. In no instances did the crystallization products entirely agree with the equilibrium ternary diagram in Figure 2.4. Amorphous $Ta_{80}Si_{20}$ films crystallize at 900°C into Ta_2Si and impurity-stabilized $Ta_{4.5}Si$ rather than the expected equilibrium phases, Ta_3Si and Ta. The nitrided films crystallize into hexagonal-Ta_2N and the ternary phase, hexagonal-$Ta_5Si_3N_{1-x}$ (also known as $Ta_5Si_3C_{1-x}$) in lieu of Ta_2N and TaN, or Ta_2N and tetragonal-Ta_5Si_3. Any silicon nitride present in the films is essentially invisible here by X-ray diffraction because of its relatively weak scattering power and probable amorphous structure.

3.2.3. Ti-Si-N

As mentioned previously, thin Ti-Si-N films yield extremely faint and broad X-ray diffraction patterns which are indicative of disordered materials. Annealing $Ti_{62}Si_{38}$ films for 1 h at 650°C reveals the presence polycrystalline Ti_5Si_3. The nitrogen-rich $Ti_{34}Si_{23}N_{43}$ and $Ti_{29}Si_{22}N_{49}$ films show incipient formation of polycrystalline TiN from annealing at 900°C.

3.2.4. W-Si-N from a W_5Si_3 target

Figure 3.2c shows the crystallization behavior of W-Si-N films deposited from the W_5Si_3 target. The amorphous silicide crystallizes at 750°C, whereas films containing 40 or more at.% of nitrogen crystallize at 850°C. Similarly, work by Thomas et al. shows amorphous $W_{72}Si_{28}$ films to also crystallize between 700 and 800°C [69]. In the nitrogen-rich W-Si-N films, crystallization appears to be associated with nitrogen loss, which occurs at temperatures as low as 800°C (Figure 2.9). In fact, capping a 140 nm $W_{36}Si_{14}N_{50}$ film with a 140 nm $Ta_{36}Si_{14}N_{50}$ layer increases the crystallization temperature of $W_{36}Si_{14}N_{50}$ to 950°C. Independent of nitrogen concentration, all of the films crystallize at sufficiently high temperature into their thermodynamically expected products given by the phase diagram of Figure 2.4. Films with initial compositions on the nitrogen-rich side of the W-Si_3N_4 tie line release nitrogen until their composition finally lies on the tie line. In other words, the nitrogen-rich films accommodate as much nitrogen at high temperatures as there exists silicon to form Si_3N_4. Like the results from Mo-Si-N, W-Si-N films also produced weak, unknown reflections at $d = 0.258$, 0.226, 0.166, and 0.126 nm. In this case, the lines may be a consequence of ß-W, which has a similar lattice constant as ß-Mo.

3.2.5. W-Si-N from a WSi_2 target

As shown in Figure 3.2d, sputter-deposition of W-Si-N from the WSi_2 target produces the largest changes in crystallization temperature as a function of nitrogen

content. $W_{44}Si_{56}$ films on oxidized Si begin to crystallize at 550°C into WSi_2 and W_5Si_3, as thermodynamically expected. Adding 40 at.% of nitrogen to make $W_{24}Si_{36}N_{40}$ increases the crystallization temperature to 900°C, which is a 50°C increase over films sputtered from the W_5Si_3 target. The additional Si-N bonding is probably the reason. With the exception of the low-scattering Si_3N_4, all of the crystallization products predicted from the W-Si-N ternary diagram are detected. Once again, however, the same unknown lines at d = 0.258, 0.226, 0.166, and 0.126 nm arise.

3.2.6 W-B-N

The summary of phases observed by X-ray diffraction of W-B and W-B-N films annealed on thermally oxidized silicon is presented in Figure 3.2e. All films retain their amorphous structure up to 600°C for 1 h. During annealing at 650°C for 1 h, the most heavily nitrogen-laden films begin to crystallize into finely-grained β-W_2N, with their nitrogen-poorer counterparts remaining amorphous. Upon heat treatment at 750°C, all of the W-B-N films show some sign of crystallization. Films with low nitrogen contents inceptively crystallize into α-W, whereas the nitrogen-rich films crystallize into oxygen-stabilized β-W_2N. β-W_2N is expected only in the samples with 24-49 at.% nitrogen, but is present here in more nitrogen-rich stoichiometries. The absence of β-W_2N in $W_{53}B_{19}N_{24}$ and $W_{50}B_{19}N_{31}$ films may be a consequence of the compositions' proximity to the W-BN tie line. Evidence of tungsten nitrides vanishes during annealing between 800 and 850°C. W_2B does not arise until the temperature reaches 850°C or higher, and only appears in films with low nitrogen contents (0-19 at.%), as thermodynamically expected (Fig. 2.4). Otherwise, only the α-W phase is seen. BN phases, possibly present, are essentially invisible by X-ray diffraction because of their relatively weak scattering power. Above ~1200°C, W_2B should be present in all of the samples because the tie lines between BN and the tungsten borides break down and are subsequently replaced by tie lines between $(1/2)N_2$ and the tungsten borides [67].

The crystallization behavior of nitrogen-rich W-B-N films closely resembles that of amorphous W_2N films [53]. Both sets of films crystallize at 650°C into ß-W_2N; after heat treatment at 800°C, only α-W is observed. For comparable compositions, amorphous W-B-N and W-Si-N thin films are remarkably dissimilar in behavior, despite similar phase diagrams (Figure 2.4). The addition of nitrogen to W-Si causes an increase in crystallization temperature, not a decrease, as seen with W-B. The crystallization products are also different. In nitrogen-laden W-B-N, ß-W_2N is an intermediary crystallization product before α-W is seen at higher temperatures. ß-W_2N does not appear in the crystallization of W-Si-N. The differences may be associated with the larger volume of Si_3N_4 vs. BN for a given amount of metalloid. Larger volumes of these highly stable dielectrics within the film likely hinder the atomic rearrangements necessary to form W-nitride.

3.3. Transmission Electron Microscopy

Because of their ability to prevent Al and/or Cu diffusion (as discussed in Chapters 4 and 5), mostly nitrogen-laden films were evaluated from the several targets used in this thesis: $Mo_{35}Si_{17}N_{48}$, $Ta_{36}Si_{14}N_{50}$, $Ti_{34}N_{23}N_{43}$, $W_{36}Si_{14}N_{50}$, $W_{24}Si_{36}N_{40}$, $W_{64}B_{20}N_{16}$, and $W_{79}B_{21}$. Samples were sputtered to a thickness of 13 to 20 nm onto single-crystal <NaCl>. After deposition, the films were floated-off from the NaCl in deionized water and collected on a 200-mesh copper grid. Some of the copper grids supported a thin, holey carbon film. Films to be vacuum-annealed were instead collected on Mo grids sputter-coated with a 100-nm layer of Si_3N_4. A Phillips EM430 microscope operating at 300 keV was used for the evaluations.

High-resolution transmission electron micrographs of the as-deposited (Mo, Ta, and W)-Si-N barriers along with their corresponding electron diffraction patterns are shown in Figure 3.3. For systems produced from TM_5Si_3 targets, oriented packets of lattice fringes measuring less than 1.5 nm across are the most salient features. Fringes from $W_{24}Si_{36}N_{40}$ films, produced from the WSi_2 target, are less pronounced, suggesting that the film may be more disordered than its metal-rich analogues. In

all of the bright-field patterns, intermixed lightly and darkly shaded domains are present, possibly indicating chemically dissimilar regions. The electron diffraction patterns are broad halos consistent with an amorphous material. In some systems, upon close inspection, the innermost halo appears to be the superposition of two closely-spaced broad diffraction rings. Dark-field sampling of the inner rings tilted through a 20 μm objective aperture reveals discrete spots measuring the equivalent of 0.5 to 1.5 nm, which gives a measure of the extent of the short-range crystallographic order (Figure 3.4). Elongation is observed from the stage drifting during the long exposures necessary to image the faint dark-field patterns.

The evolution of crystallization in $Ta_{36}Si_{14}N_{50}$ films is shown in Figure 3.5. The high-resolution micrographs of films annealed for 1 h at 600°C look virtually identical to those of the as-deposited films; dark-field images also closely resemble those from the as-deposited film, with the short-range order still measuring 0.5 to 1.5 nm. The electron diffraction patterns, however, do show a slight narrowing of the diffraction rings. After annealing at 800°C, the patches of lattice fringes appear larger, and the spots from the dark field measure 1 to 2 nm. The largest change occurs in the electron diffraction pattern, which is now representative of a nanophase material, although X-ray diffraction, with its much longer wavelength, still reveals an amorphous structure. All of the diffraction rings in the micrograph agree with reflections from hexagonal $Ta_5Si_3N_{1-x}$. Further annealing at 900°C produces incrementally more ordering, as shown by the well-defined lattice fringes. By dark-field micrographs, the extent of the local order has grown to approximiately 2 nm.

Figure 3.6 shows a high-resolution, electron micrograph of as-deposited $Ti_{34}Si_{23}N_{43}$ along with the corresponding electron diffraction pattern. Unlike the other systems discussed, there exists 1 to 3 nm domains of lattice fringes, showing that there is at least a nanophase component to the films. The binary phase, TiN, accounts for all of the visible reflections in the well-defined electron diffraction pattern. Because Cu-K_α X-rays have a much longer wavelength than 300 keV electrons,

the same rings appear diffuse by X-ray diffraction in accordance with the Scherrer formula [70]. The polycrystalline TiN found by X-ray diffraction after annealing at 900°C thus appears to be associated with grain growth or agglomeration of TiN already present in the as-deposited samples. Combined dark-field sampling of the inner rings, generated by (111) and (200) planes of TiN, yields grain sizes in the 1 to 3 nm range, in agreement with the high-resolution micrograph. Tilting the sample did not appreciably change the diffraction pattern under a variety of beam sizes. Consequently, the TiN grains may not have any strong preferred orientation. Notably lacking from the diffraction pattern is any obvious sign of the 23 at.% of silicon in the film. It is unlikely that the majority of the silicon is dissolved in TiN. Under the pretense of thermodynamic equilibrium, the composition of $Ti_{34}Si_{23}N_{43}$ should consist predominantly of TiN and Si_3N_4 (Figure 2.4) The absence of Si-based contributions to the diffraction pattern is likely a consequence of the phases' relative lack of scattering power and their plausible amorphous structure. By default, most of the silicon is probably present as a silicon nitride. A separate X-ray diffraction study by Posadowski on cosputtered Ti-Si-N has identified small TiN crystallites along with an amorphous component presumed to be Si_3N_4 [71]. Posadowski also found an increase in the TiN grain size and an increase in columnar texture as the Ti:Si ratio increases.

In some respects, the addition of Si (with nitrogen) to TiN is advantageous. For commercial barrier applications, the morphology of $Ti_{34}Si_{23}N_{43}$ is a significant improvement over commonly-used TiN. First, the random arrangement of nanophase TiN eliminates straight grain boundary paths associated with typically columnar TiN films. Second, the intergranular silicon components may be viewed as severely stuffing the grain boundaries of TiN. Because columnar TiN growing from the walls and bottoms of vias can lead to cracking at the corners, $Ti_{34}Si_{23}N_{43}$ may have mechanically advantages as well. Chapter 5 investigates the barrier performance of Ti-Si-N and TiN films with copper.

Because of some ambiguities presented by the lack of X-ray scattering, some

preliminary TEM electron-diffraction work on the nitrogen-poor Ti-Si-N stoichiometries is worth mentioning [72]. Patterns obtained from as-deposited $Ti_{62}Si_{38}$, $Ti_{47}Si_{30}N_{23}$, and $Ti_{38}Si_{26}N_{36}$ films signify an amorphous structure. Evidently, as the poor glass-former TiN is introduced to the systems, the microstructure becomes more defined.

High-resolution transmission electron micrographs of $W_{79}B_{21}$ and $W_{64}B_{20}N_{16}$ with electron diffraction patterns are shown in Figure 3.7. By the extent of the lattice fringes, the local ordering appears to be no larger than 1.5 nm. Dark-field sampling with a 20 μm objective aperture of the innermost diffraction rings revealed discrete spots measuring the equivalent of 0.5 to 1.5 nm on the photographic negatives, which gives another measure of the extent of the local order. The electron diffraction patterns of both films are virtually identical, thus suggesting that some structural components of the two films may be very similar. Close inspection of the innermost halo shows that it is actually the superposition of two broad, closely spaced rings which make a fair match with the (002) and (211) reflections of W_2B. The third ring in the pattern matches the (213) reflection of W_2B.

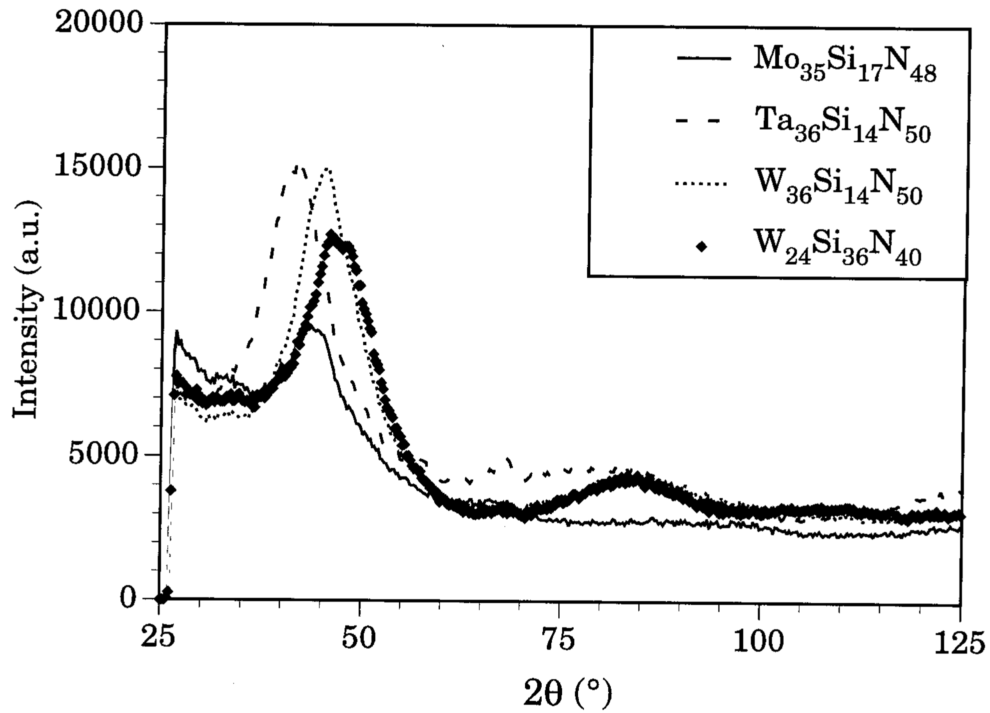

Figure 3.1. X-ray diffraction patterns taken by an Inel fixed-position sensitive detector with Co-K_{α} radiation for $Mo_{35}Si_{17}N_{48}$, $Ta_{36}Si_{14}N_{50}$, $W_{36}Si_{14}N_{50}$, and $W_{24}Si_{36}N_{40}$ films on <Si>. The beam glanced the sample at a tangent angle of 11°.

(a) Mo-Si-N from Mo_5Si_3

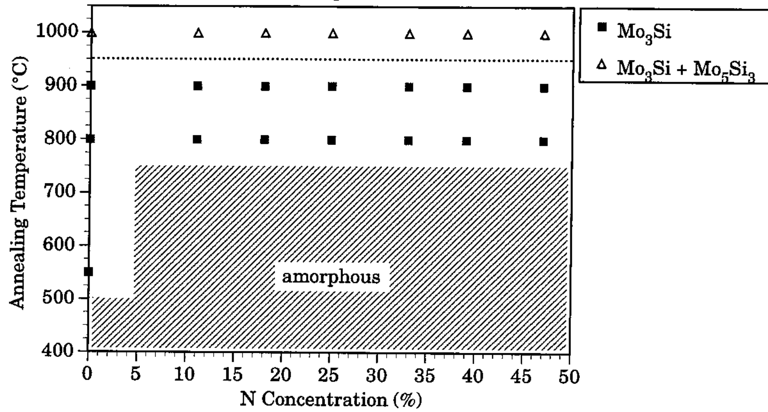

(b) Ta-Si-N from Ta_5Si_3

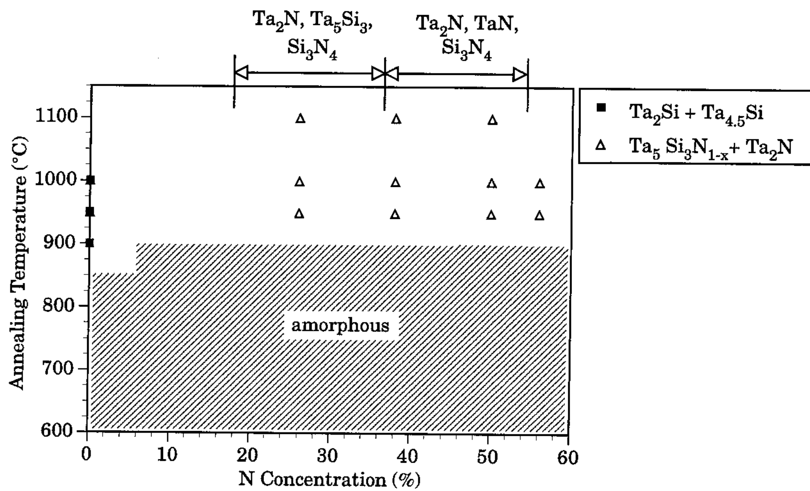

(c) W-Si-N from W_5Si_3

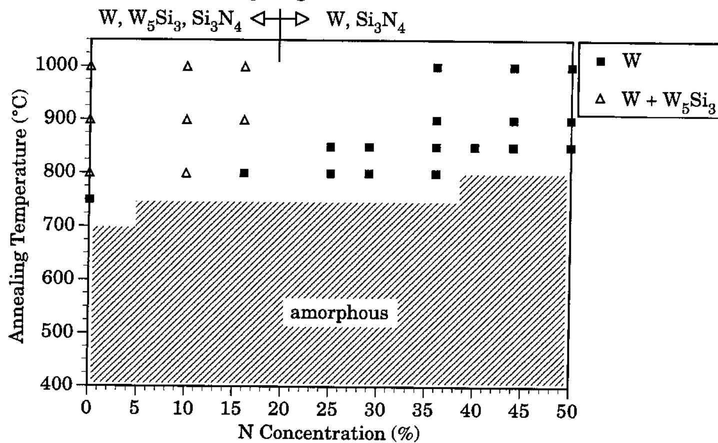

Figure 3.2. Summary of phases found by X-ray diffraction as a function of the nitrogen concentration in as-deposited films. The films were sputtered from the following targets: (a) Mo_5Si_3, (b) Ta_5Si_3, (c) W_5Si_3, (d) WSi_2, and (e) W_2B. Some of the thermodynamically-expected high-temperature products are listed on the top of the diagrams.

(d) W-Si-N from WSi_2

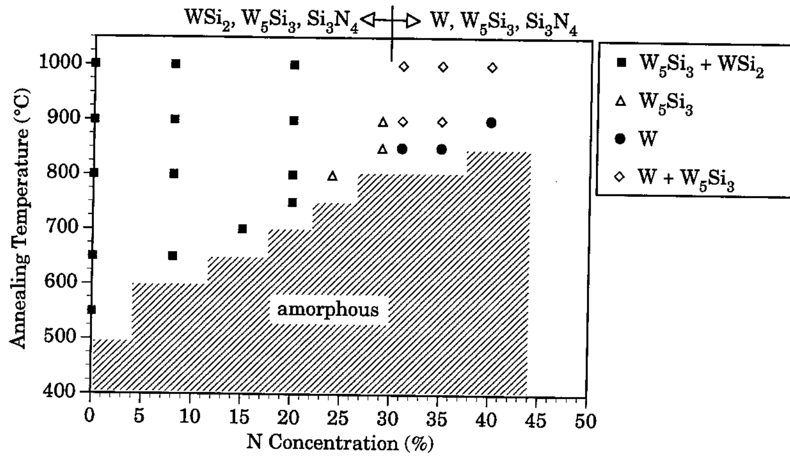

(e) W-B-N from W_2B

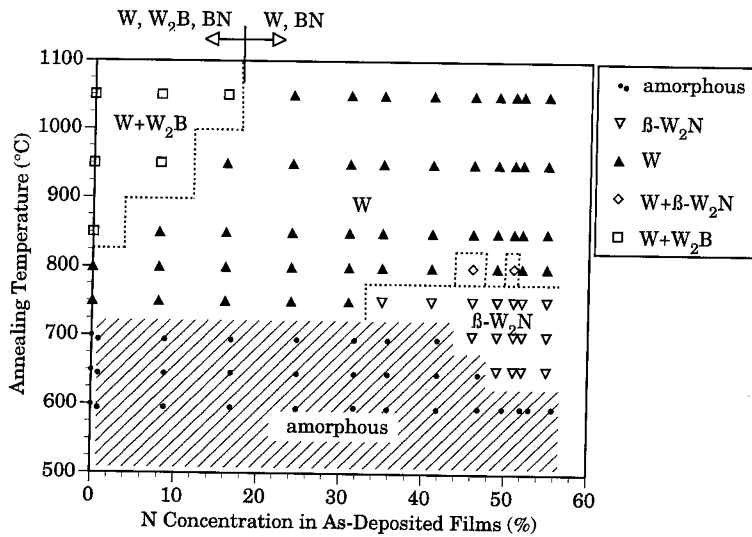

Figure 3.2. Continued.

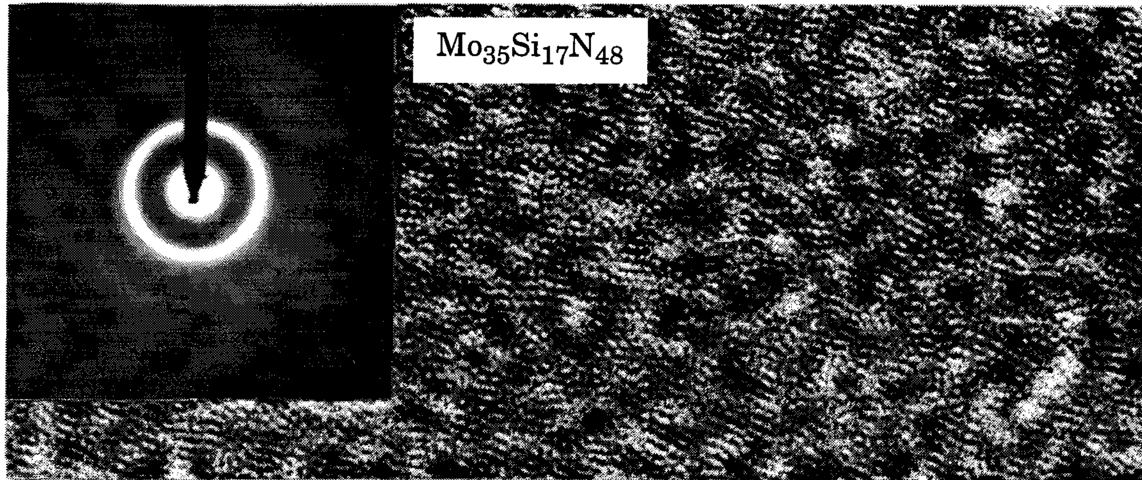

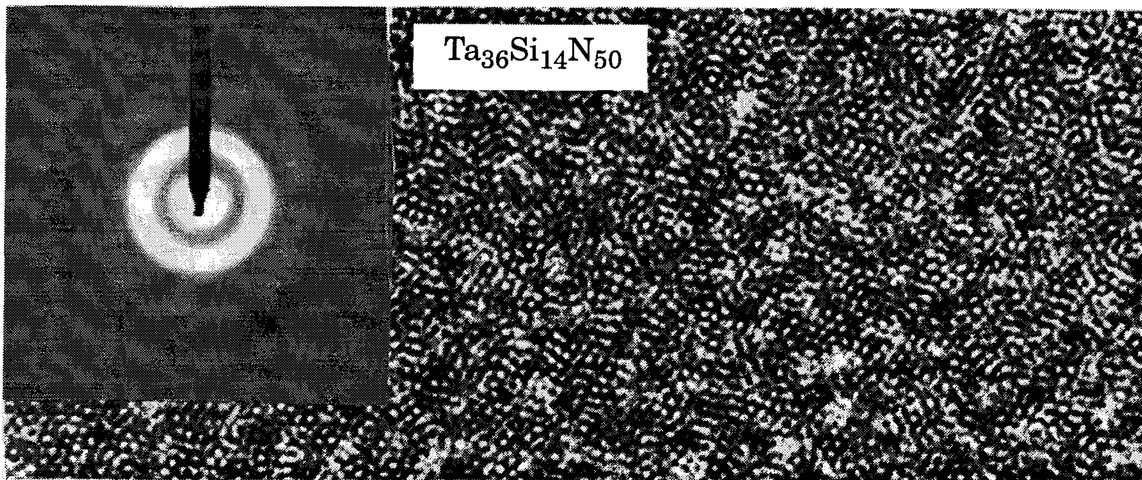

3 nm

Figure 3.3. High-resolution, plan-view, transmission electron micrographs of $Mo_{35}Si_{17}N_{48}$, $Ta_{36}Si_{14}N_{50}$, $W_{36}Si_{14}N_{50}$, and $W_{24}Si_{36}N_{40}$ films with corresponding electron diffraction patterns.

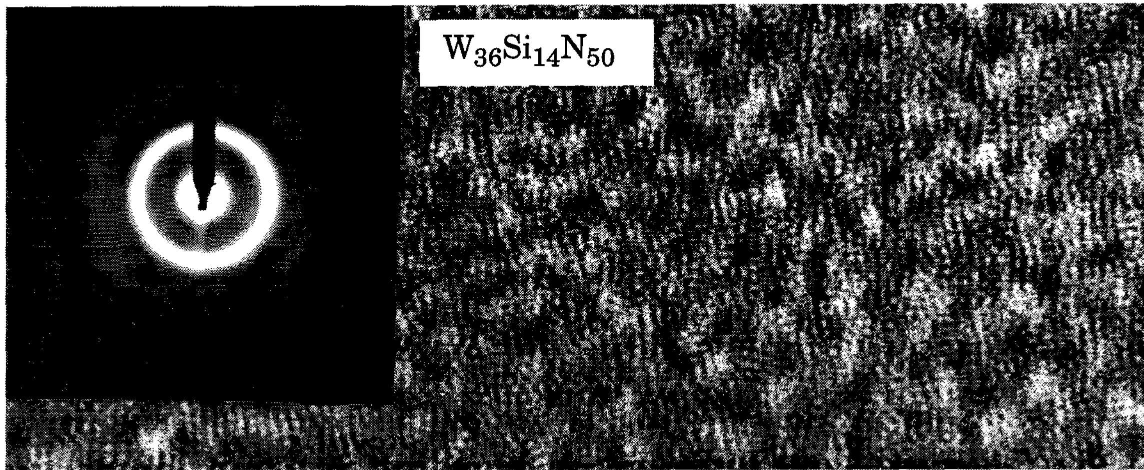

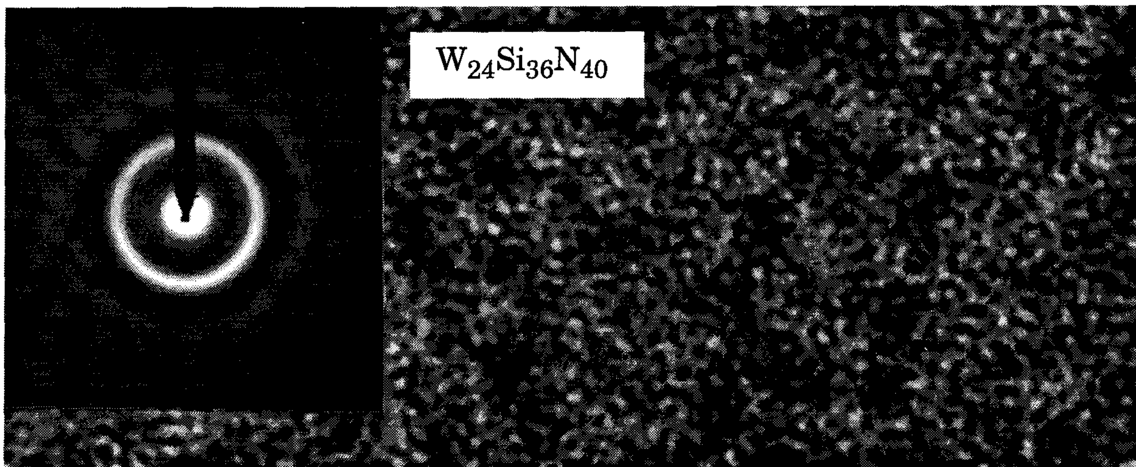

3 nm

Figure 3.3. Continued.

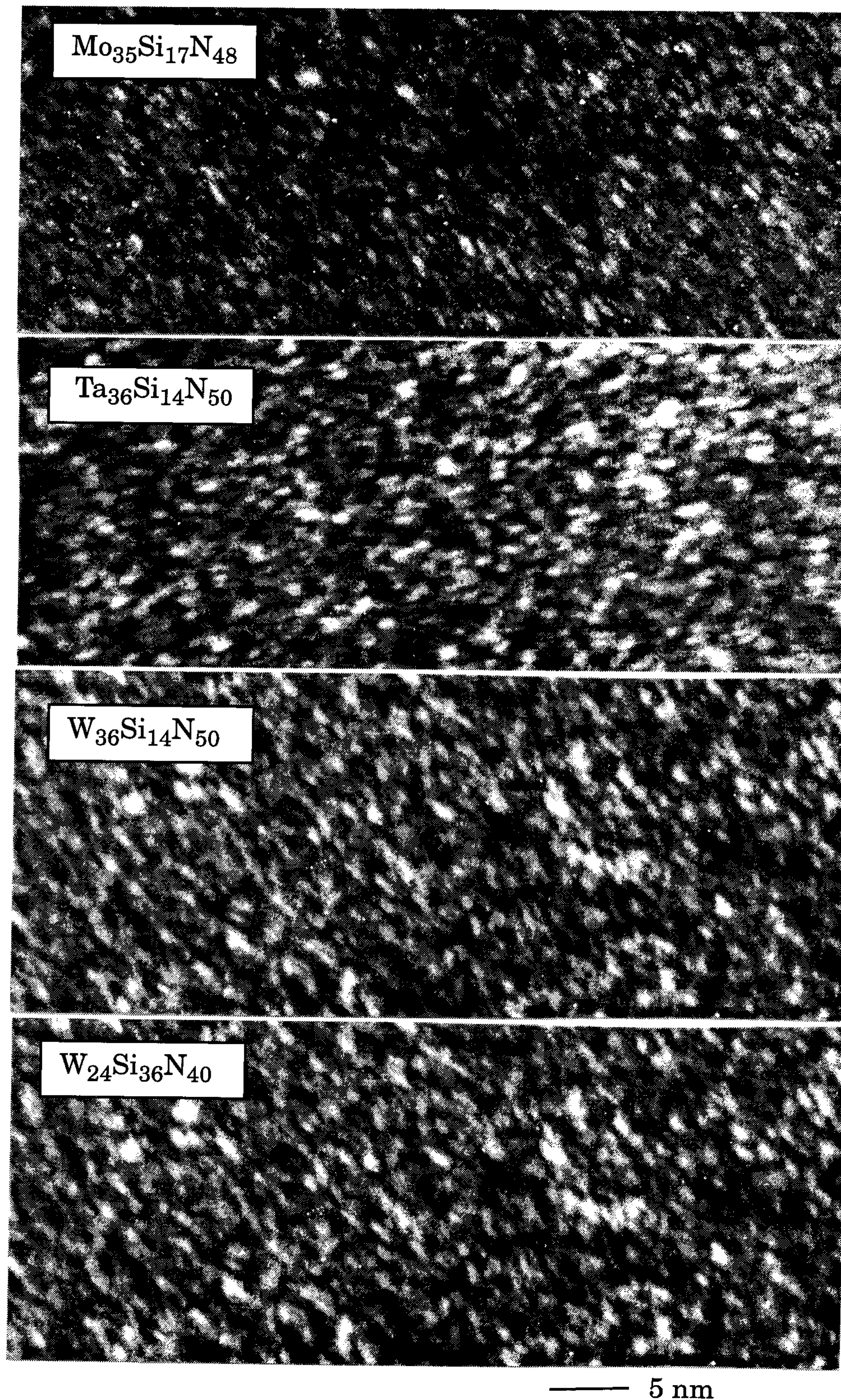

Figure 3.4. Beam-tilted, dark-field images for $Mo_{35}Si_{17}N_{48}$, $Ta_{36}Si_{14}N_{50}$, $W_{36}Si_{14}N_{50}$, and $W_{24}Si_{36}N_{40}$ films.

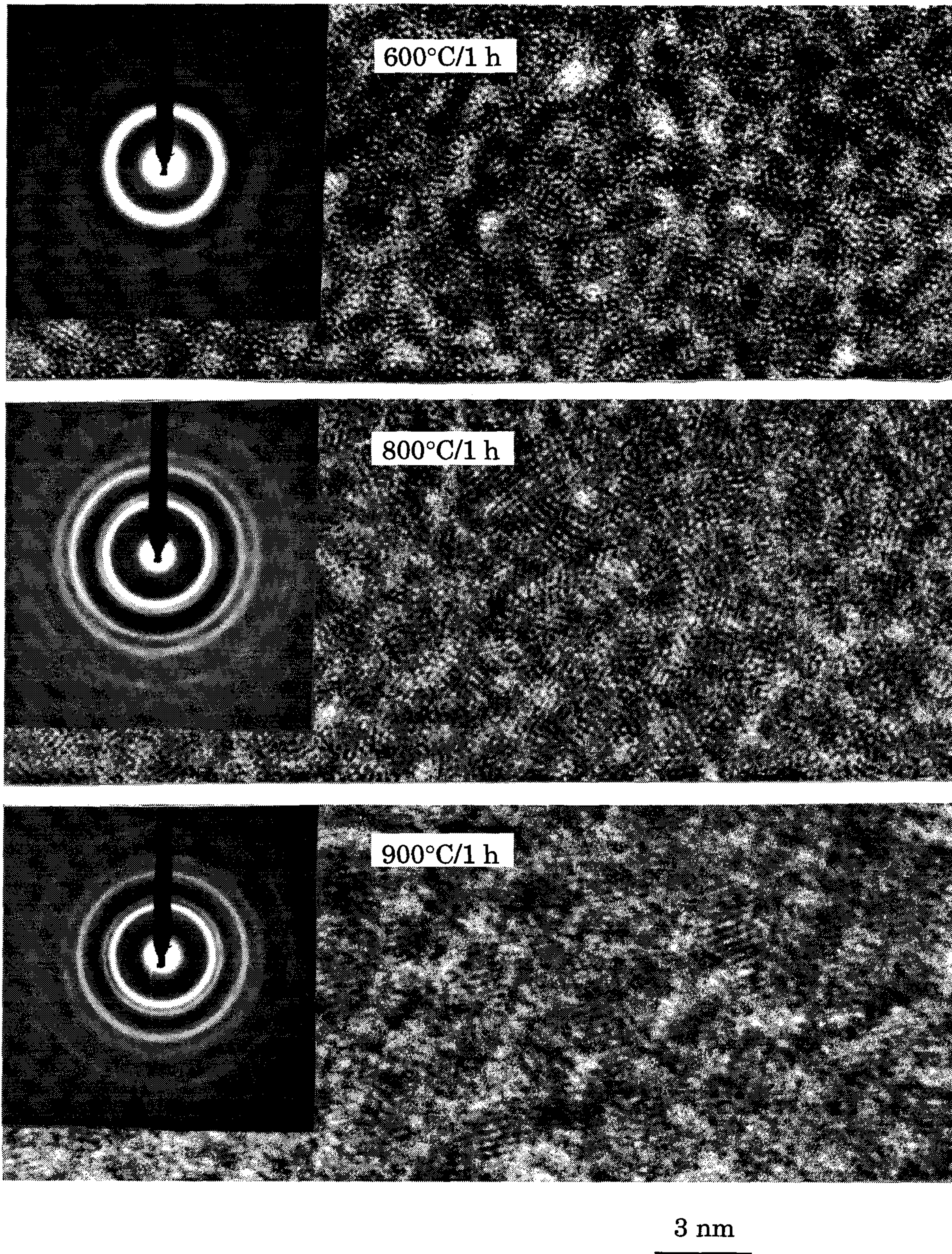

Figure 3.5. High-resolution, transmission electron micrographs of $Ta_{36}Si_{14}N_{50}$ films annealed at 600, 800, and 900°C for 1 h.

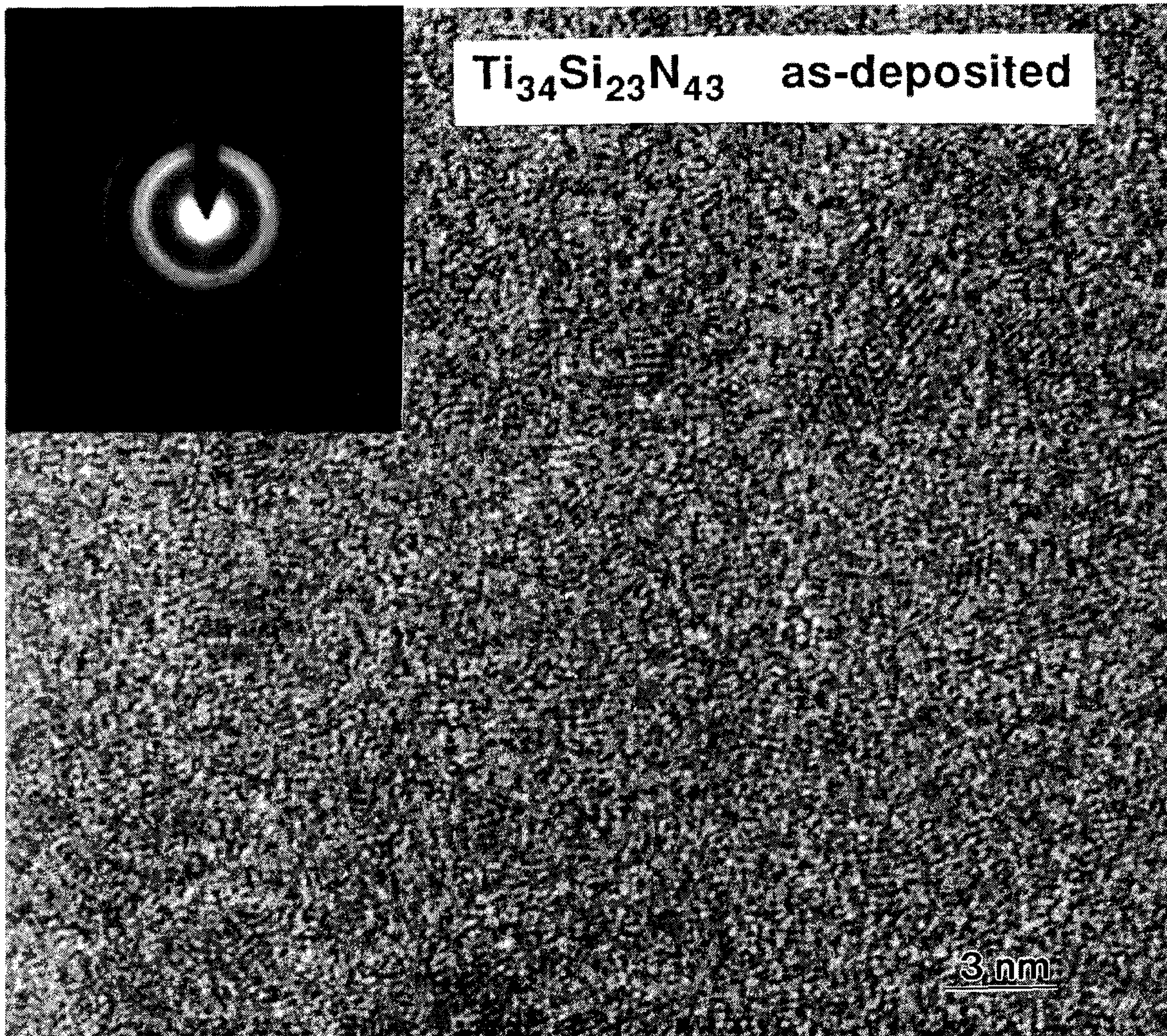

Figure 3.6. High-resolution bright-field image of as-deposited $Ti_{34}Si_{23}N_{43}$ with electron diffraction pattern.

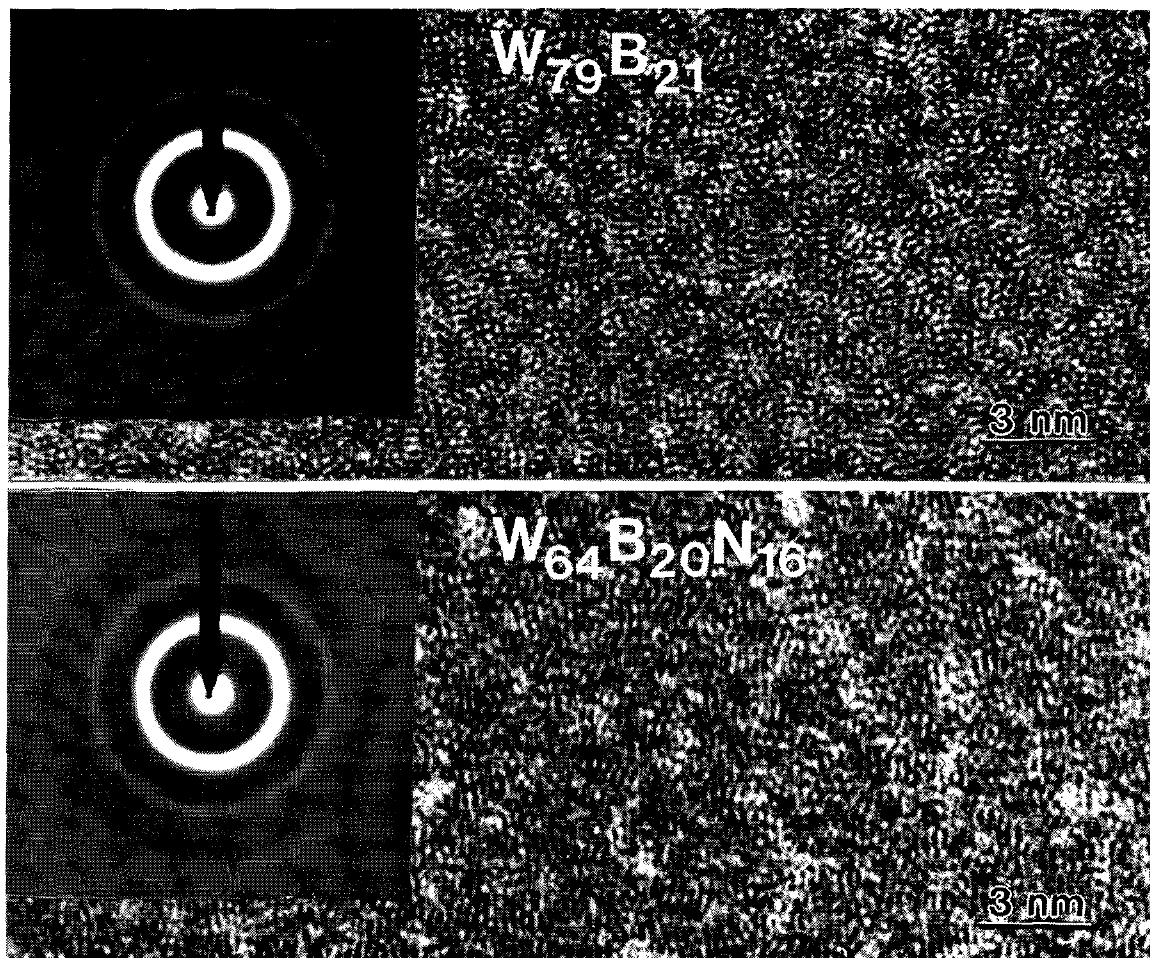

Figure 3.7. High-resolution bright-field images of as-deposited $W_{79}B_{21}$ and $W_{64}B_{20}N_{16}$ with electron diffraction patterns.

3.4. Small-Angle X-ray and Electron Scattering

So far, several measurements have suggested inhomogeneous structures for the amorphous ternary barriers: abrupt changes in resistivity with increasing nitrogen concentration, incongruous crystallization, and the existence of a well-defined local order seen by high-resolution transmission electron microscopy. Thermodynamically, multiple phases are expected in the systems as shown in the phase diagrams in Chapter 2. Given the difference in structure among the binary subcomponents of the ternary systems and the lack of mutual solubilities [67], the amorphous ternary systems may also be multiply-phased. With their sensitivity in probing average electron-density differences on length scales of roughly 1 nm to 1 μm, small-angle X-ray and electron scattering are aptly suited for probing the chemically dissimilar regions in the films. In this section, small-angle methods are applied to the ternary amorphous barriers. The results are somewhat preliminary, but they are sufficient to prove that chemical inhomogeneities do exist in the films.

Two asymptotic relations for a dilute solution of identical spherical particles in a matrix are of general use in elastic small-angle scattering (SAS) analysis. For very low scattering angles (the "Guinier" region), the scattered intensity in electron units is

$$I \cong n(\Delta\rho)^2 V^2 e^{-(R_g q)^2/3}$$

where n is the number of particles, $\Delta\rho$ is the difference in electron density between the matrix and particles, V is the volume of the particles, and R_g is the radius of gyration of the particles [73]. The quantity, q, is the magnitude of the difference between the incident and scatter vectors, i.e.,

$$q = \frac{4\pi}{\lambda}\sin\theta$$

with λ defining the wavelength of the radiation.

For larger values of q, the intensity decays in accordance with Porod's

law [73],

$$I \cong 2\pi (\Delta\rho)^2 S^2 q^{-4} .$$

Here, S defines the surface area of the two-phase regions. Porod's law has general applicability beyond dilute systems. The only criterion is a well-defined distinction in electron density for the two phases in the systems.

In denser systems, interference among the chemically dissimilar regions may superimpose oscillations on the small-angle spectra. Assuming identical spherical phases imbedded within a matrix, a radial distribution function may be easily computed using hard-sphere models. If the size and shape arrangements are complex, model distributions must be employed.

Small-angle experiments on the ternary amorphous barriers involved either Cu-K_α X-rays or 200 keV electrons with scattering in transmission. Samples for X-ray diffraction consisted of a 1.6-μm $Mo_{35}Si_{17}N_{48}$ film deposited onto a 100-nm-thick SiN membrane. Spectra were collected with the beam normal to the SiN/ $Mo_{35}Si_{17}N_{48}$ bilayer using a Bonse-Hart double-crystal camera at Brookhaven National Laboratories. The electron diffraction work consisted mainly of collecting patterns on photographic negatives from several nitrogen-laden ternary films. Films were typically sputter-deposited to a thickness of 13 or 20 nm onto <NaCl>, floated-off in deionized water, and collected on a 200-mesh Cu grid. The Phillips EM430 microscope used in the evaluations is capable of an effective 2-km camera length, which is very useful for observing diffraction effects from large-scale inhomogeneities. In the special case of $W_{24}Si_{36}N_{40}$ films, elastic and inelastic electron-scattering effects were separated using a Gatan 666 spectrometer configured as an energy filter as shown in Figure 3.8. The electrons were projected on a phosphor screen recorded by a 35-mm camera.

Figure 3.9 shows the small-angle X-ray scattering spectrum for the as-deposited $Mo_{35}Si_{17}N_{48}$ film on the thin SiN membrane. The pattern does reveal

inhomogeneities in the film and is, at first glance, suggestive of spinodal decomposition. Maxima in the oscillations occur at approximately q = 0.004, 0.006, 0.017, and 0.052 $Å^{-1}$. Substituting these values into Bragg's law gives a very rough estimate of the respective "interphase spacings," d = 1600, 1000, 370, and 120 Å. A Guinier-type fit of the low-q region gives a radius of gyration of a few thousand Angstroms. The results are in disagreement with the TEM micrographs of the 10-20 nm films, which do not show inhomogeneities on this size scale. Although it is entirely possible that such large-scale inhomogeneities do evolve during thick-film growth, a more likely candidate for the oscillations is particle inclusions flaked from the target. An abundance of particulate dust in the sputtering system is always observed after sputtering thick films from the composite targets. For the X-ray studies, the number of particles can be decreased by depositing thinner films, but at the expense of less scattering intensity. Even for the 1.6-μm-thick $Mo_{35}Si_{17}N_{48}$ film, 95% of the X-ray beam goes unattenuated. Ideally, small-angle scattering requirements require $1/e$ (37%) attenuation.

To circumvent the possible problems of particles in the film, selected-area electron diffraction was performed with much thinner films in the transmission electron microscope. All of the nitrogen-laden ternary films sputtered from the metal-rich targets exhibit electron scattering into the small-angle regime. The intensity appeared to decrease monotonically with increasing q. Given the lack of dynamic range on the photographic plates, multiple exposures were taken to capture the expeditious roll-off in intensity. However, no oscillations were observed. The absence of any obvious oscillations in the ternary systems may be related to a large degree of spatial and chemical inhomogeneity. Other reasons may include masking interference from the native oxide, voids, or microcracks in the self-supporting films, as well as insufficient dynamic range in the photographic plates.

Changing the metal-to-metalloid ratio made a marked differences in the small-angle patterns. $W_{24}Si_{36}N_{40}$ films sputtered from the WSi_2 target exhibit a broad peak at around q = 0.5 $Å^{-1}$. Evidently, a higher degree of coherence among the

chemically dissimilar regions exists in the silicon-rich films compared to the highly metal-rich films. Bragg's law gives a rough estimate of the coherence length in the system of 10-15 Å, which is comparable to the local order found by dark-field analysis in the previous section.

Two effects can be problematic in performing small-angle electron scattering experiments. First, double Bragg diffraction from identically-oriented grains will contribute to the scattering in the small-angle regime [73]. Fortunately in amorphous materials, this contribution can often be ignored. The second effect is inelastic scattering into small angles. Figure 3.10 shows the elastic and inelastic components to the small-angle scattering in the 20-nm-thick $W_{24}Si_{36}N_{40}$ samples. The spectra were obtained on 35-mm film as previously discussed. The film was then digitized using a commercial flatbed scanner. No attempt was made to correct for the possibly sizable nonlinearities in the phosphor, film, or scanner. In the elastic scattering curve, the diffuse diffraction at $q = 0.5$ Å^{-1} is readily apparent. The inelastic scattering, measured in a 7 eV window about 22 eV, contributes a relatively constant and low background to an unfiltered spectrum. Consequently, small-angle electron scattering experiments are indeed viable even in films with abundance of heavy metal, even with film thicknesses as large as 20 nm. Given the ability to perform selected-area diffraction, small-angle scattering in the TEM has the ability to avoid particles which are unavoidably scattered in the thick films necessary for X-ray techniques.

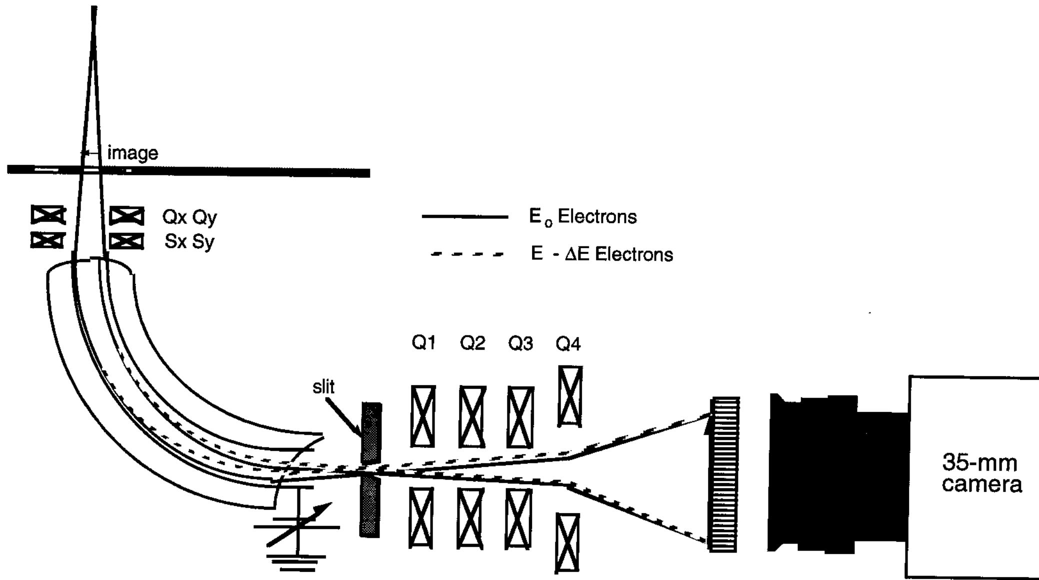

Figure 3.8. Apparatus for measuring elastically- and inelastically-scattered electrons (drawing courtesy of C.C. Ahn).

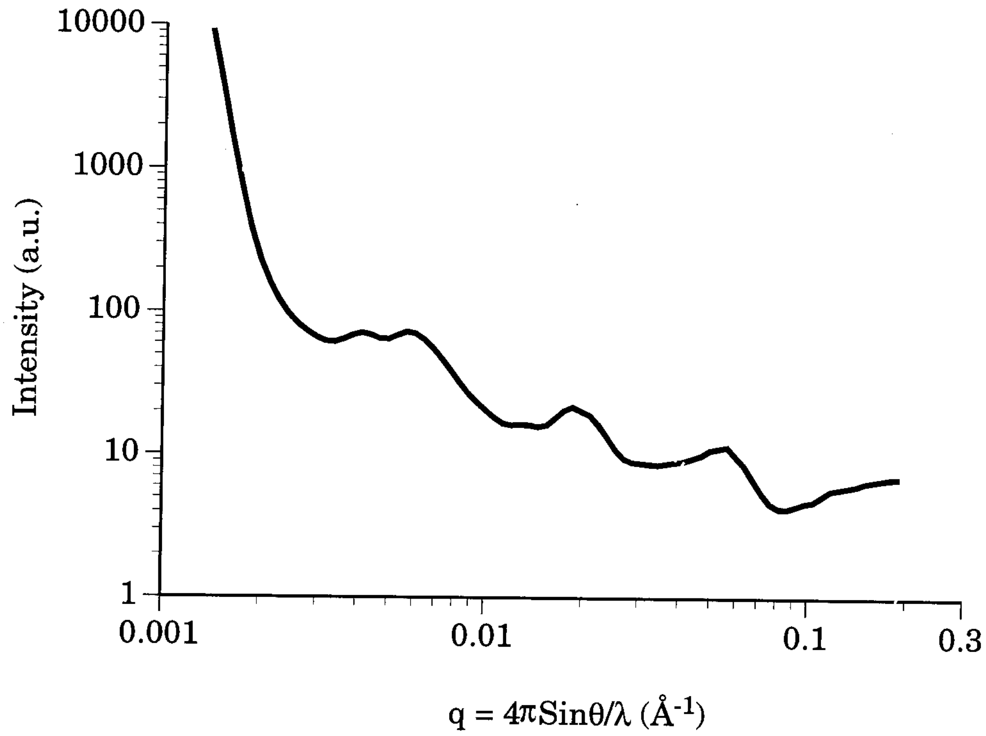

Figure 3.9. Small-angle X-ray spectra taken from a 1.6-μm-thick $Mo_{35}Si_{17}N_{48}$ film.

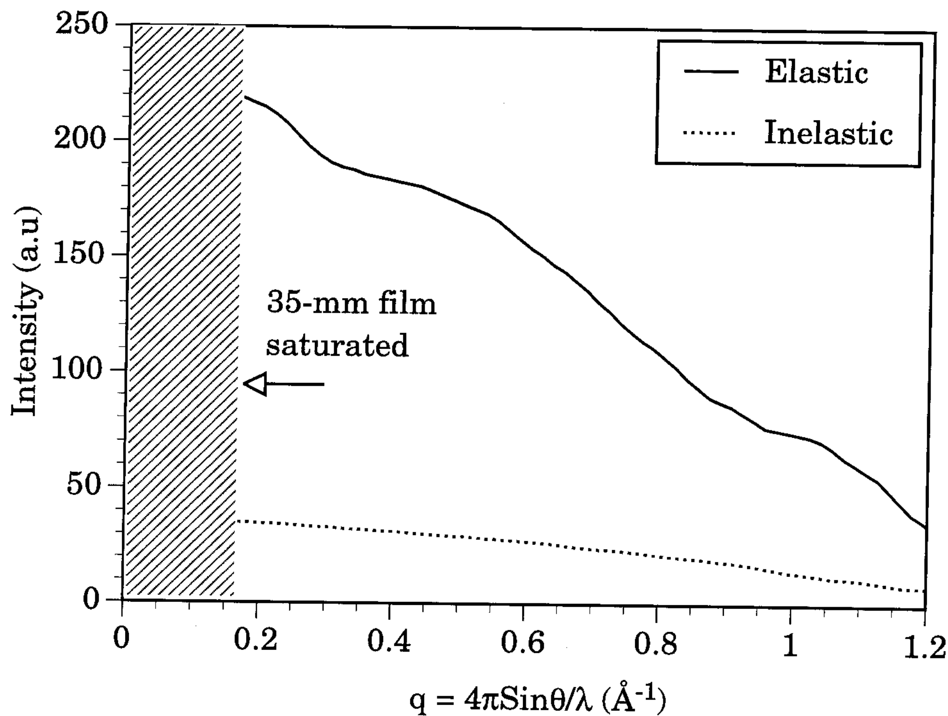

Figure 3.10. Elastic (7 eV window about 0 eV) and inelastic (7 eV window about 22 eV) small-angle electron scattering for a 20-nm-thick $W_{24}Si_{36}N_{40}$ film captured on a phosphor screen with a 35-mm camera. The incident beam energy was 200 keV (λ = 0.0251 Å). The apparent peak at q = 0.2 $Å^{-1}$ is a consequence of film nonlinearity near saturation.

3.5. Extended Energy Loss Fine Structure (EXELFS)

EXELFS involves bombarding a thin sample with monochromatic electrons and recording the distribution of energy loss in the vicinity of atomic absorption edges. Superimposed on the absorption edges are weak oscillations borne by interference effects from the backscattering of an ejected electron by neighboring atoms. The periodicities and intensities of the oscillations are indicative of the bond-lengths and neighboring species around the type of atom that produced the absorption edge. In many respects, EXELFS is identical to the more commonly used Extended X-ray Absorption Fine Structure (EXAFS) technique, except that the incident radiation consists of electrons rather than X-rays.

In single-scattering EXELFS theory under the dipole approximation [74], the oscillations on the absorption edge follow the relation originally derived by Stern [75]:

$$\chi(k) = -\sum_i \frac{N_i}{kr_i^2} f(k) e^{-2\sigma_i^2 k^2} e^{-2r_i/\lambda_i} \sin(2kr_i + 2\delta_i(k) + \varphi_i(k)) \quad (1)$$

Here, N_i is the number of atoms in the ith shell at a radial distance r_i from the central atom creating the edge; k is the wave vector of the ejected electron, $f(k)$ is the scattering amplitude of the ejected electron backscattered by an atom in the ith shell; σ_i^2 is the Debye-Waller factor used to quantify attenuation from thermal vibrations; λ_i is the mean free path of the ejected electron; δ_i is a phase factor from the ejected electron travelling to and from an atom in the ith shell; and φ_i is the phase shift from backscattering the ejected electron off an atom in the ith shell. Typically, because of multiple scattering effects, the formula is only accurate for $k > 4$ Å^{-1}.

EXELFS experiments were conducted only on the K-edges of Si in $Mo_{35}Si_{17}N_{48}$ and $Ti_{29}Si_{22}N_{49}$ films. The film thicknesses were 20 nm. The Mo-Si-N and Ti-Si-N systems were chosen because their metalloid edges do not overlap with the metal. For comparative purposes, 20-nm-thick amorphous Si_3N_4 films reactively

sputtered from a Si target were also evaluated. All films were deposited onto <NaCl>, floated-off in deionized water, and collected on a 200-mesh Cu grid. The EXELFS experiments were performed in a Phillips EM430 transmission electron microscope operating at 200 keV in diffraction mode. The sample was neither heated nor cooled externally. A Gatan 666 parallel spectrometer mounted below the column measured the energy distribution of the transmitted electrons. A schematic of the spectrometer is given in Figure 3.11. The channel-to-channel resolution of the spectrometer was nearly 2.15 eV/channel. To compensate nonlinearities in the position-sensitive detector, a few dozen spectra were taken with a retardation potential (0 to 100 V) applied to the electrons within the spectrometer in order to "gain average" the data. Each spectrum was then normalized by the instrument response obtained with no sample, shifted, and summed. The edge energy, E_o, was assumed to lie at the inflection point of the rising edge.

Data analysis followed standard guidelines [76-79]. All coding was done with commercial numerics software [80]. First, the background was removed by fitting the pre-edge region with the functional form, aE^{-b}, where E is the energy loss, and a and b are fit parameters. The energy scale was then converted to momentum through the classical relation,

$$E - E_o = \frac{\hbar^2 k^2}{2m} .$$

Next, the free atom absorption, $\mu_0(k)$, was extrapolated by removing the fine structure through fitting a cubic spline to the total absorption data, $\mu(k)$. The knots were spaced equidistantly, and only a few knots were used to avoid adding artificial periodicities in the range associated with typical bond lengths. Next, the normalized EXELFS function, $\chi(k)$, was calculated through

$$\chi(k) = \frac{\mu(k) - \mu_o(k)}{\mu_o(k)} .$$

To provide homogeneous weightings of the oscillations in k, $\chi(k)$ was multiplied by $k^3 W(k)$, where $W(k)$ is a rectangular window function with a Hanning-function

roll-off at the edges. No attempt was made to deconvolute multiple-scattering effects in the data. In many instances, the inelastic contributions give incoherent oscillations which are not greatly detrimental to the analysis [81,82].

The magnitude of the Fast Fourier Transform of $k^3W(k)\chi(k)$ yields a "pseudo" radial distribution function (RDF) about the atom specie producing the edge. Typically, only data between approximately 3 and 15 Å^{-1} are considered. The exact endpoints are chosen at the zeros of the oscillations to avoid ringing effects. $k^3W(k)\chi(k)$ is often padded with zeros for $k > 15$ Å^{-1} to give a finer partition in real space. A direct transform ignores the phase terms in Eqn. (1), thus the resulting maxima are generally shifted by a few tenths of an Angstrom. A corrected RDF may be obtained by backtransforming the individual peaks and fitting Eqn. (1) to the data. The phase terms can be experimentally extracted through model materials, or less preferably, through calculated values [83,84].

Figure 3.12 shows the K-Si absorption edges for the Si_3N_4, $Mo_{35}Si_{17}N_{48}$, and $Ti_{29}Si_{22}N_{49}$ films after background subtraction. Several million counts were necessary to sufficiently extend the oscillations above the noise beyond $k = 12$ Å^{-1}. The strong oscillations in first 60 eV or so of the edge are largely from plural scattering. At higher energies, the edge has a much smoother shape with decaying oscillations. Differences in slopes in the spectra may be a consequence of background subtraction. The $k^3\chi(k)$ functions obtained from spline fitting are given in Figure 3.13. High frequency noise in the data $Mo_{35}Si_{17}N_{48}$ sample is apparent for $k > 10$ Å^{-1}, but the low-frequency oscillations can still be seen at $k = 12$ Å^{-1}. The oscillations do have a relatively low frequency, which forced the spline points to be spread quite far apart. Thus, the spline fits had some difficulty in tracking free-atom absorption. Figure 3.14 shows the pseudo-RDF obtained from the Fourier transform of $k^3\chi(k)$. All of the systems exhibit large maxima at $r = 1.3$, which is characteristic of phase-uncorrected EXAFS [61,85,86] and EXELFS [87] RDF's for Si-N bonding in Si_3N_4. The actual Si-N bond length in Si_3N_4 is approximately 1.7 Å [59,61]. The Si_3N_4 and $Ti_{29}Si_{22}N_{49}$ samples also exhibit a peak around 2.5 Å, which is consistent with the

phase-uncorrected Si-Si interatomic distance (actual length is 3.0 Å). Truncating $\chi(k)$ of $Mo_{35}Si_{17}N_{48}$ below the noise at k = 10 Å also produces a well-defined peak at 2.5 Å. The lack of strong peaks beyond r = 3 Å in all of the spectra is indicative of amorphous materials. Maxima below 1.3 Å are considered unphysical and are attributed to multiple scattering and deficiencies in the spline fit.

In the equilibrium binary Ti-Si and Mo-Si phases, the nearest-neighbor bond lengths to Si are typically greater than 2.2 Å, as listed in Table 3.1. Considering the strength of the peak at 1.3 Å, the Si in the nitrogen-laden Mo-Si-N and Ti-Si-N films appears to be primarily bonded as amorphous silicon nitride. By default, the remaining portion of the ternary films probably consists of amorphous transition-metal nitrides. The inhomogeneities seen by small-angle diffraction in the previous section can now be partly explained by the dual presence of silicon nitride and transition metal nitrides. Given the thermodynamic and structural similarities of the TM-Si-N systems, the Ta-Si-N and W-Si-N films probably also have a similar structure, so long as the films are nearly saturated with nitrogen. In a similar vein, the microstructure of nitrogen-rich W-B-N films may consist of an amorphous blend of BN and tungsten nitrides.

It should be noted that the model structure of an amorphous mixture of transition metal nitrides and silicon nitrides is undoubtedly a simplification. Although the partial radial distribution functions of Si in Mo-Si-N and Ti-Si-N films are indeed consistent with silicon nitride, they are only indicative of most, but not all of the Si bonding in the samples. Transitions from silicon nitride to metal nitride regions arguably give silicon-metal bonding as well. Clustering of atoms ejected from the target or formed within the discharge can also give silicon-metal bonding. A narrow-band technique such as XPS is necessary to separate all of the types of bonding within the samples.

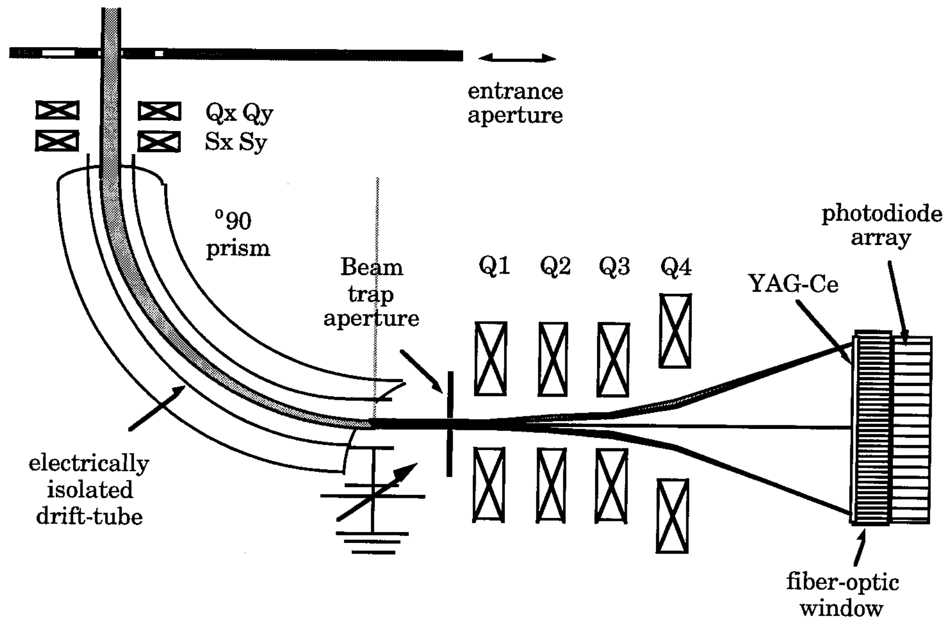

Figure 3.11. Schematic for the Gatan spectrometer used to measure the energy distribution of the electrons passed through the sample (drawing courtesy of C.C. Ahn).

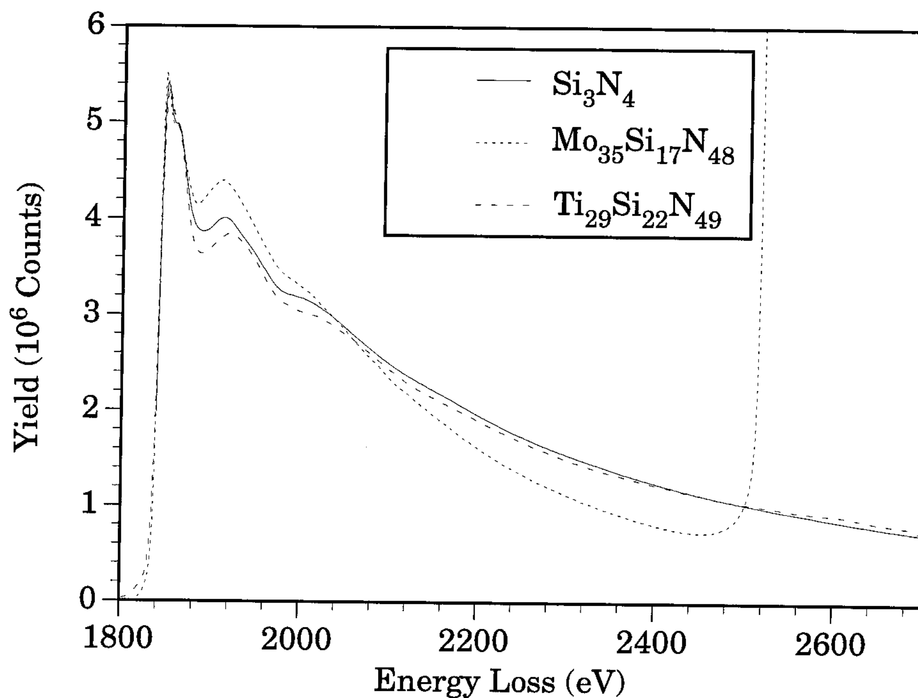

Figure 3.12. Energy-loss spectra of the K-Si edges after background removal for Si_3N_4, $Mo_{35}Si_{17}N_{48}$, $Ti_{29}Si_{22}N_{49}$ films. For comparative purposes, the $Mo_{35}Si_{17}N_{48}$ spectra was divided by 2. The upward swing in the $Mo_{35}Si_{17}N_{48}$ profile at 2700 eV is from the L_{iii} edge of Mo.

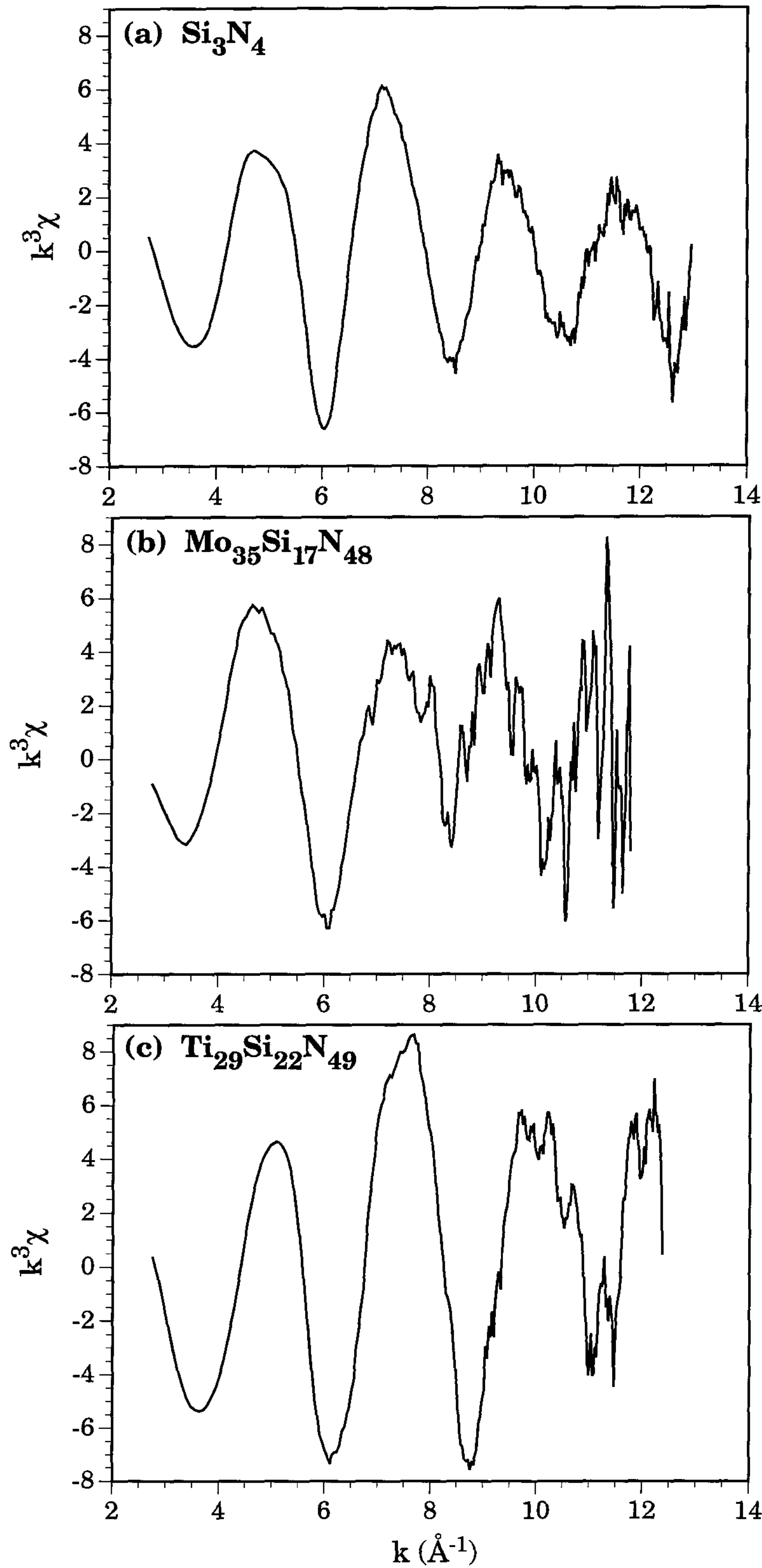

Figure 3.13. $k^3\chi(k)$ functions obtained from the K-Si edges of (a) Si_3N_4, (b) $Mo_{35}Si_{17}N_{48}$, and (c) $Ti_{29}Si_{22}N_{49}$ films.

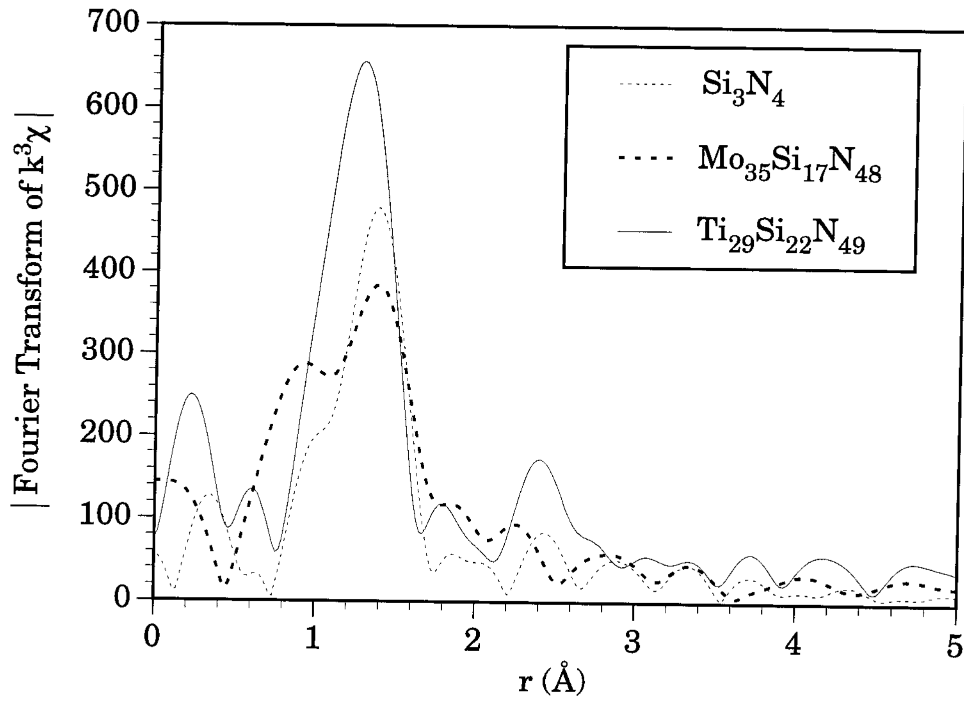

Figure 3.16. Measured pseudo radial distribution functions for Si_3N_4, $Mo_{35}Si_{17}N_{48}$, and $Ti_{29}Si_{22}N_{49}$ films.

Table 3.1. Closest neighbors to Si atoms in Mo- and Ti-silicides compared with a-Si_3N_4 and Si.

Silicide	First Nearest Neighbor to Si	First Nearest Neighbor Distance (Å)	Second Nearest Neighbor to Si	Second Nearest Neighbor Distance (Å)
Mo_3Si	Mo	2.73	Si	4.23
Mo_5Si_3	Si	2.46	Mo	2.59
$MoSi_2$	Mo,Si	2.26	Mo,Si	2.61
Ti_3Si	Ti	2.52	Ti	2.52
Ti_5Si_3	Ti	2.60-2.61	Ti	2.67
Ti_5Si_4	Ti	2.22	Si	2.25
TiSi	Ti	2.31	Ti	2.41
$TiSi_2$	Si,Ti	2.54	Ti	2.74
a-Si_3N_4	N	1.7	Si	3.0
Si	Si	2.35	Si	3.84

References, Chapter 3.

[1] S.D. Dahlgren, in *Rapidly Quenched Metals III, vol. 2*, edited by B. Cantor, The Metals Society, London, England (1978) pp. 36-47.

[2] J.B. Kortright and A. Bienstock, *Phys. Rev. B* 37, 2979 (1988).

[3] F. Nava, B.Z. Weiss, K.N. Tu, D.A. Smith, and P.A. Psaras, *J. Appl. Phys.* 60, 2445 (1986).

[4] A. Praffcke, P. Lamparter, and S. Steeb, *Zeit. fur Naturforschung A* 48, 777 (1993).

[5] C.C. Tseui, W.L. Johnson, R.B. Laibowitz, and J.M. Viggiano, *Solid State Comm.* 24, 615 (1977).

[6] F. Nava, P.A. Psaras, H. Takai, K.N. Tu, S. Valeri, and O. Bisi, *J. Mater. Res.* 1, 327 (1986).

[7] W.L. Johnson, C.C. Tseui, S.I. Raider, and R.B. Laibowitz, *J. Appl. Phys.* 50, 4240 (1979).

[8] F. Nava, G. Ottaviani, and G. Riontino, *Materials Letters* 3, 311 (1985).

[9] T. Tien, G. Ottaviani, and K.N. Tu, *J. Appl. Phys.* 54, 7047 (1983).

[10] B.Z. Weiss, K.N. Tu, and D.A. Smith, *Acta Metall.* 34, 1491 (1986).

[11] F. Nava, T. Tien, and K.N. Tu, *J. Appl. Phys.* 57, 2018 (1985).

[12] R.S. Rastogi, V.D. Vankar, and K.L. Chopra, *Thin Solid Films* 213, 45 (1992).

[13] S. Ikeda, H. Fujimori, M.Ikebe, Y. Muto, and K. Suzuki, in *Proc. Int. Conf. on Rapidly Quenched Metals*, edited by T. Masumoto and K. Suzuki, Japan Institute of Metals, Aoba Aramaki, Sendai 980, Japan (1982). pp. 1253-1256.

[14] R.E. Thomas, J.H. Perepezko, and J.D. Wiley, *Appl. Surf. Sci* 26, 534 (1986).

[15] R.E. Thomas, J.H. Perepezko, and J.D. Wiley, *Materials Research Society Symp. Proc.* 54, edited by R. J. Nemanich and P.S. Ho, Materials Research Society, Pittsburgh, PA (1986) pp. 127-132.

[16] R.E. Thomas, J.H. Perezpezko, and J.D. Wiley, *J. Vac. Sci. Technol. A* 8, 885 (1990).

[17] R.D. Thompson, H. Takai, P.A. Psaras, and K.N. Tu, *J. Appl. Phys.* 61, 540 (1987).

[18] P. Lamparter, A. Habenschuss, and A.H. Narten, *J. Non Cryst. Sol.* 86, 109 (1986).

[19] P. Lamparter and S. Steeb, *Physica B* 180, 782 (1992).

[20] I.J.M.M. Raaijmakers, A.H. van Ommen, and A.H. Reader, *J. Appl. Phys.* 65, 3896 (1989).

[21] H.G. Nam, I. Chung, and R.W. Bene, *Thin Solid Films* 227,153 (1992).

[22] T. Ichihawa, *Phys. Stat. Sol. A* 29, 293 (1975).

[23] J.L. Finney, *Proc. Roy. Soc. Cond. A* 319,479 (1970).

[24] J. Dixmer and J.F. Sadoc, in *Metallic Glasses*, edited by J.J. Gilman and H.J. Leamy, American Society for Metals, Metals Park, OH (1976) pp. 97-113.

[25] P.M. Smith, J.G. Fleming, R.D. Lujan, E. Roherty-Osmun, J.S. Reid, A.K. Hochberg, and D.A. Roberts, in *Advanced Metallization for ULSI Applications in 1993*, edited by D.P. Favreau, Y. Shacham-Diamond, and Y. Horiike, Materials Research Society, Pittsburgh, PA (1994) pp. 345-351.

[26] R.R. Ruf and C.C. Tseui, *J. Appl. Phys.* 54, 5705 (1983).

[27] T.P. Moffatt, R.M. Latanision, and R.R. Ruf, *J. Electrochem. Soc.* 138, 3280 (1991).

[28] R.M. Williams, A.P. Thakoor, S.K. Khanna, and W.L. Johnson, *J. Electrochem. Soc.* 131, 2791 (1984).

[29] W.L. Johnson and A.R. Williams, *Phys. Rev. B* 20, 1640 (1979).

[30] C.C. Koch, D.M. Kroeger, J.S. Lin, J.O. Scarbrough, W.L. Johnson, and A.C. Anderson, *Phys. Rev. B* 27, 1586 (1983).

[31] M. Mehra, W.L. Johnson, A.P. Thakoor, and S.K. Khanna, *Solid State Comm.* 47, 859 (1983).

[32] A.P. Thakoor, J.L. Lamb, S.K. Khanna, M. Mehra, and W.L. Johnson, *J. Appl. Phys.* 58, 3409 (1985).

[33] E. Kolawa, X. Sun, J.S. Reid, M-A. Nicolet, and R.P. Ruiz, *Thin Solid Films* 236, 301 (1993).

[34] I. Orue, F. Plazola, M.L. Fernandez-Gubieda, J. Gutierrez, and J.M. Barandiaran, *IEEE Magnet.* 30, 536 (1994).

[35] T.H. Noh, A. Inoue, H. Fujimori, and T. Masumoto, *J. Magnetism and Mag-*

netic Materials 123, 35 (1993).

[36] R.A. Dunlap and G. Stroink, *Canadian J. Phys.* 62, 714-719 (1984).

[37] M.S. Leu, C.S. Lin, and S.T. Lin, *Scripta Metall. et Mater.* 25, 637 (1991).

[38] C.L. Chien and K.M. Unruh, *Phys. Rev. B* 24, 1556 (1981).

[39] J.L.C. Daams, P. Villars, and J.H.N. van Vucht, *Atlas of Crystal Structure Types for Intermetallic Phases, vols. 1-4*, ASM International, Newbury, OH (1991).

[40] H.J. Goldschmidt, *Interstitial Alloys*, Plenum Press, New York (1967).

[41] G.V. Samsonov and I.M. Vinitskii, *Handbook of Refractory Compounds*, IFI Plenum, New York (1980).

[42] R.E. Watson and L.H. Bennett, *Phys. Rev. B.* 43, 11642 (1991).

[43] J.E. Crow, M. Strongin, R.S. Thompson, and O.F. Kammerer, *Physics Letters* 30A, 161 (1969).

[44] M.M. Collver and R.H. Hammond, *Phys. Rev. Lett.* 30, 92 (1973).

[45] B. Schroeder, W.L. Johnson, C.C. Teuei, P. Chaudhari, and J.F. Graczyk, *AIP Conf. Proc.* 31, edited by G. Lucovsky and F.L. Galeener, American Institute of Physics (1976) pp. 353-358.

[46] K.L. Chopra, *Thin Film Phenomena*, McGraw-Hill, New York (1969) pp, 195-215.

[47] K.L. Chopra, M.R. Randlett, and R.H. Duff, *Phil. Mag.* 16, 261 (1967).

[48] X. Sun, E. Kolawa, J-S. Chen. J.S. Reid, and M-A. Nicolet, *Thin Solid Films* 236, 347 (1993).

[49] T. Kacsich, M. Neubauer, U. Geyer, K. Baumann, F. Rose, and M. Uhrmacher, *J. Phys. D* 28, 424 (1995).

[50] P.M. Fabis, R.A., Cooke, and S. McDonough, *J. Vac. Sci. Technol. A* 8, 3819 (1990).

[51] M. Thuillard, T.W. Workman, E. Kolawa, and M-A. Nicolet, *J. Less-Common Metals* 145, 505 (1988).

[52] J.S. Reid, unpublished.

[53] K. Affolter, H.P. Kattelus, and M-A. Nicolet, *Materials Research Society Proc.* 47, edited by C.R. Aita and K.S. SreeHarsha, Materials Research Society,

Pittsburgh, PA (1985) pp. 167-173.

[54] F.C.T. So, E. Kolawa, X-A. Zhao, and M-A. Nicolet, *Thin Solid Films* 153, 507 (1987).

[55] P. Pokela, Ph.D. Dissertation, Helsinki University of Technology (1991).

[56] I. Barin, *Thermochemical Data of Pure Substances*, VCH Verlagsgesellschaft mbH, D-6940 Weinheim, Germany (1989).

[57] Y. Hirohata, N. Shimamoto, T. Hino, T. Yamashima, and K. Yabe, *Thin Solid Films* 253, 425 (1994).

[58] C.H. Drummond, *J. Non-Cryst. Sol.* 123, 114 (1990).

[59] F.H.P.M. Habraken and A.E.T. Kuiper, *Mat. Sci. and Eng.* R12, 123 (1994).

[60] S.C. Bayliss and S.J. Gurman, *J. Non-Cryst. Solids* 127, 174 (1991).

[61] N. Umesaki, N. Kamijo, I. Tanaka, and K. Niihara, *Jpn. J. Appl. Phys. pt. 1* 32, 649 (1993).

[62] S. Reinke, M. Kuhr, and W. Kulisch, *Diamond and Related Materials* 3, 341 (1994).

[63] C.R. Aita, *Materials Science Forum: Synthesis and Properties of Boron Nitride, vol. 54 and 55*, edited by J.J. Pouch and Samuel A. Alterovitz, Trans Tech Publications, Brookfield, VT (1990) pp. 1-20.

[64] D.R. McKenzie, W.G. Sainty, and D. Green, *Materials Science Forum: Synthe sis and Properties of Boron Nitride, vol. 54 and 55*, edited by J.J. Pouch and Samuel A. Alterovitz, Trans Tech Publications, Brookfield, VT (1990) pp. 193-205.

[65] W. Gissler, J. Haupt, A. Hoffmann, P.N. Gibson, and D.G. Rickerby, *Thin Solid Films* 191, 113 (1991).

[66] D.J. Kester, K.S. Ailey, and R.F. Davis, *Diamond and Related Materials* 3, 332 (1994).

[67] P. Rogl and J.C. Schuster (eds.), *Phase Diagrams of Ternary Boron Nitride and Silicon Systems*, ASM International, Materials Park, OH (1992).

[68] E. Kolawa, J.M. Molarius, C.W. Nieh, and M-A. Nicolet, *J. Vac. Sci. Technol. A* 8, 3006 (1990).

[69] R.E. Thomas, J.H. Perepeżko, and J.D. Wiley, *Appl. Surf. Sci.* 26, 534 (1986).

[70] B.D. Cullity, *Elements of X-Ray Diffraction, 2nd ed.*, Addison Wesley, Reading, Mass (1978) p. 102.

[71] W. Posadowski, *Thin Solid Films* 162, 111 (1988).

[72] X. Sun, unpublished.

[73] A. Guinier, *X-ray Diffraction in Crystals, Imperfect Crystals, and Amorphous Bodies*, Dover Publications, Mineola, NY (1994) chap. 10.

[74] D.K. Saldin and J.M. Yao, *Phys. Rev. B* 41, 52 (1990).

[75] E.A. Stern, *Phys. Rev. B* 10, 3027 (1974).

[76] J.W. Cooke, Jr. and D.E. Sayers, *J. Appl. Phys.* 52, 5024 (1981).

[77] D.C. Koningsberger, *Jpn. J. Appl. Phys.* 32, suppl. 32-2, 877 (1992).

[78] B.K. Teo, *EXAFS: Basic Principles and Data Analysis*, Springer-Verlag, Berlin, Germany (1986) chap. 6.

[79] R.F. Egerton, *Electron Energy Loss Spectroscopy in the Electron Microscope*, Plenum Press, New York (1986) pp. 278-289.

[80] HiQ for Macintosh, version 2.0.2, National Instruments, Austin, TX.

[81] J.K. Okamoto, Ph.D. Dissertation, California Institute of Technology (1993).

[82] ref 78, p. 113.

[83] ibid., pp. 316-345.

[84] A.G. McKale, B.W. Veal, A.P. Paulikas, S.-K. Chan, and G.S. Knapp, *J. Am. Chem. Soc.* 110, 3763 (1988).

[85] J. Finster, E-D. Klinkenberg, J. Heeg, and W. Braun, *Vacuum* 41, 1586 (1990).

[86] M. Imamura, H. Shimada, N. Matsubayashi, T. Sato, Y. Yoshimura, T. Hanaoka, M. Sasaki, and A. Nishijima, *Jpn. J. Appl. Phys. pt. 1* 32, 743 (1993).

[87] R.D. Leapman and C.R. Swyte, *Analytical Electron Microscopy–1981*, edited by R.H. Geiss, San Francisco Press, Inc., San Francisco, CA (1981) pp. 164-172.

Chapter 4. TM-Si-N Diffusion Barriers between Al and Si

4.1. Introduction

Because of the solubility of Si in Al, Si/Al contacts are metallurgically unstable [1-3]. When thermally processing Al films on <Si> substrates at 300°C or higher, Si diffuses through the grain boundaries of Al to satiate the equilibrium solubility of a few tenths of an atomic percent (Figure 4.1) [5,6]. The local dissolution of the Si leaves behind voids which are subsequently filled by Al. With sufficient depth to the protrusions, an underlying pn-junction shorts through spiking by the Al. If the aluminum is in contact with poly-silicon, such as on a MOS gate electrode, the reaction is even more pronounced [7]. Large-scale segregation of Al and Si may occur, giving uneven electrical properties across the gate as well as providing unfavorable surface morphologies. Once through the poly-silicon, Al attacks the SiO_2 to form a thin Al_2O_3 layer which can adversely affect the dielectric properties of the gate [2,8,9].

The obvious solution of adding small amounts of Si to Al during deposition remedies the sponging phenomenon, but poses other problems [2,3,10-12]. From the diagram in Figure 4.1, any solubility met at processing temperatures (400-500°C) results in supersaturation at lower temperatures. During subsequent cooling after thermal processing, unaccommodated silicon within the Al will grow epitaxial, p-type layers on a <Si> substrate, thus changing the intended device properties.

Therefore, direct Al contacts to silicon or silicon dioxide are considered too unreliable for most VLSI designs. Diffusion barriers must be implemented to isolate the Al. Given the high degree of reactivity of Al with many substances, the choice of materials is complicated. Developing Al barriers usually involves providing sufficient kinetic barriers to slow the reaction of Al. Implementing pure elements as barriers provides a cursory remedy. Most elements readily react with Al to form binary compounds [1]. The remaining unreacting elements are unsatisfactory for other reasons: high solubility with Al or low melting temperature; explosiveness in air; or

short half-lives. Compound barriers containing transition metals have drawn the most research interest. Transition-metal silicides, typically used for contacting layers, do not suffice as diffusion barriers also because of expeditious reaction [13-22]. Alternatively, a modest degree of stability has been achieved with TiW [23-25] as well as many transition-metal nitrides [26-35], borides [36-39], oxides [31,35,40-43], and carbides [44-48]. Complementary lists of various barrier works can be found in several review articles [13,49-51]. With the possible exceptions VB_2 and HfB_2 [38,52,53], the nitrides, borides, and carbides typically initiate reaction with Al at 450 to 500°C. By purposely growing a native oxide on the surface of the barrier, the stability can be greatly enhanced, but usually at the expense of higher contact resistivity. Al can react with the native oxide to form Al_2O_3, which acts as a diffusion barrier to retard further reaction up to 550-600°C [51]. In a similar vein, conductive oxide barriers such RuO_2 and Mo_xO_{1-x} [31,35,40-43] owe their barrier integrity up to 600°C to the sluggish formation of Al_2O_3. With the Al-Si eutectic temperature being 577°C, stability at 600°C is a matter worthy of remark.

Despite their lack of grain boundaries to provide fast diffusion paths, many amorphous diffusion barriers have had no advantage over their polycrystalline counterparts [14,54-59]. Once again, reaction with Al is the failure mode. However, one particular amorphous barrier studied by Kolawa et al., $Ta_{36}Si_{14}N_{50}$, is able to prevent Al from spiking underlying silicon at temperatures above the melting point of Al, 660°C [60,61]. In those studies, Ta-Si-N reportedly did not react with Al according to X-ray diffraction and conventional TEM analyses. Curiously, tantalum silicides [60], tantalum nitrides [33], and silicon nitride [62] are all known to react with Al.

In this chapter, Ta-Si-N's chemical relatives, Mo-Si-N and W-Si-N, will also be shown to make extremely effective diffusion barriers between <Si> and Al. Through high-resolution transmission electron microscopy of W-Si-N/Al bilayers, an explanation for the high degree of stability will be offered. For the sake of a reference point, the respective amorphous binary silicides are also included in the evaluations. For

comparative purposes, some previous results from Kolawa et al. on Ta-Si-N films are included in this chapter. However, the Ta-Si-N system will be revisited through ancillary secondary ion mass spectrometry measurements of the Al diffusivity in $Ta_{36}Si_{14}N_{50}$ films, reverse-current measurements of $Ta_{36}Si_{14}N_{50}$/Al metallizations on Si diodes after 1000 h heat treatments, as well as X-ray diffraction and shallow-junction tests of Ta-Si barriers. A discussion of Ti-Si-N films, which do not perform as well as diffusion barriers for Al, can be found in a soon-to-be-published work [63].

As mentioned in Section 2.1, all of the TM-Si-N barrier films were deposited through reactive sputtering of TM_5Si_3 and WSi_2 targets. Four different substrates were used for the Al-barrier evaluations: unpatterned (100)-silicon and oxidized silicon for ^{4}He backscattering, X-ray diffraction, scanning electron microscopy (SEM), and secondary ion mass spectrometry (SIMS) analyses; graphite for compositional determination by backscattering, photoresist-patterned silicon containing vertical n^+p shallow-junction diodes; and single crystal NaCl substrates for transmission electron microscopy. The lateral contact area and junction depth of the diodes were 250×250 μm^2 and 280 nm, respectively. The junctions were formed by implanting 8 $\times 10^{15}$ As^+ into a 30-50 Ω cm, p-epi layer on a p^+ substrate. Appendix I gives the process flow used in fabricating the diodes. Just prior to loading into the chamber, the silicon samples were etched in 1:15 HF:H_2O. Without breaking vacuum after the barrier depositions, samples additionally received an aluminum overlayer sputtered in an Ar discharge at 5 mTorr with a -50 V dc substrate bias. In most cases, the thicknesses of the barriers and aluminum were 130 and 330 nm, respectively, as measured by stylus profilometry. Samples for transmission electron microscopy (TEM) had equal barrier and aluminum thicknesses of 50 nm each. Samples for secondary ion mass spectrometry consisted of a Ta-Si-N (100 nm)/Al(6 nm)/Ta-Si-N (50 nm) trilayer on oxidized silicon. After deposition (and lift-off in acetone, where applicable), the samples were annealed for 10 min to 10 h in 4×10^{-7} Torr vacuum and characterized by 2.0 MeV ^{4}He backscattering, Read camera X-ray diffraction, and I(V) measurements. Cross-sectional samples for TEM were lifted off from NaCl in deionized H_2O, collected on a 200-mesh Mo grid

coated with sputtered Si_3N_4, annealed in vacuum, recollected and embedded in epoxy resin. After curing, the films in the epoxy were microtoned into roughly 50-nm sections using standard diamond-knife ultramicrotomy techniques and collected on holey carbon films strung across a 200-mesh Cu grid.

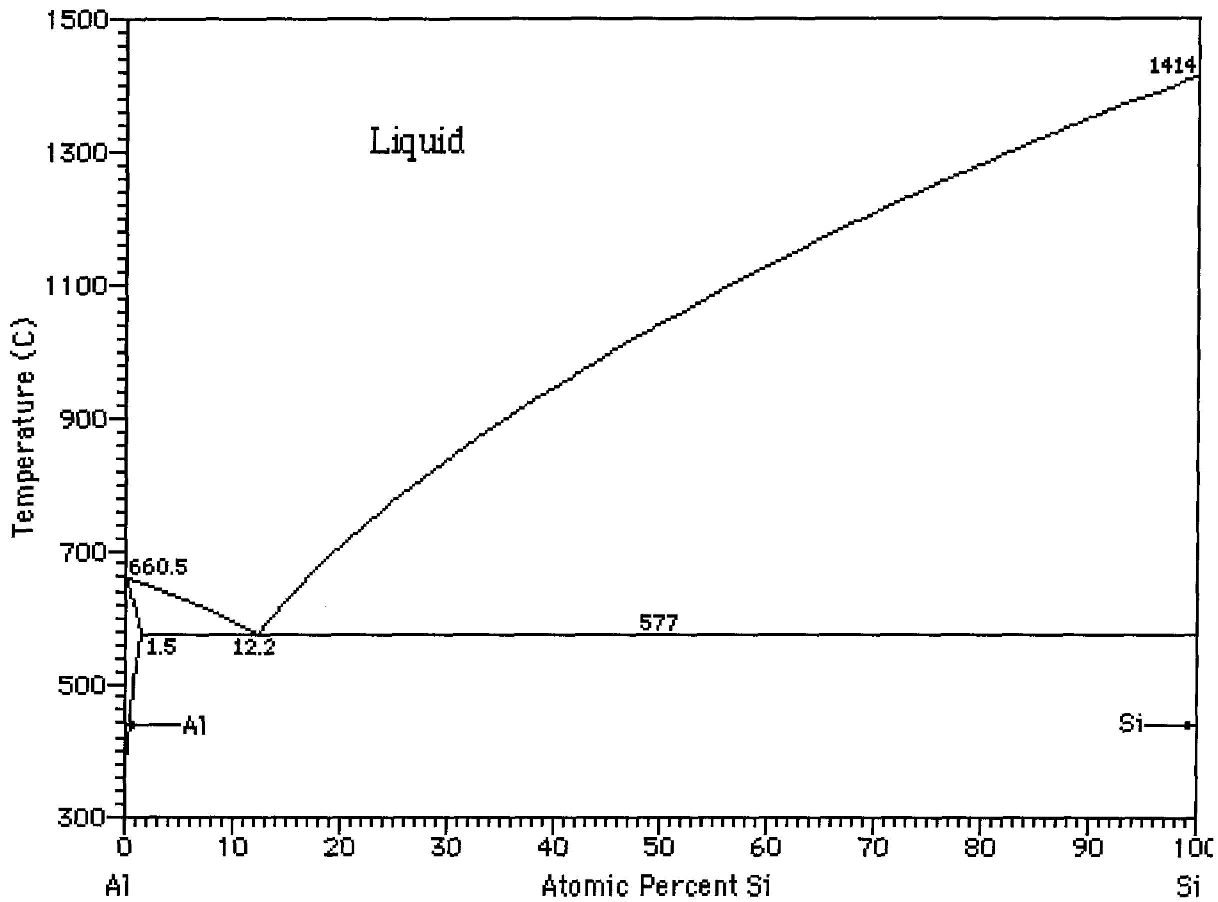

Figure 4.1. Al-Si equilibrium phase diagram [1,4].

4.2. Evaluation of Amorphous, Nitrogen-Free TM-Si Barriers

The compositions and resistivities of the evaluated amorphous binary barriers are listed in Table 4.1. All of the silicides have roughly 2 at.% each of argon and oxygen. The Al layer contains less than 1 at.% of argon and oxygen. A summary of phases detected by X-ray diffraction of M-Si/Al bilayers on silicon or oxidized silicon substrates is given in Table 4.2. In all instances, the same reaction products appeared independent of the choice of silicon or oxidized silicon substrates. Inceptive reaction between $W_{44}Si_{56}$ and Al occurs during annealing at 350°C/30 min to form WAl_{12}. The $W_{80}Si_{20}$, $Mo_{74}Si_{26}$, and $Ta_{80}Si_{30}$ films react to form WAl_{12}, $MoAl_{12}$, and $TaAl_3$ during annealing at 400°C. In these low-temperature cases, the reaction products have very weak X-ray intensities, indicating that only a small fraction of the barrier is consumed. The resulting binary aluminides are also the most aluminum-rich phases obtainable, according to equilibrium phase diagrams [1]. The reaction products remain unchanged up to 450°C, but their diffraction lines do slightly intensify. During annealing at 500°C, additional lines from $W(Si,Al)_2$ arise from the $W_{80}Si_{20}$/Al and $W_{44}Si_{56}$/Al systems. In the $Mo_{74}Si_{26}$/Al system, lines from Mo_4Al_{17} result from annealing at 550°C. Consistent with total consumption of the barrier, all traces of an amorphous diffraction halo from the barriers vanish for all nitrogen-free silicides during annealing at 550°C, with the exception of the $Ta_{80}Si_{20}$ system.

Figure 4.2 shows ^{4}He backscattering spectra from the <Si>/$Mo_{74}Si_{26}$/Al, <Si>/$W_{80}Si_{20}$/Al, and <Si>/$W_{44}Si_{56}$/Al systems before and after annealing. Spectra of metallizations including the $Ta_{80}Si_{20}$ barrier can be found in a previous work [60]. A very slight instability is detectable by backscattering in all of the systems annealed at 450°C, which reinforces the notion that the reaction products uncovered by X-ray diffraction after annealing at 450°C consume only a small portion of the barriers. The reaction of the bilayer proceeds somewhat further during heat treatment at 500°C. Annealing at 550°C completely consumes the barrier through reaction with migration of W or Mo to the surface. The backscattering yield ratio of the barrier metal to aluminum at the surface with respect to the silicon substrate is

consistent with the phases $MoAl_{12}$ and WAl_{12} for the $Mo_{74}Si_{26}$ and $W_{80}Si_{20}$ systems.

The use of shallow-junction, pn-diodes provides a practical, yet very sensitive assessment of a barrier's effectiveness. Forty-two diodes with given amorphous silicide (130 nm)/Al (350 nm) metallization were tested after annealing at temperatures between 250 and 500°C. A metallization was deemed "stable" at a certain temperature if the heat treatment did not produce any large (>5%) increases in the reverse current in any of the 42 diodes with respect to diodes annealed at 250°C/30 min. The as-deposited diodes typically had reverse current densities in the mid-10^{-7} A/cm^2 range; heat treatment at 250°C serves to remove defects induced from deposition, thus lowering the reverse currents down into the 10^{-8} A/cm^2 range. The diode results for the amorphous silicide barriers are listed in Table 4.1 under the heading, "Max. Stability Temp. (°C)." An explicit example of the histograms is shown in Figure 4.3 for the <Si>/$W_{80}Si_{20}$/Al system, which is stable up to 400°C/30 min. The other silicide systems are also stable only up to 400°C/30 min.

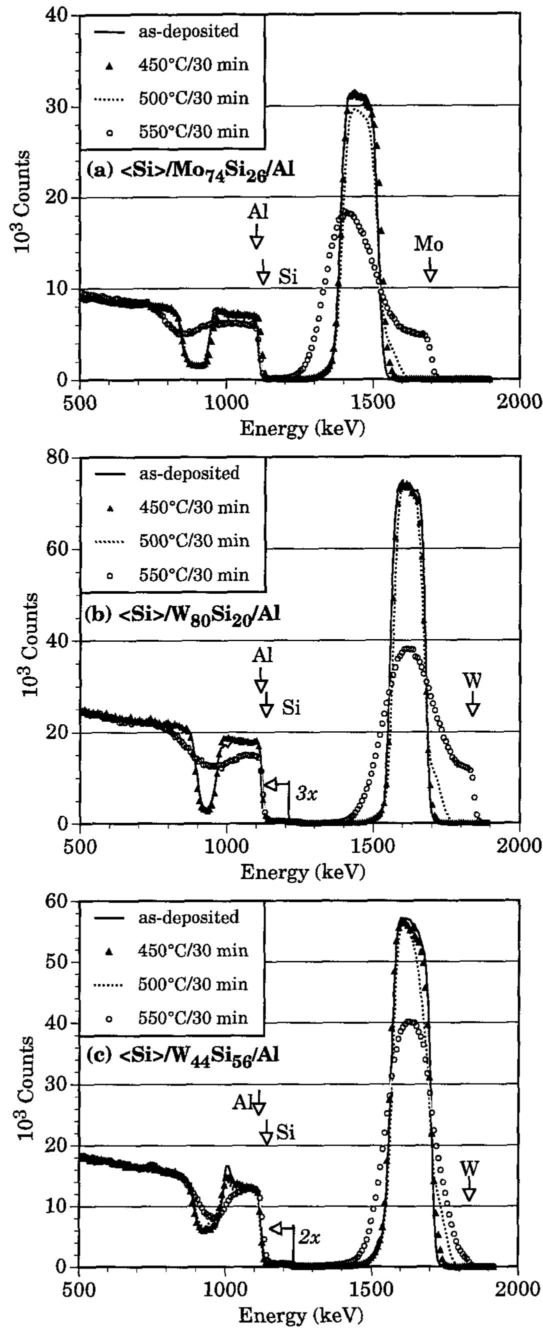

Figure 4.2. 2 MeV $^4He^{++}$ backscattering spectra of the (a) <Si>/$Mo_{74}Si_{26}$/Al, (b) <Si>/$W_{80}Si_{20}$/Al, and (c) <Si>/$W_{44}Si_{56}$/Al systems before and after annealing in vacuum for 30 min at 450, 500, and 550°C. The respective target tilt and scattering angles are 7 and 170°.

Table 4.1. Composition, resistivity, and highest stability temperature for the diode tests.

Composition	Resistivity (μΩ cm)	Max. Stability Temperature (°C)
Mo_5Si_3 target:		
$Mo_{74}Si_{26}$	180	400°C/30 min
$Mo_{36}Si_{17}N_{47}$	1400	675°C/10 min
W_5Si_3 target:		
$W_{80}Si_{20}$	200	400°C/30 min
$W_{41}Si_{17}N_{42}$	790	550°C/30 min
$W_{36}Si_{14}N_{50}$	1040	675°C/10 min
WSi_2 target:		
$W_{44}Si_{56}$	300	400°C/30 min
$W_{24}Si_{36}N_{40}$	1800	500°C/30 min
Ta_5Si_3 target:		
$Ta_{80}Si_{20}$	200	400°C/30 min
$Ta_{36}Si_{14}N_{50}$	750	675°C/15 min
	750	450°C/1000 h

Table 4.2. X-ray diffraction summary of annealed barrier(130 nm)/Al(350 nm) bilayers on <Si> and oxidized-<Si> substrates.

System	Process	Detected Phases
Mo_5Si_3 target:		
<Si> or $SiO_2/Mo_{74}Si_{26}/Al$	350°C/30 min	amorphous Mo-Si, Al
	400°C/30 min	$MoAl_{12}$, amorphous Mo-Si, Al
	450°C/30 min	$MoAl_{12}$, amorphous Mo-Si, Al
	500°C/30 min	$MoAl_{12}$, amorphous Mo-Si, Al
	550°C/30 min	$MoAl_{12}$, Mo_4Al_{17}
<Si> or $SiO_2/Mo_{36}Si_{17}N_{47}/Al$	600°C/2 h	amorphous Mo-Si-N, Al
	625°C/2 h	amorphous Mo-Si-N, Al, poly-Si
$SiO_2/Mo_{36}Si_{17}N_{47}/Al$	700°C/2 h	amorphous Mo-Si-N, Al, poly-Si
W_5Si_3 target:		
<Si> or $SiO_2/W_{80}Si_{20}/Al$	350°C/30 min	amorphous W-Si, Al
	400°C/30 min	WAl_{12}, amorphous W-Si, Al
	450°C/30 min	WAl_{12}, amorphous W-Si, Al
	500°C/30 min	WAl_{12}, $W(Si,Al)_2$,amorphous W-Si, Al
	550°C/30 min	WAl_{12}, $W(Si,Al)_2$, Al
<Si> or $SiO_2/W_{41}Si_{17}N_{42}/Al$	500°C/30 min	amorphous W-Si-N, Al
	550°C/30 min	WAl_{12}, amorphous W-Si-N, Al
	600°C/30 min	WAl_{12}, amorphous W-Si-N, Al
<Si> or $SiO_2/W_{36}Si_{14}N_{50}/Al$	600°C/2 h	amorphous W-Si-N, Al
	625°C/2 h	amorphous W-Si-N, Al, poly-Si
$SiO_2/W_{36}Si_{14}N_{50}/Al$	700°C/2 h	amorphous W-Si-N, Al, poly-Si
WSi_2 target:		
<Si> or $SiO_2/W_{44}Si_{56}/Al$	300°C/30 min	amorphous W-Si, Al
	350°C/30 min	WAl_{12}, amorphous W-Si, Al
	400°C/30 min	WAl_{12}, amorphous W-Si, Al
	450°C/30 min	WAl_{12}, amorphous W-Si, Al
	500°C/30 min	WAl_{12}, $W(Si,Al)_2$, amorphous W-Si, Al
	550°C/30 min	WAl_{12}, $W(Si,Al)_2$, Al
<Si> or $SiO_2/W_{24}Si_{36}N_{40}/Al$	450°C/30 min	amorphous W-Si-N, Al
	500°C/30 min	WAl_{12} ,amorphous W-Si-N, Al
	550°C/30 min	WAl_{12} ,amorphous W-Si-N, Al
Ta_5Si_3 target:		
<Si> or $SiO_2/Ta_{80}Si_{20}/Al$	350°C/30 min	amorphous Ta-Si, Al
	400°C/30 min	Ta_3Al, amorphous Ta-Si, Al
	450°C/30 min	Ta_3Al, amorphous Ta-Si, Al
	500°C/30 min	Ta_3Al, amorphous Ta-Si, Al
	550°C/30 min	Ta_3Al, amorphous Ta-Si, Al

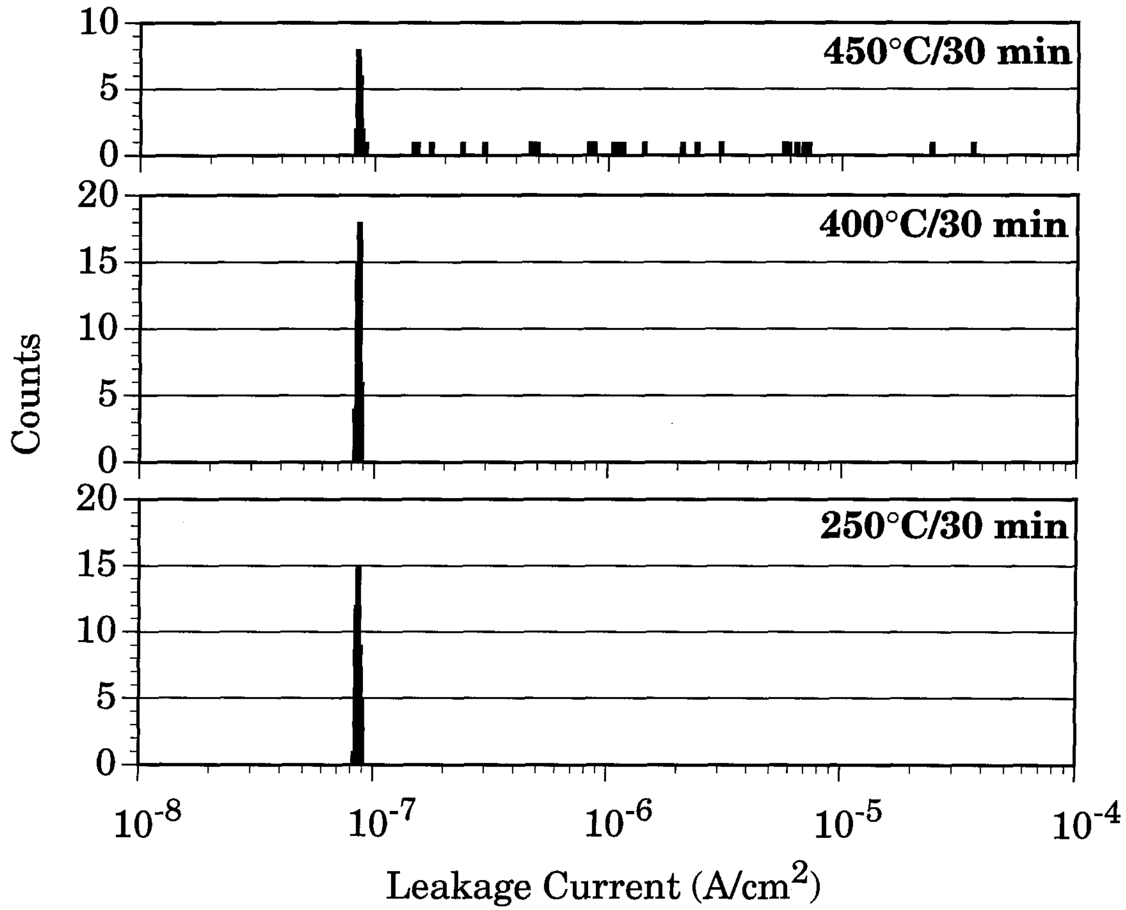

Figure 4.3. Reverse current histograms of the $W_{80}Si_{20}$ (130 nm)/Al (350 nm) system on shallow n^+p junction diodes after a 30 min heat treatment at 250, 400, and 450°C. The reverse bias applied to the diodes is - 4 V.

4.3. Evaluation of Amorphous TM-Si-N Barriers

According to RBS evaluations, the addition of nitrogen to the silicide systems gives a nearly monotonic improvement in the barrier properties for Al. Consequently, because of their superior ability, barriers heavily laden with nitrogen will be predominantly discussed in this section. Table 4.1 lists the relevant compositions. Like their silicide counterparts, most of the nitrided barriers also contained approximately 2 at.% each of argon and oxygen. The Mo-Si-N barriers, however, harbored 4 to 5 at.% of oxygen. The crystallization temperatures of the nitrided barriers are all in excess of 750°C (Chapter 3).

X-ray results of the TM-Si-N/Al bilayers on silicon or oxidized silicon substrates are given in Table 4.2. $W_{24}Si_{36}N_{40}$, produced from the WSi_2 target, reacts with Al already at 500°C. Backscattering verifies the instability as illustrated in Figure 4.4. Like the reacted silicides, the ratios of the W and Al surface signals are consistent with the phase WAl_{12} in samples annealed at 550°C. The tested compositions from the W_5Si_3 and Mo_5Si_3 targets are less reactive. As listed in Table 4.2, $W_{41}Si_{17}N_{42}$ films do not appear to react with Al at 500°C, but do react at 550°C. Increasing the nitrogen content to around 50 at.% dramatically improves the stability. No reaction is observed for $W_{14}Si_{36}N_{50}$ and $Mo_{36}Si_{17}N_{47}$ barriers with Al overlayers for annealing at 600°C for 2 h. After heat treatment at 625 and 700°C for 2 h, extremely faint reflections from polycrystalline Si arise along with the characteristic strong diffraction from the amorphous barrier and Al.

According to tests on 42 diodes, 130 nm $W_{24}Si_{36}N_{40}$ films sputtered from the WSi_2 target are able to prevent a 350 nm Al overlayer from spiking the silicon substrate only up to 500°C for 30 min. From the X-ray and backscattering results previously mentioned, the barrier evidently fails at 550°C through reaction with aluminum. Showing remarkable improvement, the nitrogen-rich films produced from the TM_5Si_3 targets prevent electrical degradation of the diodes above the melting point of aluminum, 660°C. Both the <Si>/$Mo_{36}Si_{17}N_{47}$/Al and

<Si>/$W_{36}Si_{14}N_{50}$/Al systems are electrically stable for 10 min at 675°C, as shown in Figure 4.5 and summarized in Table 4.1. A full 30-min treatment at 675°C does cause a few diodes to sustain large increases in reverse current. Even after annealing at 700°C, the majority of the diodes maintain their 10^{-8} A/cm^2 reverse currents. As discussed in in other sources, $Ta_{36}Si_{14}N_{50}$ films are also able prevent electrical degradation from Al interaction at temperatures in excess of 675°C [60,61].

The long-term stability of Ta-Si-N/Al metallizations on <Si> is also very good. Diodes metallized with $Ta_{36}Si_{14}N_{50}$ (100 nm)/Al (350 nm)/$Ta_{36}Si_{14}N_{50}$ (100 nm) trilayers do not sustain leakage current increases from annealing at 450°C for 1000 h in flowing Ar. The capping layer of $Ta_{36}Si_{14}N_{50}$ serves to prevent oxidation of the underlying Al, which otherwise occurs in the furance's slightly impure Ar ambient. X-ray diffraction of the trilayers on <Si> reveals no reaction products.

Figure 4.6 shows a scanning electron micrograph of resolidified, beaded aluminum on the $W_{36}Si_{14}N_{50}$ and $Mo_{36}Si_{17}N_{47}$ barriers on Si diodes after annealing at 675°C. 5 keV energy dispersive analysis of X-rays in the SEM does not indicate any large interaction of the Al with the barrier or Si substrate. Glancing angle spectra obtained from the beads revealed only the presence of Al. Normal-direction analysis away from the beads gave only barrier, substrate and faint Al signals. Based on the shallow geometry of the resolidified beads, Al plausibly wets the barrier.

High-resolution transmission electron micrographs of $W_{36}Si_{14}N_{50}$/Al bilayer cross-sections are given in Figure 4.7. In the as-deposited sample, lattice fringes from the Al extend completely to the barrier. However, in the sample annealed for 2 h at 600°C, the aluminum fringes terminate approximately 3 nm from the barrier. Close inspection of the interface reveals faint fringes from a nanophase layer. Microdiffraction of the layer bears weak spots consistent with the (100), (002), and (102) reflections of wurzite-structured AlN. It is entirely possible that the reflections are in fact from an aluminum oxynitride, given the ability of AlN to dissolve about 7 at.% of oxygen in the AlN-Al_2O_3 system [64,65]. Based on work by Schuster and

Nowotny [66,67], AlN does not dissolve the Group V-VII transition metals, thus the layer probably contains little transition metal. This agrees with the high degree of electron transmission through the interfacial layer. The AlN is essentially invisible here by X-ray diffraction because of the small amount, disordered nature, and weak scattering power of the compound. In one of the microdiffraction patterns, faint points matching the (220) reflection of Si were observed. As previously mentioned, X-ray diffraction also detects the poly-Si after annealing at higher temperatures.

As an attempt to measure the diffusivity of Al in the ternary barriers, secondary ion mass spectrometry was performed on <Si>/SiO_2/$Ta_{36}Si_{14}N_{50}$ (100 nm)/Al (7 nm)/$Ta_{36}Si_{14}N_{50}$ (50 nm) sandwich structures before and after annealing at 500 to 700°C. Even after heat treatment at 700°C for 10 h, there is virtually no change in the Al profile with respect to profiles obtained from as-deposited samples (Figure 4.8). Consistent with the transmission electron microscopy results, the thin Al layer may react to form a self-sealing interface with the barrier, thus helping to contain Al in place. Impurities at the interface and/or in the aluminum may be another possible explanation for the apparent lack of diffusion of Al through the barrier, an interpretation that cannot be excluded. No attempt was made to measure an oxygen profile.

4.4. Concluding Remarks

Amorphous, nitrogen-free, transition-metal silicide films are unimpressive barriers for blocking interaction of aluminum with silicon. As shown by X-ray diffraction, the barriers react with Al to form $MoAl_{12}$, WAl_{12}, and $TaAl_3$ during annealing at only 350 or 400°C. According to the diode evaluations, Al breaches the barriers during heat treatment at 450°C. ^4He backscattering proved to be the least sensitive test of the stability of the amorphous silicide/Al metallizations. In most instances, annealing at 500°C provided only a small change in spectra compared with spectra obtained from as-deposited samples. Consequently, the reaction products found in X-ray diffraction studies mentioned above are probably local

protrusions into the barrier. Similar behavior has been observed in other (Mo, Ta, and W)-silicide/Al systems [13-20].

The addition of nitrogen to the transition-metal silicide systems significantly improves the barrier performance. All of the ternary systems with approximately 50 at.% nitrogen are able to prevent Al from spiking into the shallow-junction diodes at temperatures in excess of the melting point of Al, 660°C. Based on the transmission electron microscopy observations of the W-Si-N/Al system, the stability is attributable in part to a self-sealing AlN layer which grows at the barrier/Al interface. A literature search provides no information on the diffusivity of Al in AlN, but the values are evidently very low. Because a large percentage of the diodes survive a 700°C annealing, the failure is most likely local in nature: Al probably channels through local weak spots and/or particles in the barrier films.

Analogously, Al dissociates both Si_3N_4 and $W_{36}Si_{14}N_{50}$ to form poly-Si and a thin interfacial layer of AlN [62,68,69]. The thin AlN acts as a diffusion barrier to retard further reaction. As discussed in Chapter 3, the structure of the nitrogen-rich TM-Si-N films tentatively appears to be a combination of TM-nitrides and silicon nitride, albeit with no long-range order. Aluminum thus appears to dissociate the Si_3N_4 constituent preferentially rather than the transition-metal nitride component. Otherwise, transition-metal aluminides would likely be observed. Paradoxically, the Mo, W, and Ta binary nitrides are known to be quite reactive with Al [29-33], assuming the interface to be free of native oxides [51]. However, for the preferential attack of Si_3N_4 to occur, the TM-Si-N systems need to be nearly saturated with nitrogen (i.e., near the MoN-, TaN-, or WN-Si_3N_4 tie lines). Figure 4.9 shows the tested compositions plotted on the ternary phase diagrams presented in Chapter 2. In the case of the W-Si-N system, $W_{41}Si_{17}N_{42}$ and $W_{24}Si_{36}N_{40}$, which exist compositionally near or on the nitrogen-depleted side of the ß-W_2N-Si_3N_4 tie line, react to form WAl_{12}, but the more nitrogen-rich $W_{36}Si_{14}N_{50}$ film does not react. Conceivably, the nearly saturated TM nitrides lend some nitrogen to the formation of the AlN layer.

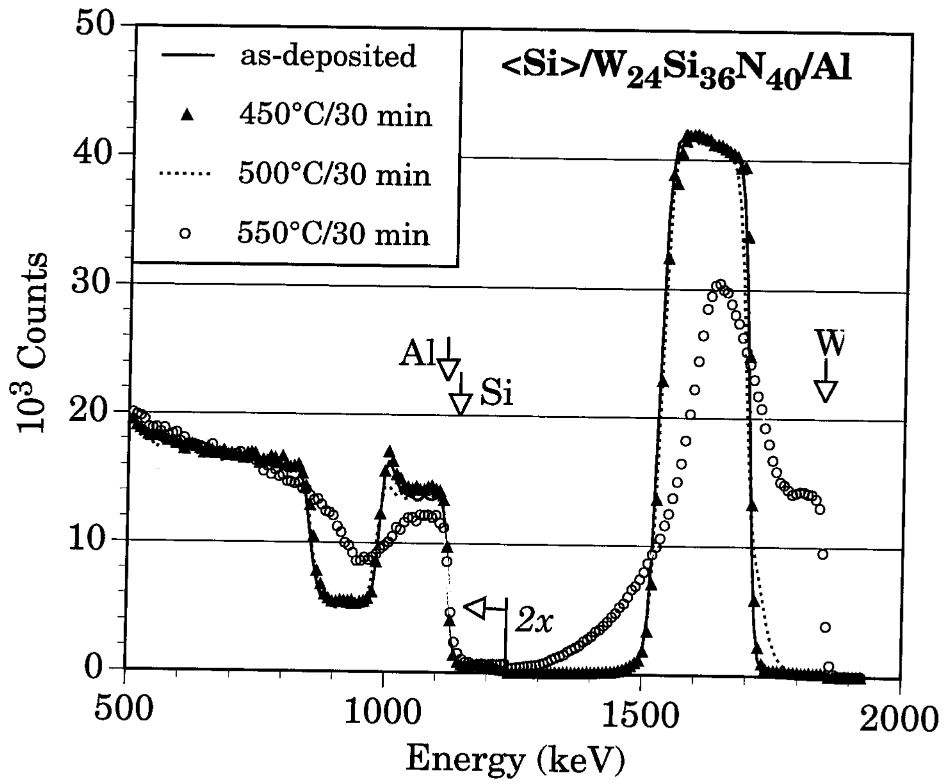

Figure 4.4. 2 MeV backscattering spectra of <Si>/$W_{24}Si_{36}N_{40}$/Al before and after annealing at 450, 500, and 550°C for 30 min.

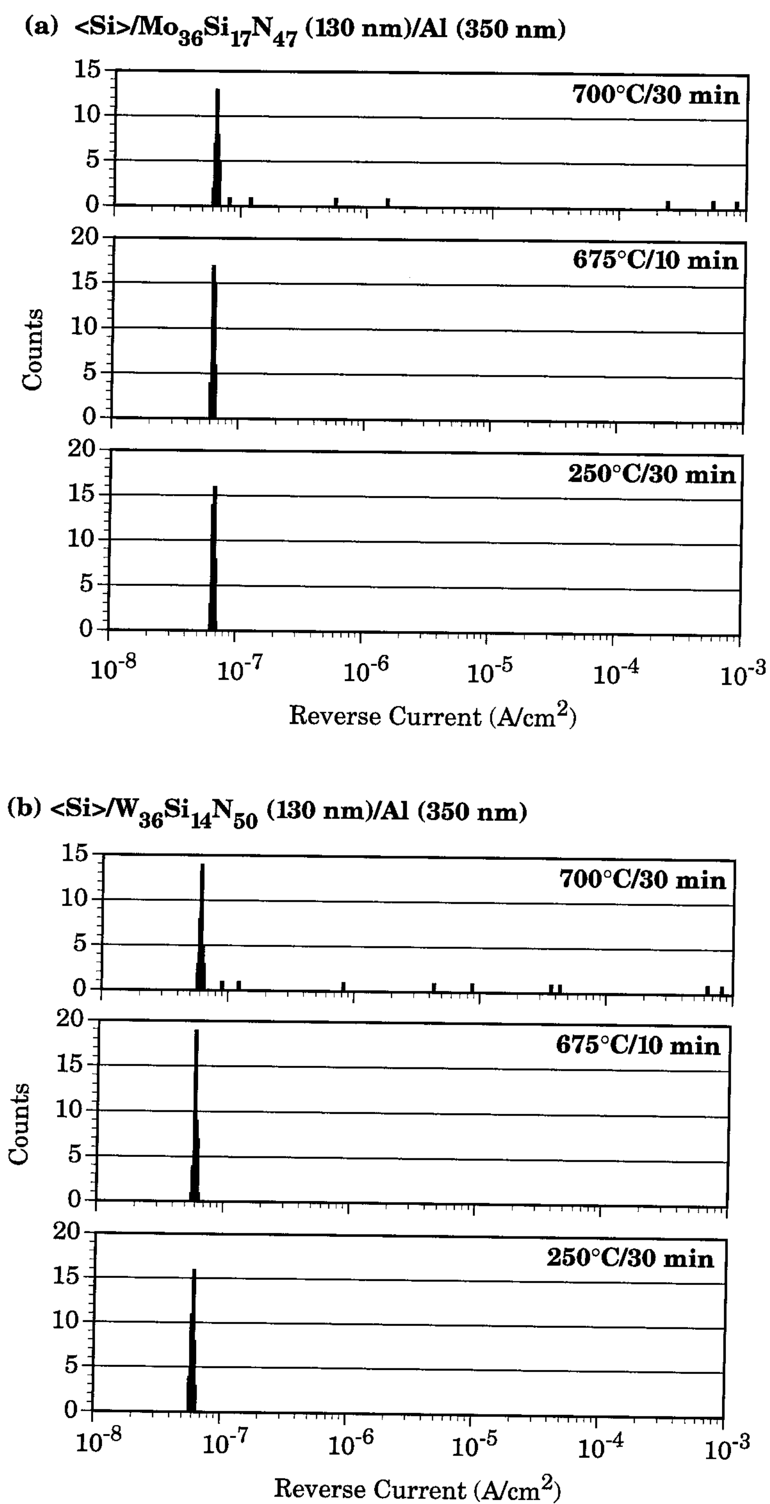

Figure 4.5. Reverse current histograms of the (a) $Mo_{36}Si_{17}N_{47}/Al$, and (b) $W_{36}Si_{14}N_{50}/Al$ metallizations on Si diodes biased at -4 V.

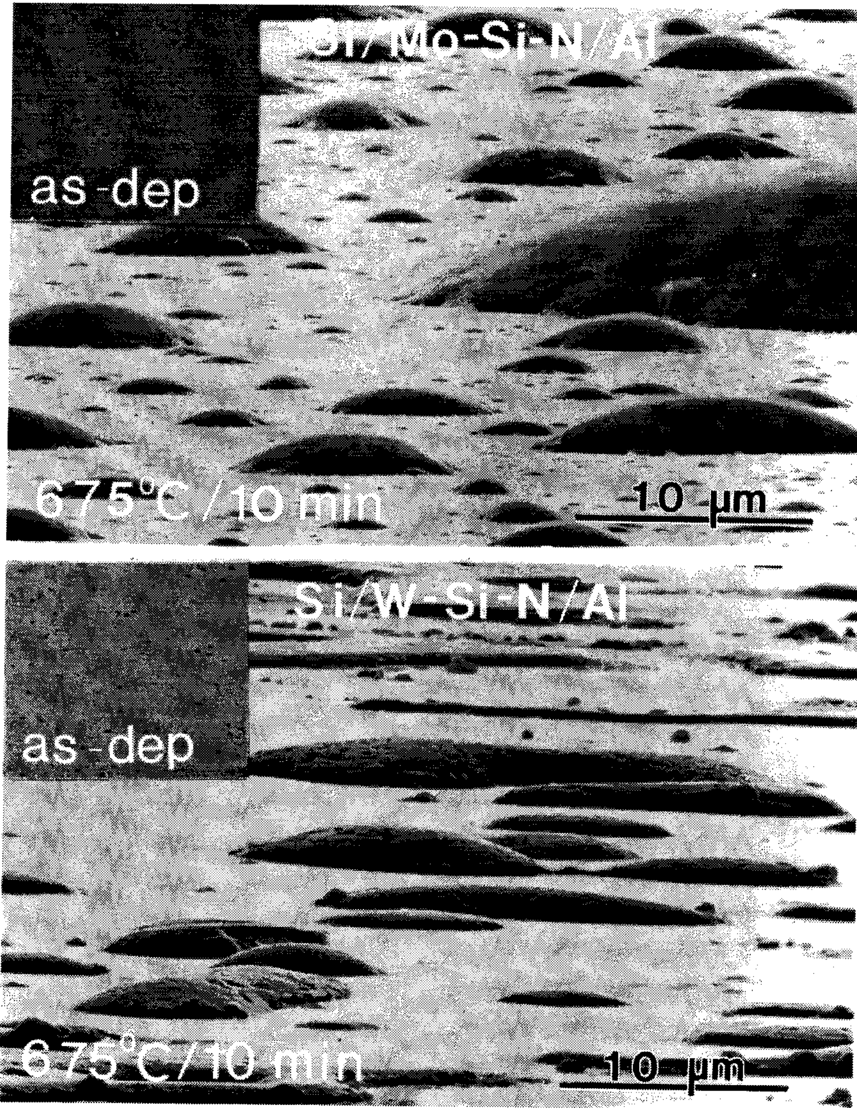

Figure 4.6. Secondary electron images of the <Si>/$Mo_{36}Si_{17}N_{47}$/Al and <Si>/$W_{36}Si_{14}N_{50}$/Al metallizations before and after a 675°C/10 min heat treatment. The incident beam energy was 20 keV. The tilt angle was approximately 80°.

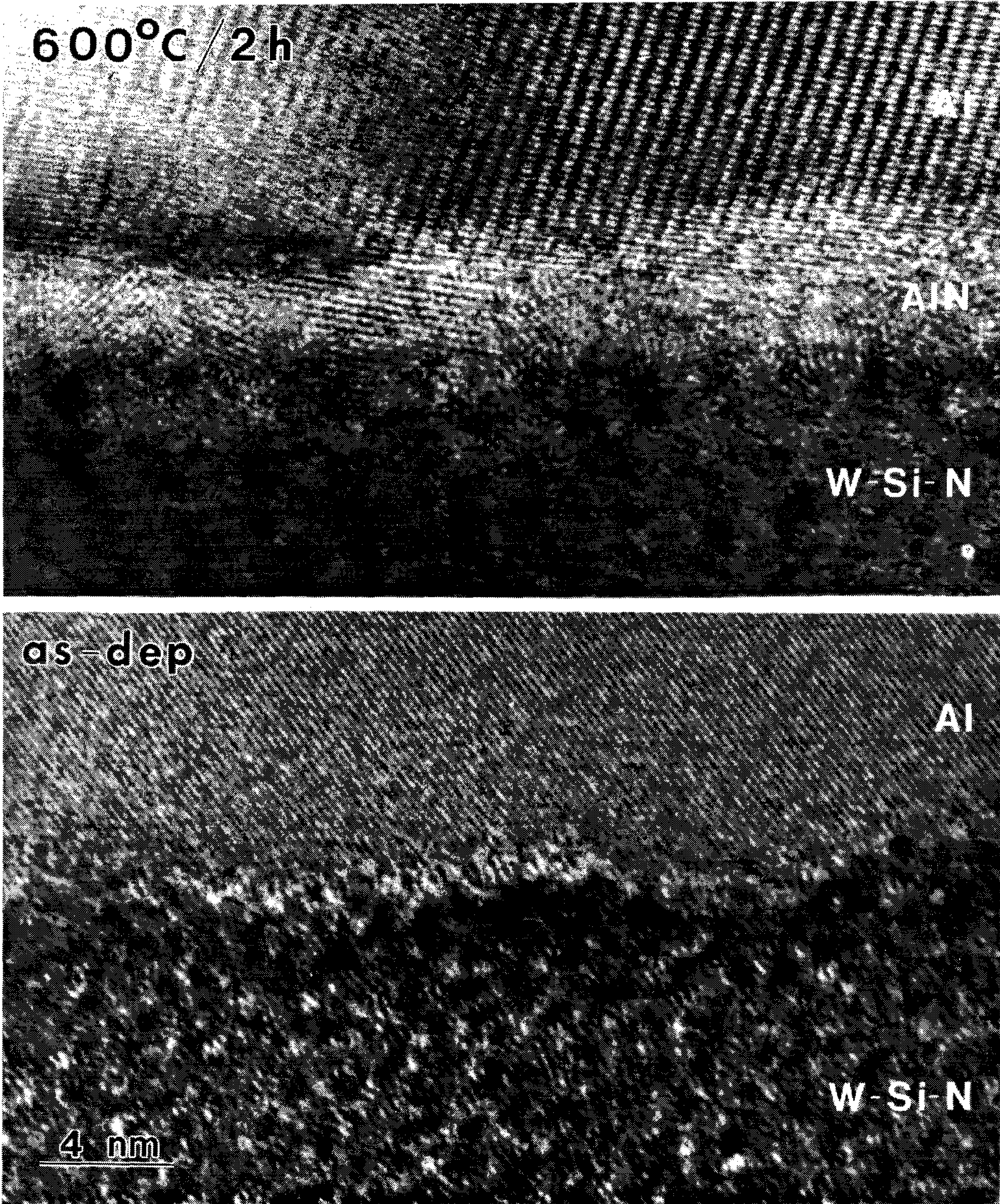

Figure 4.7. High-resolution transmission electron micrographs of as-deposited (bottom) and 600°C/2 h-annealed (top) $W_{36}Si_{14}N_{50}$/Al bilayers. Sample preparation caused the apparent interfacial roughness in the as-deposited sample.

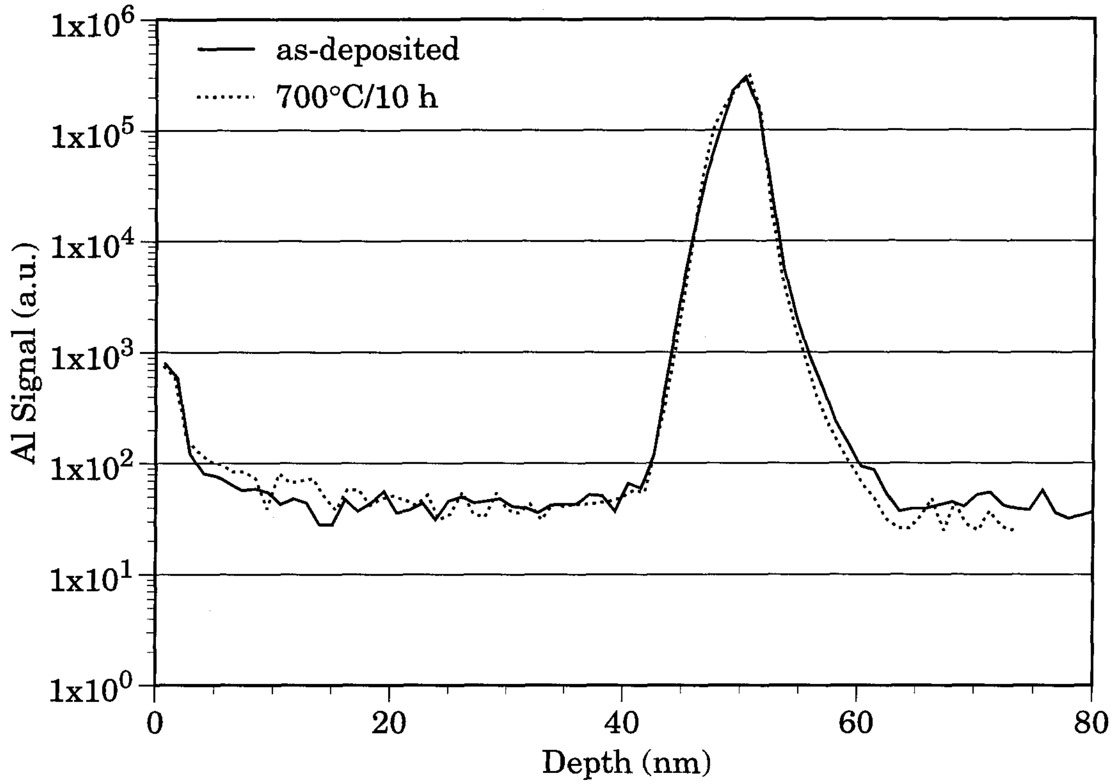

Figure 4.8. Aluminum signal from secondary ion mass spectrometry measurements of $SiO_2/Ta_{36}Si_{14}N_{50}$ (100 nm)/Al (7 nm)/$Ta_{36}Si_{14}N_{50}$ (50 nm) structures. The spectrometer was a Cameca model 4F; the beam was 5.5 keV Ar^+.

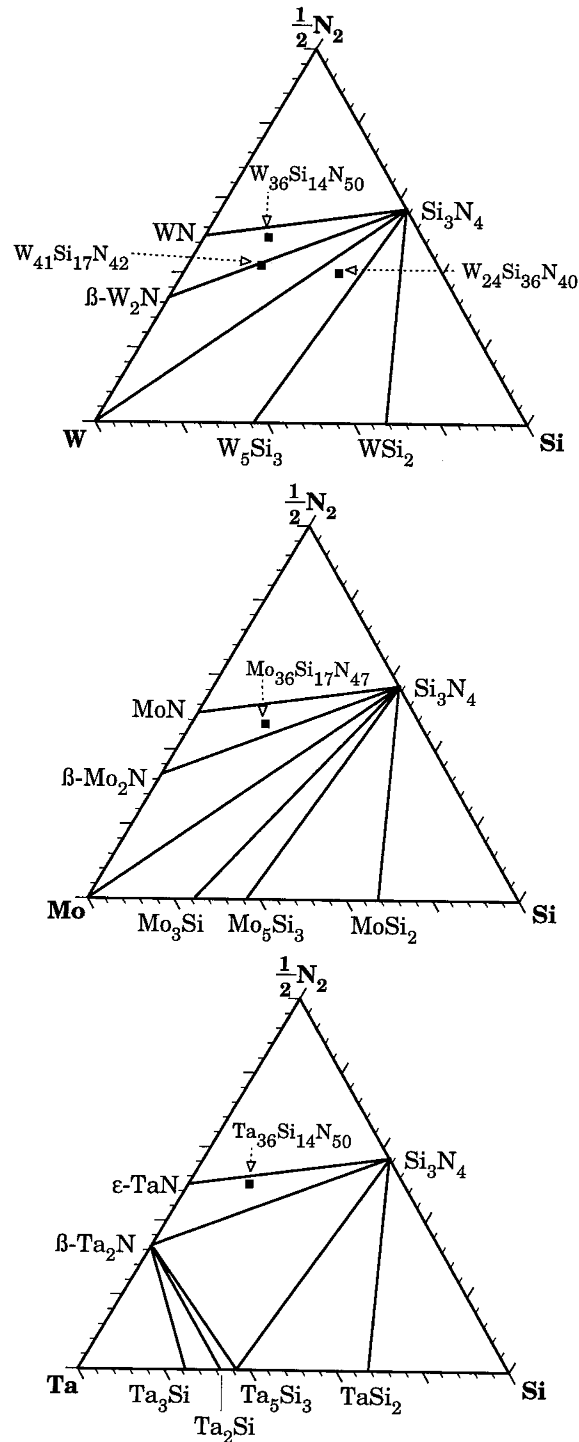

Figure 4.9. Ternary phase diagrams of the W-Si-N, Mo-Si-N, and Ta-Si-N systems denoting the tested barrier compositions.

References, Chapter 4.

[1] T.B. Massalski, *Binary Alloy Phase Diagrams. 2 ed.*, ASM International, Materials Park, OH (1990).

[2] S. Wolf, *Silicon Processing for the VLSI Era, Vol. 2*, Lattice Press, Sunset Beach, CA (1990) pp. 113-117.

[3] S.P. Murarka, in *VLSI Technology, 2nd Ed.*, edited by S.M. Sze, McGraw-Hill, New York (1988) pp. 375-419.

[4] TAPP Software for Macintosh, version 2.1, ES Microware, Hamilton, OH 1994.

[5] J.O. McCaldin, *J. Vac. Sci. Technol.* Nov., 990 (1974).

[6] N. Thangaraj, S. Hinderberger, K.H. Westmacott, and U. Dahmen, in *Advanced Metallization for ULSI Applications in 1993*, edited by D.P. Favreau, Y. Shacham-Diamond, and Y. Horiike, Materials Research Society, Pittsburgh, PA (1994) pp. 247-256.

[7] K. Nakamura, M-A. Nicolet, J.W. Mayer, R.J. Blattner, and C.A. Evans, Jr., *J. Appl. Phys.* 46, 4678 (1975).

[8] M. Tsukada and S.I. Ohfuji, *J. Vac. Sci. Technol. A* 12, 1 (1994).

[9] J. Derrien, M.Commandre, J.M. Layet, F. Salvan, and A. Cros, *Appl. Phys A* 28, 247 (1982).

[10] P.A. Totta and R.P. Sopher, *IBM J. Res. Dev.* 13, 226 (1969).

[11] G.J. van Gurp, *J. Appl. Phys.* 44, 2040-2050 (1973).

[12] H. Sankur, J.O. McCaldin, and J. Devaney, *Appl. Phys. Lett.* 22, 64 (1973).

[13] M. Wittmer, *J. Vac. Sci. Technol. A* 2, 273 (1984).

[14] O. Thomas, F.M. d'Heurle, and S. Delage, *J. Mat. Res.* 5, 1453 (1990).

[15] G.J. van Gurp, J.L.C. Daams, A. van Oostrom, L.J.M. Augustus, and Y. Tamminga, *J. Appl. Phys.* 50, 6915 (1979).

[16] S. Fukada, M. Suwa, Y. Koubuchi, and J. Onuki, *J. Vac. Sci. Technol. B* 9, 215 (1991).

[17] F.-M. Yang and M.-C. Chen, *J. Vac. Sci. Technol. B* 11, 744 (1993).

[18] Y.K. Fang and H.M. Yang, *IEEE Transactions on Electron Devices* 35, 706

(1988).

[19] T. Hara, H. Hayashida, S. Takahashi, and A. Yamanoue, *Thin Solid Films* 177, 9 (1989).

[20] T. Kikkawa and N. Endo, *J. Appl. Phys.* 70, 2370 (1991).

[21] Y.S. Hwang, S.H. Paek, Y.S. Song, H.C. Cho, J.S. Choi, J.K. Jung, J.K. Lee S.I. Lee, and J.G. Lee, *J. Mat. Sci.-Mat. Electrn.* 5, 163 (1994).

[22] D.S. Gardner, H.P. Longworth, and P.A. Flinn, *J. Vac. Sci. Technol. A* 10, 1426 (1992).

[23] C.Y. Ting and M. Wittmer, *Thin Solid Films* 96, 327 (1982).

[24] C. Canali, F. Fantini, and E. Zanoni, *Thin Solid Films* 97, 325 (1982).

[25] A.G. Dirks, R.A.M. Wolters, and A.J.M Nellissen, *Thin Solid Films* 193, 201 (1990).

[26] R.J. Schutz, *Thin Solid Films* 104, 89 (1983).

[27] N. Cheung, H. von Seefeld, M-A. Nicolet, *Proc. Symp. Thin Film Interfaces and Reactions* 80-2, edited by J.E.E. Baglin and J. Poate, The Electrochemical Society, Princeton, NJ (1980), p. 323.

[28] M. Okihara, N. Hirashita, K. Hashimoto, H. Onoda, *Appl. Phys. Lett.* 66, 1328 (1995).

[29] H.P. Kattelus, E. Kolawa, K. Affolter, and M-A. Nicolet, J. *Vac. Sci. Technol. A* 3, 2246 (1985).

[30] F.C.T. So, E. Kolawa, X.-A. Zhao, and M-A. Nicolet, *Thin Solid Films* 153, 507 (1987).

[31] S.E. Hörnström, A. Charai, O. Thomas, L. Krusinelbaum, P.M. Fryer, J.M.E. Harper, S. Gong, and A. Robertsson, *Surface and Interface Analysis* 14, 7 (1989).

[32] V.P. Anitha, A. Bhattacharya, N.G. Patil, and S. Major, *Thin Solid Films* 236, 306 (1993).

[33] M.A. Farooq, S.P. Murarka, C.C. Chang, and F.A. Baiocchi, *J. Appl. Phys.* 65, 3017 (1989).

[34] L. Krustin-Elbaum, M. Wittmer, C.-Y. Ting, and J.J. Cuomo, *Thin Solid Films* 104, 81 (1983).

[35] A. Charai, S.E. Hörnström, O. Thomas, P.M. Fryer, and J.M.E. Harper, *J. Vac. Sci. Technol.* A 7, 784 (1989).

[36] J.R. Shappirio and J.J. Finnegan, *Thin Solid Films* 107, 81 (1983).

[37] J.R. Shappirio, J.J. Finnegan, R.A. Lux, and D.C. Fox, *Thin Solid Films* 119, 23 (1984).

[38] E. Kolawa, J.M. Molarius, W. Flick, C.W. Nieh, L. Tran, M-A. Nicolet, F.C.T. So, and J.C.S. Wei, *Thin Solid Films* 166, 29 (1988).

[39] E. Kolawa, X. Sun, J.S. Reid, J.S. Chen, M-A. Nicolet, and R.P. Ruiz, *Thin Solid Films* 236, 301 (1993).

[40] F.C.T. So, E. Kolawa, S.C.W. Nieh, Z.-A. Zhao, and M-A. Nicolet, *Applied Physics A* 45, 265 (1988).

[41] E. Kolawa, C. Garland, L. Tran, C.W. Nieh, J.M. Molarius, W. Flick, M-A. Nicolet, and J. Wei, *Appl. Phys. Lett.* 53, 2644 (1988).

[42] E. Kolawa, F.C.T. So, E.T-S. Pan, and M-A. Nicolet, *Appl. Phys. Lett.* 50, 854 (1987).

[43] E. Kolawa, C.W. Nieh, J.M. Molarius, L. Tran, C. Garland, and M-A. Nicolet, *Thin Solid Films* 166, 15 (1988).

[44] H.-Y. Yang, X.-A. Zhao, and M-A. Nicolet, *Thin Solid Films* 158, 45 (1988).

[45] M. Wittmer, *J. Appl. Phys.* 53, 1007 (1982).

[46] M. Eizenberg, S.P. Murarka, and P. Heimann, *J. Appl. Phys.* 54, 3195 (1983).

[47] M. Eizenberg, R. Brenerl, and S.P. Murarka, *J. Appl. Phys.* 55, 3799 (1984).

[48] A. Appelbaum and S.P. Murarka, *J. Vac. Sci. Technol. A* 4, 637 (1986).

[49] R. de Reus, in *Intermetallic Compounds–Principles and Practice*, edited by J.H. Westbrook and R.L. Fleischer, John Wiley and Sons, Chicester, England (1993 preprint).

[50] H.P. Kattelus and M-A. Nicolet, in *Diffusion Phenomena in Thin Films and Microelectronic Materials*, edited by D. Gupta and P.S. Ho, Noyes Publications, Park Ridge, New Jersey (1988) pp. 432-491.

[51] J.M.E. Harper, S.E. Hörnström, O. Thomas, A. Chairai, and L. Krusin-Elbaum, *J. Vac. Sci. Technol. A* 7, 875 (1989).

[52] L.E. Halperin, E. Kolawa, Z. Fu, M-A. Nicolet, in *Materials Research Soc.*

Proc. 181, Materials Research Society, Pittsburgh, PA (1990) pp. 47-52.

[53] E. Kolawa, thermochemical calculations, unpublished.

[54] I. Suni, M-A. Nicolet, C.S. Pai, and S.S. Lau, *Thin Solid Films.* 107, 73 (1983).

[55] F.C.T. So, X.-A. Zhao, E. Kolawa, J.L. Tandon, M.F. Zhu, and M-A. Nicolet, *Mat. Res. Soc. Symp. Proc.* 54 (1986).

[56] L.-S. Hung, E.G. Colgan, and J.W. Mayer, *J. Appl. Phys.* 60, 4177 (1986).

[57] F.W. Saris, L.-S. Hung, M. Nastasi, J.W. Mayer, and B. Whitehead, *Appl. Phys. Lett.* 46, 646 (1985).

[58] S.E Hörnström, T. Lin, O. Thomas, P.M. Fryer, and J.M.E. Harper, *J. Vac Sci. Technol. A* 6, 1650 (1988).

[59] J.D. Wiley, J.H. Perepezko, J.E. Nordman, and K.-J. Guo, *IEEE Trans. Ind. Electron.* 29, 154 (1982).

[60] E. Kolawa, J.M. Molarius, C.W. Nieh, and M-A. Nicolet, *J. Vac. Sci. Technol. A* 8, 3006 (1990).

[61] E. Kolawa, P.J. Pokela, J.S. Reid, J.S. Chen, and M-A. Nicolet, *Appl. Surf. Sci.* 5, 373 (1991).

[62] P. Rogl and J.C. Schuster (eds.), *Phase Diagrams of Ternary Boron Nitride and Silicon Systems*, ASM International, Materials Park, OH (1992).

[63] X. Sun, J.S. Reid, E. Kolawa, and M-A. Nicolet, in preparation.

[64] G.A. Slack, *Acta Cryst.* B35, 2281 (1979).

[65] M. Hilber and S. Johnsson, *Z. Metallkunde* 88, 720 (1992).

[66] J.C. Schuster and H. Nowotny, *Z. Metallkunde* 76, 728 (1985).

[67] J.C. Schuster and H. Nowotny, *J. Mat. Sci.* 20, 2787 (1985).

[68] R. Brener, F. Edelman, and E.Y. Gutmanas, *Appl. Phys. Lett.* 54, 901 (1989).

[69] M. Naka, H. Mori, M. Kubo, I. Okamoto, and H. Jujita, *J. Materials Sci. Lett.* 5, 696 (1986).

Chapter 5. TM-Si-N and W-B-N Diffusion Barriers between Cu and Si, and Cu and SiO_2

5.1. Introduction

Exigent requirements on the submicron level, particularly low resistivity and low susceptibility to electromigration, may inaugurate copper as the next-generation material for interconnects and contacts in integrated circuits. Impedances to copper's incorporation include its expeditious diffusion or drift through silicon [1], silicon dioxide [2-10], and polyimide [9,11]. Once in silicon, copper is a very effective killer of minority carrier lifetimes [12]. In the interlevel dielectric, copper can increase the capacitance and leakage between interconnects, which leads to time delays. An exceptional class of diffusion barriers is therefore necessary for copper metallizations.

Whereas barriers for Al tend to be sacrificial films, barriers for Cu are typically inert to reaction. Many transition metals do not form compounds with copper, and in some instances (Ta and W), are immiscible with Cu. Many compounds also do not react with copper. Nitrogen, as well as the metalloids, B and C, do not form stable compounds with Cu, thus providing a large number of interstitial compounds which do not react with Cu. Even if a transition metal is known to react with Cu (e.g., Ti), the transition metal can form borides, carbides, or nitrides that do not react with copper. Nonetheless, despite the lack of chemical reactivity, many of the intermetallic barriers provide only modest protection from Cu diffusion. Because of their typical polycrystalline structure, grain boundaries may serve as fast diffusion paths for Cu. Moreover, the barrier properties of polycrystalline materials can depend strongly on impurity content and the "stuffing" of grain boundaries [13-14]. Representative of the polycrystalline barriers for Cu metallizations are Ta [13-18], W [16-18], V [16], Cr [18], Nb [19], TiW [16,20,21], TiN [16,22-24], TaN [14], and $W_{46}N_{54}$ [25]. As in Chapter 4, the reader is referred to several review articles for extensive compendia of Cu barrier studies [9,20,26,27]. It should be noted, however,

that reported barrier failure temperatures tend to be overestimated unless diode or similarly sensitive methods are used in the evaluations.

Amorphous materials, with their lack of grain boundaries, provide an attractive class of diffusion barriers for Cu metallizations. Many amorphous binary systems combining early and late transition metals have been investigated, including $Ir_{45}Ta_{55}$ [28], $Ir_{54}Zr_{46}$ [29], $Ni_{60}Nb_{40}$ [30], $Fe_{37}W_{63}$ [31], and $Co_{50}Mo_{50}$ [32]. Their effectiveness at elevated temperatures is often limited by crystallization or reaction with the Si substrate. The reaction temperature with Si usually lies between that of the two individual components. Another class of amorphous barriers that has been considered are the transition metal nitrides, borides, and phosphides. Examples include $W_{74}N_{26}$ [25], TiB_2 [33], $TiPN_2$ [34], and $W_{40}Re_{40}B_{20}$ [35] alloys.

This chapter discusses the use of amorphous TM-Si-N and W-B-N diffusion barriers for exceptionally stable Cu metallizations. In formulating reliable metallizations, thermodynamic stability is desirable. Consequently, the discussion of Cu barriers begins with the thermodynamics of the TM-Si-N-Cu and W-B-N-Cu quaternary systems in the context of the ternary subsystems. In Sections 5.3 and 5.4, 100- and 10-nm-thick barriers are tested in between Si substrates and copper overlayers. Because of the sensitivity of the technique, diode tests will be the primary mode of analysis here. For comparative purposes, results from polycrystalline TiN barriers are also presented. In Section 5.5, the thermal diffusivity of Cu in $Ta_{36}Si_{14}N_{50}$ films is reported. In Section 5.6, the attention will shift from barrier reliability during device processing to device operation with an evaluation of $Ta_{36}Si_{14}N_{50}$ films used to block Cu drift through MOS capacitors. Finally, in Section 5.7, the barrier/Cu contact resistivity will be discussed.

5.2. TM-Si-N/Cu and TM-B-N/Cu Thermodynamics

Understanding the equilibrium thermodynamics of potential barriers with copper is an essential step towards developing stable metallizations. No reaction

with Cu is obviously welcomed. However, because quaternary diagrams of the TM-Si-N-Cu and TM-B-N-Cu systems do not exist, the thermodynamics must be inferred from the various binary and ternary subcomponents. In this section, the thermodynamics of the TM-N, TM-Si, TM-B, Si-N, and B-N binary systems in contact with Cu will be reviewed. For the purposes of formulating other barriers than those considered in this thesis, all of the Group V and VI transition metals will be included in the thermodynamic evaluations along with the Group IV element, Ti.

5.2.1. TM-N-Cu Systems

Transition metals from the group V and VI columns: V, Nb, Ta, and Cr, Mo, W (henceforth designated as $TM_{v,vi}$), do not form binary compounds with Cu. Solubilities tend to be very low with a few exceptions. V and Nb can dissolve almost 2 at.% of Cu at 700°C [36]. Solubility of Cr in Cu is about a tenth of a percent at 700°C. Nitrogen does not form stable compounds with Cu and has little, if any, solubility in Cu. In most of the systems, ternary $TM_{v,vi}$-N-Cu phases are not known to exist [37]. However, by reacting $NaTaN_2$ and CuI powders at 400°C in flowing N_2, Zachwieja and Jacobs synthesized rhombohedral $CuTaN_2$ [38] The compound was reportedly stable at 750°C, which is far above the temperature at which metastable Cu_3N decomposes. In contrast, heating Ta_2N/Cu bilayers does not produce a reaction in the layers, according to cross-sectional transmission electron micrographs [14]. Solubility of Cu in the binary nitrides is unknown, but it is likely to be small. Thus, barring solubility effects and the possible presence of ternaries, all of the $TM_{v,vi}$-nitride barriers may be thermodynamically stable with Cu. Experimentally, W-N along with Ta-N films are in fact known not to react with Cu [14,25].

Because of compound formation in the Ti-Cu system [36], the situation for the Ti-N-Cu system is a bit more complicated. By X-ray diffraction, TiN/Cu bilayers do not react during an 850°C/30 min heat treatment in vacuum [39]. Diagrams calculated by Bhansali (presented in Wang et al. [22]) using Gibbs free energy data show stoichiometric TiN to be stable with Cu and all Cu-Ti compounds. Assumptions

made in the calculations include neglecting solubilities and homogeneity ranges. No stable Ti-N-Cu ternary phases are known to exist [37].

5.2.2. TM-B-Cu Systems

The $TM_{v,vi}$-B-Cu systems are very much like the $TM_{v,vi}$-N-N systems. Cu does not react to form binary compounds with either $TM_{v,vi}$ or B. A literature search reveals no $TM_{v,vi}$-B-Cu ternary phases. Boron solubility in Cu is approximately 1 at.% at 700°C. Based on the lack of Cu compounds in the systems, Cu should be stable with all $TM_{v,vi}$ binary borides, barring unknown solubility effects.

A ternary diagram for the Ti-B-Cu system is not available. No ternary phases have been observed in the system [37]. Experimentally, TiB_2 barriers produced by chemical vapor deposition do not react with Cu overlayers at 750°C for 30 min [33]. Reacting powders at 1200°C with the compositions TiB_2Cu_x produces only Cu and TiB_2, according to work by Dallaire and Legoux [40]. Consequently, a TiB_2-Cu tie line in the Ti-B-Cu phase diagram is plausible. The rest of the diagram is unclear. Work by Li et al. on cold-pressed, acetylene-torched Ti, B, and Cu powders revealed TiB, TiB_2, and Ti_2Cu for compositions in the TiB-TiB_2-Ti_2Cu portion of the ternary phase diagram. However, they also found Ti and Ti_3Cu_4, which indicates that the powders have not completely reacted.

5.2.3. Si-N-Cu and B-N-Cu Systems

Excellent reviews of the Cu-Si-N and Cu-B-N systems can be found in the literature [41]. As redrawn from those references, in Figure 5.1, Si_3N_4 and BN are stable with Cu and Cu silicides. From lattice parameter measurements, copper is not soluble in Si_3N_4 or BN. Additionally, nitrogen is not soluble in the copper silicides.

5.2.4. $TM_{v,vi}$-Si-Cu Systems

Experimentally-based ternary diagrams for the Nb-Si-Cu [42,43], Ta-Si-Cu [43], V-Si-Cu [43] and W-Si-N [44] systems are available. Phase diagrams by Zankel and Malter on the Nb-Si-Cu system show that Cu dissociates Nb_5Si_3 and $NbSi_2$ at 800 and 875°C [42]. The diagram for the 800°C system is redrawn in Figure 5.2. Both niobium silicides dissolve about 4 at.% of copper, however Cu_3Si does not readily dissolve Nb. At 1000°C, work by Ganglberger indicates the presence of two ternary phases, NbSiCu ($Nb_5Si_4Cu_4$?) and $Nb_4Si_2Cu_3$ [43,45].

Investigations by Ganglberger on the Ta-Si-Cu and V-Si-Cu powders annealed at 1000°C and cooled to room-temperature yielded no ternary phases [43]. As shown in Figure 5.2, only the refractory silicides, Ta_3Si, Ta_2Si, and V_3Si, were found to be in equilibrium with copper at 1000°C, which is above the melting point of copper silicides. Solubility issues were not addressed in his work. The presence of the low-temperature copper silicides is probably a consequence of the rate of cooling after annealing.

Efimov et al. studied arc-melted W, Si and Cu starting material before and after a 300 h heat treatment at 800°C [44]. By X-ray diffraction, they concluded that tie lines connect W_5Si_3 and WSi_2 with the Cu-Si homogeneity range of Cu. Their results also indicate a 1.5 at.% maximum solubility of Cu in W_5Si_3. No ternary phases were found. Their diagram is presented in Figure 5.2. Jangg et al. investigated the precipitation of tungsten silicides within liquid copper melts [46]. After a selective etch of the cooled system in nitric acid to remove Cu and possibly-present Cu silicides, they also found no W-Si-Cu ternary phases by X-ray diffraction. In ancillary experiments, no Mo-Si-Cu ternary phases were found.

In all instances, the bulk powder anneals for the $TM_{v,vi}$-Si-Cu systems were done nearly at or above the copper-silicon eutectic temperature, 802°C (Figure 5.3). At temperatures relevant to device processing (<500°C), the behavior may be much

different because of changes in the Gibbs free energies. Table 5.1 lists Gibbs free energy data, *G(T)*, for $TM_{v,vi}$- and Cu-silicides. For the majority of the $TM_{v,vi}$-silicides, experimental data from Barin [48] are listed. Unfortunately, as is often the case with thermochemical data, the accuracy of these values is uncertain. In some instances, superseding data from reviews by Schlesinger [50] and Chart [51,52] are given. Minor adjustments are made here to satisfy the binary phase diagrams. Because of the lack of experimental data, modeled data by Lüdecke [53] are listed for the copper silicides. The values were extracted through a least-squares optimization technique developed by Lukas [54] used on experimental data taken from the liquid-phase Cu-Si system. The low heat of formation for copper silicides predicted by Lüdecke roughly compares with modeled values from Miedema [55,56] and experimental values from Meschel and Kleppa [58] (Table 5.2).

Under the assumptions of strict stoichiometry of the binary phases and no solid solubility, Gibbs free energy comparisons for the data in Table 5.1 predict that tie lines couple copper with all $TM_{v,vi}$-silicides containing a metal:silicon ratio greater than or equal to 5:3 at 700°C. For Mo and W, additional tie lines span the disilicides with copper and the copper silicides. Alternative tie lines connecting $(Mo,W)_5Si_3$ with κ-Cu_7Si would arise by minimal adjustments in the thermodynamic data. Inversely for the Cr, Nb, Ta, and V systems, the disilicide-Cu lines are not predicted, but only by small positive margins of $\Delta G_{reaction}$. Instead, competing tie lines connect $(Cr,Nb,Ta,V)_5Si_3$ with κ-Cu_7Si. Calculations for the room-temperature systems yield equilibrium between all of the $TM_{v,vi}$-silicides and copper. The results are not in total agreement with some of the diagrams for higher temperature systems in Figure 5.2.

5.2.5. Thin-Film Experiments on $TM_{v,vi}$-Si-Cu Systems

In order to corroborate the diagrams presented in Figure 5.2, for this thesis, amorphous silicide/Cu multilayers were deposited on oxidized silicon, annealed in 4×10^{-7} Torr vacuum, and subsequently characterized by X-ray diffraction or

cross-sectional transmission electron microscopy. Only the Mo-, Ta-, and W- based systems sputtered from (Mo,Ta, or W)$_5$Si$_3$ and (Ta or W)Si$_2$ targets were evaluated. All depositions were performed without breaking vacuum between layers. Most of the evaluated systems consisted of silicide/Cu/silicide trilayers annealed for 10 h at 700°C. In the case of silicide systems sputtered from a Ta_5Si_3 target, only $Ta_{80}Si_{20}$/Cu bilayers annealed for 1 h at 700 to 1000°C were considered.

Table 5.3 summarizes the results obtained by X-ray diffraction of the silicide/Cu or boride/Cu systems after the vacuum anneal. The tested compositions are also plotted on the ternary diagrams of Figure 5.2. All of the silicides sputtered from the (Mo,Ta,W)$_5$Si$_3$ targets appear to be thermodynamically stable with copper. Consequently, the predicted tie lines from Cu to Mo_5Si_3, Mo_3Si, Ta_2Si, and W_5Si_3 in Figure 5.2 do exist for the thin-film systems. Given the proximity of the measured compositions to the Mo_3Si-Cu tie line, the presence of Mo_5Si_3 indicates that Mo_3Si is in equilibrium with copper containing little or no dissolved silicon. In the $Ta_{80}Si_{20}$ system, Ta_2Si and $Ta_{4.5}Si$ are observed rather than the thermodynamically expected Ta_3Si and Ta phases presumably because of impurity content [59]. Figure 5.4 shows cross-sectional transmission electron micrographs of as-deposited and 1 h, 900°C-annealed $Ta_{80}Si_{20}$/Cu bilayers. Some segregation of the Ta-Si and copper layers has occurred during annealing. The lightly-toned areas in the micrograph of the annealed sample, as determined by electron diffraction and dark-field analyses, represent Cu. Diffraction from the sample returns no evidence of copper silicides. Local energy dispersive spectrometry (EDS) of X-rays reveals that the copper contains a slight amount of dissolved silicon. Because of the beam-attenuating nature of the opaque areas shown in the micrograph, microdiffraction could not be performed on these areas. EDS analysis, however, demonstrated that the dark areas principally contained tantalum and silicon.

Changing the Ta and W silicides to more silicon-rich stoichiometries alters their reactivity with Cu (Table 5.3). In the copper-poor system stoichiometries, $Ta_{26}Si_{36}Cu_{36}$ and $W_{31}Si_{38}Cu_{31}$ (the compositions here designate the combined sto-

ichiometry of the multilayers) all traces of Cu vanish during annealing at 700°C for 10 h. $(Ta, W)_5Si_3$ and $(Ta, W)Si_2$ are unambiguously present, with several lines remaining from copper silicides. Making a definitive match for copper silicides is somewhat difficult for several reasons. First, where known, Cu silicides [60,61] share many Bragg reflections with the more strongly scattering Ta and W silicides. Additionally, structural information for many copper silicides is simply lacking. A plethora of metastable phases and polymorphs are also known to exist [62]. Increasing the Cu content to obtain the compositions $Ta_{14}Si_{18}Cu_{68}$ and $W_{17}Si_{22}Cu_{61}$ eliminates the presence of WSi_2 and η-Cu_3Si and introduces γ-Cu_5Si reflections. Impurity-stabilized hexagonal-Ta_5Si_3 is also present in the Ta-Si-Cu system. Adding additional Cu to the W-Si-Cu system yields elemental Cu in the X-ray patterns after annealing. The results for W-Si-Cu system suggests the presence of a W_5Si_3-Cu, W_5Si_3-γ-Cu_5Si, and WSi_2-η-Cu_3Si tie lines at 700°C.

Other experimental works provide complementary information on the Cr-Si-Cu and W-Si-Cu thin-film systems. Olowolafe et al. observed no dissociation of $CrSi_2$ in <Si>/$CrSi_2$/Cu systems annealed at 500°C [63]. Although Si presumably from the substrate reacted with Cu to form Cu_3Si, the $CrSi_2$ was left relatively intact, according to Auger electron spectrometry and X-ray diffraction measurements. As the case with the results presented in this section, X-ray diffraction measurements by Thomas et al. on $W_{72}Si_{28}$ /Cu bilayers annealed at 800°C for 1 h did not reveal any reaction products [64].

5.2.6. Ti-Si-Cu and Ti-Si-N-Cu Systems

The phase diagram for the Ti-Si-Cu system at 800°C is redrawn in Figure 5.2 from Sprenger [65]. With two ternary phases in the system, TiSiCu and Ti_2Si_4Cu, along with Ti-Cu binary compounds, titanium silicides are not thermodynamically stable in the presence of elemental Cu. In thin film work, Olowolafe et al. have observed the reaction of $TiSi_2$ with Cu to form $TiCu_3$ and copper silicides [63]. Adding nitrogen to the system gives a variety of interesting phases. In studying the

brazing of Si_3N_4 and Ag-Cu-Ti alloys, Carim found several Ti-Si-Cu-N phases by TEM: orthorhombic, C-centered Ti-Si-Cu-N; fcc-$(Ti,SiCu)_6N$; and hexagonal Ti-Si-Cu-N [66].

5.2.7. Summary of Thermodynamics

From the phase diagrams in Figures 5.1 and 5.2, BN, Si_3N_4, possibly all of the TM-nitrides, and most of the borides appear to be stable with Cu with some questions of solubility remaining. The silicide systems are more complex. Assuming the metal-rich stoichiometries, many of the silicides should not react with copper. However, the known solubilities of Si in Cu, and Cu in some of the $TM_{v,vi}$-silicides could pose problems for diffusion barrier applications, even though large-scale reaction will not occur in the TM-rich systems. In contrast, all of the binary titanium silicides are known to react with copper.

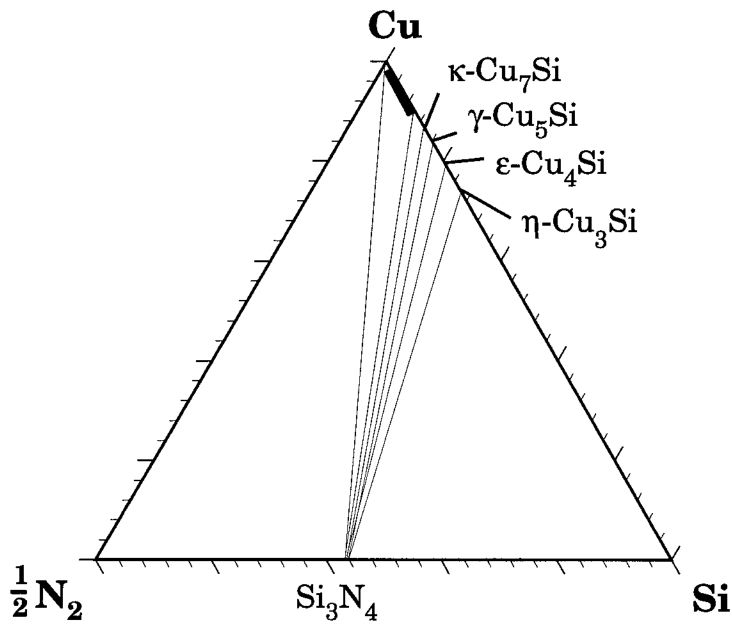

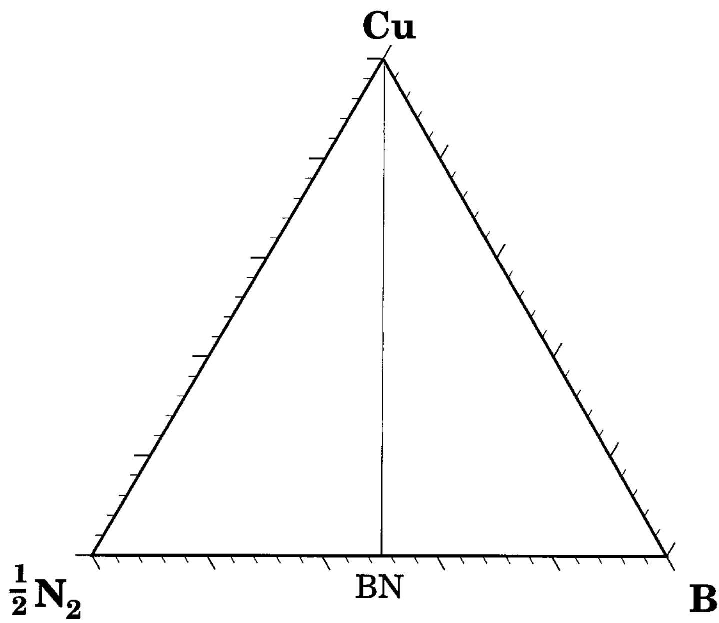

Figure 5.1. Ternary phase diagrams of the Si-N-Cu and B-N-Cu systems at 700°C redrawn from [41].

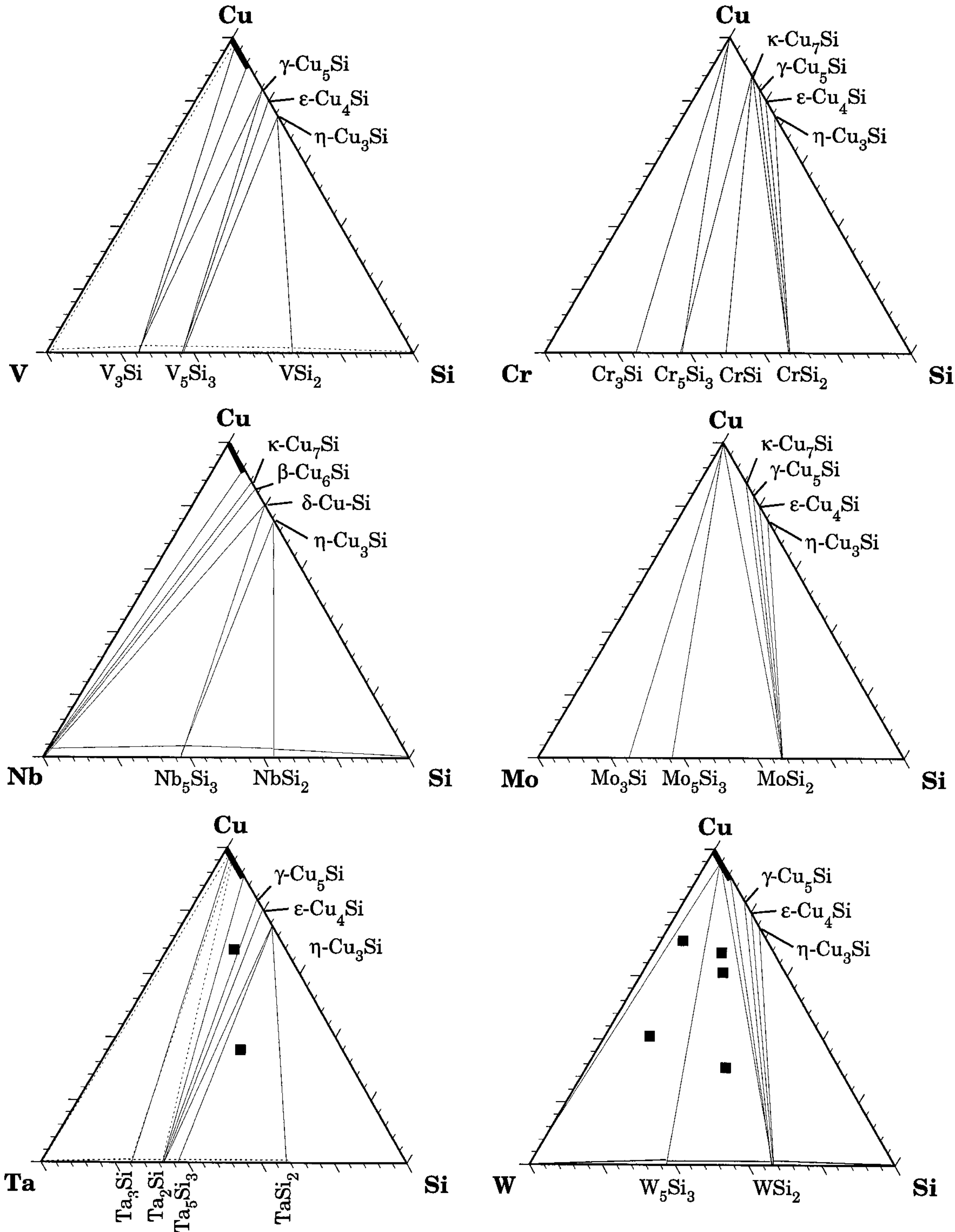

Figure 5.2. Ternary phase diagrams of the TM-Si-Cu systems. The V and Ta diagrams are based on Ganglberger's work with systems at 1000°C [43]. Diagrams for Nb [42] and W [44] are for 800°C treatments. Dotted-lines in the diagrams represent speculative equilibria. The Cr and Mo diagrams are from the modelling of Section 5.2.4 of systems at 700°C without regard to solubilities.

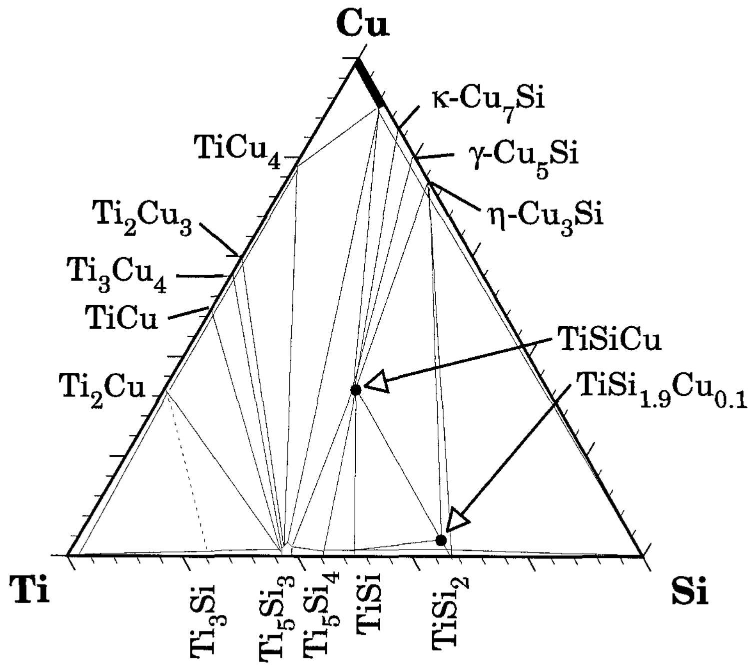

Figure 5.2 Continued: Ti-Si-Cu system at 800°C redrawn from Sprenger [65].

Table 5.1. Negative Gibbs free energy values for $TM_{v,vi}$-silicides, copper silicides, $TM_{v,vi}$, Cu and Si at 700°C (in kJ/g-at.) using the convention of Barin and Knacke [49]. Top and bottom values respectively denote 700 and 25°C.

		X	XSi_2	XSi	X_5Si_3	X_2Si	X_3Si	$X_{19}Si_6$	X_4Si	X_5Si	X_7Si
	V	40.8	70.4	...	98.0	...	79.0	...	...	...	...
		8.6	46.7	...	66.4	...	52.0	52.0	...	...	...
	Nb	47.7	75.5	...	106.0	...	...	...	...	...	...
		10.9	48.8	...	73.2	...	...	...	...	...	...
	Ta	52.9	69.4	...	87.5	87.8	85.6	...	...	...	...
		12.4	45.3	...	52.3	52.3	49.4	...	...	...	...
X	Cr	35.5	58.8	63.5	66.6	...	67.6	...	...	...	...
		7.1	31.8	37.0	40.8	...	41.0	...	...	...	...
	Mo	40.0	71.9	...	76.1	...	64.3	...	...	...	...
		8.5	46.1	...	45.5	...	33.3	...	...	...	...
	W	43.8	62.8	...	58.5	...	...	...	...	...	...
		9.7	37.4	...	26.1	...	...	...	...	...	...
	Cu	45.0	...	...	...	...	...	45.4	45.6	45.8	45.9
		9.9	...	...	...	...	...	8.4	8.7	9.1	...

Si: 29.1, 5.6

Table 5.2. Enthalpy of formation, ΔH°_{f} for copper silicides at 25°C from various sources (in kJ/g-at).

reference	η"-$Cu_{19}Si_6$	ε-Cu_4Si	γ-Cu_5Si
Lüdecke[a] [53]	+2.7	+2.2	+1.7
Miedema et al.[a] [55,56]	-3.1	-2.7	-2.3
Kaufman[a] [57]	-26.3	-29.3	-29.4
Meschel and Kleppa[b] [58]	-6.1	...	...

[a]Modeled.
[b]Experimental.

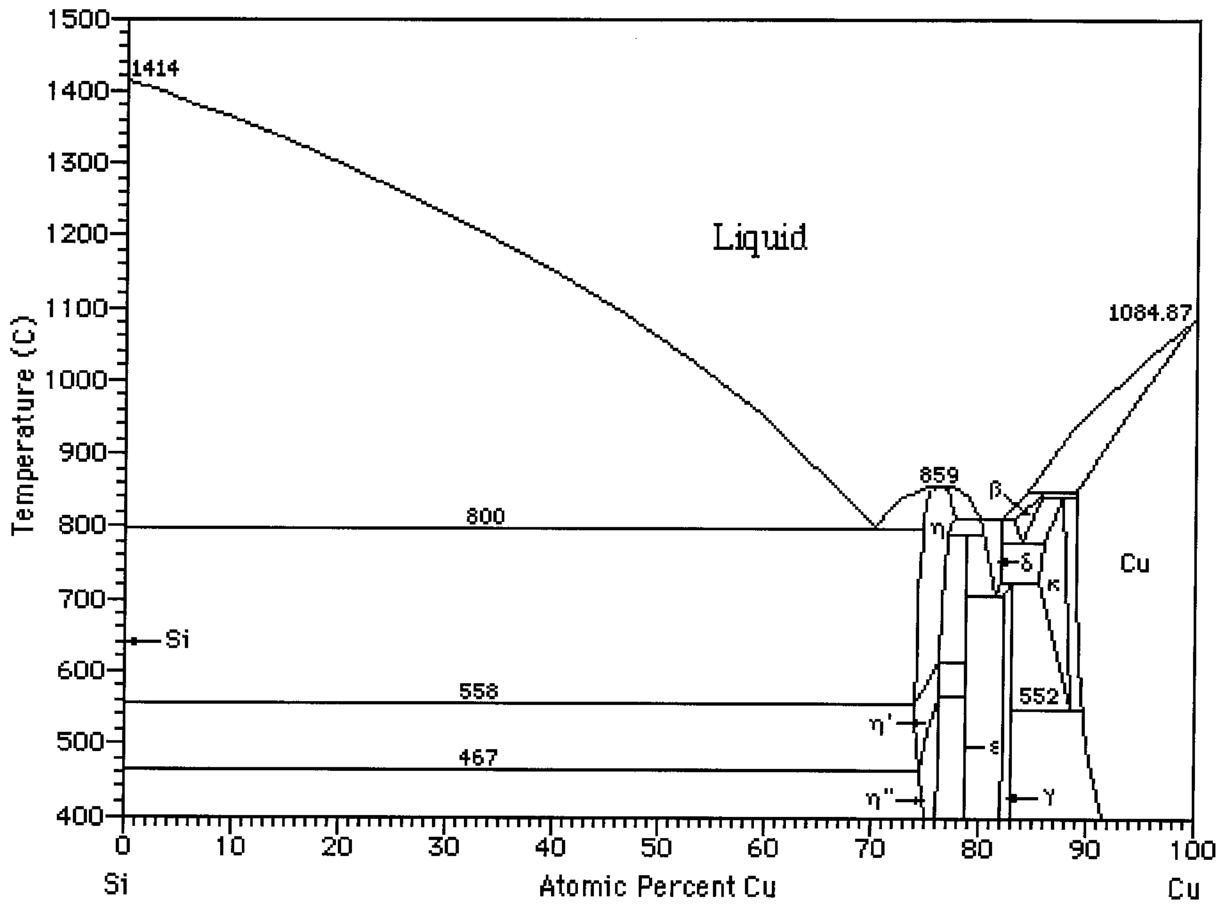

Figure 5.3. Cu-Si binary phase diagram. Produced from TAPP [47].

Table 5.3. Reaction of copper with Mo, Ta, and W silicides. The TM, Si, and Cu columns denote the combined atomic composition of the multilayer samples. The silicides typically had 2 at.% each of argon and oxygen, whereas the copper contained less than 1 at.% of those species.

system	TM	Si	Cu	process	detected phases
Mo_5Si_3 target:					
$Mo_{74}Si_{26}$ (110 nm)/Cu (80 nm)/$Mo_{74}Si_{26}$ (75 nm)	46	16	38	700°C/10 h	Mo_5Si_3, Mo_3Si, Cu
$Mo_{74}Si_{26}$ (110 nm)/Cu (380 nm)/$Mo_{74}Si_{26}$ (75 nm)	19	7	74	700°C/10 h	Mo_5Si_3, Mo_3Si, Cu
Ta_5Si_3 target:					
$Ta_{80}Si_{20}$ (140 nm)/Cu (5-140 nm)	62-35	15-9	23-57	700-1000°C/1 h	Ta_2Si, $Ta_{4.5}Si$, Cu
$TaSi_2$ target:					
$Ta_{44}Si_{56}$ (140 nm)/Cu (80 nm)/$Ta_{44}Si_{56}$ (100 nm)	26	36	36	700°C/10 h	$TaSi_2$, α-Ta_5Si_3, η-Cu_3Si
$Ta_{44}Si_{56}$ (130 nm)/Cu (3700 nm)/$Ta_{44}Si_{56}$ (100 nm)	14	18	68	700°C/10 h	α-Ta_5Si_3, h-Ta_5Si_3, γ-Cu_5Si
W_5Si_3 target:					
$W_{80}Si_{20}$ (120 nm)/Cu (80 nm)/$W_{80}Si_{20}$ (80 nm)	53	13	33	700°C/10 h	W_5Si_3, W, Cu
$W_{80}Si_{20}$ (120 nm)/Cu (370 nm)/$W_{80}Si_{20}$ (80 nm)	23	6	71	700°C/10 h	W_5Si_3, W, Cu
WSi_2 target:					
$W_{44}Si_{56}$ (200 nm)/Cu (100 nm)/$W_{44}Si_{56}$ (160 nm)	17	22	61	700°C/10 h	WSi_2, W_5Si_3, η-Cu_3Si
$W_{44}Si_{56}$ (200 nm)/Cu (400 nm)/$W_{44}Si_{56}$ (160 nm)	31	38	31	700°C/10 h	W_5Si_3, γ-Cu_5Si
$W_{44}Si_{56}$ (120 nm)/Cu (550 nm)/$W_{44}Si_{56}$ (90 nm)	9	12	82	700°C/10 h	W_5Si_3, Cu, γ-Cu_5Si

as-deposited 900°C/1 h

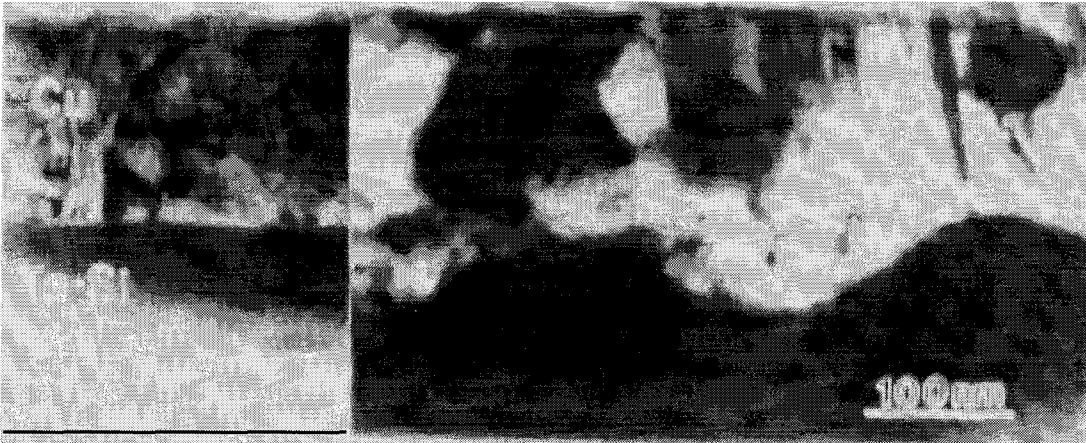

Figue 5.4. Bright-field, cross-sectional micrographs of as-deposited and 1 h, 900°C-annealed <Si>/SiO_2/$Ta_{80}Si_{20}$ (140 nm)/Cu (140 nm) samples. The bottom portion of the as-deposited Ta-Si layer was ion-milled away during sample preparation

5.3. Stability of Nitrogenless TM-Si/Cu and W-B/Cu Metallizations

Sample preparation for the amorphous barrier/Cu evaluations was analogous to the procedure given for the Al metallizations. Unpatterned or patterned (100)-Si containing the shallow-junction diodes was etched in dilute HF just prior to loading into the sputtering system for pump-down. Other substrates included graphite and oxidized silicon. Binary barrier depositions were made under the same conditions described in Chapter 2. Without breaking vacuum, 250 to 350 nm copper overlayers were added. After deposition, the samples were annealed for 30 min in 4×10^{-7} vacuum and subsequently characterized by RBS, diode measurements, and X-ray diffraction.

Table 5.4 summarizes some of the results obtained from the X-ray diffraction and diode tests for the six binary amorphous barriers investigated. The barriers may be classified into two categories as per the previous section of this thesis: the four films that do not react to form compounds with copper, namely $Mo_{74}Si_{26}$, $Ta_{80}Si_{20}$, $W_{80}Si_{20}$, and $W_{79}B_{21}$; and those that do react, $W_{44}Si_{56}$ and $Ti_{62}Si_{38}$. As described in Chapter 3 and retabulated in Table 5.4, the crystallization temperature of the nonreacting films ranges from 650°C for $Mo_{74}Si_{26}$ to 900°C for $Ta_{80}Si_{20}$. However, in the presence of a copper overlayer, the crystallization temperature of the barriers can drop by as much as 200°C (fifth column of Table 5.4). The crystallization products mentioned in Chapter 3 do not change with a copper overlayer; they just occur at a lower temperature. Of the four nonreacting systems, the tungsten boride film is the least susceptible to the effect.

As shown in the last two columns of Table 5.4, the stability of the nonreacting barrier/Cu metallizations on diodes tends to scale with the Cu-reduced crystallization temperatures. With the lowest crystallization temperature, 110 nm $Mo_{74}Si_{76}$, barriers prevent copper diffusion into the shallow junction only up to 450°C for the 30 min heat treatment. With higher crystallization temperatures, $W_{80}Si_{20}$, $W_{79}B_{21}$, and $Ta_{80}Si_{20}$ barriers prevent electrical degradation up to 500, 500, and 600°C,

respectively.

The cause of failure in the unreacting binary silicides and boride barriers is not immediately clear. Backscattering spectrometry of samples annealed at temperatures above the diode failure temperature (50°C above the "maximum stability" temperature listed in Table 5.4) reveals no detectable instabilities. As a prototypical example, Figure 5.5 shows spectra of <Si>/$W_{80}Si_{20}$/Cu metallizations annealed at 550°C, which is the electrical failure temperature. There is no difference in spectra obtained from as-deposited and 550°C-treated samples. Consequently, only very minute quantities of copper are traversing the barrier. Barrier failure in the diode tests occurs at temperatures 100 to 200°C below the Cu-reduced crystallization temperature. Once a barrier crystallizes, grain boundaries are introduced, thus presumably providing fast diffusion paths for Cu. Although Read-camera X-ray diffraction does not indicate crystallization at the diode failure temperature, copper-induced structural modifications of the barriers may still have occurred. As discussed in Chapter 3 for annealed $Ta_{36}Si_{14}N_{50}$ films, electron diffraction, with its shorter wavelength, is a far more sensitive technique for probing structural changes.

The mechanism for the precrystallization of the barriers in the presence of Cu overlayers may stem from solubility effects. As noted in the previous section, Cu may dissolve Si or B from the barriers. Reciprocally, the transition metal silicides can dissolve a few percent of Cu. The structural instabilities actuated by the solubilities may lead to crystallization. Interestingly, in a study by Thomas et al., sputtered, amorphous $W_{72}Si_{28}$ films with an evaporated Cu overlayer do not undergo premature crystallization [64]. The lack of premature crystallization may be a consequence of breaking vacuum between barrier and copper depositions. Thus, a native oxide on the barrier may hinder the premature crystallization effect. Additionally, the films sputtered by Thomas et al. may have contained higher impurity levels than the $W_{80}Si_{20}$ films discussed here because of a higher base pressure.

The discussion in this section has thus far focussed on barriers which do not

react to form compounds with copper. Considering next the two barriers in Table 5.4 that do react with Cu, $W_{44}Si_{56}$ and $Ti_{62}Si_{38}$, one notices that their ability to block copper diffusion is poor. Figure 5.6 shows backscattering spectra of a $W_{44}Si_{56}$/Cu bilayer on oxidized silicon after annealing. The oxidized silicon was chosen to isolate the effects of the substrate. After annealing at 400°C, some mixing of the bilayers has occurred. Silicon from the barrier appears to be moving into the Cu, with Cu moving into the barrier. The situation on a silicon substrate is very similar after the 400°C treatment. Annealing at 450°C produces discrete steps in the silicon signal, with silicon present at the surface. Copper diffuses completely to the oxide. Tungsten in the barrier appears to be relatively immobile. Remarkably, despite the diffusion, X-ray diffraction of the bilayers on oxidized silicon does not reveal the presence of any reaction or crystallization products up to 600°C, which is 50°C above the crystallization temperature of $W_{44}Si_{56}$ without an overlayer. Only an amorphous halo and copper reflections are observed. It is conceivable that an amorphous W-Si-Cu ternary phase has formed.

Table 5.4. Summary of amorphous barriers for Cu: barrier thickness, resistivity, barrier crystallization temperature determined by X-ray diffraction after a 1 h anneal, barrier crystallization temperature in the presence of a copper overlayer after a 30-min anneal, and maximum stability temperature and time determined by I(V) tests on shallow-junction diodes. Films with the best stability for each system are printed in bold face.

Composition	Barrier Thickness (nm)	Resistivity (μΩ.cm)	Crystallization Temp.(°C)	Crystallization Temp. w/ Cu(°C)	Max. Stability of Barrier/Cu on Diodes
Mo_5Si_3 target:					
$Mo_{74}Si_{26}$	110	180	650	550	450°C/30 min
$Mo_{44}Si_{20}N_{36}$	**130**	**710**	**800**	**800**	**800°C/30 min**
$Mo_{42}Si_{19}N_{39}$	130	980	800	...	800°C/30 min
$Mo_{37}Si_{18}N_{45}$	130	1020	800	...	800°C/30 min
$Mo_{35}Si_{17}N_{48}$	130	1800	800	...	800°C/30 min
$Mo_{44}Si_{20}N_{36}$	10	...	...	...	650°C/30 min
Ta_5Si_3 target:					
$Ta_{80}Si_{20}$	100	260	900	700	600°C/30 min
"	10	260	...	...	450°C/30 min
$Ta_{36}Si_{14}N_{50}$	**100**	**1000**	**950**	**850**	**900°C/30 min**
"	100	1000	950	850	350°C/1000 h
$Ta_{36}Si_{14}N_{50}$	10	...	650	...	650°C/30 min
Ti_5Si_3 target:					
$Ti_{62}Si_{38}$	100	300	900	...	400°C/30 min
$Ti_{38}Si_{26}N_{36}$	100	500	...	...	500°C/30 min
$Ti_{34}Si_{23}N_{43}$	**100**	**650**	**900**	**900**	**900°C/30 min**
$Ti_{34}Si_{23}N_{43}$	10	650	900	...	650°C/30 min

(continued on next page)

Table 5.4. Continued.

Composition	Barrier Thickness (nm)	Resistivity (μΩ.cm)	Crystallization Temp.(°C)	Crystallization Temp. w/ Cu(°C)	Max. Stability of barrier/Cu on diodes
W_5Si_3 target:					
$W_{80}Si_{20}$	110	200	750	650	500°C/30 min
$W_{45}Si_{17}N_{38}$	130	630	850	...	700°C/30 min
$W_{41}Si_{17}N_{42}$	130	790	850	...	750°C/30 min
$W_{38}Si_{15}N_{47}$	**130**	**870**	**850**	**850**	**800°C/30 min**
$W_{36}Si_{14}N_{50}$	130	1040	850	...	750°C/30 min
$W_{38}Si_{15}N_{47}$	10	...	...	...	600°C/30 min
WSi_2 target:					
$W_{44}Si_{56}$	130	300	550	600	350°C/30 min
$W_{33}Si_{43}N_{24}$	130	570	700	...	600°C/30 min
$W_{30}Si_{41}N_{29}$	130	800	850	...	650°C/30 min
$W_{27}Si_{38}N_{35}$	130	1100	900	...	750°C/30 min
$W_{24}Si_{36}N_{40}$	**130**	**1800**	**900**	**850**	**900°C/30 min**
$W_{24}Si_{36}N_{40}$	10	...	...	...	800°C/30 min
W_2B target:					
$W_{79}B_{21}$	100	190	750	700	500°C/30 min
$W_{72}B_{20}N_8$	100	200	750	...	700°C/30 min
$W_{64}B_{20}N_{16}$	**100**	**220**	**750**	**750**	**800°C/30 min**
$W_{57}B_{19}N_{24}$	100	320	750	...	750°C/30 min
$W_{50}B_{19}N_{31}$	100	440	750	...	700°C/30 min
$W_{42}B_{17}N_{41}$	100	530	750	...	650°C/30 min
$W_{35}B_{14}N_{51}$	100	1070	650	...	600°C/30 min
Ti target:					
unbiased TiN	100	200	...	...	450°C/30 min
unbiased TiN	10	...	...	...	350°C/30 min
biased TiN	**100**	**40**	**...**	**...**	**700°C/30 min**
biased TiN	10	...	...	...	400°C/30 min

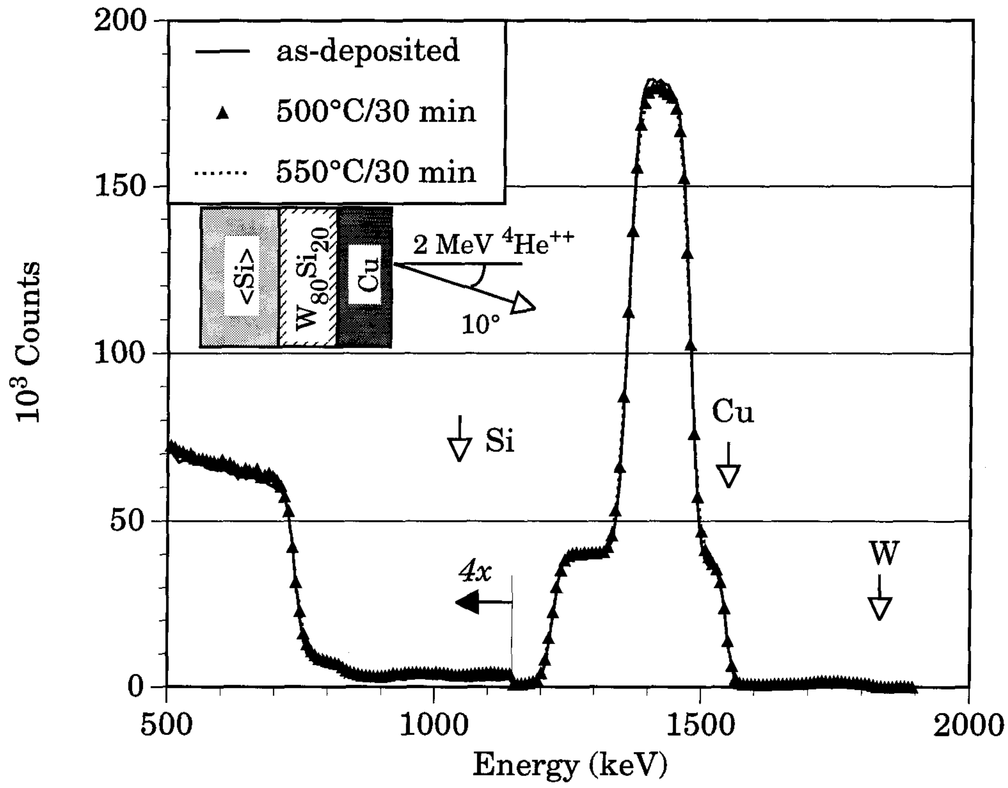

Figure 5.5. 2 MeV ^{4}He backscattering of <Si>/$W_{80}Si_{20}$ (110 nm)/Cu (260 nm) metallizations before and after annealing for 30 min at 500 and 550°C.

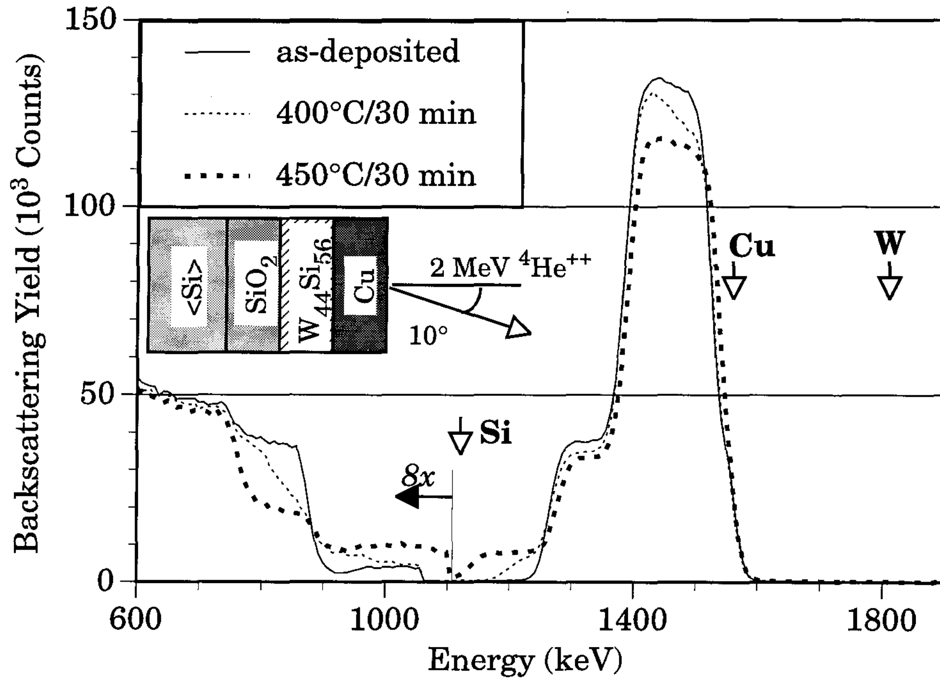

Figure 5.6. 2 MeV ^{4}He backscattering of <Si>/$W_{80}Si_{20}$ (110 nm)/Cu (260 nm) metallizations before and after annealing for 30 min at 500 and 550°C. The hump in the spectra between 900 and 1060 keV for the as-deposited sample is trapped Ar in the barrier.

5.4. Stability of TM-Si-N/Cu and W-B-N/Cu Metallizations on <Si>

Adding nitrogen to the silicide and boride systems greatly impedes copper diffusion. Table 5.4 summarizes the results obtained from the diode and X-ray diffraction studies. At the proper compositions, 100-nm-thick films are able to preserve the I(V) characteristics of the Si diodes at 800°C for 30 min or higher. A summary of each system is given in the following subsections.

5.4.1. Mo-Si-N/Cu

Four compositions of Mo-Si-N films were evaluated, ranging from 36 to 48 at.% nitrogen with approximately 4-5 at.% oxygen and 1 at.% argon. As discussed in Chapter 2, the Mo-Si-N films crystallize into Mo_3Si and Mo_5Si_3 at 800°C, but begin to lose nitrogen at 700°C. With a copper overlayer, 100-nm-thick barriers of all four compositions preserve the I(V) characteristics of the shallow-junction diodes up to 800°C for a 30-min heat treatment. The presence of a copper overlayer does not induce premature crystallization according to X-ray diffraction. Samples annealed at 850°C for 30 min yield only X-ray reflections from Mo_3Si, Mo_5Si_3, and Cu. Scanning electron micrographs of the <Si>/$Mo_{44}Si_{20}N_{36}$ (130 nm)/Cu (260 nm) scheme, which yield the smoothest morphology of the four compositions after annealing at 850°C, show ~1 μm bumps on the surface (Figure 5.7a). Energy dispersive spectrometry of X-rays taken with the electron beam on and off the bumps gives identical spectra, thus the morphological changes may be due to stress and are not chemically related. Optically, <Si>/Mo-Si-N/Cu systems with higher nitrogen contents contain pinholes after heat treatment at 800°C. The behavior may be related to disintegration of the barriers from nitrogen volatilization.

Although 100-nm-thick barriers give convenient quantities of material to analyze by many laboratory techniques, commercial integrated circuit technology is rapidly approaching 0.25 μm via sizes. Accordingly, 10-nm barriers may very soon become commonplace to minimize ohmic losses through such vias. With TM-Si-N

barriers typically having a resistivity of 1000 μΩ cm, minimizing the transverse resistance by minimizing the barriers' thickness may be critical in some applications. Table 5.4 lists the Si diode test results for several 10-nm-thick TM-Si-N barriers with 250 nm copper overlayers. Unlike their 100 nm counterparts, the 10 nm barriers do present some nagging problems with diode yield. With 42 devices tested at a given temperature, roughly 5% of the 42 diodes metallized with the 10 nm barriers and 250 nm copper overlayers would fail at temperatures far below those listed in Table 5.4. The remaining 95% yield of stable diodes does not change up to the listed Table 5.4 temperature. The ultrathin barriers seem to be susceptible to having a small number of weak spots probably produced by the particulate contamination in the film, which gets buried with a thicker barrier. A commercial deposition system may alleviate these problems. Additionally, because the diodes were fabricated with a LOCOS technique [67,68], local thinning or cracking of the barrier may occur where the barrier runs off the silicon onto the peripheral, "bird-beaked" oxide. In any case, it is clear that 10 nm $Mo_{44}Si_{20}N_{36}$ films are able to prevent copper from diffusing into the shallow junctions up to 650°C for 30 min.

5.4.2. Ta-Si-N/Cu

$Ta_{36}Si_{14}N_{50}$ barriers produced from the Ta_5Si_3 target crystallize at 950°C, according to X-ray diffraction. Introducing a copper overlayer causes the observed crystallization temperature to dip to 850°C and 700°C, respectively, for 30 min and 10-h heat treatments. Other than the crystallization, no other reaction products are found by X-ray diffraction. On diodes, $Ta_{36}Si_{14}N_{50}$ (100 nm)/Cu (350 nm) bilayers are stable up to 900°C/30 min. In a paper which can be considered as a supplement to this thesis, cross-sectional transmission electron microscopy shows a slow-moving crystallization front emanating from the $Ta_{36}Si_{14}N_{50}$-Cu interface [15]. Once crystallization consumes the barrier, the metallization fails. In this sense, $Ta_{36}Si_{14}N_{50}$ films can be regarded as a sacrificial barrier with crystallization replacing a reaction front. Long-term stability of $Ta_{36}Si_{14}N_{50}$ (100 nm)/Cu (500 nm)/$Ta_{36}Si_{14}N_{50}$ (50 nm) metallization of diodes is also quite good. In flowing Ar, the system is stable for at

least 1000 h at 350°C. In this test, the top $Ta_{36}Si_{14}N_{50}$ film serves as a cap to prevent oxidation of the Cu. Another extreme test, reducing the thickness of $Ta_{36}Si_{14}N_{50}$ films to 10 nm, still affords electrical stability in the diodes after 650°C/30 min.

In an effort to gain insight into the premature crystallization process, Ag and Au overlayers were sputtered in lieu of Cu onto $Ta_{36}Si_{14}N_{50}$ films. During annealing at 700°C for 10 h, no crystallization occurred, according to X-ray diffraction. Only diffraction halos from the $Ta_{36}Si_{14}N_{50}$ barrier and reflections from the Ag or Au overlayers were observed. The lack of crystallization contrasts the behavior of $Ta_{36}Si_{14}N_{50}$/Cu system. Thermodynamically, one marked difference is that Ag and Au dissolve virtually no silicon, whereas Cu can dissolve almost 10 at.% of silicon. Speculatively, the premature crystallization in Ta-Si-N films may then involve the dissolution of Si from the barrier into Cu. However, this behavior is not expected if all of the silicon is bonded as stoichiometric silicon nitride.

Resistivity changes can be a very sensitive indicator of impurity contents in Cu. For example, the dissolution of only 1 at.% of Si nearly triples the bulk resistivity of Cu [69]. Figure 5.8 shows the changes in sheet resistance as a function of vacuum annealing temperature in <Si>/SiO_2/Cu (300 nm) and <Si>/SiO_2/$Ta_{36}Si_{14}N_{50}$ (100 nm)/Cu (300 nm) systems. Given the large resistivity of the barrier, the sheet resistance of the bilayer samples is dominated by the Cu. Not unexpectedly, annealing the samples initially generates a drop in the resistivity, presumably from the annihilation of defects. For Cu films deposited directly on the oxide, the change in resistivity is independent of the annealing temperature ranging from 400 to 850°C. However, Cu films on $Ta_{36}Si_{14}N_{50}$ exhibit a higher resistivity than those on oxide after annealing at temperatures above 600°C. Although morphological and mechanical effects may contribute to the observed differences in resistivity, the results are consistent with the absorption of small amounts of atomic species from the barrier.

5.4.3. Ti-Si-N/Cu

Figure 5.9 shows the reverse current histograms for <Si>/$Ti_{34}Si_{23}N_{43}$ (100 nm)/Cu (350 nm) metallizations on shallow-junction diodes before and after annealing at 250, 850, and 900°C for 30 min. None of the 42 diodes tested sustain any increase in reverse current from annealing 850°C for 30 min. X-ray diffraction of the $Ti_{34}Si_{23}N_{43}$ annealed at 900°C/30 min with and without the Cu overlayer reveals only the phases TiN and Cu. Although present in electron diffraction patterns (Chapter 3), the nanophase TiN is X-ray amorphous in the as-deposited and 850°C-annealed samples. Barrier failure at 900°C appears to be associated with the grain growth or agglomeration of TiN. Reducing the nitrogen concentration severely degrades barrier performance. Films with 23 and 36 at.% nitrogen are unable to prevent Cu from diffusing into the silicon at 500°C/30 min, according to RBS analyses. As explained in Chapter 3, the structure of the nitrogen-poor films most likely has a silicide component which can be attacked by Cu. In the nitrogen-rich films, the local structure consists of a nanophase blend of TiN_x and SiN_y.

Additional diode tests with 10 nm $Ti_{34}Si_{23}N_{43}$ barriers in lieu of a 100 nm barrier also gave good results. The <Si>/$Ti_{34}Si_{23}N_{43}$ (10 nm)/Cu (350 nm) system on the 42 diodes tested was stable up to 650°C/30 min. After annealing at 700°C, the majority of the 42 diodes sustained an increase in leakage current.

5.4.4. W-Si-N/Cu

As shown in Table 5.4, four different nitrogen-laden films generated from sputtering a W_5Si_3 target in an Ar/N_2 discharge were evaluated, ranging from 38 to 50 at.% nitrogen. Each film contained about 2 at.% each of oxygen and argon. The composition, $W_{38}Si_{15}N_{47}$, will be predominantly discussed because of its optimal barrier performance in the I(V) tests. As discussed in Chapter 2, $W_{38}Si_{15}N_{47}$ on oxidized silicon incompletely crystallizes into elemental W during annealing at 850°C for 1 h, according to X-ray diffraction. Roughly 7 at.% of nitrogen is lost during

annealing at 800°C for 1 h. On diodes, $W_{38}Si_{15}N_{47}$ (110 nm)/Cu (260 nm) metallizations are stable at 800°C for 30 min, but induce large increases in reverse currents after annealing at 850°C. Failure corresponds to the crystallization temperature of the barrier, which is unaltered by the presence of copper. Morphologically, as seen in Figure 5.7b, the copper film contains openings after annealing for 30 min at 850°C. Energy dispersive spectrometry of X-rays emanating from the openings reveals only the presence of W, Si, and N. Therefore, the openings are voids in the copper overlayer and may not be related to the failure of the barrier. Instead, the openings may be associated with nitrogen loss from the barrier. Voids in the copper also occur after annealing at 800°C, but they exist in fewer numbers and smaller sizes. Trimming the barrier thickness down to 10 nm reduces the barriers effectiveness to 600°C/30 min.

Sputtering W-Si-N from a WSi_2 target in a Ar/N_2 discharge produces films with somewhat higher crystallization temperatures than with a W_5Si_3 target, but at the expense of higher resistivities. The film containing the most nitrogen in the evaluation, $W_{24}Si_{36}N_{40}$, crystallizes into only elemental W during annealing at 900°C (Chapter 3). Unlike the tungsten-rich films, no nitrogen is lost even after annealing at 1000°C. Barrier effectiveness against copper diffusion appears to be virtually linear with nitrogen concentration when the barrier thickness is approximately 100 nm. The best performance is obtained with $W_{24}Si_{36}N_{40}$ films, which preserve the I(V) characteristics of the shallow-junction diodes up to 900°C for a 30-min heat treatment in vacuum. Morphologically, the surface of the $Si/W_{24}Si_{36}N_{40}/Cu$ system is relatively smooth after annealing at 850°C, as shown in Figure 5.7c. The observed crystallization temperature of $W_{24}Si_{36}N_{40}$ films in contact with Cu drops to 850°C, according to X-ray diffraction. Figure 5.10 shows a cross-sectional transmission electron micrograph of the <Si>/$W_{24}Si_{36}N_{40}$/Cu system annealed at 900°C for 30 min. Ion milling from sample preparation produced nonuniformities in sample thickness. In the thin area of the barrier, which is near the barrier/Cu interface, small grains of W, and to a lesser extent, W_5Si_3 are evident. In the Cu layer, small nodules emanate from the barrier/Cu interface. Microdiffraction indicates that the

nodules may be a copper silicide. Annealing at 950°C vaporizes much of the copper into the vacuum, leaving behind droplets on the barrier (Figure 5.11). The surface morphology is similar independent of the choice of <Si> or oxidized silicon substrates. Uncalibrated energy dispersive analysis of the droplets in both cases gives a rough estimate of a Cu:Si solution of 70:30 at.%, which suggests a Cu-Si eutectic. Because the oxidized silicon substrate is (presumably) inert, the silicon in the droplets was probably leached from the barrier. X-ray diffraction of the system does reveal the presence of Cu_3Si.

Given that the resistivity of $W_{24}Si_{36}N_{40}$ films is quite high (1800 μΩ cm), minimizing the transverse resistance by minimizing the barrier thickness is especially important. With a 10-nm thickness, $W_{24}Si_{36}N_{40}$ prevents copper diffusion into the shallow-junction diodes at 800°C/30 min, which is the best performance of all the systems presented in this section. The abundance of Si-N bonding in the film undoubtedly gives the high degree of stability.

5.4.5. W-B-N/Cu

Six different compositions of the W-B-N films were tested as diffusion barriers between silicon substrates and copper overlayers. 100-nm-thick $W_{72}B_{20}N_8$ films are stable up to 700°C/30 min. The best performance is obtained with a bit more nitrogen in the system. $W_{64}B_{20}N_{16}$ barriers are stable up to 800°C/30 min, as shown with leakage current histograms in Fig. 5.12. A copper overlayer on $W_{64}B_{20}N_{16}$ makes no difference in the crystallization products and does not alter the crystallization temperature, according to X-ray diffraction. The 850°C failure temperature is 100°C higher than the temperature at which α-W begins to nucleate in $W_{64}B_{20}N_{16}$, but 100°C below the observation of W_2B. Scanning electron micrographs of the surface of <Si>/$W_{64}B_{20}N_{16}$/Cu annealed at 850°C for 30 min show coarsening, twinning, and grain growth of the copper overlayer, but no obvious sign of the failure mode (Figure 5.13). Despite the increase in film density, adding more nitrogen to the films appears to have a deleterious effect on the barrier properties. $W_{50}B_{19}N_{31}$, $W_{42}B_{17}N_{41}$, and

$W_{35}B_{14}N_{51}$ films provide stability only up to 750, 650, and 600°C, respectively. The degradation with higher nitrogen contents is probably a consequence of the reduced crystallization temperatures and destabilization associated with the volatilization of nitrogen.

For comparable compositions, some interesting dissimilarities exist between amorphous W-B-N and W-Si-N films. Although both films afford excellent protection against copper diffusion up to 800°/30 min, they do so at very different compositions: $W_{64}B_{20}N_{16}$ vs. $W_{38}Si_{15}N_{47}$, with respective resistivities of 230 and 870 μΩ cm. The relatively low resistivity of $W_{64}B_{20}N_{16}$ is an obvious advantage in integrated circuit applications. The inability of nitrogen-rich W-B-N films to effectively block copper diffusion probably stems from the intermediate crystallization of ß-W_2N at temperatures as low as 650°C. As discussed in Chapter 3, no such intermediate crystallization occurs in the W-Si-N system.

5.4.6. Comparison with Polycrystalline TiN Films

For comparative purposes, sputtered TiN barriers were also evaluated as diffusion barriers between the Si diodes and copper overlayers. Two stoichiometric TiN films were deposited with and without a -75 V dc substrate bias. Both films were reactively sputtered from a Ti target in Ar/N_2 discharges at 550 W forward power. Applying bias during the sputter deposition tends to densify the films and lower the resistivity, but very high compressive stress is usually a by-product (see references in Section 2.6). In this case, the unbiased TiN films contained approximately 3 at.% each of argon and oxygen and had a resistivity of 200 μΩ cm. Biasing reduced the argon and oxygen levels to less than 1 at.% and lowered the resistivity down to 40 μΩ cm.

As listed at the end of Table 5.4, the TiN films do not perform nearly as well in the diode evaluations as their amorphous ternary counterparts. 100-nm-thick unbiased TiN films are only able to prevent Cu from reaching the Si at 450°C for 30 min.

Biasing the films improves the barrier's effectiveness up 700°C/30 min. However, reducing the thickness of the TiN to 10 nm results in very poor barrier performance. The unbiased and biased barriers yield stable metallizations only up to 350 and 400°C. The reason for the poor performance probably stems from the polycrystalline structure of TiN films. With their characteristic columnar structure, very thin TiN barriers invariably offer direct channels between grains which act as fast diffusion paths for Cu.

5.4.7. Remarks on TM-Si-N/Cu and W-B-N/Cu Metallizations

Collectively, amorphous TM-Si-N and W-B-N barriers represent a nascent and unparalleled class of diffusion barriers between silicon substrates and copper overlayers. Each 100- to 130-nm-thick barrier, at the optimum nitrogen concentration, is able to prevent copper from degrading the I(V) characteristics of shallow-junction diodes during heat treatment in vacuum for 30 min at 800°C or higher. Reducing the barrier thickness to 10 nm affords stability up from 600 to 800°C for 30 min. The results for the very thin barriers convincingly show the advantages of amorphous barriers over polycrystalline barriers for future generations of integrated circuits. As demonstrated with the W-Si-N system, changing the W to Si ratio from about 2.5:1 to 1:1.5 still provides an excellent barrier. Consequently, the barrier properties in all three systems discussed may be quite good over a broad ratio of metal to metalloid, and holds promise for applications with a large process window. Barrier failure in the thick films appears to be associated with grain boundary diffusion introduced by the crystallization of the barrier. Copper-induced premature crystallization of the barriers predominantly occurs in the silicon-based systems that do not liberate significant amounts of nitrogen, particularly films sputtered the Ta_5Si_3 and WSi_2 targets. The mechanism for the crystallization may stem from solubility of silicon from the barrier in Cu. The effect may also be present in the $W_{64}B_{20}N_{16}$ film, but the much lower solubility of B in Cu compared to Si in Cu may be the reason. In the studied systems sputtered from the Mo_5Si_3 and W_5Si_3, nitrogen-loss is evidently a greater driving force for crystallization than the presence of copper.

Thermodynamically, copper was not observed to react to form compounds with most of the barriers. Given the inertness of Si_3N_4, BN, and the TM-nitrides with Cu, the result is not unexpected.

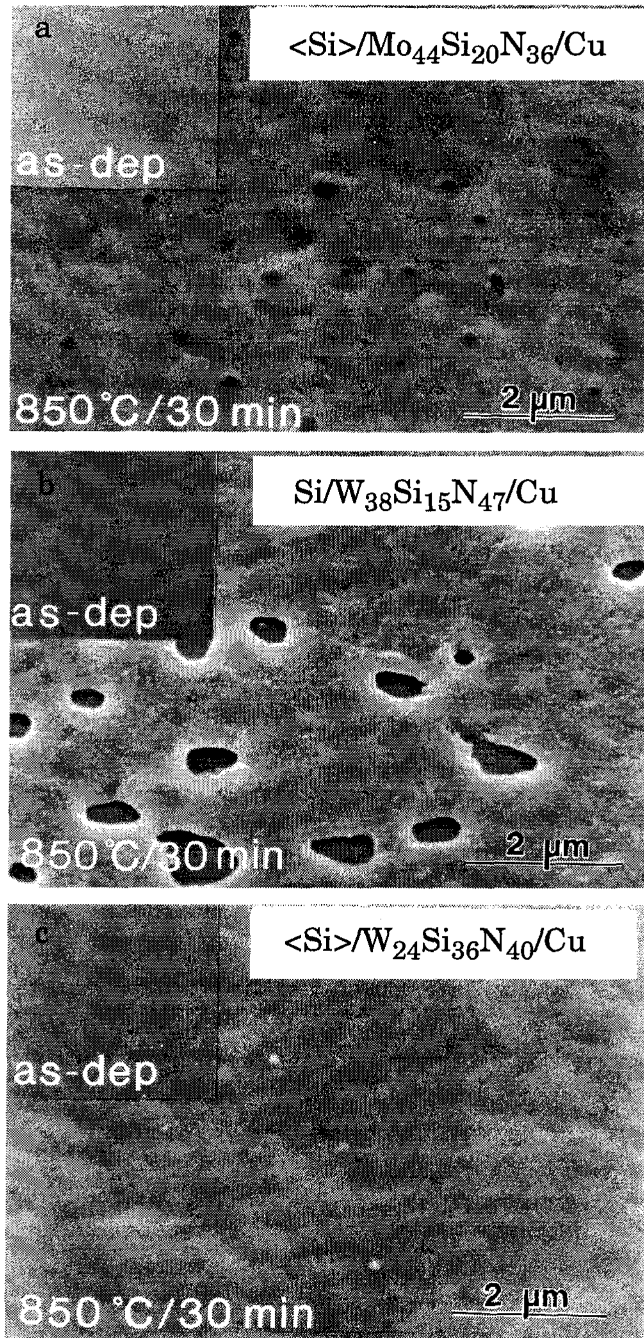

Figure 5.7. Scanning electron micrographs of the surface of the large-area (250 × 250 μm^2) before and after annealing at 850°C: (a) <Si>/$Mo_{44}Si_{20}N_{36}$/Cu, (b) <Si>/$W_{38}Si_{15}N_{47}$/Cu, and (c) <Si>/$W_{24}Si_{36}N_{40}$/Cu. Barrier and Cu thicknesses were about 120 nm and 260 nm, respectively.

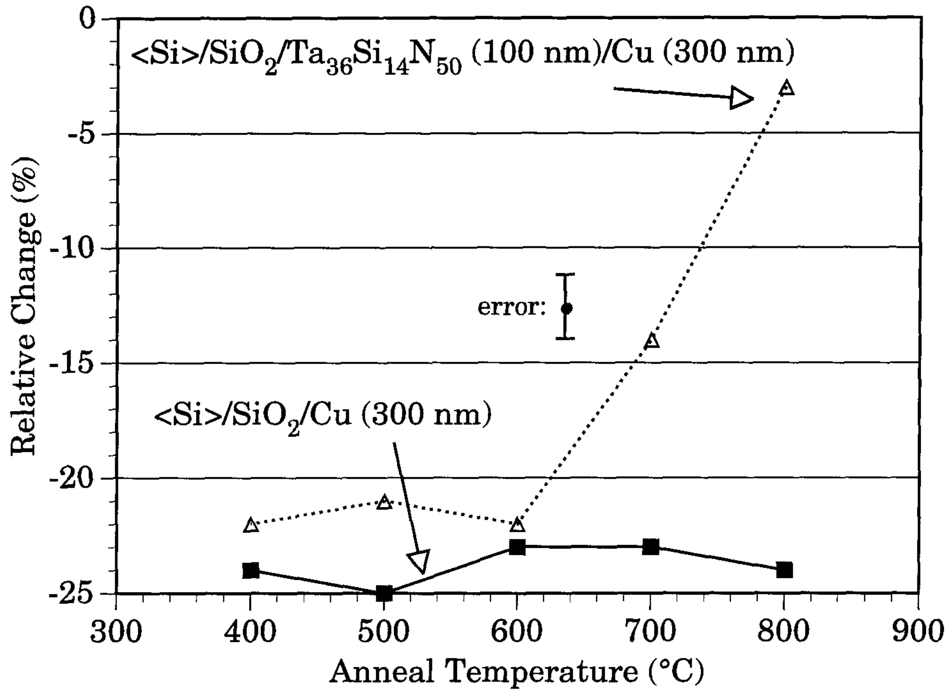

Figure 5.8. Change in sheet resistance incurred from 30 min anneals for <Si>/SiO_2/Cu (300 nm) and <Si>/SiO_2/$Ta_{36}Si_{14}N_{50}$ (100 nm)/SiO_2/Cu (300 nm) systems. After the anneals, the resistivity of Cu on plain oxidized silicon was about 2.0 $\mu\Omega$ cm.

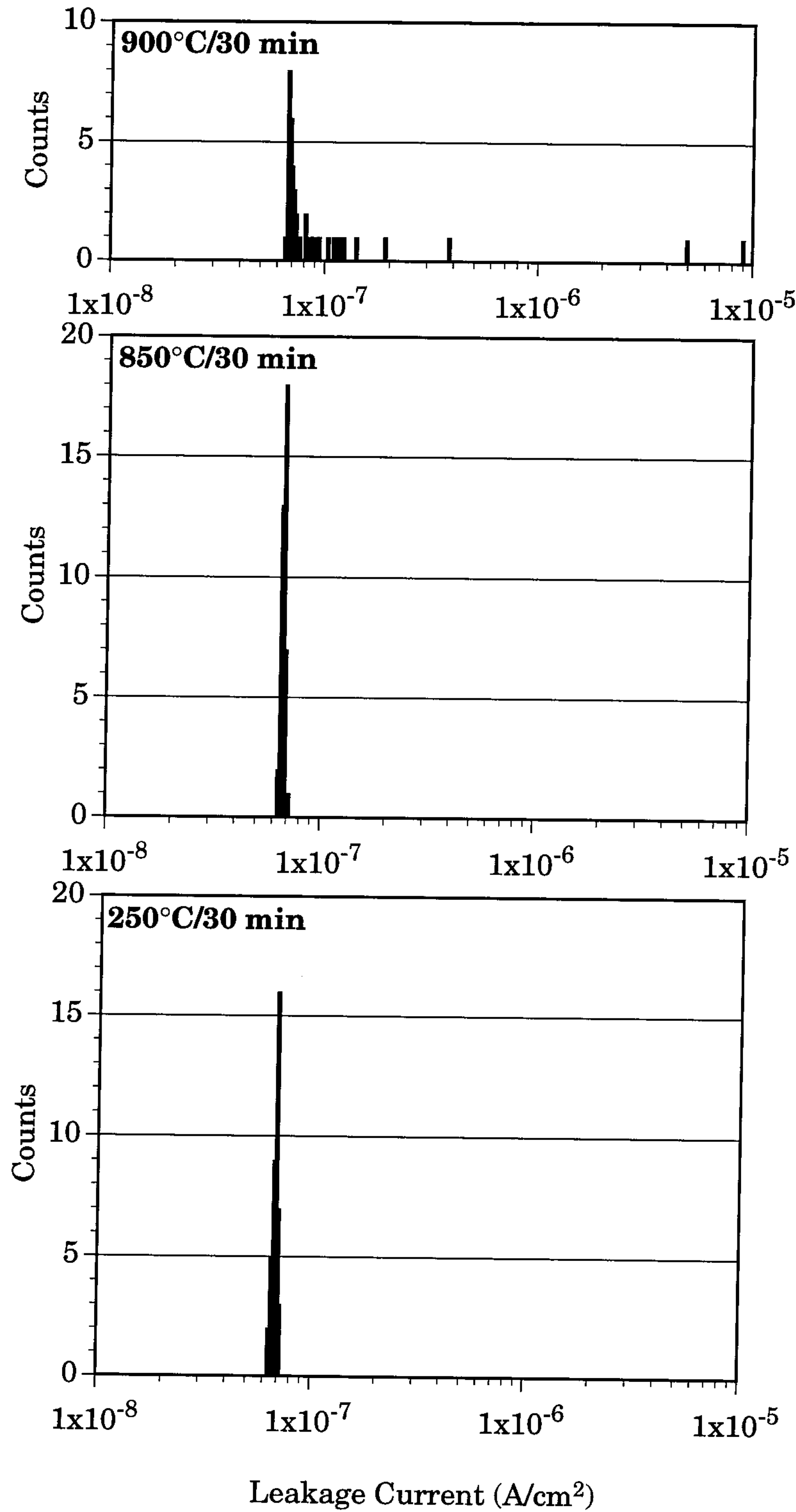

Figure 5.9. Reverse current histograms of the <Si>/$Ti_{34}Si_{23}N_{43}$ (100 nm)/Cu (350 nm) shallow-junction diodes annealed at 250, 850, and 900°C. The reverse bias is -4 V.

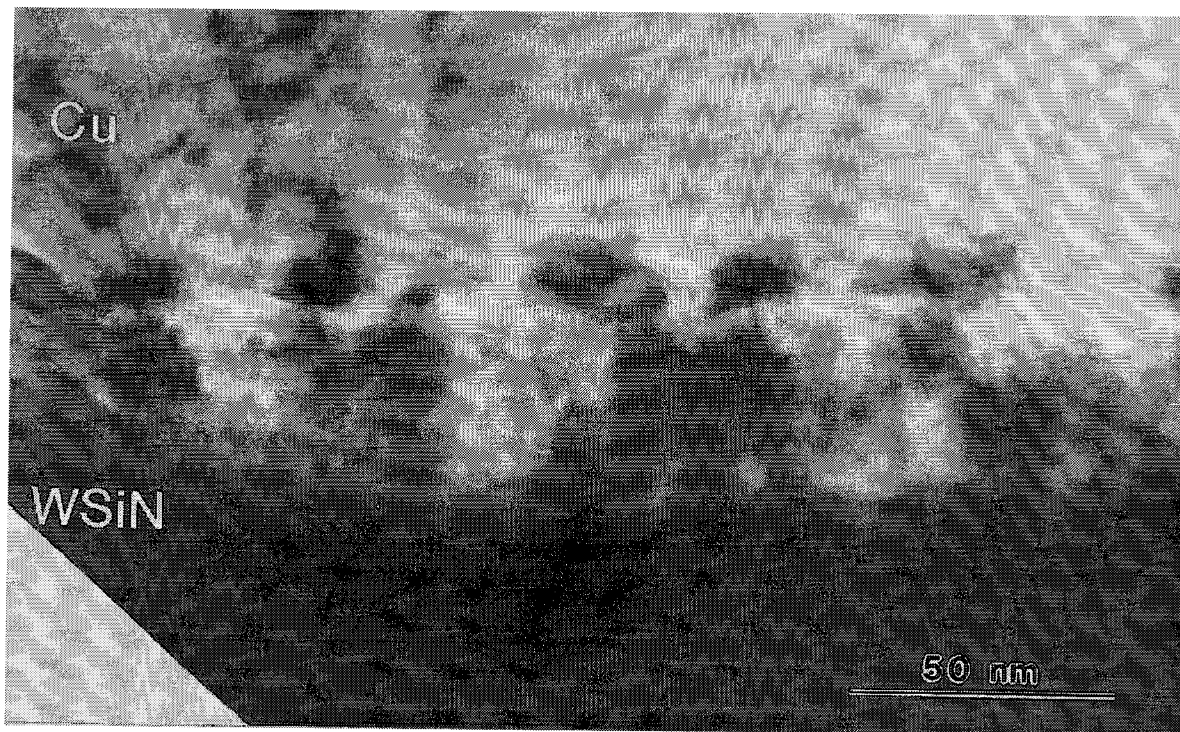

Figure 5.10. Cross-sectional TEM micrograph of the <Si>/$W_{24}Si_{36}N_{40}$/Cu system annealed at 900°C for 30 min. From ion milling, the cross-sectional thickness of the barrier is nonuniform.

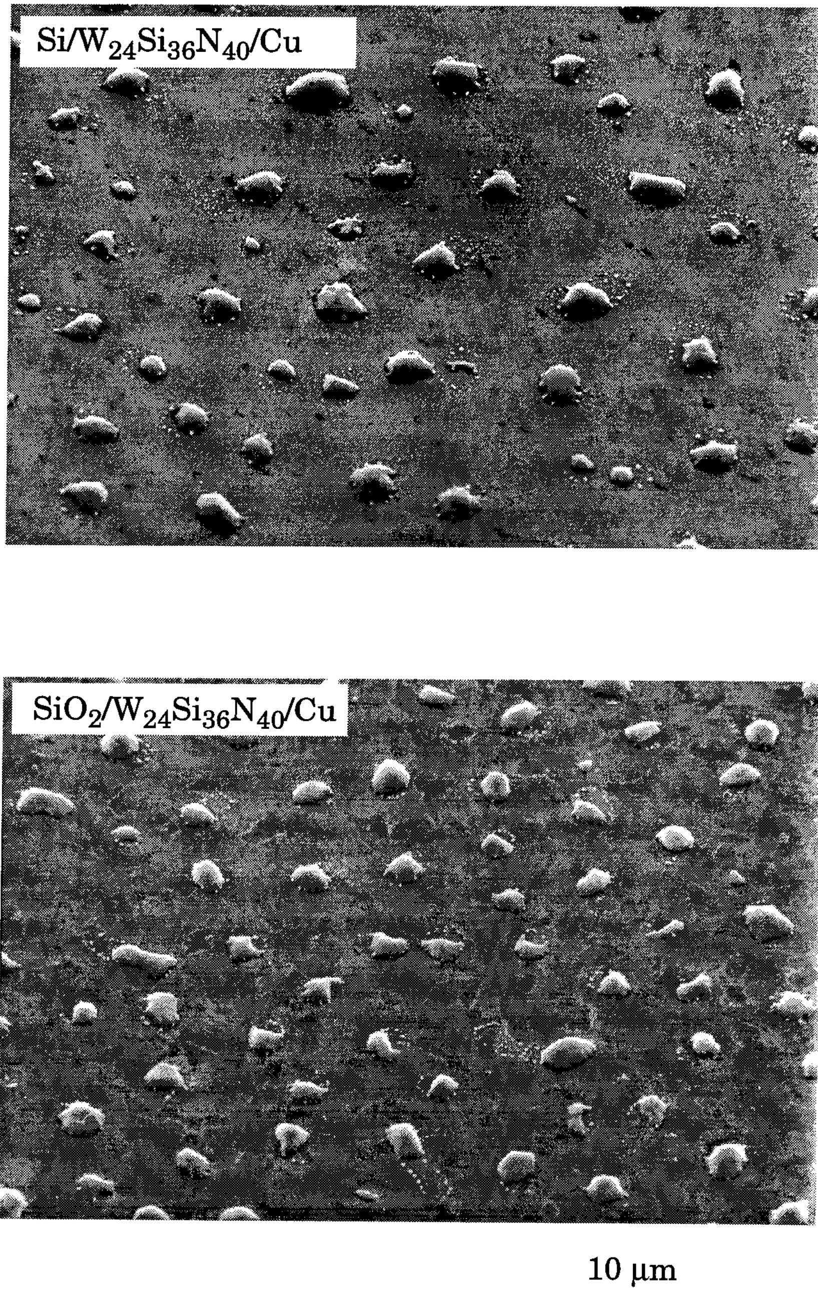

Figure 5.11 Secondary electron micrographs of $W_{24}Si_{36}N_{40}$(130 nm)/Cu (260 nm) bilayers on <Si> and oxidized silicon substrates after vacuum annealing at 900°C for 30 min. The droplet like features contain both Cu and Si in a ratio of 70:30 at.%, which agrees with the Cu-Si eutectic composition shown in Figure 5.3.

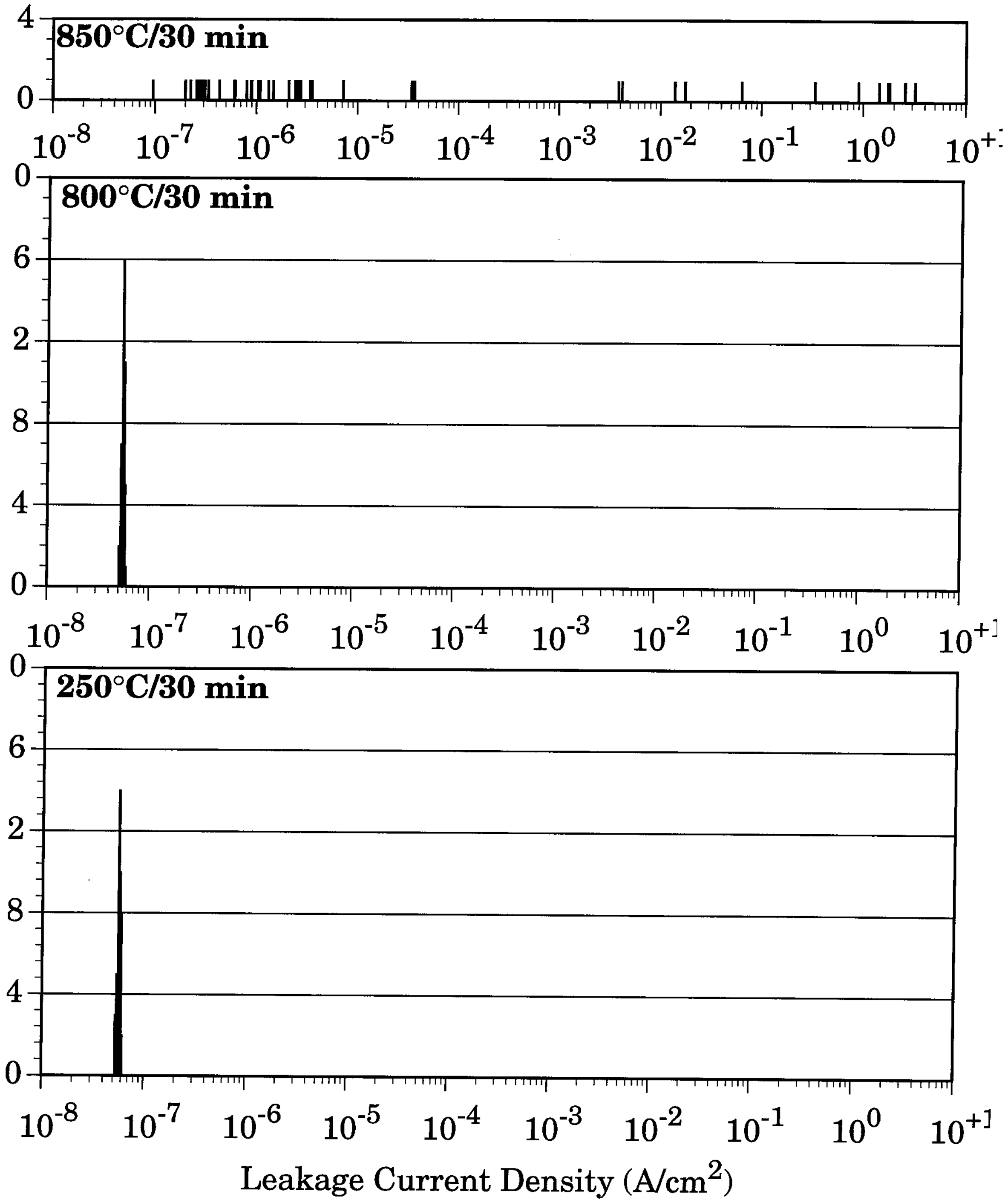

Figure 5.12. Reverse current histograms of the <Si>/$W_{64}B_{20}N_{16}$ (100 nm)/Cu (350 nm) shallow-junction diodes annealed at 250, 850, and 900°C. The reverse bias is -4. V.

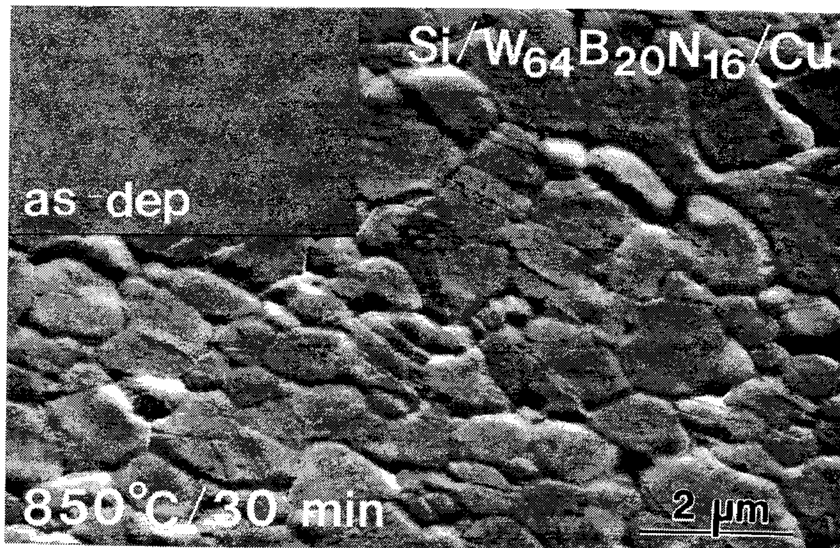

Figure 5.13. Secondary electron images of <Si>/$W_{64}B_{20}N_{16}$ (100 nm)/Cu (260 nm) metallizations before and after annealing at 850°C for 30 min.

5.5. Thermal Diffusion of Cu in $Ta_{36}Si_{14}N_{50}$ Films

The diode results of the previous section provide a sensitive test for the presence of copper in silicon; however, they do not directly yield quantitative values of the diffusivity. In this section, the diffusivity of Cu in amorphous $Ta_{36}Si_{14}N_{50}$ films is examined.

Samples for diffusion measurements consisted of $Ta_{36}Si_{14}N_{50}$ (100 nm)/Cu (7 nm)/$Ta_{36}Si_{14}N_{50}$ (50 nm) trilayers deposited onto oxidized silicon substrates. The very thin and probably discontinuous Cu layer served to simulate a delta function within Ta-Si-N film. Vacuum was not broken in between the depositions of the layers. During deposition, the samples passed cyclically beneath the active target in a "planetary" mode of operation. The rotating stage floated electrically. After deposition, the samples were annealed in 4×10^{-7} vacuum at a temperature between 500 and 700°C for a duration of 30 min to 80 h. By X-ray diffraction, samples annealed at 700°C for 10 or more hours crystallized and were excluded from the diffusion analysis. Depth profiles of Cu were obtained by secondary ion mass spectrometry (SIMS) with a Ar^+ beam in a Cameca 3f. A linear conversion of erosion time to spatial depth was made by assuming the centroid of the copper signal to lie at a depth of x_o = 50 nm.

In extracting the diffusion coefficients, a standard Gaussian Cu profile was assumed, i.e.,

$$C = \frac{Q}{\sqrt{\pi D t}} \cdot e^{(x-x_o)^2/(4Dt)}$$

where,

$$D = D_\circ \cdot e^{-E_a/(kT)} .$$

To provide relatively equal weightings, asymptotic linear fits were applied to the logarithm of the copper concentration as a function of $(x - x_o)^2$ outside the immediate vicinity of x_o. Corrected diffusion parameters were obtained from the quadrature

deconvolution, $(4Dt)_{corrected} = (4Dt)_{measured} - (4Dt)_{as\text{-}deposited}$. Because of asymmetries in the SIMS spectra, a separate deconvoltion procedure was performed on each side of x_o to approximate the true diffusivities.

Figure 5.14 shows the Cu profiles in the trilayer structure before and after annealing at 600 and 650°C for several durations. The bump on the top of the spectra is probably undiffused Cu in the trilayer stack. In most instances, the Cu profile is nonsymmetrical about its centroid. The asymmetries may be attributed to a variety of effects: variable sputter-erosion rates; nonuniform Cu thickness; ion mixing; interfacial impurities; and stress gradients. Figure 5.15 shows a plot of the logarithm of the raw copper profile vs. $(x\text{-}x_0)^2$ for some of the processing conditions. The behavior is largely linear, thus verifying the Gaussian assumption. Table 5.5 gives a complete summary of annealing conditions and the extracted diffusion coefficients for both sides of the Cu distribution. The average diffusivity of Cu in $Ta_{36}Si_{14}N_{50}$ varies from 7×10^{-19} cm^2/s at 550°C to 1×10^{-17} cm^2/s at 650°C. Because of the significant spread in the data, the average values must be regarded as rough estimates of the true diffusivities.

An Arrhenius plot of the averaged diffusion coefficients in Table 5.5 is linear, as shown in Figure 5.16. The fitted values of E_a and D_o are 2.74 eV and 0.014 cm^2/s, respectively. However, from the diode results of the previous section, the extracted value of E_a may be underestimated. With a 10 nm $Ta_{36}Si_{14}N_{50}$ barrier, a copper overlayer did not significantly diffuse into the shallow-junction during a 30-min treatment at 650°C. To avoid degradation in the diode reverse currents, the copper concentration in the junction should be below roughly 10^{12} atoms/cm^3 or lower [70]. Using a "constant source" (i.e. thick copper overlayer) complementary error function profile with the above E_a and D_o values, the copper concentration in $Ta_{36}Si_{14}N_{50}$ is about 10^{18} atoms/cm^3 at a depth of 10 nm (Figure 5.17). Assuming D_o not to increase beyond 10^4 cm^2/s, raising E_a to 2.85 eV is enough to protect the junction.

Despite uncertainties, the diffusion of Cu in $Ta_{36}Si_{14}N_{50}$ compares quite

favorably to other systems relevant for electronic device applications. Data for various systems are shown in Table 5.6. Diffusivities of Cu in PSG (phosphorus-silicate glass), SiN:H, and polyimide films are only around 10^{-14} cm^2/s at 500°C vs 10^{-20} cm^2/s in $Ta_{36}Si_{14}N_{50}$. Although not measured for Cu, diffusivities in fully stoichiometric silicon nitride (Si_3N_4) are probably much lower than the value given for SiN:H in Table 5.6. For example, Ni diffusion in Si_3N_4 extrapolates to about 10^{-20} cm^2/s at 500°C. The same work also shows the advantages of structurally relaxing the amorphous film before introducing the diffusing species. SiO_2 thermally grown at 1100°C affords one-third lower diffusivity for Ni than SiO_2 films deposited by CVD at 800°C. For Ta-Si-N barrier applications, a preanneal before deposition of the copper overlayer may prove advantageous.

The mechanism for Cu diffusion in the Ta-Si-N film is ambiguous, given the inhomogeniety in the structure. As explained in Chapter 3, the $Ta_{36}Si_{14}N_{50}$ film appears to consist of an amorphous blend of silicon nitride and tantalum nitrides. Although direct comparisons with Cu diffusion are difficult because of the lack of experimental data, the lower diffusion of Ni in Si_3N_4 versus Au in tungsten nitride suggests that the SiN_x component of Ta-Si-N limits the diffusion of Cu (Table 5.6). Other studies have shown the drift of Cu in bulk vitreous silica to be partly associated with the exchange of Cu^+ with alkali metal impurities [10]. The ionization of copper also decreases the atomic radius, thus enhancing interstitial diffusion. Considering the large amount of calcium in the Ta-Si-N films (~300 ppm, see Table 2.1), a similar exchange mechanism may enhance thermal diffusion of Cu. Coordination of copper cations with negatively-charged trap states may also play a role in the diffusion. Nitrogen, and to a lesser extent silicon, can form negatively-charged dangling bonds in silicon nitride [73]. The states may afford coordination with the Cu cation, as they are believed to do with Na^+ [74,75]. The density of the Si- and N-dangling bonds in Ta-Si-N films is probably greatest in the SiN_x-TaN_y transition regions. In the next section, the drift of Cu cations will be investigated through bias-thermal stress testing of Ta-Si-N/Cu layers on MOS capacitors. Aside from the metal depostions, the work was largely done by M.S. Angyal at Cornell University, but it is

included here for the sake of completeness.

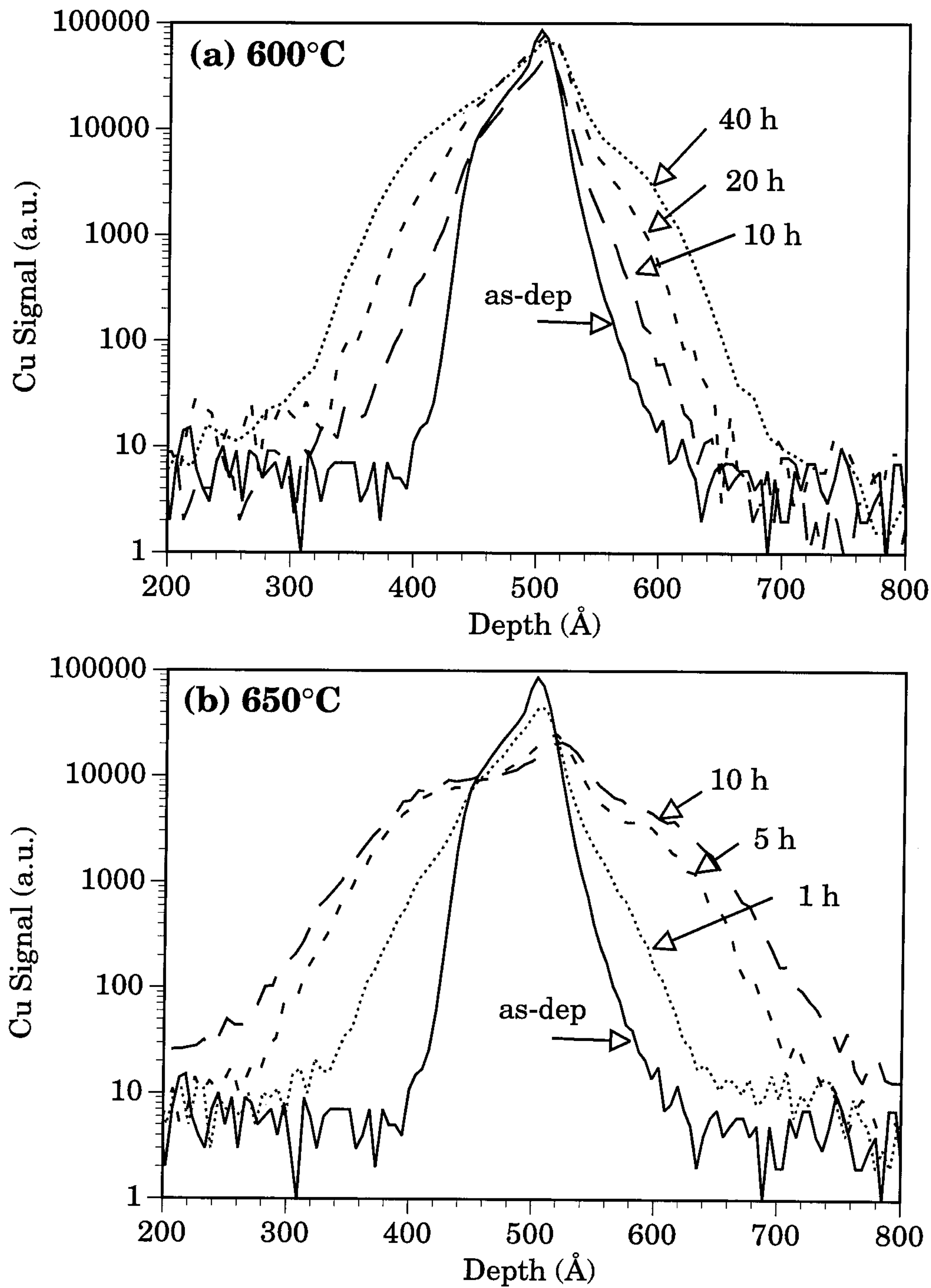

Figure 5.14. SIMS profiles of Cu diffusion in the $Ta_{36}Si_{14}N_{50}$(100 nm)/Cu(70 nm)/$Ta_{36}Si_{14}N_{50}$(50 nm) system: (a) 600°C, and (b) 650°C.

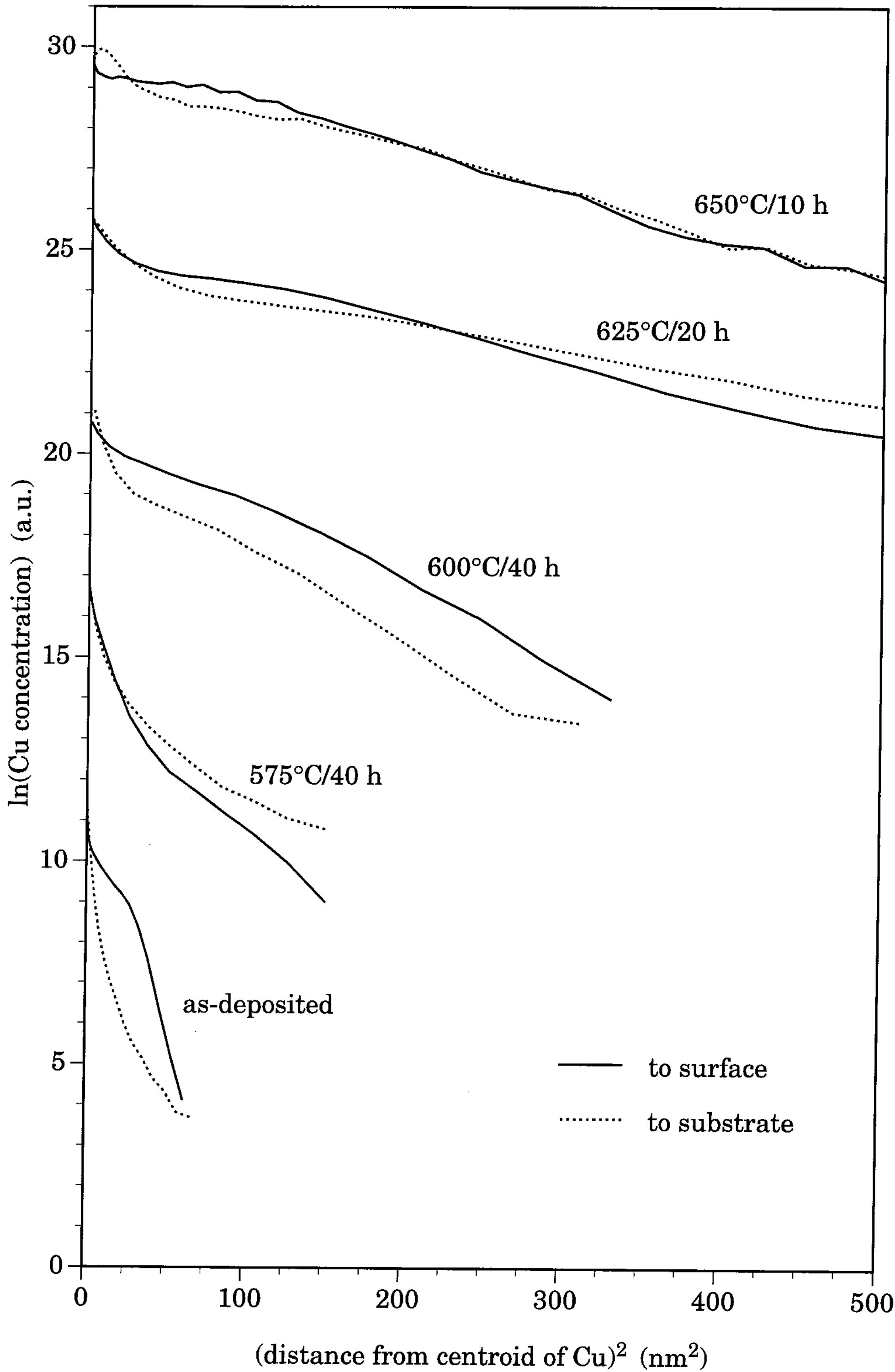

Figure 5.15. Logarithm of the raw copper signal vs. the square of the distance from the centroid (x_o = 50 nm) of the Cu ($(x-x_o)^2$). The solid line denotes the profile from the Cu centroid to the surface ($x < x_o$). The dashed line represents the profile from the Cu centroid to the substrate ($x > x_o$).

Table 5.5. Diffusion coefficients of Cu in $Ta_{36}Si_{14}N_{50}$ films. The respective $(4Dt)_{as\text{-}deposited}$ values for $x < x_o$ and $x > x_o$ are 6.69×10^{-14} and 1.59×10^{-13} cm^2. $D_{average}$ is the average of the two $D_{corrected}$ values for a given process.

Temperature (°C)	Time (s)	$D_{corrected}$ $x < x_o$ (cm^2/s^2)	$D_{corrected}$ $x > x_o$ (cm^2/s)	$D_{average}$ (cm^2/s)
650	3600	2.4×10^{-17}	1.2×10^{-17}	1.8×10^{-17}
650	18000	8.4×10^{-18}	7.4×10^{-18}	7.9×10^{-18}
650	36000	5.8×10^{-18}	5.5×10^{-18}	5.7×10^{-18}
	average:	1.3×10^{-17}	8.3×10^{-18}	1.1×10^{-17}
625	18000	4.3×10^{-18}	7.1×10^{-18}	5.7×10^{-18}
625	36000	5.1×10^{-18}	6.9×10^{-18}	6.0×10^{-18}
625	72000	3.7×10^{-18}	5.3×10^{-18}	4.0×10^{-18}
625	144000	1.4×10^{-17}	1.8×10^{-17}	1.6×10^{-17}
625	288000	8.9×10^{-18}	1.4×10^{-17}	1.1×10^{-17}
	average:	7.2×10^{-18}	1.0×10^{-17}	8.6×10^{-18}
600	36000	1.3×10^{-18}	6.3×10^{-19}	6.8×10^{-19}
600	72000	1.2×10^{-18}	5.8×10^{-19}	8.9×10^{-19}
600	14400	7.9×10^{-18}	4.8×10^{-18}	6.3×10^{-18}
	average:	3.5×10^{-18}	2.0×10^{-18}	2.7×10^{-18}
575	72000	2.3×10^{-19}	1.6×10^{-18}	6.1×10^{-19}
575	144000	4.0×10^{-19}	1.1×10^{-18}	5.3×10^{-18}
575	288000	2.9×10^{-19}	1.2×10^{-18}	3.8×10^{-18}
	average:	3.3×10^{-19}	1.1×10^{-18}	7.3×10^{-19}
550	72000	1.6×10^{-19}	2.7×10^{-19}	2.1×10^{-19}

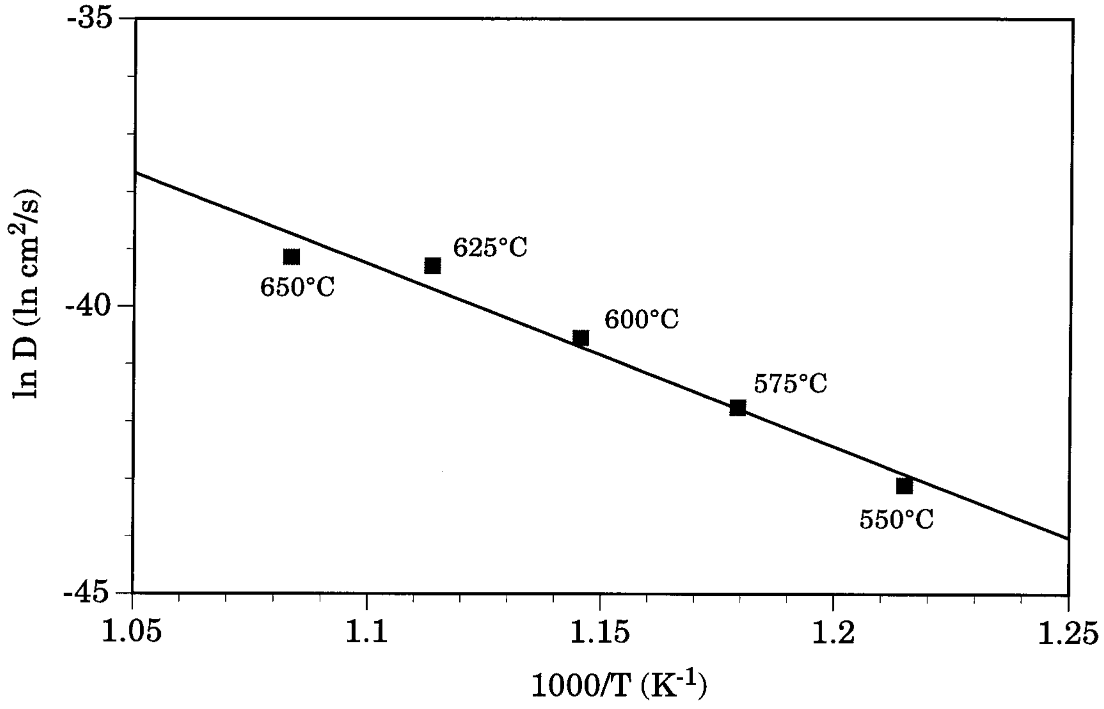

Figure 5.16. Arrhenius plot of Cu diffusion in amorphous $Ta_{36}Si_{14}N_{50}$ films.

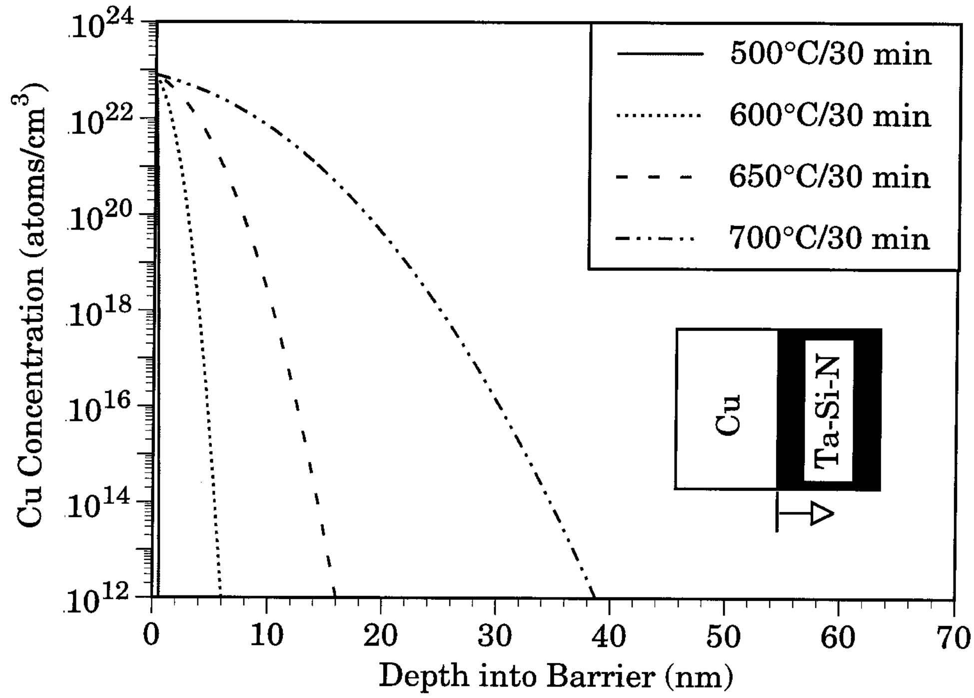

Figure 5.17. Constant source Cu diffusion into a semi-infinite $Ta_{36}Si_{14}N_{50}$ layer at various temperatures for 30 min assuming E_a = 2.74 eV and D_o = 0.014 cm^2/s.

Table 5.6. Diffusion in selected amorphous electronic films. When diffusion data at 500°C was unavailable, linear extrapolations were made.

Material	Diffusing Species	Temperature Range (°C)	E_a (eV)	D_o (cm^2/s)	D at 500°C (cm^2/s)	ref.
SiN:H (CVD)	Cu	300-450	1.1	4×10^{-6}	3×10^{-13}	[3]
4% PSG (CVD)	Cu	200-500	0.5	6×10^{-11}	3×10^{-14}	[3]
1% PSG (CVD)	Cu	500-800	1.6	...	...	[2]
SiO_2 (thermal)	Cu	500-800	1.2	...	...	[2]
polyimide (spin-on)	Cu	...	...	...	1×10^{-14}	[11]
$W_{80}N_{20}$ (spttrd)	Au	460-500	2.0	6×10^{-5}	6×10^{-18}	[71]
Si_3N_4 (CVD)	Ni	830-1220	2.1	2×10^{-6}	4×10^{-20}	[72]
SiO_2 (CVD)	Ni	830-1220	1.6	2×10^{-9}	7×10^{-20}	[72]
SiO_2 (thermal)	Ni	830-1220	1.6	7×10^{-10}	3×10^{-20}	[72]
$Ta_{36}Si_{14}N_{50}$	Cu	550-650	2.7	1×10^{-2}	3×10^{-20}	(here)

5.6. Bias-Thermal-Stress Testing of Ta-Si-N/Cu on MOS Capacitors

Copper diffusion in silicon dioxide is believed to be largely interstitial [10,76]. Substitutional diffusion of Cu into Si or O sites is unlikely in part because of differences in ionic charges [76]. Within the local channels of SiO_2, Cu has a tendency to form cations. The probability of the ionization has been estimated by McBrayer et al. through mass-action arguments [7]. The ionization can be enhanced by impurities in the oxide such as O_2 or H_2O, which can create deep level acceptors. By capturing electrons that may otherwise recombine with the Cu cation, the acceptors increase the relative ion concentration. While possessing a positive charge, Cu can be very mobile in SiO_2 under an electric field [7-10]. Consequently, diffusion barriers are necessary to prevent the penetration of copper into the oxide. This section discusses the ability of very thin $Ta_{36}Si_{14}N_{50}$ films to block Cu drift through SiO_2 at 300°C.

Processing for the capacitors was done almost entirely at the National Nanofabrication Facility at Cornell University. Starting material for the experiments was 5-10 Ω cm, boron-doped (100)-Si cleaned using the standard "RCA" method [77]. The wafers were thermally oxidized at 1100°C in an O_2/trichloroethane ambient, followed by a 10-min densification treatment in N_2 at the same temperature. The oxide thickness was approximately 45 nm, according to ellipsometry measurements. Photoresist to delineate 0.8-mm-diameter contact areas for lift-off was then applied. After developing the resist, the wafers were briefly exposed to an O_2 plasma etch to remove organic residues. The wafers were then sent to Caltech for deposition. Just prior to loading into the sputtering system, the wafers were dipped for 5 sec in 50:1 HF, rinsed in deionized water, and blown dry with N_2. After pump-down, a 10-nm-thick $Ta_{36}Si_{14}N_{50}$ barrier layer was deposited. Without breaking vacuum, subsequent 200 nm Cu and 60 nm $Ta_{36}Si_{14}N_{50}$ layers were added. The top Ta-Si-N layer served as a cap to prevent oxidation of the Cu during the bias-thermal-stress experiments. After deposition, the wafers were returned to Cornell. Following lift-off in acetone and a rinse in methanol and isopropanol, Al was evaporated on the backside

of the wafers, and sintered at 450°C for 30 min in forming gas (10% H_2, 90% N_2). Room-temperature C-V characteristics at 100 kHz were then recorded after 300°C biasing at -1, 0, and +1 MV/cm (-5, 0, +5 V applied bias) for 0, 20, 40, and 80 h. The biasing at 300°C was performed in air.

Figure 5.18a shows the C-V curves before and after a 20-h bias-thermal-stress treatment. The curves are typical of a p-type MOS capacitor at high frequencies, i.e., frequencies with a period shorter than the minority carrier lifetimes. As the applied voltage measured with respect to the top $Ta_{36}Si_{14}N_{50}$ contact is increased, the capacitor shifts through accumulation, depletion, and inversion modes of operation. Using Kingston and Neustadter relations for an ideal MOS capacitor [78,79], the flat band capacitance should occur at approximately six tenths of the accumulation capacitance, C_{ox} = 400 pF. The equivalent flat band voltage is thus approximately - 1 V [80]. After 20 h of bias-thermal-stress testing, there is no change in the C-V curves for the unbiased sample, however samples biased at ± 1 MV/cm do show a negative shift in the flat-band voltage. In general, the redistribution and creation of charge within the oxide and the <Si>/SiO_2 interface is responsible for the bias-induced flat band shifts. By Gauss' law, a movement of sodium cations induced by the electric field will cause negative shifts in the flat-band voltage for a positive bias, and positive shifts for a negative bias. Slow trapping effects in the interfacial SiO_x region induced from a negative applied bias will decrease the flat band voltage [81]. Biasing can also dislodge hydrogen which previously passivated dangling bonds, thus creating charged states. Since the biasing was done in air, oxygen or water may be incorporated to create acceptor levels in the oxide. Additionally, hot electrons may become lodged in the oxide to bring further changes in the charge distribution. Lengthy reviews of flat-band shifts can be found in a book by Nicollian and Brews [82].

The reduction of the capacitance seen in the accumulation mode (at negative biases) is caused by anodic oxidation of the copper on the periphery of the capacitor, which reduces the capacitor's area. The effect escapes detection in the inversion

mode (positive biases) because of the limited resolution of the meter at low capacitances. In the transition from depletion to inversion, the C-V curves for the biased samples display a plateau before dropping to full inversion. The behavior is consistent with the generation of slow interfacial traps which cannot charge or discharge fast enough to satisfy steady-state during the sweeps of the gate voltage (0.05 V/s) [83]. Increasing the frequency to over 1 MHz, increasing the temperature of the sweeps, or increasing the sweep rate of the applied bias will mask the effect.

If Cu diffuses into the oxide and silicon during the bias-thermal-stress treatment, it is most likely to occur during application of the positive bias. Although the slope of the +1 MV/cm curve does decrease in depletion with respect to the as-deposited sample, the change appears to be associated with the creation of additional interfacial states rather than the presence of Cu. Once in the Si, copper introduces generation/recombination centers, thus increasing the inversion capacitance (examples in [7-9]). Figure 5.18a shows no such increase.

Figure 5.18b shows the C-V curves after 40 h of bias-thermal-stress treatment. The negative and zero bias produces virtually no change in behavior compared with the 20-h treatment. Applying the positive bias produces an additional drop in the accumulation capacitance, flat band voltage, and depletion C-V slope. Most importantly, there is no change in the inversion capacitance.

Eighty hours of bias-thermal-stress treatment yields very similar trends. The C-V characteristics of negatively-biased and unbiased samples are unchanged with respect to the 20 and 40 h treatments (Figure 5.18c). In the positively biased sample, further anodic oxidation occurs and along with the creation of more interfacial trap states. The traps give greater negative shifts in the flat band voltage and reduce the slope of the C-V curve in the depletion region. However, the inversion capacitance does not change, thus indicating that Cu has not compromised the barrier. Reversing the bias to -1 MV/cm after the 80 h treatment at +1 MV/cm does yield some recovery in the C-V characteristics. Not only does the flat band shift positively,

which indicates that sodium is driven back toward the oxide/barrier interface, but depletion slope increases as well. Evidently, the sodium pile-up at the <Si>/oxide interface during positive bias also affects the interface states.

In sum, 10-nm-thick amorphous $Ta_{36}Si_{14}N_{50}$ films provide excellent protection against copper drift through silicon dioxide. Given that very little potential is dropped across the barrier on the MOS capacitors, the result is not surprising when considering the low thermal diffusivity of Cu through $Ta_{36}Si_{14}N_{50}$. Nonetheless, the bias-thermal-stress tests reaffirms the stability of the films in ambients other than vacuum and represents a practical evaluation. Stability at 300°C for 80 h may predict reliability for many years at typical device operation temperatures of less than 100°C.

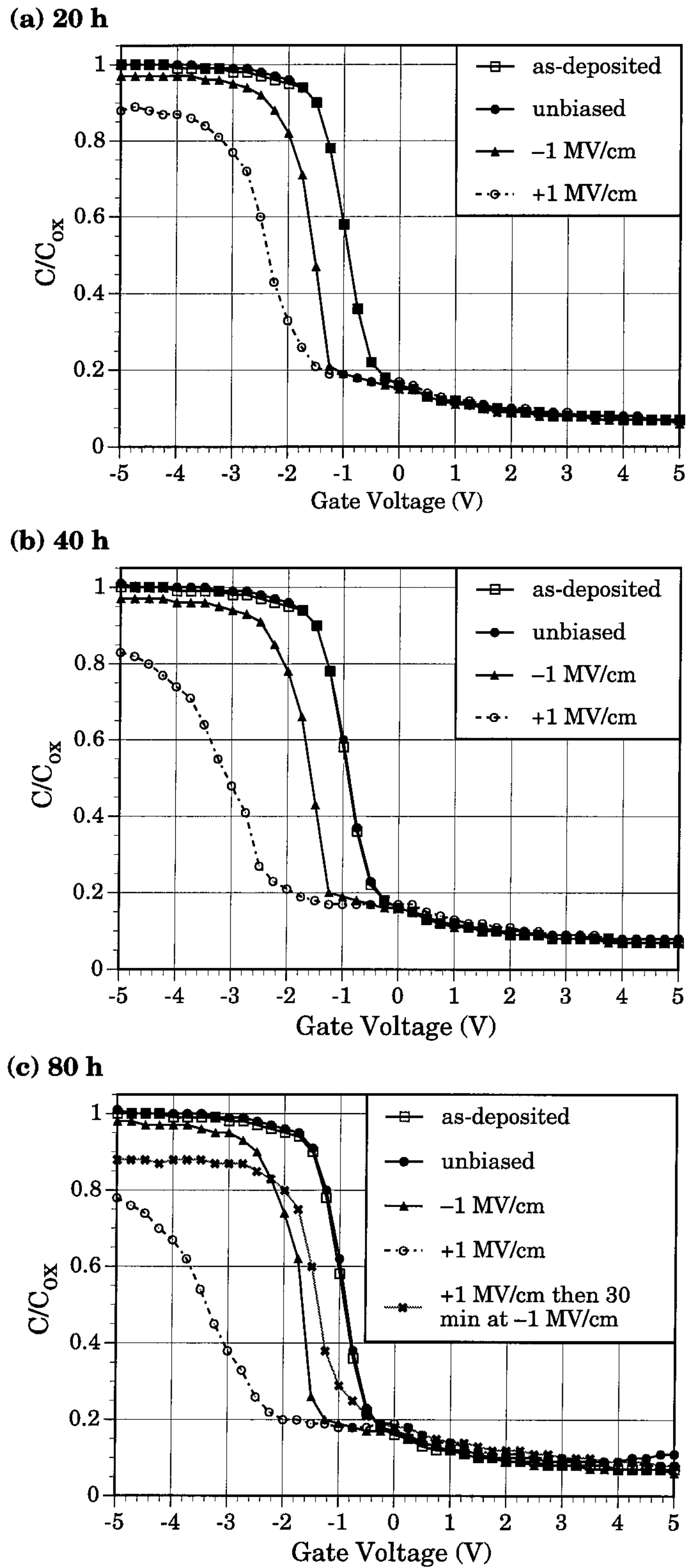

Figure 5.18. Normalized 100 kHz C-V curves after (a) 20 h, (b) 40 h, and (c) 80 h of bias-thermal-stress treatment. The oxide capacitance is C_{ox} = 400 pF.

5.7. Barrier/Cu Contact Resistance

In measuring the specific contact resistance between two metals, device manufacturers often implement a “Kelvin” structure [84]. In its simplest form, the structure consists of a via which electrically connects two planes of metal. A probe to source or sink the current contacts each plane. Two additional probes are used to measure the voltage, V, across the planes. Usually, the voltmeter probes are placed on areas that accurately represent the potential at the via. From Ohm’s law, the resistance of the via is $R_{via} = V/I$. By knowing the resistivity and spatial dimensions of the via material, the contribution of the total interfacial resistance of the via with the planar metals may be extracted. Assuming the interfaces to be identical, the specific contact resistance is then (1/2)(total interfacial resistance)(area of via). In the cases where the contact resistance is very low, numerous vias may be chained together to increase the summed potentials up to measurable levels [85-87].

Although Kelvin structures are conceptually simple and do mimic the environment within an integrated circuit, they are difficult to implement. Fabrication usually requires exposing the sample to air after deposition of each metal. Consequently, *in situ* surface cleaning is required to remove native oxides from the metals if very low resistances are involved. In many deposition systems, such as the one used for the barrier work in this thesis, *in situ* cleans are not possible.

A four-point probe method developed by Vu et al. for planar multilayers offers an attractive alternative to Kelvin structures [88]. Figure 5.19 demonstrates the geometry of the technique. Current and voltage probes are in contact with planar layers of metal which may be deposited without breaking vacuum. Assuming the probes to be colinear and equidistant, the potential between the inner probes is

$$V = \frac{I\ln 2}{\pi}\rho_o + \frac{I}{\pi}\frac{\rho_o\rho_{s1}}{\rho_{s2}}\left(K_o\left(\frac{s}{a}\right) - K_o\left(\frac{2s}{a}\right)\right) \qquad (1)$$

where,

$$\rho_o = (1/\rho_{s1} + 1/\rho_{s2})^{-1}$$

and

$$a = \left(\frac{\rho_c}{\rho_{s1} + \rho_{s2}}\right)^{\frac{1}{2}} .$$

Here, ρ_{s1} and ρ_{s2} are the sheet resistances of each layer (units of Ω/square), ρ_c is the contact resistivity between the two layers (units of Ω cm^2), s is the probe separation, and I is the current. K_0 is the zeroth order Bessel function of the second kind. The first term in (1) is the potential given by the two layers in parallel without any contact resistance. It has no dependence on the probe separation, s. The second term, which depends on s, is the contribution of contact resistance to the potential. As s increases, the second term monotonically decreases to zero. Consequently, to measure the lowest possible contact resistances, s should be minimized. In deriving Eqn. (1), a two-dimensional, thin-layer approximation is made. That is to say, the vertical potential gradient is neglected within a given layer. For a single homogenous layer, the approximation is excellent if the probe separation is at least twice the layer thickness [84].

In applying the four-point probe approach to measure barrier/Cu contact resistances, it is advantageous to interpose the high-resistivity barrier film between two copper films. In doing so, the contact resistivity term in (1) makes the largest achievable contribution to the measured potential. The two interfaces along with the barrier film then constitute a single effective contact resistance in the model. To measure the lowest possible contact resistance, the Cu sheet resistivities should be made as small as possible and satisfy $\rho_{s1} \approx 2\rho_{s2}$.

To date, the four-point probe method has been applied only once. By placing mechanical probes at spacings of 250, 600, and 1240 μm, Vu et al. extracted a specific contact resistance of 6×10^{-5} Ω cm^2 for the RuO_2/Al interface [88]. The rather high value has been attributed to a thin interfacial layer of Al_2O_3 [89,90]. For most VLSI

applications, a contact resistance of mid-10^{-9} Ω cm^2 or lower is necessary. Consequently, mechanically-placed probes will be difficult to implement in measuring very low contact resistances because large *s* makes the second term of Eqn. (1) immeasurably small. Lithographically-defined probes and interconnects afford the necessary micron-range separations.

For the barrier/Cu contact resistances study, trilayer stacks of Cu (900 nm)/barrier (40-50 nm)/Cu (420 nm) were sputter-deposited onto oxidized silicon substrates covered with a 100 nm layer of CVD Si_3N_4. All depositions were performed in a planetary mode of operation without vacuum breaks for a given stack. Copper was deposited with 450 W at 5 mTorr, with a -50 V dc substrate bias. The barrier films were $Mo_{74}Si_{26}$, $Mo_{35}Si_{17}N_{48}$, and biased-TiN, and $W_{37}Si_{15}N_{48}$ under conditions previously described in this thesis. W barriers were also evaluated. They were deposited with 300 W, 10 mTorr, and -50 V dc substrate bias. Following deposition at Caltech, the wafers were sent to the National Nanofabrication Facility at Cornell University for subsequent processing. A complete process flow can be found in Appendix II, but the major steps are as follows. First, a 20-nm TiW layer was sputter deposited onto the trilayer stack to act as a glue layer. Next, a 500-nm plasma-enhanced CVD SiO_2 layer was added. Vias were then etched though the oxide to the underlying TiW. Blanket sputter depositions of TiW (20 nm)/Al (500 nm) followed. The TiW/Al layer was then etched to define the interconnects, vias, and contact pads. Colinear sets of probes had center-to-center probe separations of s = 7.5, 9.7, 13.0, 21.5, 52.0, and 204.0 μm with respective via widths of 0.5, 0.7, 1, 1.5, and 4 μm.

Because of the tight geometries involved, the currents must be kept low (< 10 mA through the 0.5 μm via) to avoid damaging the samples. The resulting voltage between the inner probes is then on the order of microvolts, which does not readily lend itself to dc measurement techniques. As a remedy, a 1000 Hz phase-lock detection scheme was utilized (Figure 5.20). To extract the contact resistances from a trilayer stack, a measurement was taken for each set of probe spacings. The data

were then fit with Eqn. (1) using standard least-squares methods. Two parameters were allowed to float in the fit: the specific contact resistivity, ρ_c, and the copper resistivity, ρ_{Cu}. The copper resistivity was included in Eqn. (1) by substituting ρ_{Cu}/t_i for ρ_{si}, where t_i is the thickness of copper layer i. Additionally, $2\rho_c$ replaced ρ_c in (1) to account for the two separate barrier/Cu interfaces in the trilayer stack.

Figure 5.21 shows the measured V/I data and least-squares fits. For probe spacing between s = 13 and 204 μm, the measured data are relatively flat for all of the systems. In this wide-probe regime, the measured potential is from the parallel sheet resistances of the copper layers. However, as the probe separation is decreased to 9.7 and 7.5 μm, V/I increases through contact resistance contributions. Curve fitting yields contact resistivities typically in the low-to-mid 10^{-9} Ω cm^2 range with a copper resistivity of approximately 2.1×10^{-6} Ω cm. The actual copper resistivity, measured with a standard four-point probe on a blanket copper film is about 2.0 μm cm. Table 5.7 summarizes the results. Considering experimental uncertainty, the relative differences among the various barriers are probably not meaningful. Additional data points on the ascending portion of the curve fits are necessary to further quantify the data.

The lack of dissimilarities in the fitted data for the various systems may be a consequence of interfacial impurities absorbed from the deposition process. As noted in Chapter 2, the background pressure of water with the pump throttled for deposition is around 2×10^{-7} Torr. In other words, a few monolayers of water vapor bombard the samples every 10 seconds. Given that the samples reside in this vacuum for 5 to 25 min to allow for presputtering between depositions of each layer, there is ample time to grow a thin surface oxide. The effect is easily observed through reflection-mode ("θ-2θ") small-angle X-ray scattering. Figure 5.22 shows a scan taken from $Ta_{36}Si_{14}N_{50}$ films made by planetary deposition. The sample was swept under a shutter opening beneath the sputter target every 20 seconds. With every sweep, approximately 3 nm of material was deposited. The small-angle X-ray scan clearly shows periodicities associated with the cycling of substrates beneath the target.

Rough simulations of the X-ray spectrum indicate that the oxide thickness grown with each pass is a few Angstroms.

The sensitivity of the four-point structures can be enhanced by decreasing the Cu sheet resistivities or decreasing the probe separation. Attempts to lower the Cu sheet resistivities by doubling the Cu thickness resulted in a ten-fold increase in contact resistivities from an observed lack of adhesion in the samples. The behavior reaffirms the importance of good adhesion when measuring contact resistivities. At this writing, a second approach of reducing the probe spacings has been partially implemented. Structures containing probe separations as small as 3 μm have been constructed, but no measurements have been performed. Instead of patterning a four-point probe arrangement on top of the trilayer stack, the probes are patterned though 500 nm SiO_2 layers on the surface of the wafer. Al interconnects run underneath the oxide to provide a conduction path. Appendix III gives a complete process flow. The new "upside-down" four-point probe structures were fabricated at Sandia National Laboratories, Albuquerque.

Comparatively, the specific contact resistivities measured here are less than Lakshminarayanan et al.'s values of $1.5 \times 10^{-8}\ \Omega\ cm^2$ obtained with Cu/Ti/Cu four-terminal Kelvin structures [91]. The larger values obtained with the Kelvin structure may be in part due to current crowding effects [92,93] as well as different processing conditions and a different barrier layer. With the large geometry associated with the four-point probe technique, current crowding effects are small. Thus, although Kelvin structures yield very practical values for device applications, the four-point probe scheme may more accurately reflect the true specific contact resistance of an interface.

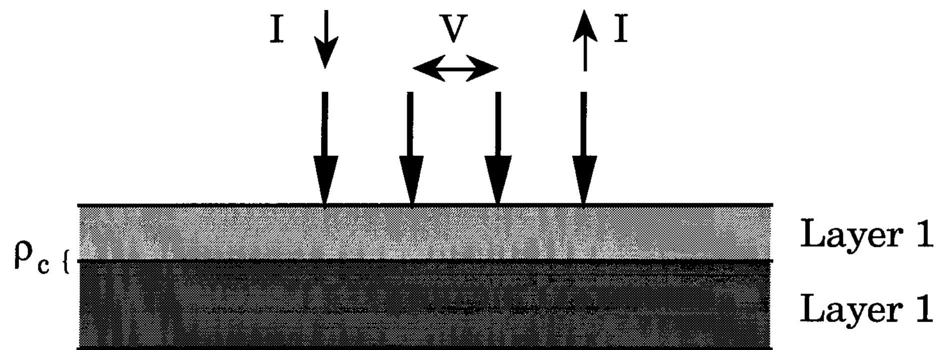

Figure 5.19. Schematics of the four-point probe method for obtaining contact resistivities.

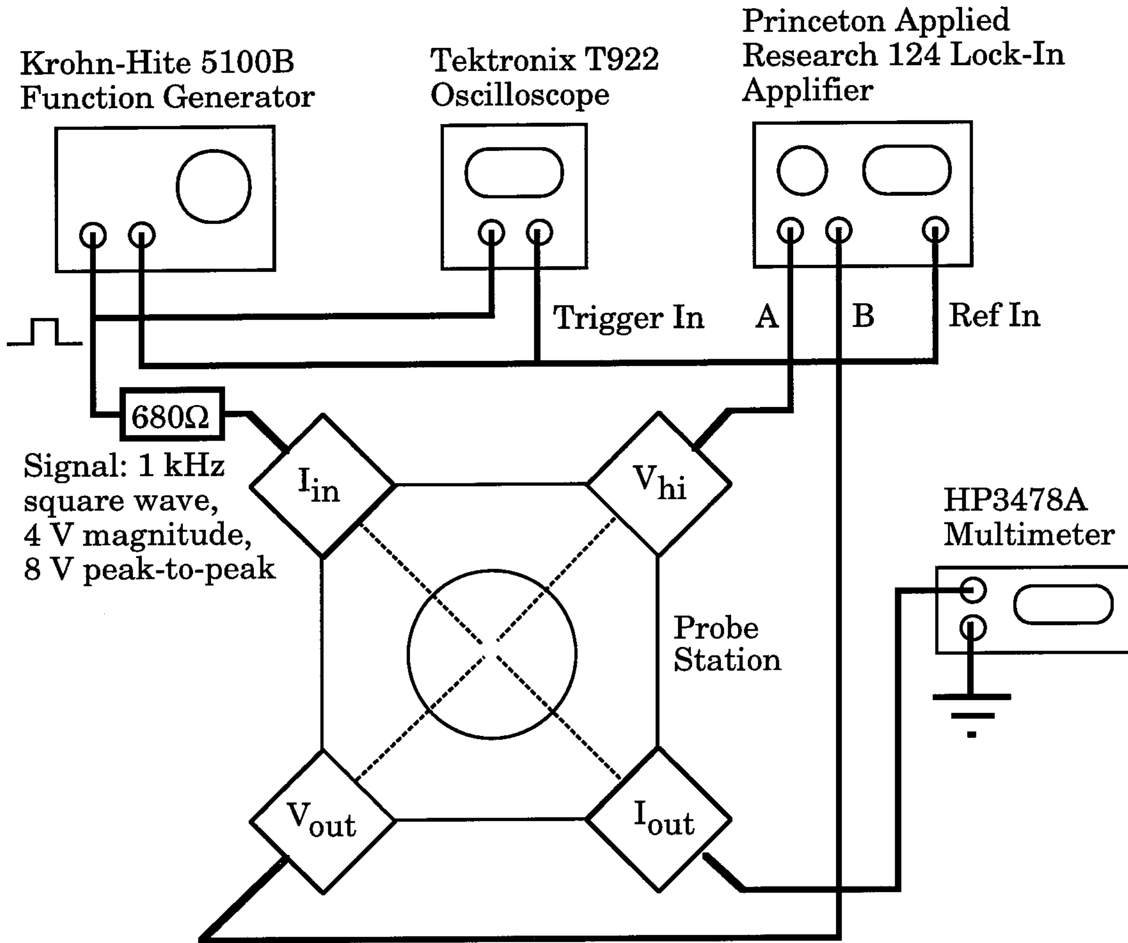

Figure 5.20. Apparatus to measure contact resistivities.

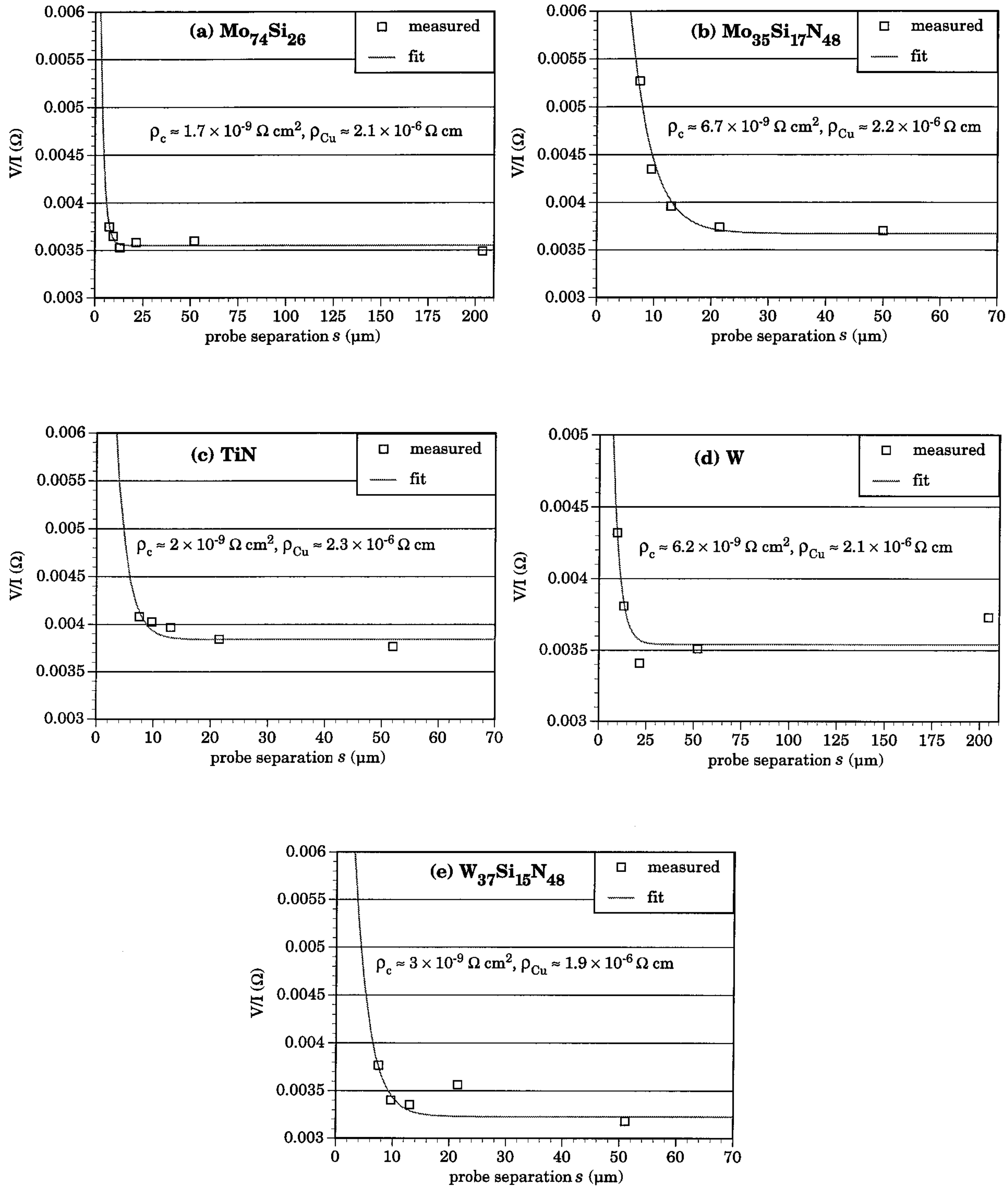

Figure 5.21. Measured V/I values vs. probe separation s, along with fits of Equation (1) for various diffusion barriers. (a) a-$Mo_{74}Si_{26}$, (b) a-$Mo_{35}Si_{17}N_{48}$, (c) polycrystalline, biased-TiN, (d) polycrystalline α-W, and (e) a-$W_{37}Si_{15}N_{48}$. Uncertainty in each data point is ± 8%. Note the suppressed zeros of the ordinates.

Table 5.7. Summary of curve fitting of contact resistivity data. The two fitted parameters were the copper resistivity, ρ_{Cu}, and the effective specific contact resistivity (barrier/Cu interfacial resistivity + transverse resistance across the barrier), ρ_c. For comparative purposes, the contribution of the contact resistance from the transverse resistance across the barrier is also listed.

barrier	ρ_{Cu} (10^{-6} Ω cm)	ρ_c (10^{-9} Ω cm^2)	$(\rho_c)_{transverse}$ (10^{-9} Ω cm^2)
a-$Mo_{74}Si_{26}$	2.1	1.7	~1
a-$Mo_{35}Si_{17}N_{48}$	2.2	6.7	~3
TiN	2.3	2.0	~0.2
W	2.1	6.1	~0.005
a-$W_{37}Si_{15}N_{48}$	3.0	2.9	~3

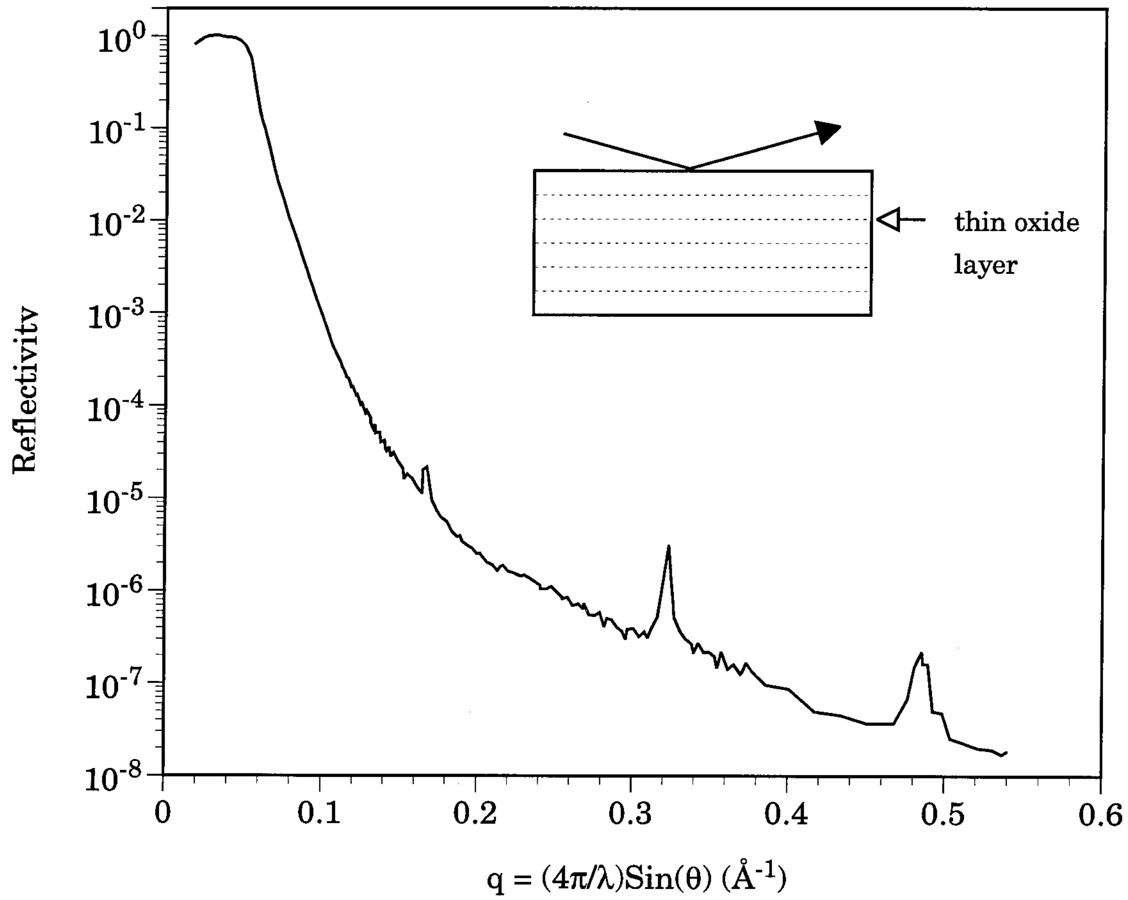

Figure 5.22. Small-angle X-ray reflectivity pattern of a $Ta_{36}Si_{14}N_{50}$ deposited in a planetary mode.

References, Chapter 5.

[1] A. Mesli, T. Heiser, and E. Mulheim, *Materials Sci. and Eng.* B25, 141 (1994).

[2] H. Miyazaki, H. Kojima, A. Hiraiwa, Y. Homma, and K. Murakami, *J. Electrochem. Soc.* 139, 3264 (1992).

[3] D. Gupta, K. Vieregge, and K.V. Srikrishnan, *Appl. Phys. Lett.* 61, 2178 (1992).

[4] B. Arcot, Y.T. Shy, S.P. Murarka, and W.A. Lanford, *Materials Research Soc. Symp. Proc.* 203, edited by E.D. Lillie, P. Ho, F.J. Jaccodine, and K. Jackson, Materials Research Society, Pittsburgh, PA (1991) pp. 27-32.

[5] P.J. Ding, W.A. Lanford, S. Hymes, and S.P. Murarka, *Appl. Phys. Lett.* 64, 2897 (1994).

[6] P.J. Ding, W.A. Lanford, S. Hymes, and S.P. Murarka, *J. Appl. Phys.* 75, 3627 (1994).

[7] J.D. McBrayer, R.M. Swanson, and T.W. Sigmon, *J. Electrochem. Soc.* 133, 1242 (1986).

[8] Y. Shacham-Diamond, A. Dedhia, D. Hoffstetter, and W.G. Oldham, *J. Electrochem. Soc.* 140, 2427 (1993).

[9] J.Li, Y. Shacham-Diamand, and J.W. Mayer, *Materials Science Reports* 9, 1 (1992).

[10] T. Dunn, G. Hetherington, and K.H. Jack, *Physics and Chemistry of Glasses* 6, 16 (1965).

[11] F. Faupel, D. Gupta, B.D. Silverman, and P.S. Ho, *Appl. Phys. Lett.* 55, 357 (1989).

[12] A.G. Milnes, *Deep Impurities in Semiconductors*, Wiley, New York (1970).

[13] L.A. Clevenger, N.A. Bojarczuk, K. Holloway, J.M.M. Harper, C. Cabral, R. G. Schad, F. Cardone, and L. Stolt, *J. Appl. Phys.* 73, 300 (1993).

[14] K. Holloway, P.M. Fryer, C. Cabral, J.M.E. Harper, P.J. Bailey, and K.H. Kelleher, *J. Appl. Phys.* 71, 5433 (1992).

[15] E. Kolawa, J.S. Chen, J.S. Reid, P.J. Pokela, and M-A. Nicolet, *J. Appl. Phys.* 70, 1369 (1991).

[16] C.-K. Hu, S. Chang, M.B. Small, and J.E. Lewis, in *Proceedings of the VLSI*

Multilevel Interconnection Conference, IEEE Electron Devices Society, New York (1986) p. 181.

[17] C-A. Chang, *J. Vac. Sci. Technol. A* 8, 3796 (1990).

[18] L.C. Lane, T.C. Nason, G.-R. Yang, T.-M. Liu, and H. Bakhru, *J. Appl. Phys.* 69, 6719 (1991).

[19] N. Mattoso, C. Achete, and F.L. Freire, Jr., *Thin Solid Films* 220, 184 (1992).

[20] S.-Q. Wang, S. Suthar, C. Hoeflich, and B.J. Burrow, *J. Appl. Phys.* 73, 2301 (1993).

[21] J.S.H. Cho, H-K. Kang, C. Ryu, and S.S. Wong, *IEEE IEDM Technical Digest* 265 (1993).

[22] S.-Q. Wang, I. Raaijmakers, B.J. Burrow, S. Suthar, S. Redkar, and K.-B. Kim, *J. Appl. Phys.* 68, 5176 (1990)

[23] T.S. Chang, W.C. Wang, L.P. Wang, J.C. Hwang, and F.S. Huang, *J. Appl. Phys.* 75, 7847 (1994).

[24] J.O. Olowolafe, J.A. Li, J.W. Mayer, and E.G. Colgan, *Appl. Phys. Lett.* 58, 469 (1991).

[25] P.J. Pokela, C.K. Kwok, E. Kolawa, S. Raud, and M-A. Nicolet, *Appl. Surf. Sci.* 53, 364 (1991).

[26] S.-Q. Wang, *MRS Bulletin* 19, 30 (1994).

[27] R. de Reus, in *Intermetallic Compounds–Principles and Practice*, edited by J.H. Westbrook and R.L. Fleischer, John Wiley and Sons, Chicester, England (1993).

[28] F. de Reus, R.J.I.M. Koper, H. Zeijlemaker, and F.W. Saris, *Materials Lett.* 9, 500 (1990).

[29] H. Yang, C.M. Gilmore, and D.E. Ramaker, *J. Vac. Sci. Technol. A* 11, 1454 (1993).

[30] R.E. Thomas, K.-J. Guo, D.B. Aaron, E.A. Dobisz, J.H. Perepezko, and J.D. Wiley, *Thin Solid Films* 150, 245 (1987).

[31] I. Suni, M-A. Nicolet, C.S. Pai, and S.S. Lau, *Thin Solid Films* 107, 73 (1983).

[32] Private communication with M.S. Angyal, Cornell University. MoCo (1000

nm)/Cu (300 nm) metallizations fail according to RBS measurements after 500°C/30 min.

[33] C.S. Choi, G.A. Ruggles, A.S. Shah, G.C. Xing, C.M. Osburn, and J.D. Hunn *J. Electrochem. Soc.* 138, 3062 (1991).

[34] E. Kolawa, L.E. Halperin, P.J. Pokela, Q.T. Vu, C.W. Nieh, and M-A. Nicolet, in *Materials Research Society Symp. Proc.* 181, edited by A. Katz, S.P. Murarka, and A. Appelbaum, Materials Research Society, Pittsburgh, PA (1990) pp. 33-38.

[35] E. Kolawa, X. Sun, J.S. Reid, M-A. Nicolet, and R.P. Ruiz, *Thin Solid Films* 236, 301 (1993).

[36] T.B. Massalski, *Binary Alloy Phase Diagrams. 2 ed.*, ASM International, Materials Park, OH (1990).

[37] P. Villars and L.D. Calvert, *Pearson's Handbook of Crystallographic Data for Intermetallic Phases*, America Society for Metals, Metals Park, OH (1985).

[38] U. Zachwieja and H. Jacobs, *Eur. J. Solid State Inorg. Chem.* 28, 1055 (1991).

[39] J.S. Reid, presented at the MRS Spring Meeting, 1991 (unpublished).

[40] S. Dallaire and J.-G. Legoux, *Materials Sci. and Eng.* A183, 139 (1994).

[41] P. Rogl and J.C. Schuster (eds.), *Phase Diagrams of Ternary Boron Nitride and Silicon Systems*, ASM International, Materials Park, OH (1992).

[42] R. Zankl and R. Malter, *Z. Metallkunde* 72, 720 (1981).

[43] E. Ganglberger, Ph.D. Dissertation, University of Vienna (1966).

[44] Y.V. Efimov, T.M. Frolova, O.I. Bodak, and O.I. Kharchenko, *Inorganic Materials* 20, 1374 (1985).

[45] E. Gangleberger, *Monatshefte für Chemie* 99, 549 (1968).

[46] G. Jangg, R. Kieffer, and H. Kögler, *Z. Metallkunde* 59, 546 (1968).

[47] TAPP Software for Macintosh, version 2.1, ES Microware, Hamilton, OH 1994.

[48] I. Barin, *Thermochemical Data of Pure Substances*, VCH Verlagsgesellschaft mbH, D-6940 Weinheim, Germany (1989).

[49] I. Barin and O. Knacke, *Metall. Trans.* 5, 1769 (1974).

[50] M.E. Schlesinger, *Chem. Rev.* 90, 607 (1990).

[51] T.G. Chart, *National Physical Laboratory, Report DSC 18* (1972).

[52] T.G. Chart, *High Temp.-High. Press.* 5, 241 (1973).

[53] D. Lüdecke, *CALPHAD* 11, 135 (1987).

[54] H.L. Lukas, E. Th. Henig, and B. Zimmerman, *CALPHAD* 1, 225 (1975).

[55] A.R. Miedema, R. Boom, and F.R. De Boer, *J. Less-Common Metals* 41, 283 (1975).

[56] A.R. Miedema, *J. Less-Common Metals* 46, 67 (1976).

[57] L. Kaufman, *CALPHAD* 3, 45 (1979).

[58] S.V. Meschel and O.J. Kleppa, *Metall. Trans. A* 22A, 2162 (1991).

[59] L. Brewer and O. Krikorian, *J. Electrochem. Soc.* 103, 38 (1956).

[60] Joint Committee on Powder Diffraction Standards (JCPDS), *Standard Powder Diffraction File*, International Center for Powder Diffraction, Swathmore, PA (1991).

[61] J.K. Solberg, *Acta Crystallogr. A* 34,684 (1978).

[62] R.W. Olesinski and G.J. Abbaschian, *Bulletin of Alloy Phase Diagrams* 7, 170 (1986).

[63] J.O. Olowolafe, J. Li, and J.W. Mayer, *J. Appl. Phys.* 68, 6207 (1990).

[64] R.E. Thomas, J.H. Perepezko, and J.D. Wiley, *Appl. Surf. Sci.* 26, 534 (1986).

[65] H. Sprenger, *J. Less-Common Metals* 34, 39 (1974).

[66] A.H. Carim, *J. Am. Ceram. Soc.* 73, 2764 (1990).

[67] E. Kooi and J.A. Appels, in *Semiconductor Silicon 1973*, edited by H.R. Huff and R. Burgess, The Electrochemical Symp. Series, Princeton, NJ (1973) p. 860.

[68] S. Wolf, *Silicon Processing for the VLSI Era, Vol. 2*, Lattice Press, Sunset Beach, CA (1990) pp. 17-45.

[69] J.M.E. Harper, E.G. Colgan, C-K. Hu, J. P. Hummel, L.P. Buchwalter, and C.E. Uzoh, *MRS Bulletin* 19, 23 (1994).

[70] J.R. Davis, Jr., A. Rohatgi, R.H. Hopkins, P.D. Blais, P. Rai-Choudhury, J.R. McCormick, and H.C. Mollenkopf, *IEEE Trans. Electron. Dev.* ED-27, 677 (1980).

[71] W. Dorner, H. Mehrer, P.J. Pokela, and M-A. Nicolet, *Materials Sci. and Eng.*

B 10, 165 (1991).

[72] R.N. Ghostagore, *J. Appl. Phys.* 40, 4374 (1969).

[73] F.H.P.M. Habraken and A.E.T. Kuiper, *Materials Sci. and Eng.* R12(3), 123 (1994).

[74] J.W. Osenbach and S.S. Voris, *J. Appl. Phys.* 63, 4494 (1988).

[75] T.E. Burgess, J.C. Baum, F.M. Fowkes, and R. Holstrom, and G.A. Shirn, *J. Electrochem. Soc.* 116, 1005 (1969).

[76] B. Mason and L.G. Berry, *Elements of Mineralogy,* W.H. Freeman and Company, San Francisco, CA (1968) pp. 84-88.

[77] W. Kern and D.A. Poutinen, *RCA Rev.* 31, 187 (1970).

[78] S.M. Sze, *Physics of Semiconducotr Devices, 2nd ed*, John Wiley and Sons, New York (1981) p. 372.

[79] R.H. Kingston and S.F. Neustadter, *J. Appl. Phys.* 26, 718 (1955).

[80] A. Geotzberger, *Bell System Tech. J.* 45, 1097 (1966).

[81] B.E. Deal, M. Sklar, A.S. Grove, and E.H. Snow, *J. Electrochem. Soc.* 144, 266 (1967).

[82] E.H. Nicollian and J.R. Brews, *MOS (Metal Oxide Semiconductor) Physics and Technology,* John Wiley and Sons, New York (1982).

[83] L.S. Wei and J.G. Simmons, *Solid State Elect.* 17, 1021 (1974).

[84] D.K. Schroder, *Semiconductor Material and Device Characterization*, John Wiley and Sons, New York (1990) Chap. 1.

[85] V.M. Dubin, *J. Electrochem. Soc.* 139, 633 (1992).

[86] K. Ohto, K. Ueno, K. Tsunenari, K. Numarjiri, M. Okamura, and H. Jinba, in *Advanced Metallization for ULSI Applications*, edited by D.P. Favreau, Y. Shacham-Diamond, and Y. Horiike, Materials Research Society, Pittsburgh, PA (1994) pp. 151-157. In the same proceedings: K.-I. Lee, B.-Y. Kim, Y.-S. Kim, and S.-K. Joo, pp. 309-315.

[87] T. Ohta, N. Takeyasu, E. Kondoh, Y. Kawano, and H. Yamamoto, in *1994 Proceedings, Eleventh International VLSI Multilevel Interconnection Conference (VMIC)*, (1994) pp. 329-335.

[88] Q.T. Vu, E. Kolawa, L. Halperin, and M-A. Nicolet, *Solid State Electr.* 34, 279

(1991).

[89] A. Charai, S.E. Hörnström, O. Thomas, P.M. Fryer, and J.M.E. Harper, *J. Vac. Sci. Technol. A* 7, 784 (1989).

[90] C.W. Nieh, E. Kolawa, F.C.T. So, and M-A. Nicolet, *Materials Lett.* 6, 177 (1988).

[91] S. Lakshminarayanan, J. Steigerwald, D. Price, M. Bourgeois, T.P. Chow, R.J. Gutman, and S.P. Murarka, in 1994 *Proceedings, Eleventh International VLSI Multilevel Interconnection Conference (VMIC)*, (1994) pp. 49-55. also in *IEEE Electron Dev. Lett.* 15, 307 (1994).

[92] S.J. Proctor, L.W. Linholm, and J.A. Mazer, *IEEE Trans. Electron Dev.* ED30, 1535 (1983).

[93] S.E. Swirhun, W.M. Loh, R.M. Swanson, and K.C. Saraswat, *IEEE Electron Dev. Lett.* EDL-6, 639 (1985).

Appendix I. Diode Process Flow

Process flow by J.S. Reid
Structures built almost entirely by the staff of the MDL, Sandia National Labs

Starting material: ~15 μm, 30-50 Ω cm, p-epi layer on 0.01 Ω cm, p^+ <Si> substrates (backside w/ poly gettering and 1000-2000 Å of oxide)

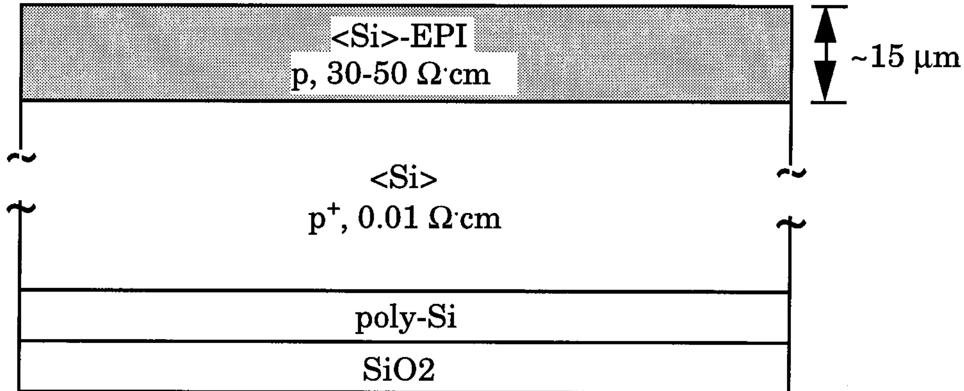

Mask 1 (“250 um Squares A”) and Mask 2 (“300 um Squares B”) :

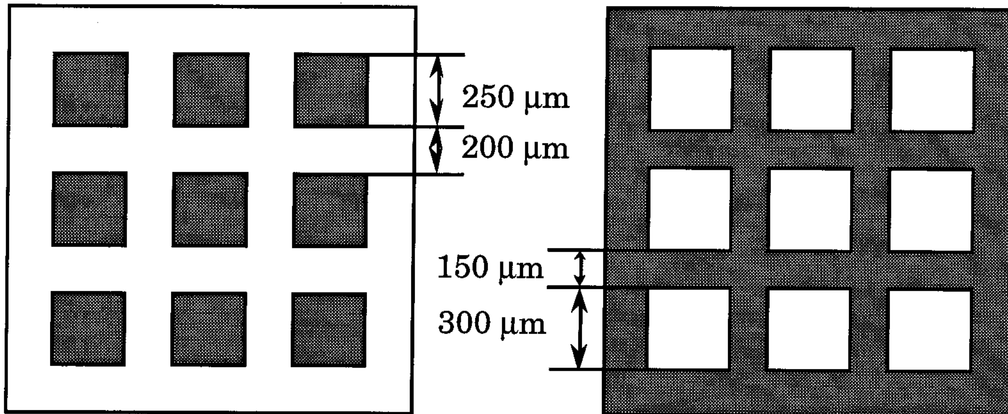

START LOT	1	(use ~15 μm, 30-50 Ω cm, p-epi on 0.01 Ω cm p^+ substrates)
PTUB FILM	8612	PART COUNT
	1002	5:1 DIFFCLN (5 min, H_2SO_4/H_2O_2)
	8613	PARTCL INS
	7220	TUB PAD OX (DRY, 365 Å)
	8030	ELLIP MEAS
	8035	ELLIP ACT
	2700	NITRIDE DEP (1175 Å)
	8031	ELLIP MEAS
	8036	ELLIP ACT

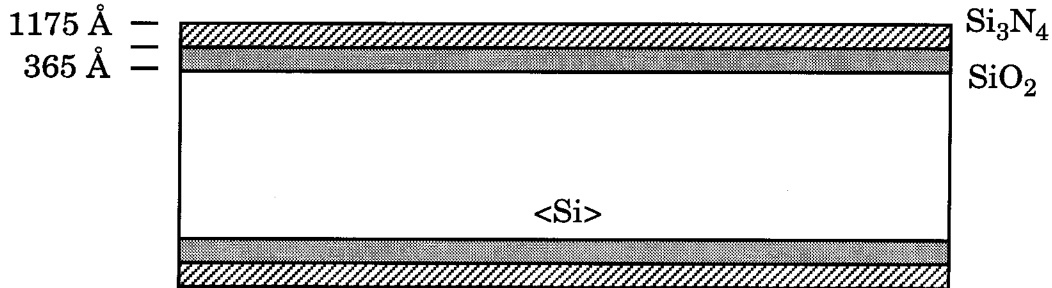

SCRIBE 2MM	9120	SCRIBE 2MM
	1210	AMHYDPEROX

SUSS POLYA

5010 APPLY PR (1.45 μm, Hunt 2O4)
5510 PR BAKE
5341 SUSS EXP (Mask 1)
5400 DEVELOP
5500 BAKE PR
8710 DET PR INS

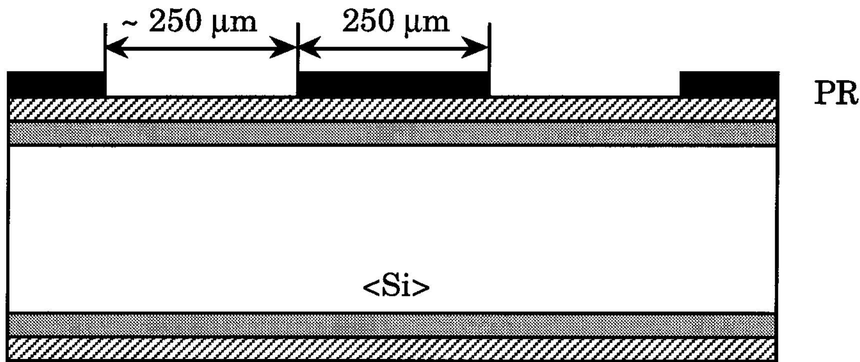

PTUB ETCH

4110 NITRIDE ETCH (RIE)
8730 FINAL INSP
8025 NSPEC ACT

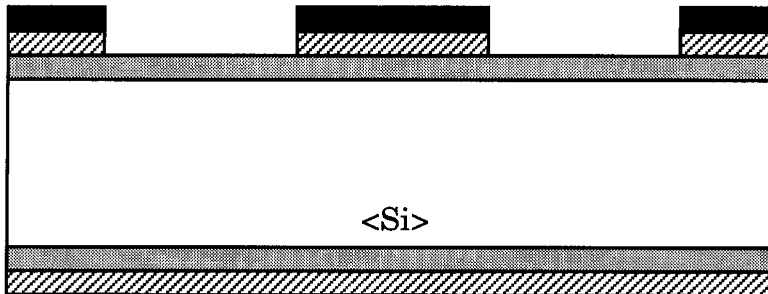

PTUB IMP 3230 P-TUB IMP ($5.7 \times 10^{12}cm^{-2}$, ^{11}B, 50 kev)
8910 RS IMPCON1 (Therma Probe 200)

BORON IMP 3220 BORON IMP (6×10^{12}, ^{11}B, 100 kev)
8910 RS IMPCON1 (Therma Probe 200)

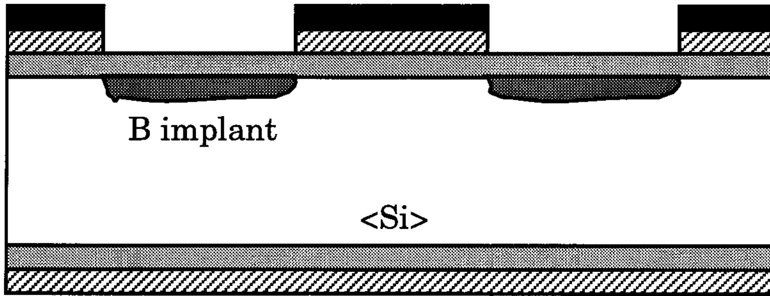

DIOD1 PRST 4200 PR STRIP (O_2 ash)
1010 10:1 SULPER (Piranha strip, H_2SO_4/H_2O_2)

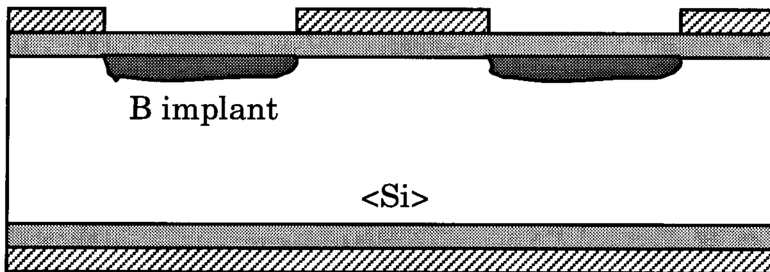

TUB OX	1002	5:1 DIFFCLN
	7120	N TUB OX (5.5 h, 1050°C, 6000-6600 Å, wet)
	8020	NSPEC MEAS (film thickness w/ Nanospec)
	8021	NSPEC MEAS

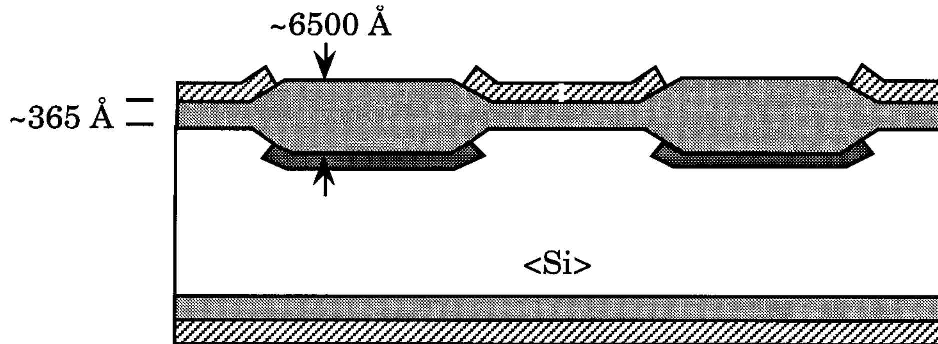

NIT STRIP	1310	BHF ETCH (30 sec, 1:30)
	5025	BK ETCH PR
	5601	UV HRDN PR
	4145	RIE NITBCK
	1312	BHF BKETCH
	4200	PR STRIP
	1010	10:1 SULPER
	4140	RIE NITSTP

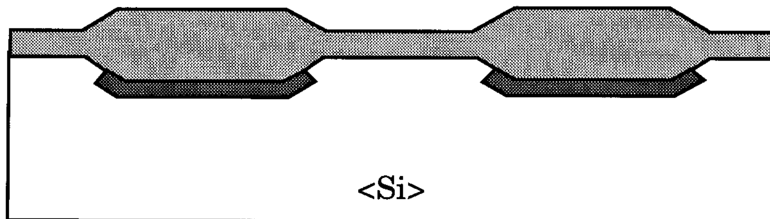

"PAD STRIP" (new route)

1002 5:1 DIFFCLN
1199 NON-STD HF ETCH: 90-120 sec, 15:1 H_2O:HF

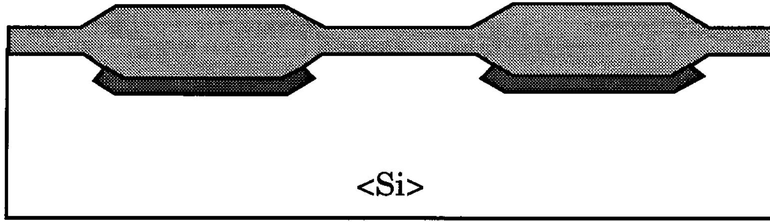

TEOS DENS

1002 5:1 DIFFCLN
7013 TEOS DN (850°C/30 min, dry O_2, 100 Å)

"DIODE IMP" (new route)

3299 SPEC IMP: As^+, 60 keV, 8×10^{15} cm^{-2}
8910 RS IMPCON1 (Therma Probe 200)
1002 5:1 DIFFCLN
7099 SPEC ANNEAL: 950°C/1.5 h, N_2

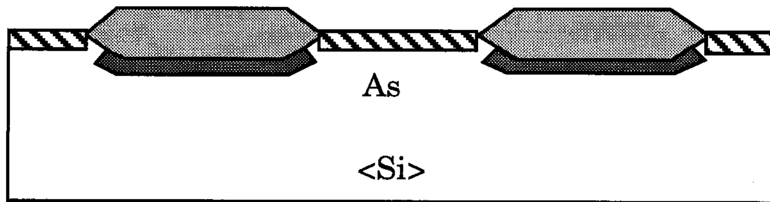

SUSS POLYB	5010	APPLY PR (1.45 μm, Hunt 204)
(really renamed	5510	PR BAKE
SUSS POLYA)	5341	SUSS EXP (Mask 2)
	5400	DEVELOP
	5500	BAKE PR
	8710	DET PR INS

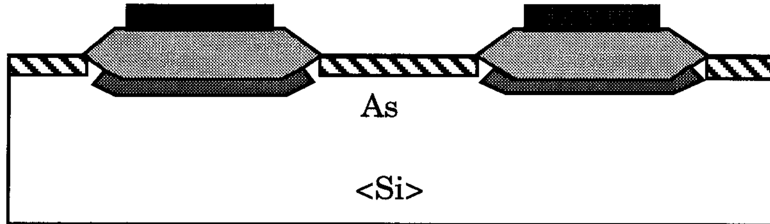

END LOT 10

Appendix II. Process Flow for Fabricating Four-Point Probe Contact Resistivity Structures (topside approach)

Process flow developed and implemented by M. Angyal and D. Lilienfeld at the National Nanofabrication Facility, Cornell University.

I. Wafer Clean

A. Base Bath (removes organics and some metals)

Parameters

- Temperature: 75 °C
- Mixture : 5:1:1 (H_2O:NH_4OH:H_2O_2)
- Time : 10 min
- Rinse : 10 min in DI H_2O with N_2 agitation

B. Acid Bath (removes most metals)

Parameters

- Temperature: 75 °C
- Mixture : 6:1:1 (H_2O:HCl:H_2O_2)
- Time : 10 min
- Rinse : 10 min in DI H_2O with N_2 agitation

C. Buffered HF Bath (removes native oxide)

Parameters

- Temperature: 25 °C
- Mixture : 10:1(H_2O:HF)
- Time : 30 sec
- Rinse : 10 min in DI H_2O with N_2 agitation
- Dry : 3 min spin dry with heat and N_2
- Notes : water resistivity must exceed 16 MΩ·cm

II. Thermal Oxidation

Equipment : Thermco Oxidation Furnace

Parameters

- H_2 flow : 4500 sccm
- O_2 flow : 2500 sccm
- TCA flow : 400 sccm
- Temperature: 1100 °C
- Time : 50 min
- Anneal : 10 min in N_2 at 1100 °C
- Notes : final thickness ~ 540 nm (0.5 μm target)

III. Wafer Clean (not required if wafers do not stand for more than 24 hours)

A. Base Bath (removes organics and some metals)
Parameters
Temperature: 75 °C
Mixture : 5:1:1 (H_2O:NH_4OH:H_2O_2)
Time : 10 min
Rinse : 10 min in DI H_2O with N_2 agitation

B. Acid Bath (removes most metals)
Parameters
Temperature: 75 °C
Mixture : 6:1:1 (H_2O:HCl:H_2O_2)
Time : 10 min
Rinse : 10 min in DI H_2O with N_2 agitation
Rinse : 10 min in DI H_2O with N_2 agitation
Dry : 3 min spin dry with heat and N_2
Notes : water resistivity must exceed 16 MΩ·cm

IV. LPCVD Nitride Deposition

Equipment : Thermco LPCVD Nitride Furnace
Parameters
SiH_2Cl_2 flow: 30 sccm
NH_3 flow : 90 sccm
Pressure : 250 mTorr
Temperature: 800 °C
Time : 23 min
Notes : final thickness ~ 95 nm (100 nm target)

V. Wafers sent to J. S. Reid at Caltech for metal deposition

VI. Wafer Clean

Parameters :
Temperature: 22 °C
Mixture : 10:1 (H_2O:HCl)
Time : 1 min
Rinse : 5 min in DI H_2O
Notes : move to solvent hood with wafers in DI H_2O, spray with isopropanol, blow dry with N_2 and immediat load into PECVD system

VII. PECVD Oxide Deposition

Equipment : IPE Model 1000 PECVD System
Parameters :
- SiH_4 flow : 15 sccm
- N_2O flow : 50 sccm
- Pressure : 450 mTorr
- Temperature: 240 °C
- Power : 50 W
- Time : 15 min (final thickness ~ 500 nm)
- Notes : do not load if platen temperature is greater than 35 °C

VIII. Via Lithography

A. Resist Application

1. Wafer Clean
   Parameters : spin rinse with acetone and isopropanol
2. P-20 Prime
   Parameters : 10 sec puddle; 30 sec at 2500 rpm
3. OCG 897-07 Positive Resist
   Parameters : 10 sec puddle; 30 sec at 2500 rpm
4. Pre-Exposure Bake
   Parameters : 90 sec on 90 °C hot plate
   Notes : final thickness ~ 1.0 μm

B. Pattern Exposure
   Equipment : GCA 6300 10:1 Stepper
   Notes : see Sandia via job file summary

C. Post-Exposure Bake
   Parameters : 90 sec on 115 °C hot plate

D. Resist Development
   Parameters
   - Solution : OCG OPD 262
   - Time : 90 sec with no agitation
   - Rinse : 60 sec immersion in DI H_2O
   - Dry : 30 sec spin dry

E. Post-Development Bake
   Parameters : 60 sec on 115 °C hot plate

IX. Via Etch

A. Resist Descum

Equipment	: PlasmaTherm 72 Reactive Ion Etch System
Parameters	
O_2 flow	: 30 sccm
Pressure	: 60 mTorr
RF power	: 150 W
Time	: 2 min
Notes	: etch rate ~ 100 nm/min

B. Oxide Etch

Equipment	: PlasmaTherm 72 Reactive Ion Etch System
Parameters	
CHF_3 flow	: 50 sccm
O_2 flow	: 2 sccm
Pressure	: 40 mTorr
RF power	: 150 W
Time	: 27 min (20% overetch for 0.5 μm thick oxide)
Notes	: etch rate ~ 24 nm/min; selectivity PR:SiO_2 ~ 1:2; confirm etch rate and selectivity on dummy wafer

C. Resist Strip

Equipment	: PlasmaTherm 72 Reactive Ion Etch System
Parameters	
O_2 flow	: 30 sccm
Pressure	: 60 mTorr
RF power	: 150 W
Time	: 12 min
Notes	: etch rate ~ 100 nm/min; best if done in 4 intervals of 3 min each to minimize resist cross-linking

X. Via and Pad Metal Deposition

A. Ion Beam Clean

Equipment	: NNF Ion Mill System
Parameters	
Pressure	: 0.2 mTorr
Beam voltage	: 500 V_{DC}
Beam current	: 100 mA
Notes	: copper rate ~ 70 nm/min; oxide rate ~ 20 nm/min; load into sputtering system immediately after clean

B. TiW Pre-sputter
Equipment: CVC AST 601 Sputtering System
Parameters

Ar flow	: 40 sccm
Pressure	: 10 mTorr
Current	: 5 A
Voltage	: 460-500 V
Power	: 2.3-2.4 kW
Time	: 15 min

C. TiW Sputter Deposition
Parameters

Ar flow	: 40 sccm
Pressure	: 10 mTorr
Current	: 5 A
Voltage	: 420-460 V
Power	: 2.2-2.3 kW
Time	: 3 min
Notes	: final thickness ~ 50 nm

D. Al Pre-sputter
Parameters

Ar flow	: 40 sccm
Pressure	: 10 mTorr
Current	: 5 A
Voltage	: 380 V
Power	: 1.9 kW
Time	: 15 min

E. Al Sputter Deposition
Parameters

Ar flow	: 40 sccm
Pressure	: 10 mTorr
Current	: 5 A
Voltage	: 370 V
Power	: 1.9 kW
Time	: 30 min
Notes	: final thickness ~ 600 nm

XI. Pad Lithography

A. Resist Application
1. Wafer clean
   Parameters : spin rinse with acetone and isopropanol
2. HMDS Vapor Prime
   Parameters : YES Oven Standard Process
3. Shipley 812L positive resist
   Parameters : 10 sec puddle; 30 sec at 4000 rpm

4. Pre-exposure bake
   - Parameters : 60 sec on 115 °C hot plate
   - Notes : final thickness ~ 1.3 μm

B. Pattern Exposure
   - Equipment : GCA 6300 10:1 Stepper
   - Notes : see Sandia pad job file summary

C. Resist Development
   - Parameters
     - Solution : 3:1 (H_2O:MDC)
     - Time: 2 min with mild agitation
     - Rinse: 60 sec in DI H_2O with mild agitation
     - Dry: 30 sec spin dry

XII. Pad Metal Etch

A. Resist Descum
   - Equipment : Applied Materials Reactive Ion Etch System
   - Parameters
     - O_2 flow : 30 sccm
     - Pressure : 30 mTorr
     - RF power : 90 W
     - Time : 20 sec
     - Notes : etch rate ~ 100 nm/min

B. Al Etch
   - Equipment : Plasma Therm PK-1250 Reactive Ion Etch System
   - Parameters
     - Cl_2 flow : 20 sccm
     - BCl_3 flow : 40 sccm
     - CH_4 flow : 1.4 sccm
     - Pressure : 20 mTorr
     - DC bias : 300 V
     - Time : 7 min (20% overetch)
     - Notes : etch rate ~ 1100 nm/min; appears to etch TiW as well

C. TiW Etch I (higher selectivity to oxide)
   - Equipment : Plasma Therm 72 Reactive Ion Etch System
   - Parameters
     - SF_6 flow : 30 sccm
     - O_2 flow : 2 sccm
     - Pressure : 40 mTorr
     - RF power : 200 W
     - Time : 2 min (10% overetch)
     - Notes : etch rate ~ 60 nm/min; selectivity TiW:SiO_2 ~ 1.5:1

D. TiW Etch II (clears residual TiW)

Equipment : Plasma Therm 72 Reactive Ion Etch System
Parameters
- CF_4 flow : 30 sccm
- Pressure : 40 mTorr
- RF power : 200 W
- Time : 1 min (10% overetch)
- Notes : etch rate ~ 40 nm/min; selectivity TiW:SiO_2 ~ 1:1

E. Resist Strip

Equipment : Plasma Therm 72 Reactive Ion Etch System
Parameters
- O_2 flow : 30 sccm
- Pressure : 60 mTorr
- RF power : 150 W
- Time : 12 min
- Notes : etch rate ~ 100 nm/min; best if done in 4 intervals of 3 min each to minimize resist cross-linking

XIII. Post Process Anneal

Equipment: AG Associates Heatpulse 610
Parameters
- Gas : 95% Ar with 5% H_2
- Gas flow : 25 sccm
- Pressure : atmospheric
- Temperature: 450 °C
- Ramp : 50 °C/sec
- Time : 3 min

Appendix III. Process Flow for Fabricating Four-Point Probe Contact Resistivity Structures (upside-down approach)

Process Flow by J.S. Reid
Fabrication by the staff of the MDL at Sandia National Laboratories, Albuquerque

---

START LOT	1	START LOT
PTUB FILM	1002	5:1DIFFCLN
	7120	N TUB OX
	8020	NSPEC MEAS
	8021	NSPEC MEAS

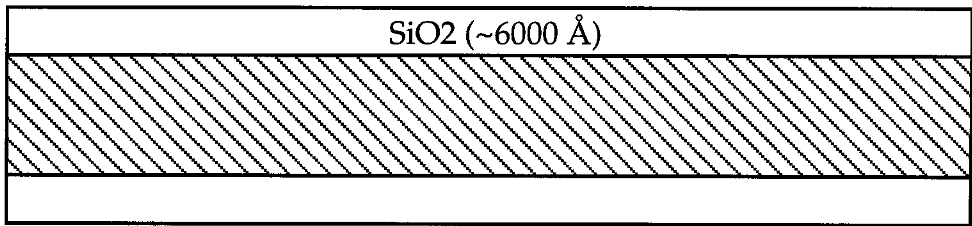

SCRIBE 2MM	9120	SCRIBE 2MM
	1210	AmHydPerox

METAL1A (*new route)	1517	ST CLEAN
	1252	SC-2 CLEAN
	6899	SPCL MET (**DROP THE Ti in 6821 M1 STAK)

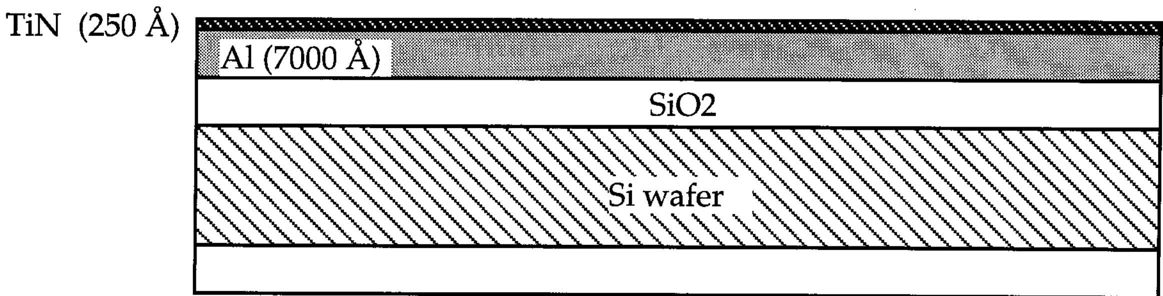

MET1 PHOTO	5054	THMR 1.7um
	5310	GCA EXPOSE
	5430	PR DEV DP1
	8119	CMOSVI REG (skip: unnecessary)
	8108	SEM MEA PR
	8710	DET PR INS
	5800	PHOTO LOG
MET1 ETCH	5630	UV HRDN L
	4399	SPCL METET
	1515	ST METSTRP
	4210	AL PR STRP
	1517	ST CLEAN
	8118	SEM MEA ET

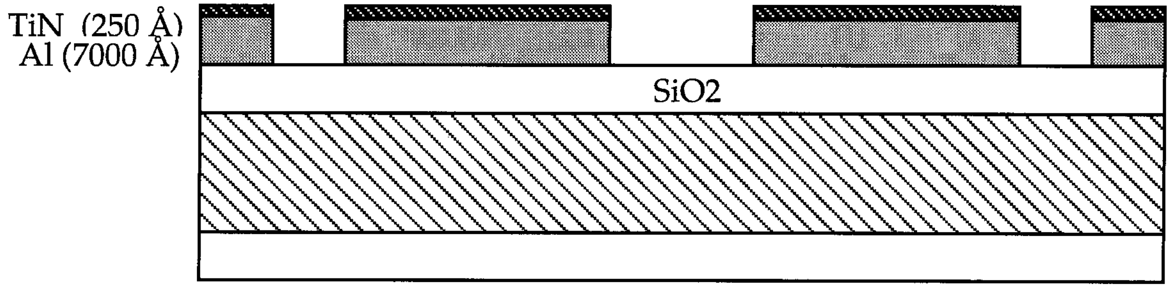

ILD2	2862	PTEOS DEP

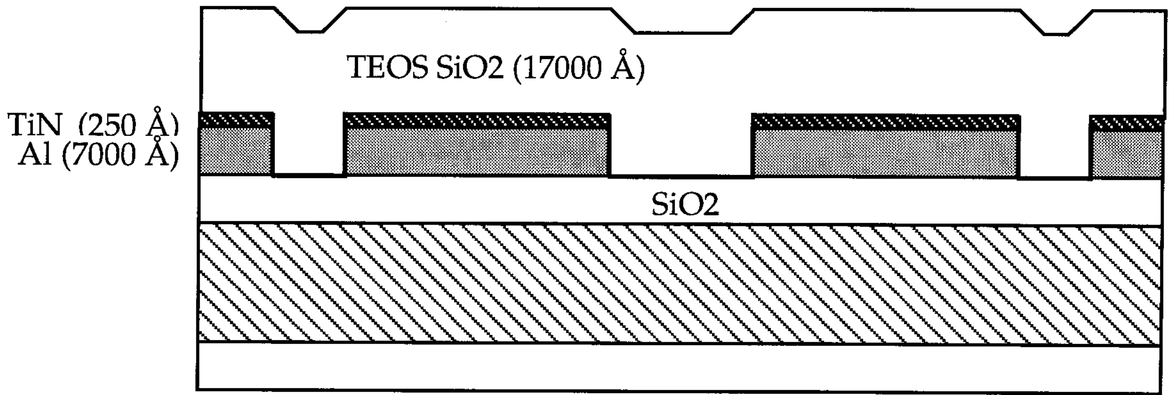

CMP ILD2A 1999 *SPCL CMP
1899 *SPCL PCMP

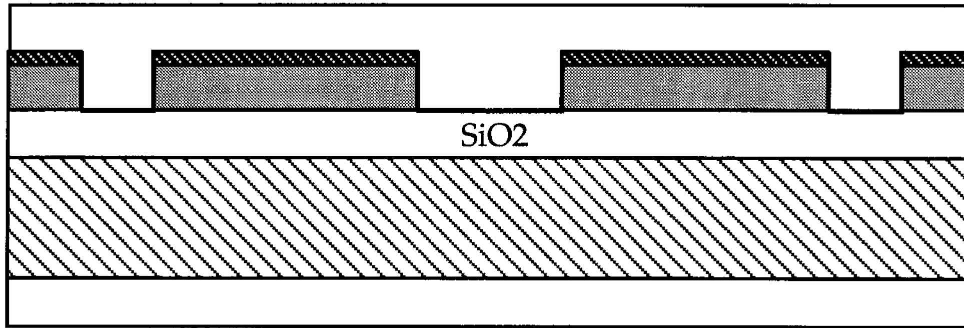

OX BKSTRIP 5025 BK ETCH PR
1320 BHF BKETCH
4200 PR STRIP
1010 10:1SULPER
1003 5:1WET CLN

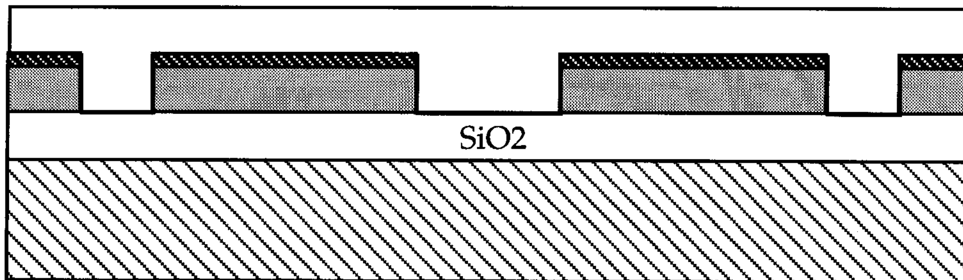

V1 FOTO	5052	THMR 1.2 μm
	5310	GCA EXPOSE
	5430	PR DEV DP1
	8119	CMOSVI REG
	8108	SEM MEA PR
	8710	DET PR INS
	5800	PHOTO LOG
V1 ETCH	5630	UV HRDN L
	4499	*SP OXET
	4210	AL PR STRP
	1510	PRS 1000
	8118	SEM MEA ET

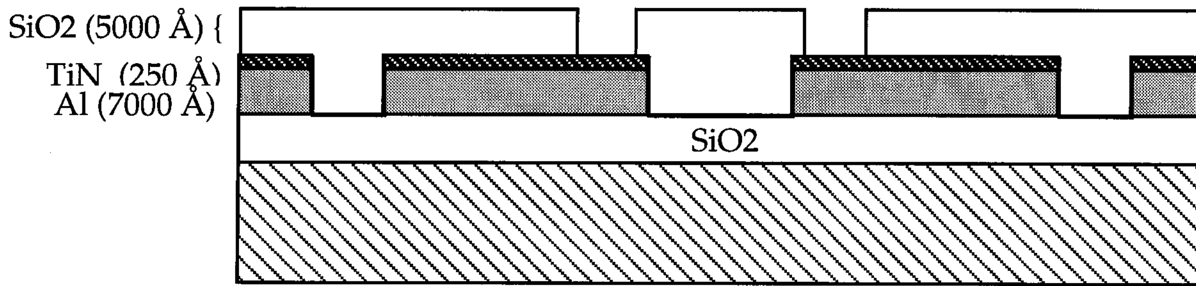

V1 FILL	1517	ST CLEAN
	6811	TIN LINR
	2008	BLKT W.8K

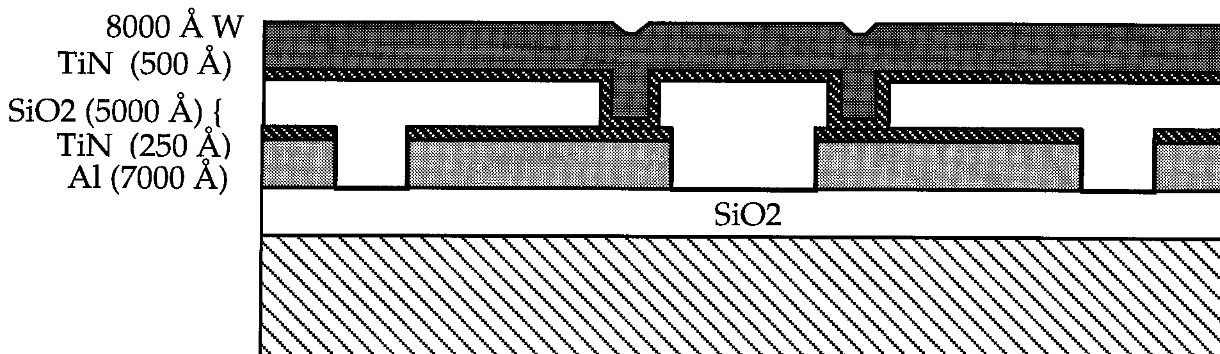

CMP W2A

1999 *SPCL CMP
1899 *SPCL PCMP

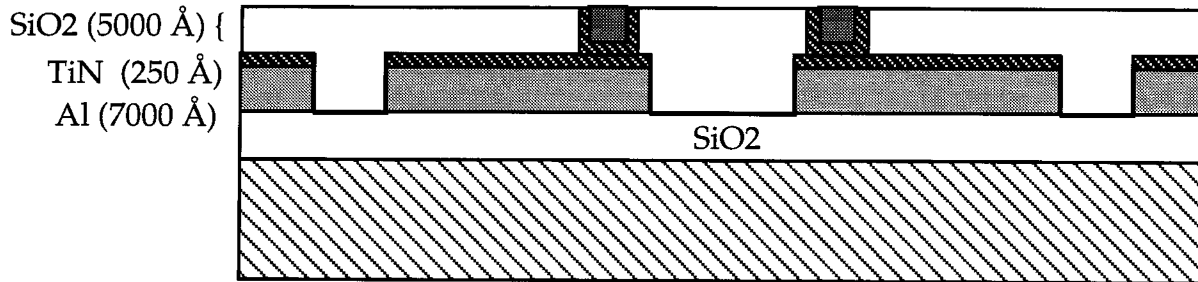

PAD PR
(*new route)

5054 THMR 1.7 µm
5310 GCA EXPOSE
5430 PR DEV DP1
8710 DET PR INS

PAD ETCH
(*new route)

1399 *SPCL WTET (1:15 HF)
1515 ST METSTRP
6899 SPCL MET (150 Å Ar sputter etch)

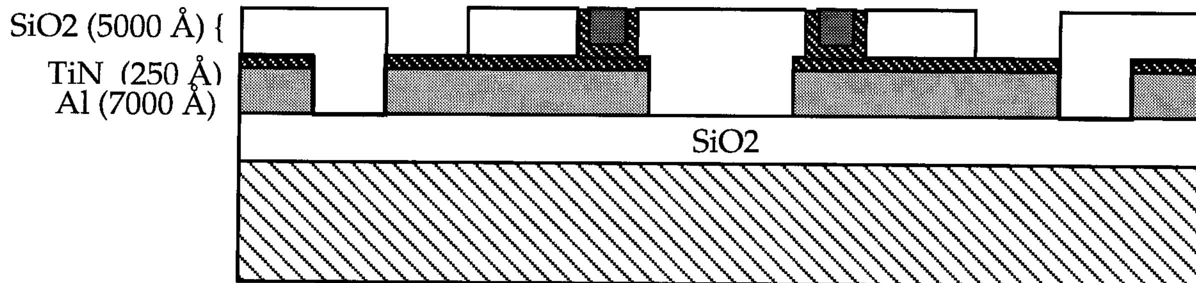

THK LFT PR	5099	*SPCL PR (5 μm Shipley 1045)
(*new route)	5399	*SP EXPOSE (expose on GCA 1300 ms, +1.0 um focus)
	5499	*SPCL DEV (develop for 1:50)
	8710	DET PR INS

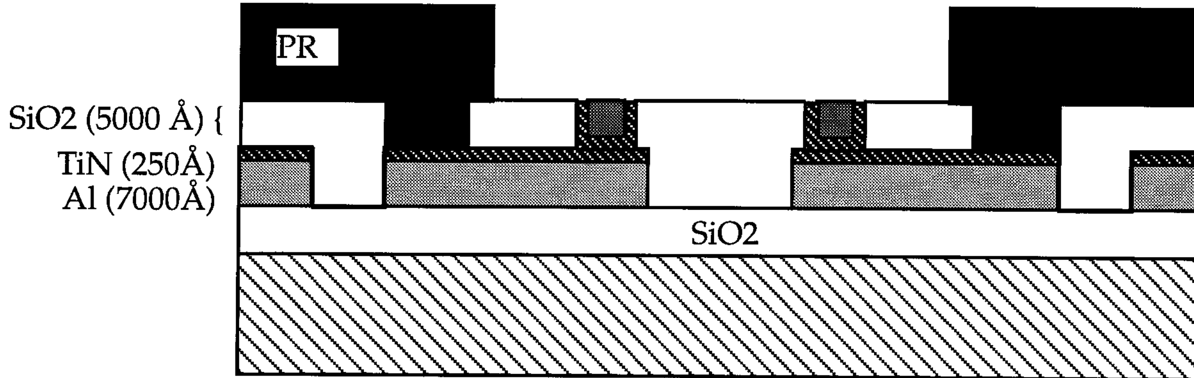

Actual structure has several colinear tungsten plugs serving as probes. After processing at Sandia, the wafers were sent to Caltech for deposition of Cu/barrier/Cu trilayer stack and subsequent lift-off.